

S H Lin
A A Villaeys
Y Fujimura

ADVANCES IN MULTI-PHOTON PROCESSES
AND SPECTROSCOPY

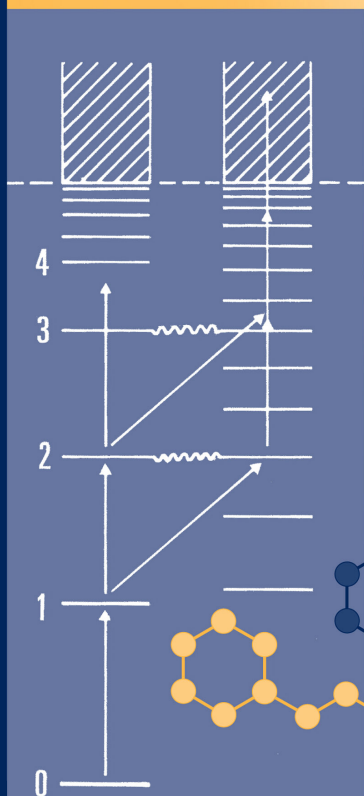
Vol. 17

ADVANCES IN MULTI-PHOTON PROCESSES AND SPECTROSCOPY

Volume 17

Edited by

S H Lin
A A Villaeys
Y Fujimura



World Scientific



ADVANCES IN
MULTI-PHOTON
PROCESSES AND
SPECTROSCOPY

This page intentionally left blank

ADVANCES IN MULTI-PHOTON PROCESSES AND SPECTROSCOPY

Volume **17**

Edited by

S H Lin

*Institute of Atomic and Molecular Sciences,
TAIWAN & Arizona State University, USA*

A A Villaeys

*Institut de Physique et Chimie des
Matériaux de Strasbourg, FRANCE*

Y Fujimura

*Graduate School of Science
Tohoku University, JAPAN*

 **World Scientific**

NEW JERSEY • LONDON • SINGAPORE • BEIJING • SHANGHAI • HONG KONG • TAIPEI • CHENNAI

Published by

World Scientific Publishing Co. Pte. Ltd.

5 Toh Tuck Link, Singapore 596224

USA office: 27 Warren Street, Suite 401-402, Hackensack, NJ 07601

UK office: 57 Shelton Street, Covent Garden, London WC2H 9HE

British Library Cataloguing-in-Publication Data

A catalogue record for this book is available from the British Library.

ADVANCES IN MULTI-PHOTON PROCESSES AND SPECTROSCOPY

Advances in Multi-Photon Processes and Spectroscopy — Vol. 17

Copyright © 2006 by World Scientific Publishing Co. Pte. Ltd.

All rights reserved. This book, or parts thereof, may not be reproduced in any form or by any means, electronic or mechanical, including photocopying, recording or any information storage and retrieval system now known or to be invented, without written permission from the Publisher.

For photocopying of material in this volume, please pay a copying fee through the Copyright Clearance Center, Inc., 222 Rosewood Drive, Danvers, MA 01923, USA. In this case permission to photocopy is not required from the publisher.

ISBN 981-256-646-5

Typeset by Stallion Press

Email: enquiries@stallionpress.com

Printed in Singapore.

CONTENTS

<i>Preface</i>	<i>vii</i>
1 Probing Orbital Symmetries and Ionization Dynamics of Simple Molecules With Femtosecond Laser Pulses	1
<i>C. D. Lin and X. M. Tong</i>	
2 Generalization and Application to Molecular Systems of Keldysh's Atomic Photoionization Theory	29
<i>K. Mishima, K. Nagaya, M. Hayashi, S. H. Lin and E. W. Schlag</i>	
3 Ionization and Fragmentation of Some Organic Molecules with Intense Femtosecond Laser Pulses	179
<i>Nobuaki Nakashima, Tomoyuki Yatsunami, Masanao Murakami, Ryuji Mizoguchi and Yoshinori Shimada</i>	

This page intentionally left blank

PREFACE

In view of the rapid growth in both experimental and theoretical studies of multiphoton processes and multiphoton spectroscopy of atoms, ions and molecules in chemistry, physics, biology, material sciences, etc., it is desirable to publish an Advanced Series that contains review papers readable not only by active researchers in these areas, but also by non-experts who intend to enter the field. The present series attempts to serve this purpose. Each review article is written in a self-contained manner by the experts in the area so that the readers can grasp the knowledge in the area without too much preparation.

The topics covered in this volume are "Probing Orbital Symmetries and Ionization Dynamics of Simple Molecules with Femtosecond Lasers", "Generalization and Application to Molecular Systems of Keldysh's Atomic Photoionization theory" and "Ionization and Fragmentation of Some Organic Molecules with Intense Femtosecond Laser Pulses". The editors wish to thank the authors for their important contributions. It is hoped that the collection of topics in this volume will be useful not only to active researchers, but also to other scientists in biology, chemistry, material sciences and physics.

S. H. Lin
A. A. Villaeys
Y. Fujimura

This page intentionally left blank

1

PROBING ORBITAL SYMMETRIES AND IONIZATION DYNAMICS OF SIMPLE MOLECULES WITH FEMTOSECOND LASER PULSES

C. D. LIN* and X. M. TONG

*J. R. Macdonald Laboratory, Physics Department,
Kansas State University, Manhattan, Kansas 66506-2604, USA,
cdlin@phys.ksu.edu.*

It is shown that by measuring the angular distributions of fragmented ions of simple molecules by sub-10 fs laser pulses at intensities in the non-sequential double ionization regime the electron density of the highest occupied molecular orbital can be probed directly. It is also shown that using a single laser pulse, from the kinetic energy release of the fragmented ions following the double ionization of H_2 , the time interval between the two ionizations can be controlled and determined to sub-fs accuracy by varying the pulse duration and laser intensity. Furthermore, using a pump-probe scheme the time evolution of the vibrational wave packet on two potential surfaces can be mapped directly using two sub-10 fs lasers. Theoretical models are used to explain these recent experiments.

1.1. Introduction

The production of ultra-short optical pulses has opened up an exciting new chapter in the study of molecular dynamics in the last two decades. The wide availability of laser pulses of durations of fractions of picosecond and intensity of the order of 10^{11} W/cm² since the 1990s has led experimentalists to study the molecules' external degrees of freedom such as their orientation in space, or their center-of-mass motion. Such control of molecules offers many new opportunities in the study of stereodynamical effect in chemical reactions and in gas-surface research. In the last decade, continuing development of laser technology has pushed laser pulses of durations to tens of

*Corresponding author.

femtoseconds. Similarly, laser intensity of the order of 10^{14} W/cm² or more are routinely available in most laboratories these days. Within the last few years, new pulse compression technology has made pulses to as short as 5 fs or 4 fs. For such short few-cycle pulses the stabilization and characterization of the carrier-envelope phase is essential, especially in connection with the generation and characterization of attosecond XUV or soft-X-ray pulses.

In this article, we will review some recent progress from the study of simple molecules with femtosecond laser pulses, especially for pulses with duration in the tens to sub-ten femtoseconds, and peak intensity in the range of 10^{13} – 10^{15} W/cm². Our goal is not to offer a comprehensive review of this field. Rather, we would select a few highlights where interesting laser-molecule interaction dynamics have been extracted from experimental results and the results have been quantitatively explained by theoretical calculations. Since direct solution of the time-dependent Schrödinger equation for molecular systems in a laser field under realistic experimental conditions is not practical, theoretical calculations have to be based on some simple models. It is through this close check-and-balance between experiments and theories that our understanding of the dynamics of the interaction of simple molecules with short laser pulses has emerged.

We have chosen three subjects that we will cover in this article:

- (1) We will show that with proper choice of laser intensity and pulse duration, it is possible to map out directly the electron density distribution of the highest occupied molecular orbital (HOMO) from the angular distributions of the atomic ions following the double ionization of molecules by a sub-10 fs laser.
- (2) We will show that by measuring the kinetic energy release of the fragmented ions from the double ionization of H₂ or D₂ molecules, it is possible to measure the time between the two ionizations to sub-femtosecond precision by a single femtosecond laser pulse. In other words, the molecular clock can be read to sub-fs accuracy using a single laser pulse. The time is measured directly with respect to the optical period of the laser (2.6 fs for 800 nm Ti-Sapphire laser), not its pulse duration. By changing the laser intensity and/or pulse duration one can control the time interval between the two ionizations.
- (3) We will show that in a pump-probe arrangement, the motion of the vibrational wave packet on two potential surfaces can be probed directly. The initial pump pulse is used to ionize the molecule and to create a vibrational wave packet. The time evolution of the vibrational wave packet is probed by further ionization with another laser pulse. By varying the time delay between the two pulses, the vibrational wave

packet is mapped from the kinetic energy release of the fragmented ions. For H_2 and D_2 molecules, the motion of the wave packets is shown to be highly nonclassical.

Experimentally the angular distributions and the kinetic energy release of the fragmented ions are determined using the COLTRIMS apparatus^{1,2} where the momentum vectors of the ion fragments are determined at 4π angles simultaneously. The momentum vectors are used to reconstruct the double ionization events. Theoretically, double ionization of molecules leading to the fragmentation is simulated with simple models, by focusing on the different “mechanisms”, and by tracing the time development of the molecule during and after the interaction with laser. Depending on the laser intensity and pulse duration, double ionization can proceed either by sequential double ionization or rescattering double ionization. In the former, double ionizations occur through two successive interactions between the laser’s electric field and the electrons. In the rescattering double ionization, the first ionization occurs through laser-electron interaction. This electron is then driven in the laser field and returns to ionize and remove another electron from the ion. Since the electric field of the laser reaches maximum at each half optical cycle and the electron returning to the ion occurs at well-defined times, double ionization dynamics offers an opportunity to measure the time interval between the two ionizations in terms of the optical period of the laser. This is different from the conventional pump-probe experiments where the time interval is limited by the duration of each pulse. To do the theoretical simulation, it is essential that there is a simple theory to calculate the ionization rate of molecules at any internuclear separations. For the rescattering process, the impact ionization cross sections of the molecular ions by the returning electron are also needed. The time evolution of the electron wave packet and the vibrational wave packet of the molecular ion has to be followed as well in the simulation. Since the molecules are randomly distributed, the alignment of the molecules with respect to the laser polarization direction also has to be considered. Our goal in this review is to address all the elements used in such theoretical simulations. By comparing the theoretical results with experiments, we learned how to understand and how to control the breakup of molecules under intense laser fields.

In Sec. 1.2, we first discuss the simple tunneling ionization theory of molecules by lasers, including its alignment dependence. This theory, with additional assumptions which are valid for short sub-10 fs laser pulses, is used to show that the angular distributions of the double ionization fragments of diatomic molecules directly mimic the electron density

distributions of the highest occupied molecular orbitals. In Sec. 1.3, we show how to read the molecular clocks to sub-fs accuracy using the double ionization of H_2 and D_2 molecules. The time evolution of the vibrational wave packet on two potential surfaces is examined in Sec. 1.4 for H_2^+ and D_2^+ ions theoretically — showing their highly non-classical behavior. It is shown that these wave packets can be probed directly by further ionizing the molecular ions after a time delay and by measuring the energies of the fragmented ions. The experimental results are then shown to be in agreement with theoretical simulations.

1.2. Probing Molecular Orbital Symmetry with Sub-10 fs Laser Pulses

When neutral molecules are subjected to intense laser fields they can undergo single or multiple ionizations, followed possibly by immediate dissociations. Many experiments^{3–5} since the 1990s have shown that the ionized fragments are strongly forward peaked in the direction of the laser polarization. The nature and the mechanism leading to such strong anisotropic angular distributions have been rather unclear. In general one can expect that the ionization rates of molecules depend on the alignment and/or orientation of the molecular axis with respect to the laser polarization direction, but it is also well known that molecules can be aligned by the laser field.⁶ Typically the time it takes to align molecules is of the order of fractions to tens of picoseconds, but experiments using lasers with pulse durations of a few tens of femtoseconds still showed strong forward peaking in the fragment's angular distributions. This has been taken to imply that all molecules are favorably ionized when their molecular axis is aligned with the laser polarization direction. However, recent experiments^{7–10} with laser pulses of duration of less than 10 fs showed that this conclusion is not correct. For such short pulses the angular distributions of the fragments are not always forward peaked. In fact, the experimental angular distributions are in agreement with the alignment-dependence predicted by the recently developed molecular tunneling ionization theory.¹¹ This theory shows that the alignment-dependent ionization rates of molecules are determined predominantly by the orbital symmetries of the highest occupied molecular orbital (HOMO). In these experiments, it has also been shown that the angular distributions are strongly forward peaked if the laser pulses have durations in the tens of femtoseconds, or for the sub-10 fs pulses when the laser intensity is higher.

The latter results have now been attributed to the post-ionization alignment (PIA) effect by Tong *et al.*⁹ For lasers of durations of several tens of femtoseconds, the molecules are hardly aligned by the pulse. However, for such pulses each molecule acquires enough angular momentum (or angular velocity) before ionization. When such a rotating molecule breaks apart by Coulomb explosion, each fragment would rotate an additional angle toward the polarization axis direction before they come to a stop. This PIA effect has been shown to be the most effective in aligning the fragmented ions in the laser polarization direction. Thus to extract alignment-dependent tunneling ionization rates from the angular distributions of fragmented ions, laser pulses of sub-10 fs durations and moderate intensity are needed. We first summarize the molecular tunneling ionization theory.

1.2.1. Molecular tunneling ionization theory

The tunneling ionization theory for atomic hydrogen by a static electric field is a standard textbook subject in quantum mechanics.¹² In the version for the tunneling ionization of atoms by laser fields, in the so-called ADK (Ammosov-Delone-Krainov) model,¹³ the ionization rate has been given analytically. For tunneling ionization, besides the barrier penetration probability, the rate is proportional to the electron density at the far region near the top of the potential barrier (from the combined Coulomb potential and the static field potential). Since the electronic charge density in a molecule is not isotropic it is clear that the ionization rates of molecules in an intense laser field will depend on the alignment of the molecules. For many years such alignment dependence cannot be readily evaluated theoretically until the molecular tunneling ionization theory (MO-ADK)¹¹ was developed. The ionization rates of molecules are also given analytically according to the MO-ADK theory. It further predicts simple alignment dependence of the ionization rates.

For an atom, the wavefunction of the valence electron at large distance where tunneling occurs can be written as

$$\Psi^m(\mathbf{r}) = C_l F_l(r) Y_{lm}(\hat{\mathbf{r}}), \quad (1)$$

where

$$F_l(r \rightarrow \infty) \approx r^{Z_c/\kappa - 1} e^{-\kappa r}, \quad (2)$$

with Z_c as the effective Coulomb charge, $\kappa = \sqrt{2I_p}$, and I_p is the ionization energy. The $Y_{lm}(\hat{\mathbf{r}})$ is the usual spherical harmonics. These expressions are

for an electron with angular momentum quantum numbers ℓ and m . For molecules, the electronic wavefunction is multi-center in nature. To employ the ADK formula directly, one needs to expand the wavefunction in the asymptotic region in terms of one-center expressions. Thus, one writes the molecular wavefunction in the asymptotic region as

$$\Psi^m(\mathbf{r}) = \sum_l C_l F_l(r) Y_{lm}(\hat{\mathbf{r}}), \quad (3)$$

where the summation over ℓ is needed. The quantization axis in this case is along the internuclear axis and $|m|$ is a good quantum number. The coefficients C_l are obtained by fitting the asymptotic molecular wavefunction calculated from other quantum chemistry codes in the form of Eq. (3). The coefficients depend on the internuclear separation and on the electronic state. For molecules at or near the equilibrium distance, only a few partial waves will be needed in the summation. Once the coefficients C_l are available the ionization rate for a diatomic molecule with its axis aligned with the laser polarization is given by

$$w_{\text{stat}}(F, 0) = \frac{B^2(m)}{2^{|m|} |m|!} \frac{1}{\kappa^{2Z_c/\kappa-1}} \left(\frac{2\kappa^3}{F} \right)^{2Z_c/\kappa-|m|-1} e^{-2\kappa^3/3F}, \quad (4)$$

where

$$B(m) = \sum_l C_l Q(l, m), \quad (5)$$

and

$$Q(l, m) = (-1)^m \sqrt{\frac{(2l+1)(l+|m|)!}{2(l-|m|)!}}. \quad (6)$$

Clearly, the factor $B^2(m)$ contains all the information about the electron density in the tunneling region along the direction of the electric field. For electrons in the σ orbitals the electron density is large along the molecular axis. Thus, ionization rates will be large if the molecular axis is aligned in the direction of the laser polarization. For molecules which have outermost electrons in π orbitals, the electron density along the molecular axis vanishes, such that tunneling ionization rates would be zero if the molecular axis is aligned in the laser polarization direction. This is the most transparent consequence of tunneling ionization theory for molecules in a laser field.

If the molecular axis is not aligned along the field direction, but at an arbitrary angle \mathbf{R} with respect to it, then the $B(m)$ in Eq. (4) is obtained through a rotation, and is expressed as

$$B(m') = \sum_l C_l D_{m',m}^l(\mathbf{R}) Q(l, m'), \quad (7)$$

with $D_{m',m}^l(\mathbf{R})$ being the rotation matrix and \mathbf{R} the Euler angles between the molecular axis and the field direction. The static field ionization rate is

$$w_{\text{stat}}(F, \mathbf{R}) = \sum_{m'} \frac{B^2(m')}{2^{|m'|} |m'|!} \frac{1}{\kappa^{2Z_c/\kappa-1}} \left(\frac{2\kappa^3}{F} \right)^{2Z_c/\kappa-|m'|-1} e^{-2\kappa^3/3F}. \quad (8)$$

The ionization rate in a low frequency laser field is obtained by averaging the rates over an optical cycle and is given by

$$w(F, \mathbf{R}) = \left(\frac{3F}{\pi\kappa^3} \right)^{1/2} w_{\text{stat}}(F, \mathbf{R}). \quad (9)$$

where F now stands for the peak field strength.

An immediate direct consequence of the MO-ADK theory is that the ionization rates for any space-fixed molecules are proportional to the electron density in the direction of the laser polarization direction. In other words, by measuring the alignment-dependence of the ionization rates, the electron density of the outermost molecular orbital can be directly probed. This is the most significant prediction of the MO-ADK theory.

1.2.2. *Alignment dependence of tunneling ionization rates and the symmetry of molecular orbitals*

How can one extract the alignment-dependent ionization rates of molecules experimentally? Neutral molecules are not easily aligned by external fields. The angular distributions of singly charged molecular ions after single ionization by a laser pulse are not easily determined due to their small recoil momenta. To measure the orientation of the molecule, or more precisely, the direction of the molecule at the time of ionization, it is most convenient if the ionized molecules break up into two fragmented ions, where the events are clearly identified by their momenta adding up to zero. Such techniques are routinely employed in experiments using COLTRIMS apparatus where the momentum of each individual fragmented ion is measured over 4π angles.

In order to extract the alignment-dependent ionization rates of molecules from such double ionization experiments, additional conditions must be met. First, the laser pulses should not align the molecules before ionization, and that the axis between the two fragmented ions does not entail additional rotation during the breakup process. In other words, there is no adiabatic alignment before the ionization, and the post-ionization alignment effect (PIA) can be neglected. Both effects have been considered

theoretically in Tong *et al.*⁹ and it was concluded that these aligning factors become negligible by going to a short pulse of sub-10 fs duration with moderate intensity (say near or below 10^{14} W/cm²).

In the experiments, since the molecules are doubly ionized by the laser pulse, it is advantageous to choose laser parameters such that the second ionization is isotropic or nearly isotropic with respect to the orientation of the molecules. This is accomplished by using lasers with intensity in the nonsequential double ionization regime. For such processes, the first ionization is by tunneling, and the second ionization is due to the electron impact excitation or ionization by the tunneling ionized electron which has been driven back to collide with the molecular ion by the laser fields. By choosing relatively weak laser intensity with sub-10 fs durations, such experiments have been carried out recently at Kansas State University⁷⁻¹⁰ for a number of molecules. The angular distributions of the fragmented ions give directly the alignment-dependence of the ionization rates which can be compared to the prediction of the MO-ADK theory.

In Fig. 1, we show the angular distributions of the fragmented ions from double ionization by a linear polarized laser⁷⁻¹⁰ and the comparison with the alignment-dependence of the tunneling ionization rates predicted by the MO-ADK theory. Shown are the results for N₂, O₂, CO, CO₂ and C₂H₂. For CO₂, the breakup channel considered was CO₂²⁺ → CO⁺ + O⁺. For C₂H₂²⁺, it is the fragmentation into two CH⁺ ions. These distributions are compared to the alignment-dependent ionization rates of molecules using the MO-ADK theory (2nd column) and with the density distributions of the molecular orbitals (3rd column) from which the electrons have been ionized. The molecular orbitals were calculated from the GAMESS code¹⁴ for molecules at their equilibrium distances and the calculated electronic wavefunctions were visualized by the MOLEKEL program.¹⁵

In Fig. 1, the angular distributions for N₂ and CO are quite similar. The HOMO of N₂ has σ_g symmetry and of CO has σ symmetry, and their angular distributions are peaked in the direction of the laser polarization, in agreement with the fact that the electron density for σ_g (or σ) orbital peaks in the direction of the internuclear axis. (The experiments cannot separate C–O from O–C in the sample so their angular distribution is symmetric.)

In Fig. 1, we also note that the angular distributions for O₂ and CO₂ are very similar. Their angular distributions peak away from the laser polarization direction. The HOMO of each molecule has π_g symmetry, and according to the MO-ADK theory the ionization rate peaks when the molecules are aligned at an angle of about 40° for O₂ and 25° for CO₂, respectively. The latter has a smaller angle because of the larger O–O bond

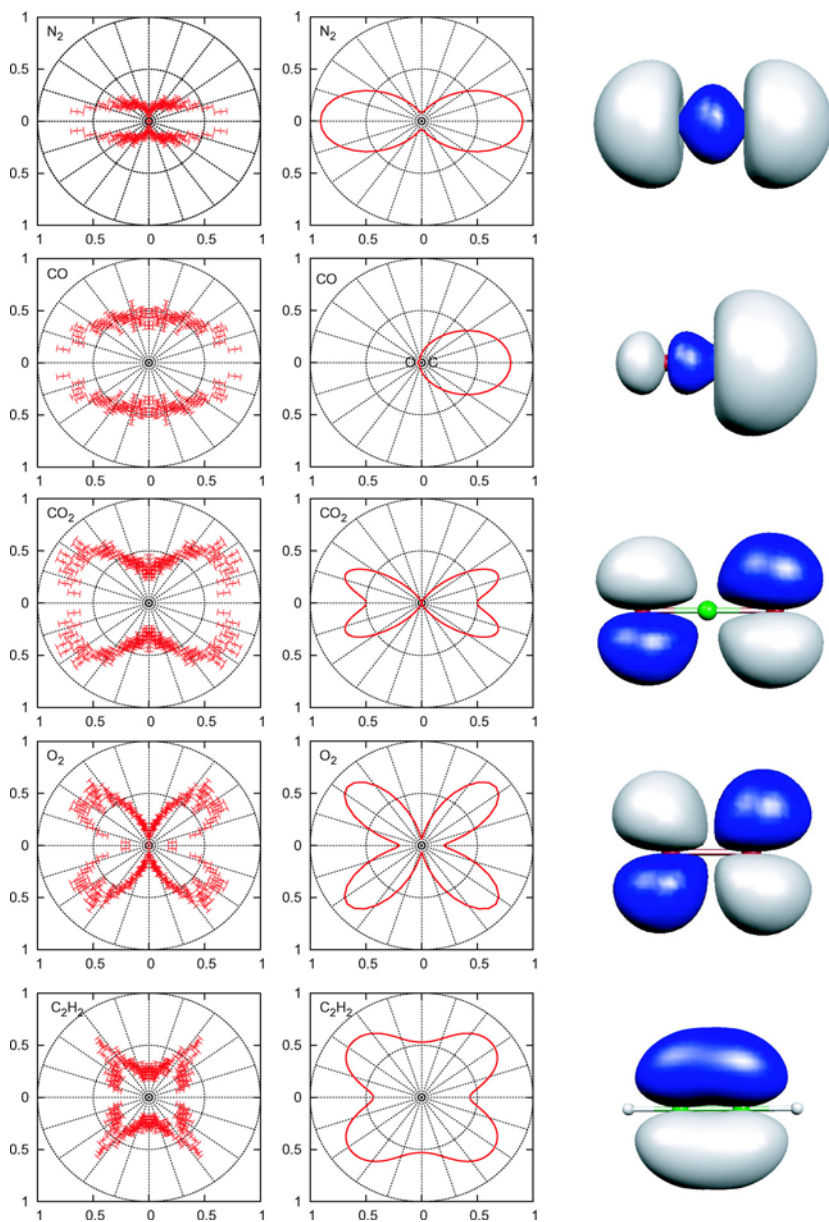


Fig. 1. Comparison of the measured angular distributions of the fragmented ions of the double ionization of molecules (first column) with the alignment-dependent tunneling ionization rates predicted by the MO-ADK theory (second column) for N_2 , CO , CO_2 , O_2 and C_2H_2 , respectively. For each molecule, the laser intensity was chosen in the nonsequential double ionization regime where the second ionization is by electron impact ionization. Sub-10 fs laser pulses are used to avoid additional alignments that modify the measured angular distributions. The corresponding highest occupied molecular orbital for each molecule is also plotted (third column). Experimental data are taken from Refs. 7, 8 and 10.

length. The ionization rates show a minimum in the laser polarization direction instead of zero as would be expected for a pure π_g orbital, reflecting the approximate nature of the pure MO description of the HOMO orbital for wavefunctions in the asymptotic region.

In Fig. 1, the angular distributions of C_2H_2 are also shown. For C_2H_2 , its HOMO has the π_u symmetry. Again, the angular distributions measured are in good agreement with the prediction of the MO-ADK theory and with the symmetry property of the π_u orbital.

The results shown in Fig. 1 clearly indicate that the measurement of the alignment-dependence of tunneling ionization rates provides an experimental verification of the “physical reality” of molecular orbitals (MO). The MO is often considered as a mathematical construct. Its utility is tied closely to the validity of the shell model or the Hartree–Fock approximation for the ground state of molecules. Granted that the results of Fig. 1 only provide the density distributions. However, the approximate nodal planes can be identified from the measured angular distributions such that wavefunctions can be deduced. We note that in most quantum measurements the signal is proportional to the square of the matrix element of an operator taken between the initial and the final states. Thus, it is often difficult to unravel from the measured angular distributions the geometric effect of the initial state and the final state separately. For tunneling ionization of molecules, ionization occurs primarily from electrons initially in the direction of the electric field. In the tunneling process by linearly polarized light the ionized electrons remain in the direction of the electric field. By measuring the breakup of the molecular ion thus gives a direct measurement of the electron density distribution of the outermost orbital if the molecular axis does not undergo additional rotation in the breakup process. These conditions are met for non-sequential double ionization of simple molecules by sub-10 fs laser pulses.

We stress that the use of sub-10 fs laser pulses with relative low laser peak intensity is essential to guarantee that the molecules are not aligned by the lasers before the ionization, nor that the axis of the fragmented ions are rotated in the breakup process. In Fig. 2, we show the comparison of the angular distributions of the nonsequential double ionization of O_2 by 8 fs and 35 fs pulses at peak intensity of $2.0 \times 10^{14} \text{ W/cm}^2$ and $2.2 \times 10^{14} \text{ W/cm}^2$, respectively.⁹ The experimental angular distributions of the O^+ ions are shown on the right. On the left theoretical calculated angular distributions are shown. In the figure, $R(\theta)$ is the angular distribution from the MO-ADK theory alone, $S_0(\theta)$ is the angular distribution predicted by including the alignment of the neutral molecules before

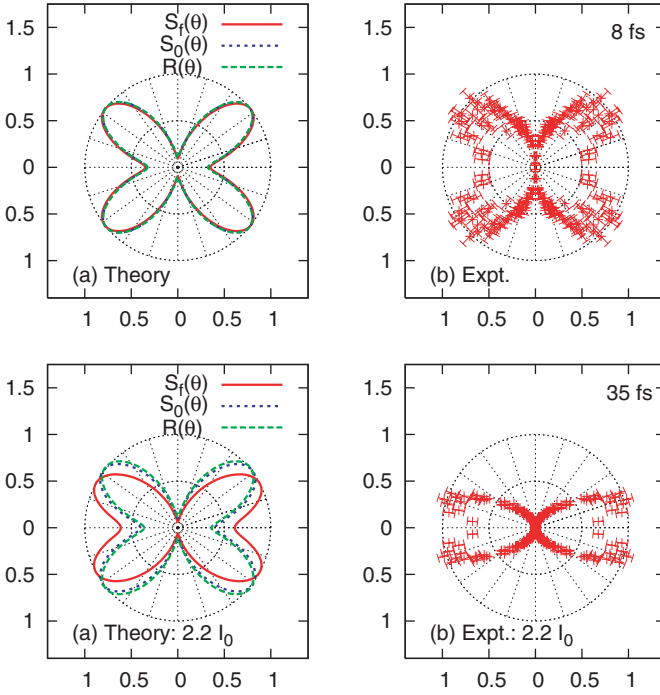


Fig. 2. (upper panel) Comparison of the simulated angular distributions of the fragmented O^+ ions for the double ionization of oxygen molecules by an 8 fs laser pulse at peak intensity of $2.0 \times 10^{14} \text{ W/cm}^2$. $R(\theta)$ is the alignment-dependent ionization signal calculated from MO-ADK theory; $S_0(\theta)$ is the simulated angular distributions calculated including the effect of adiabatic alignment before molecules are ionized; and $S_f(\theta)$ is the same distribution including additional effect from post-ionization alignment (PIA). (lower panel) Same as above but for a 35 fs laser pulse at peak intensity of $2.2 \times 10^{14} \text{ W/cm}^2$.

ionization, assuming that the molecules are ionized at the peak of the laser pulse. For both pulses, this alignment is insignificant. In the figure, the angular distributions $S_f(\theta)$ are also shown. In this case, the post-ionization alignment effect is included. Recall PIA accounts for the additional rotation of the axis of the fragment ions during the breakup process. This effect is small for the 8 fs pulse but significant for the 35 fs pulse. The inclusion of the PIA effect explains why the fragmented ions are strongly forward peaked in the laser polarization direction. For the 35 fs pulse, even though it does not have time to align the molecules significantly, the laser does impart enough angular momentum to each molecule. The PIA is the result of the additional rotation of the molecular axis during the breakup process.

1.3. Attosecond Molecular Clocks: Time-Resolved Double Ionization Dynamics of H₂ and D₂ Molecules

1.3.1. *Dynamics of double ionization of H₂ by femtosecond lasers*

Since the advent of femtosecond lasers, femtochemistry has become possible where chemical reaction dynamics can be probed at the atomic time scale.¹⁶ Pump-probe experiments have been widely used to study the rotational and vibrational wave packets in the presence of laser pulses of durations of tens or hundreds of femtoseconds. Clearly, femtosecond laser pulses are not suitable for measuring or controlling the vibrational motion of simple molecules like H₂ or D₂ which have vibrational periods of about 14 fs and 20 fs, respectively. Recently, however, following the initial suggestion of Corkum and coworkers,^{17,18} it has been shown that it is possible to make time-resolved measurements of the fragmentation of H₂ molecules (our discussions will directly refer to H₂ even though the same description can be used for D₂ as well) using lasers of durations of tens of femtoseconds. The time can be read with the precision of attoseconds, or more precisely, at sub-femtoseconds, using the concept of a molecular clock which ticks with the period of the optical cycle of the laser. The clock is "started" by the first ionization and "stopped" by the second ionization. In this approach, the kinetic energy release of the measured fragments is used to read the internuclear distance of the wave packet as a function of time which is triggered only after the first ionization. By changing the laser intensity, the mean wavelength of the laser, and/or the pulse duration, the time interval between the two ionizations can be read and can be controlled.

Double ionization of H₂ molecules by an intense laser can proceed via (1) sequential double ionization (SI); (2) rescattering double ionization (RES) and (3) enhanced ionization (EI). Their relative importance depends on the laser intensity. These processes are depicted schematically in Fig. 3. For the rescattering double ionization, H₂ is first singly ionized near the peak field of an optical cycle. Upon this ionization, the clock begins to tick. This first ionization launches a correlated electron wave packet and a vibrational wave packet. Under the oscillating electric field, the electron released in the first ionization returns to the parent ion at relatively well-defined times, to excite it to the excited electronic states or to ionize it. If the H₂⁺ is in the excited electronic state, it can dissociate to H⁺ + H, or it can be further ionized by the laser when its electric field reaches

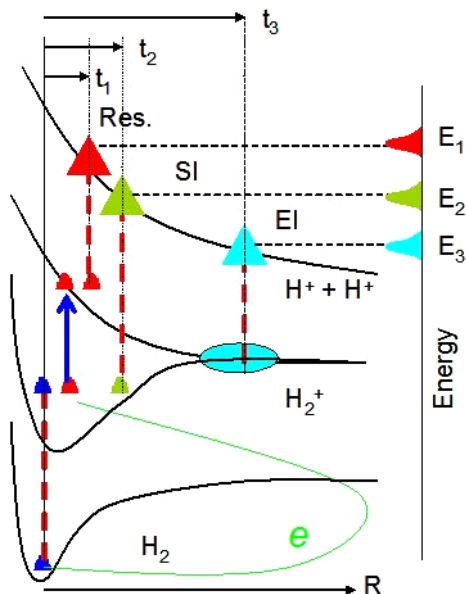


Fig. 3. Schematic of different processes leading to the double ionization of H₂ molecules in an intense laser field.

the peak again. The second ionization leads to H⁺ + H⁺. From the released kinetic energy E₁, the internuclear separation R, where the second ionization occurs, can be determined. Since the propagation of the vibrational wave packet in the ground electronic potential curve of H₂⁺ is well understood, the time t₁ of the second ionization can be read. In the sequential double ionization, the second ionization occurs at time t₂ when the laser electric field reaches the maximum again. Since tunneling ionization rate depends strongly on the ionization energy, SI tends to occur at larger internuclear distances where the ionization potential is smaller, thus resulting in smaller kinetic energy E₂. If the H₂⁺ is not ionized by RES or by SI, some part of the vibrational wave packet can reach large internuclear separation where H₂⁺ can be ionized by charge resonance enhanced ionization (CREI)¹⁹ or enhanced ionization (EI) in short. The released kinetic energies from the EI process are much smaller and have been extensively studied previously.^{20–25} The EI process occurs in the flat region of the potential curve so that time cannot be accurately read.

By choosing proper laser intensity and duration, all of the three processes can be made to contribute to the double ionization of H₂. Figure 4

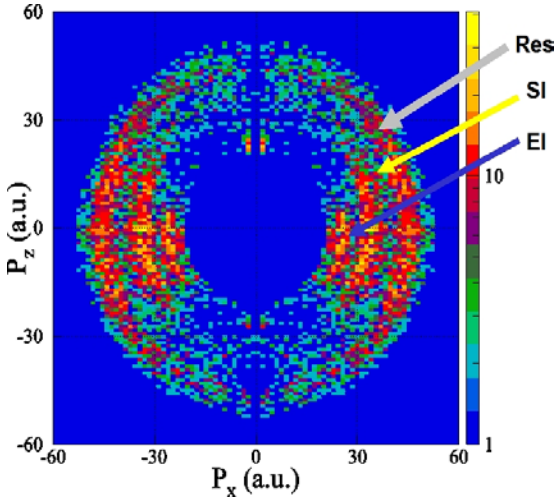


Fig. 4. Momentum image of H^+ pairs from the double ionization of H_2 molecules by a laser pulse of intensity $3 \times 10^{14} \text{ W/cm}^2$. The laser polarization is along the x -direction. The image is taken from Ref. [26].

shows the momentum image of the H^+ pairs produced in the double ionization of H_2 by a 14 fs pulse with peak intensity of $3 \times 10^{14} \text{ W/cm}^2$ as reported by Alnaser *et al.*⁷ The coexistence of RES, SI and EI for the double ionization of H_2 is clearly seen. Figure 4 also shows the angular distributions of the two proton pairs. Clearly, EI is favored only when the molecules are lying nearly parallel to the laser polarization direction. This is consistent with the fact that CREI is the result of the coupling between the ground σ_g and the excited σ_u electronic states. This coupling requires that the laser polarization and the internuclear axis to be parallel to each other. Figure 4 also shows that the angular distributions from the rescattering cover a larger range of angles. This shows that the rescattering process is not very sensitive to the alignment of the H_2^+ ion. Since in the RES, the second ionization is triggered by the impact excitation or ionization of the returning electron. This wave packet is sufficiently broad in the transverse direction and the excitation and ionization cross sections are expected to depend weakly on the alignment of the molecules.

1.3.2. Theory of double ionization of H_2 by femtosecond lasers: rescattering region

To understand and interpret the time-resolved double ionization dynamics of H_2 molecules in a laser field quantitatively, we have developed a

theoretical model that follows the time-evolution of the reaction processes. A more complete schematic diagram of the rescattering processes is given in Fig. 5. On the second row, the time-dependent electric field of the laser is shown. At time t_0 , the H_2 molecule is first ionized from its equilibrium distance. The vibrational wave packet created at this time is sketched on the top row. At t_1 , the ionized electron is driven back to the H_2^+ ion. The electron can excite H_2^+ from the ground electronic state to the excited σ_u or π_u electronic states. Once it is in the excited electronic states, it can dissociate to $\text{H}^+ + \text{H}$, with the release of total kinetic energy characterizing the wave packet at time t_1 . Or it can be ionized by the laser again a quarter optical cycle later at time t'_1 . The resulting doubly charged H_2^{2+} will then Coulomb explode. The two protons can be detected at the end with the total kinetic energy release characteristic of the internuclear separation at the time t'_1 of the second ionization.

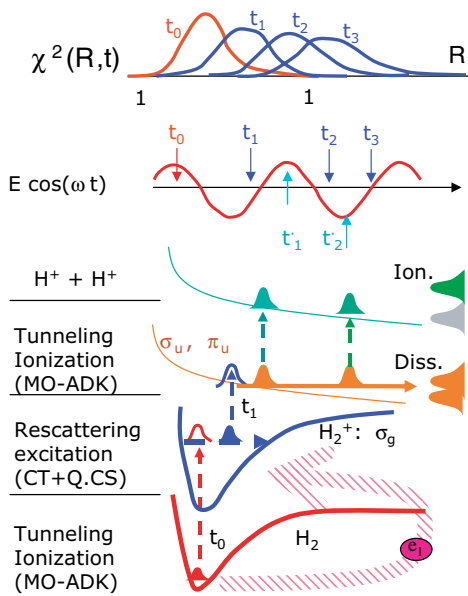


Fig. 5. Schematic of the major physical processes leading to the formation of H^+ ions. The H_2 is first ionized at t_0 creating an electron wave packet which returns to collide with H_2^+ at time t_1 . In the meanwhile the initial vibrational wave packet, measured by $\chi^2(\text{R},t)$, created at t_0 , is shifted to a larger R and broadened at later time. At t_1 , the H_2^+ is excited from σ_g to σ_u and π_u by electron impact. The excited H_2^+ can dissociate directly to give H^+ , or can be further ionized at t'_1 , t'_2 , etc. to produce two H^+ ions by Coulomb explosion. Note that similar rescattering processes can be initiated at later time, t_2 , t_3 , etc., and are included in the calculated H^+ spectra.

For a femtosecond laser pulse, the rescattering process discussed above occurs within one optical cycle after the first ionization. However, additional processes occur after one optical cycle. At time t_2 , the rescattered electron will revisit the ion core, and similarly at time t_3 . At both times the electron can contribute to the excitation of the molecular ion and the further dissociation or ionization. In the meanwhile, the vibrational wave packet continues to move outward to a larger R and the excitation or ionization cross sections have to be calculated from the molecular ions at these internuclear distances.

In Tong *et al.*,^{27,28} the theoretical model for simulating the kinetic energy release spectra for the rescattering double ionization has been discussed in details. It involves the following steps:

- (1) The ionization rate of H_2 from the equilibrium distance at time t_0 is calculated using the MO-ADK theory. The initial vibrational wave packet is given by the Frank–Condon principle. It then freely propagates in the ground potential curve of H_2^+ . This propagation leads to wave packet spreading as time goes on.
- (2) The model for describing the motion of the ionized electron in the laser field is similar to the method used by Yudin and Ivanov²⁹ for He. The electron in the laser field and the Coulomb field of the residual ion is calculated classically by solving Newton’s equation of motion. The initial velocity is assumed to have the distribution as given by the ADK model and the electron’s initial position is along the polarization axis, at the top of the barrier where ionization starts. The electron’s trajectory is calculated for over seven optical cycles (or till when the pulse is over for the short pulses) and the distance of the electron from the ion core is monitored. The time and the kinetic energy when the electron reaches the distance of closest approach are recorded. From these data, we further extract the equivalent asymptotic scattering energy and impact parameters without the presence of the laser field.
- (3) We next need the electron impact excitation cross sections for H_2^+ from the ground state to the excited $2p\sigma_u$ and $2p\pi_u$ states, for the molecular ion fixed in space and for different internuclear separations. Such elementary cross sections are not available. Since the united-atom limit of H_2^+ is He^+ and the separated-atom limit is $H^+ + H$, we fit the excitation cross sections of H and of He^+ from the close-coupling calculations and scaled the scattering energy in terms of excitation energy. We found that the cross sections for both H and He^+ ³⁰ can be well-fitted with only a few parameters. The fitted excitation cross sections are then used to

calculate the excitation cross sections from H_2^+ at different internuclear separations.

- (4) Once the H_2^+ are in the excited states, they can dissociate. Depending on rescattering occurring at t_1, t_3, \dots (the contribution from t_2 is always negligible due to its small return energy), the release kinetic energy from the dissociation will be different. If the excited H_2^+ ions are further ionized by the laser, depending on it occurring at t'_1, t'_2, \dots etc., the released kinetic energy from the Coulomb explosion will be different.
- (5) Recall that at each time t , the vibrational wave packet has a spread and thus the kinetic energy release will have a spread. The kinetic energy release also depends on which excited electronic state is populated by the excitation process.
- (6) Since the first ionization will occur near the peak of the electric field in an optical cycle, we need to integrate over all the contributions over t_0 near the peak of the field. Since the tunneling ionization rate is strongly dependent on the instantaneous electric field, this integration should cover only a small fraction of a femtosecond near the peak field.

By putting all these calculations together, the kinetic energy release can be obtained. Figure 6 shows the kinetic release of D^+ measured by Niikura *et al.*¹⁷ for a 35 fs pulse at a peak intensity of $1.5 \times 10^{14} \text{ W/cm}^2$. In this experiment, only one D^+ ion is measured. Thus the contribution includes both dissociation and double ionization. The results from the theoretical simulation are shown for the three intensities indicated and the results for the three intensities from the theory are normalized at the peak. It shows that the simulation reproduced well the kinetic energy release spectra, particularly at the main peak region.

The theoretical simulation allows us to disentangle the various contributions to the calculated kinetic energy release spectra. This is shown in Fig. 7. We separate contributions occurred within the first cycle or the second cycle after the initial ionization and distinguish D^+ resulting from dissociation or ionization. We clearly see that ionization is much more significant than dissociation and that the main peak in Fig. 6 is the result of double ionization where the rescattering occurs near t_3 . A similar simulation showed that dissociation would become more important for laser intensity of $8 \times 10^{13} \text{ W/cm}^2$.

This comparison demonstrates that to read the molecular clock precisely the mechanism of double ionization of the simple H_2 molecule has to be understood well.

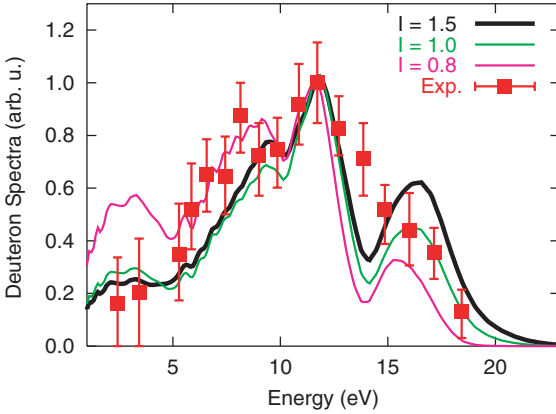


Fig. 6. D^+ ions yield at several intensities for a 35 fs laser pulse ionizing D_2 molecules. The experimental data are from Ref. 18 for intensity at $1.5 I_0$, where $I_0 = 10^{14} \text{ W/cm}^2$. The peak values from the experiment and from the theory for $1.5 I_0$ are normalized to each other. For peak intensities of $1.0 I_0$ and $0.8 I_0$, the yields have been multiplied by 1.4 and 3.0, respectively, to have the same peak ion yield height.

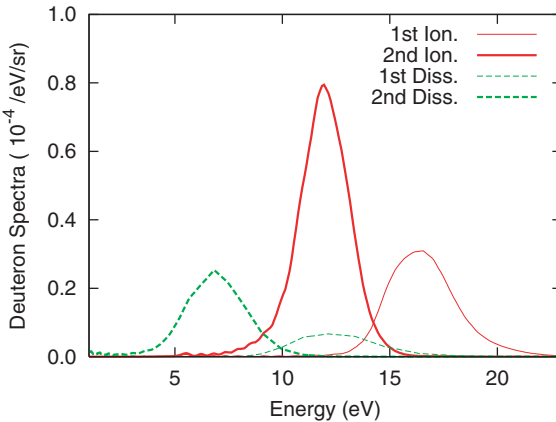


Fig. 7. Decomposition of D^+ ion yields into contributions from dissociation and ionization, and for rescattering occurring within the first and the second optical cycle after the initial tunneling ionization. The peak laser intensity is $1.5 \times 10^{14} \text{ W/cm}^2$ and pulse length is 40 fs.

1.3.3. Control the time sequence of double ionization by tuning laser parameters

From the rescattering theory it is clear that the kinetic energy of the returned electron at the ion core depends on the laser peak intensity, while the relative importance of the first return, the third return, etc., depends on the laser

pulse durations. By changing the laser peak intensity and pulse length, the rescattering-induced Coulomb explosion can be controlled. In Fig. 8, we show the experimental KER spectra resulting from double ionization of H_2 by 30 fs pulse with intensities of 0.9×10^{13} and 2.2×10^{13} W/cm^2 . The experimental data²⁶ are compared with the theoretical calculations.^{27,28} Note that for the higher intensity, the relative contribution from the first return becomes more significant. With the higher intensity the kinetic energy of the returned electron is higher such that the electron impact excitation to the excited state at short time or small internuclear separation is possible. By going to the shorter pulse, say, 8 fs, the data²⁶ shown in Fig. 8 clearly indicate that rescattering from the first return is more important. For the short pulse, the electric field of the laser at the third return is already much weaker such that the third return has much less contribution. Thus from the kinetic energy spectra, in the rescattering double ionization regime, the subsequent

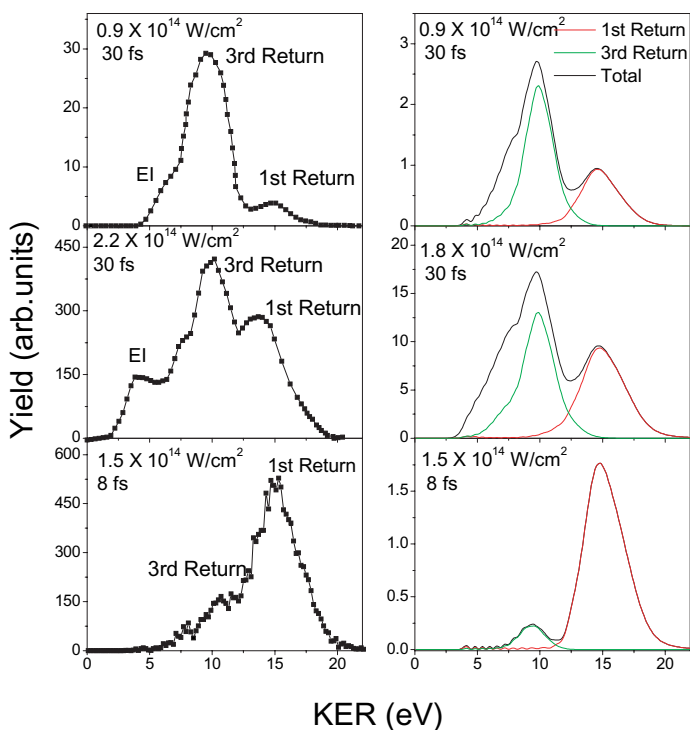


Fig. 8. Comparison of the measured rescattering KER spectra of H_2 in 30 and 8 fs laser pulses.²⁶ The right column shows this comparison as predicted by the rescattering model.^{27,28}

time for the second ionization by the laser following the first ionization can be controlled by changing the laser intensity. The second ionization occurs at a well-specified time, within the first return or the third return. These well-defined return times lead to well-specified internuclear separations at which double ionization occurs, and subsequently, well-defined kinetic energy release. The width of the kinetic energy peaks gives the uncertainty of the time measurements to sub-femtoseconds. They form the basis of the “molecular clocks” where time can be read at sub-femtosecond accuracy. Alternatively, one can also use lasers of different wavelengths. Since the rescattering is measured in terms of the optical period of the laser, by using lasers of different mean wavelengths, the kinetic energy release peaks will shift with the mean wavelength of the laser. This method was used in Niikura *et al.*¹⁸ where the concept of molecular clocks was first reported.

As the laser intensity becomes large, double ionization occurs sequentially.³¹ The first electron is ionized at the beginning part of the laser pulse, followed by the second ionization later where the vibrational wave packet has moved to a larger internuclear separation such that further ionization of H_2^+ is possible. Clearly, each ionization occurs only when the laser intensity reaches the peak at each half optical cycle. By changing the pulse duration, the time for the laser to reach an intensity high enough for the second ionization is longer if the pulse length is longer. Figure 9 shows the time and the internuclear distance where the second ionization occurs for a laser pulse of durations of 5 fs, 10 fs and 15 fs, for laser of peak intensity of $2.8 \times 10^{15} \text{ W/cm}^2$. In this case, the molecular clock is triggered at the first ionization. For the second ionization, it occurs after one, one-and one-half, and two optical laser cycles later, respectively, for the three pulses listed above. Clearly, the kinetic energy release spectra in the sequential double ionization region depend not

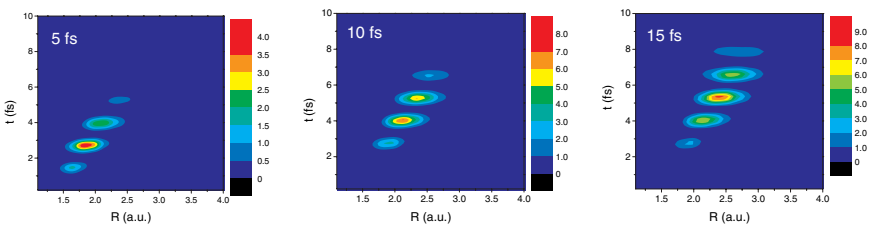


Fig. 9. 2D plots of sequential double ionization spectra of D_2 vs time interval after the first ionization and the internuclear separation. The lasers have pulse durations of 5, 10, and 15 fs and a peak intensity at $2.8 \times 10^{15} \text{ W/cm}^2$.

sensitively with respect to the laser's peak intensity, but the pulse duration is important.

At the higher intensity just discussed, the contribution from the rescattering is negligible. By taking an "intermediate" intensity, both the rescattering and the sequential double ionization can occur and their respective kinetic energy peaks are characterized by the clock for either rescattering or sequential ionization.

1.4. Probing Nonclassical Vibrational Wave Packets on Two Potential Surfaces

The double ionization dynamics described in the previous section focused on the laser- H_2^+ interaction following the first ionization of H_2 from its initial equilibrium distance. This initial ionization creates a vibrational wave packet which propagates outward in the σ_g ground potential curve of H_2^+ . Assuming that the Frank–Condon principle applies, this initial wave packet is given by the ground vibrational wavefunction of H_2 . As this wave packet propagates outward, it will be reflected back as it reaches near the outer classical turning point. In an intuitive classical picture, this vibrational wave packet is to oscillate indefinitely between the inner and outer classical turning points. Quantum mechanical calculations, however, show that the wave packet does not behave this way. The wave packet is rather dispersive, and it will spread as it moves in the σ_g ground potential. The electric field from the laser is not important till at large R where the σ_g potential is separated from the upper σ_u curve by about one unit of photon energy. The strong coupling between these two curves is what is responsible for the dissociation of H_2^+ to $\text{H}^+ + \text{H}$ via bond-softening. Experimentally they are identified by the low energy peaks below 1 eV in the dissociation kinetic energy spectra.³² In other words, the laser can couple σ_g and σ_u potential curves, and the wave packet which rides only on the lower σ_g curve can now be split into two wave packets after the first encounter in the outer turning point region. Now we ask what will happen subsequently to the two wave packets.

From the theoretical point of view, the effect of laser coupling of the two wave packets can be easily calculated by solving the time-dependent wave functions involving the two σ_g and σ_u potential curves by the laser. The modulus square of the two wave packets are shown in Fig. 10 where the density of each wave packet has been displayed vs time. In the model calculation,³³ we assumed a Gaussian laser pulse of width (FWHM) of 8 fs and the D_2 was ionized initially at the peak of the laser pulse. The tail

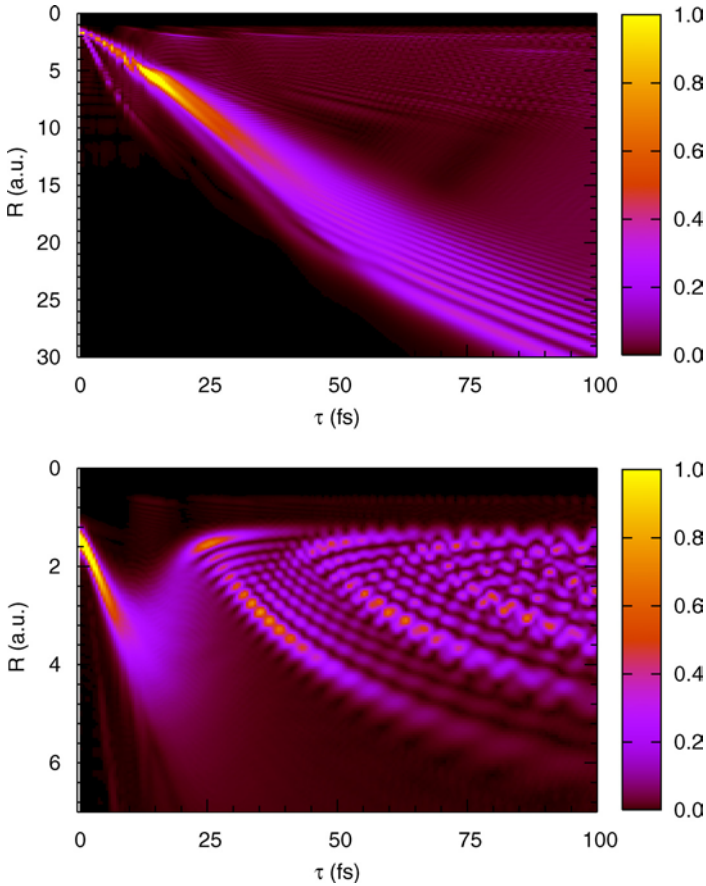


Fig. 10. Time-dependence of the distribution of the vibrational wave packet on the σ_u (upper panel) and σ_g (lower panel) potential surfaces of D_2^+ molecular ions after the initial ionization of D_2 by an 8 fs pulse. Time is measured from the peak of the laser pulse.

of the laser pulse couples the two electronic states. For the wave packet riding on the upper repulsive σ_u potential curve, it moves monotonically outward. At large time one can see broadening, and also splitting, due to the interference of the different components of the wave packet.

The wave packet that is riding on the bound ground σ_g potential shows surprisingly complicated time evolution. In the first half vibrational period, this wave packet simply moves outward to a larger R , with a bit of spreading. Within the next half vibrational period, this wave packet does not return as a recognizable localized wave packet. At each instant, the wave packet is quite spread out. As the time goes on, the wave packet

gradually rebuilds itself near the inner classical turning point. After about one vibrational period, it begins its outward journey again, albeit with a slower mean velocity. In the meanwhile, small interference peaks are clearly seen, resulting from the two oppositely travelling wave packets within the σ_g potential. Clearly, the figure shows that the wave packet that is riding on the bound potential curve is highly nonclassical, and has complicated interference structures.

How should the theoretical simulation for the wave packet dynamics be probed experimentally? With the present-day laser technology, this is most easily done by using a coherent probe laser with sufficient range of time delay to ionize the D_2^+ ion. Such an experiment has been carried out at Kansas State University recently.³³ After the initial pump with an 8 fs pulse with a peak intensity of 3×10^{14} W/cm², an intense 8 fs probe pulse with a higher peak intensity 8×10^{14} W/cm² was used to ionize the D_2^+ ion. This intensity is strong enough to fully ionize the D_2^+ ion if it is in the excited state. It can ionize the D_2^+ ion with probability of the order of 0.1 if the ion is in the ground electronic state, and if the internuclear distance is about 4 a.u. or higher. In other words, the portion of the wave packet associated with the σ_g potential curve can be probed directly if the wave packet has significant distribution in the region larger than 4 a.u. After ionization, the kinetic energy from the Coulomb explosion identifies the internuclear separation where the ionization occurs.

In Fig. 11, the experimental kinetic energy release from the Coulomb explosion is displayed vs the time delay. The stripes of islands of peaks near 6–10 eV clearly can be identified with the wave packet associated with the ground potential curve. There is no indication of the “reflecting” wave packet, in agreement with the simulated wave packet. The single long low energy streak at decreasing kinetic energy clearly indicates that it is the result of ionization from the upper repulsive σ_u potential curve. The kinetic energy release decreases since the ionization occurs at larger internuclear distances with increasing time delay. The experimental results can be compared to the calculated kinetic energy spectra obtained from the theoretical simulation. The agreement between the simulation and the experimental data is very good, supporting the assertion that the wave packet motion is not classical in nature.

There are at least two lessons learned from this elementary experimental study. First, the wave packet dynamics in general is not very classical. Besides the general broadening, the wave packet can undergo major distortion, in regions near classical reflections and in regions where coupling to other channels becomes important. Second, the wave packet can be probed

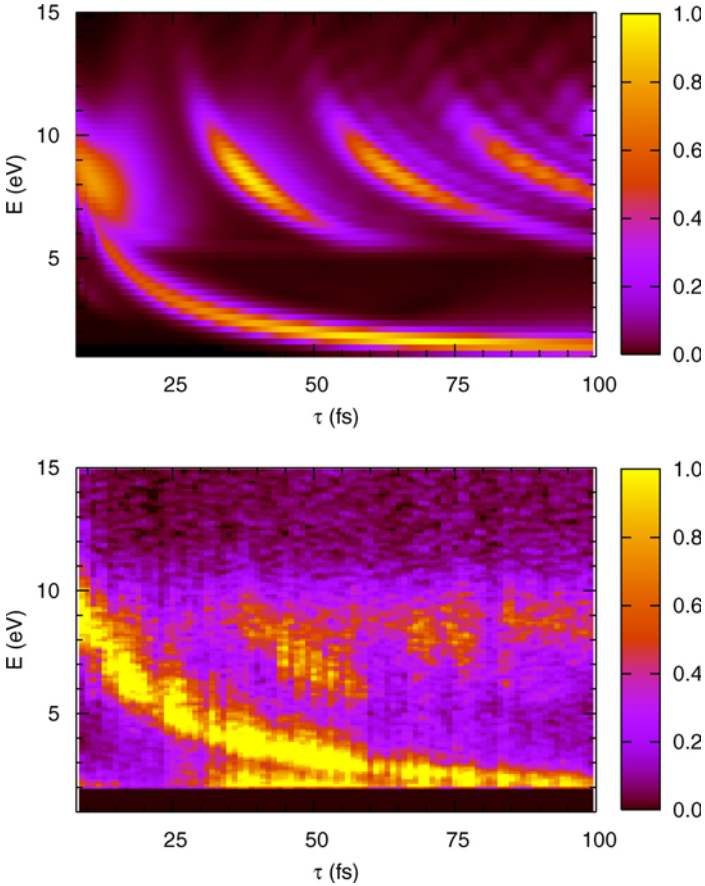


Fig. 11. Kinetic energy release spectra of D^+ ions as a function of time delay between the pump and probe lasers from theoretical simulation (upper panel) and experimental measurement (lower panel). The pulse width of each laser is 8 fs and the peak intensity is $3 \times 10^{14} \text{ W/cm}^2$ for the pump laser and $8 \times 10^{14} \text{ W/cm}^2$ for the probe laser.

or modified in ways depending strongly on the second laser or light source. Using 8 fs laser pulse of a moderate intensity of $8 \times 10^{14} \text{ W/cm}^2$, only the wave packet in the outer region (or larger internuclear separations) can be probed or modified. In other words, the snapshot by the probe pulse did not map out the whole wave packet. To map out the whole wave packet, or to modify the whole packet significantly, one would need to have a photon source with broad energy band. This is achievable only with attosecond pulses with mean wavelength in the extreme ultraviolet regime. Clearly, a “movie” made out of attosecond pulses would see the

whole wave packet that cannot be achieved with present-day femtosecond pulses.

1.5. Summary and Discussion

In this article, we have selected three examples to show how insightful information on the structure and the dynamics of simple molecules can be probed using short intense laser pulses. In the first example, we showed that by properly choosing the laser pulse intensity and duration, the angular distribution of the fragments of ions following the double ionization of molecules can be used to map out directly the geometry (or shape) of the elementary molecular orbitals. Essential to this mapping is the fact that in tunneling ionization the ionization rate is proportional to the electron density in the direction of the laser polarization. By rotating the internuclear axis, one maps out the electron density in the direction of the laser polarization and thus the tunneling ionization rates. We emphasized that sub-10 fs laser pulses are essential and proper laser intensity is needed for such mapping. In the second example, we studied the time sequence of the double ionization of H_2 or D_2 molecules. After the initial ionization by the laser, we showed that the second ionization can occur either by the returning rescattering electron, or by the succeeding peak fields of the laser. The times for rescattering and for sequential ionization are tied directly to the laser's optical period. Thus, double ionization can occur at well-defined time intervals and these time intervals can be measured experimentally from the kinetic energy release of the double ionization fragments. By changing the laser intensity and/or the pulse length, the relative importance of these ionization events can be controlled. Thus, the time interval between the two ionization events can be controlled and can be determined. This forms the idea of the molecular clock where time can be measured accurately to better than 1 fs. In the third example, we showed how to probe simple wave packet dynamics. The wave packet was generated by first ionizing the ground state of H_2 and probed by another short laser pulse after a sequence of time delays. The propagation of the wave packet in the laser field undergoes additional coupling, resulting in the splitting of the wave packet, and subsequently, the wave packet is riding on two potential surfaces. The motion of these two correlated wave packets can be probed simultaneously by another probe laser. The results shows that the wave packets are highly nonclassical. We have shown that to map out the whole wave packet, XUV attosecond pulses would be needed in the future.

In this article, we have shown new insights of the dynamics of molecules have been revealed with the availability of new Ti-Sapphire lasers with pulse durations of less than 10 fs. As the laser pulses are being pushed to shorter durations, to attosecond pulses, and to different mean wavelengths, the tools available to the experimentalists are to increase significantly. By using these different tools, one day the reaction dynamics and its pathway can be controlled completely by experimentalists. On the other hand, without theoretical guidance progress would be greatly hampered in view of the large number of parameters that the experimentalists have to face.

Acknowledgments

This work was supported in part by Chemical Sciences, Geosciences and Biosciences Division, Office of Basic Energy Sciences, Office of Science, U. S. Department of Energy.

References

1. J. Ullrich, R. Moshhammer, R. Dorner, O. Jagutzki, *et al.*, *J. Phys. B* **30**, 2917 (1997).
2. R. Dörner, V. Mergel, O. Jagutzki, L. Spielberger, *et al.*, *Phys. Rep.* **330**, 95 (2000).
3. L. J. Frasinski, K. Codling, P. Hatherly, J. Barr, *et al.*, *Phys. Rev. Lett.* **58**, 2424 (1987).
4. D. T. Strickland, Y. Beaudoin, P. Dietrich, P. B. Corkum, *Phys. Rev. Lett.* **68**, 2755 (1992).
5. C. Guo, M. Li, J. P. Nibarger, G. N. Gibson, *Phys. Rev. A* **61**, 033413 (2000).
6. H. Stapelfeldt, T. Seideman, *Rev. Mod. Phys.* **75**, 543 (2003).
7. A. S. Alnaser, S. Voss, X. M. Tong, C. M. Maharjan, *et al.*, *Phys. Rev. Lett.* **93**, 113003 (2004).
8. S. Voss, A. S. Alnaser, X. M. Tong, C. Maharjan, *et al.*, *J. Phys. B* **37**, 4239 (2004).
9. X. M. Tong, Z. X. Zhao, A. S. Alnaser, S. Voss, *et al.*, *J. Phys. B* **38**, 333 (2005).
10. A. S. Alnaser, C. M. Maharjan, X. M. Tong, B. Ulrich, *et al.*, *Phys. Rev. A* **71**, 031403 (2005).
11. X. M. Tong, Z. X. Zhao, C. D. Lin, *Phys. Rev. A* **66**, 033402 (2002).
12. L. D. Landau, E. M. Lifshitz, *Quantum Mechanics: Non-Relativistic Theory* (Pergamon Press, New York, 1977).
13. M. V. Ammosov, N. B. Delone, V. P. Krainov, *Zh. Eksp. Teor. Fiz.* **91**, 2008 (1986), [*Sov. Phys. JETP* **64**, 1191 (1986)].
14. M. W. Schmidt, K. K. Baldrige, J. A. Boatz, S. T. Elbert, *et al.*, *J. Comput. Chem.* **14**, 1347 (1993).
15. S. Portmann, H. P. Lüthi, *CHIMIA* **54**, 766 (2000).
16. A. H. Zewail, *J. Phys. Chem. A* **104**, 5660 (2000).
17. H. Niiikura, F. Legare, R. Hasbani, A. D. Bandrauk, *et al.*, *Nature* **417**, 917 (2002).
18. H. Niiikura, F. Legare, R. Hasbani, M. Y. Ivanov, *et al.*, *Nature* **421**, 826 (2003).

19. T. Zuo, A. D. Bandrauk, Phys. Rev. A **52**, R2511 (1995).
20. K. Codling, L. J. Frasinski, P. A. Hatherly, J. Phys. B **22**, L321 (1989).
21. T. Seideman, M. Y. Ivanov, P. B. Corkum, Phys. Rev. Lett. **75**, 2819 (1995).
22. E. Constant, H. Stapelfeldt, P. B. Corkum, Phys. Rev. Lett. **76**, 4140 (1996).
23. A. Giusti-Suzor, F. H. Mies, L. F. DiMauro, E. Charron, B. Yang, J. Phys. B **28**, 309 (1995).
24. K. Codling, L. J. Frasinski, J. Phys. B **26**, 783 (1993).
25. A. Bandrauk, Comments At. Mol. Phys. **1 D**, 97 (1999).
26. A. S. Alnaser, X. M. Tong, T. Osipov, S. Voss, *et al.*, Phys. Rev. Lett. **93**, 183202 (2004).
27. X. M. Tong, Z. X. Zhao, C. D. Lin, Phys. Rev. A **68**, 043412 (2003).
28. X. M. Tong, Z. X. Zhao, C. D. Lin, Phys. Rev. Lett. **91**, 233203 (2003).
29. G. L. Yudin, M. Y. Ivanov, Phys. Rev. A **64**, 035401 (2001).
30. I. Bray, <http://atom.murdoch.edu.au/CCC-WWW/index.html>.
31. X. M. Tong, C. D. Lin, Phys. Rev. A **70**, 023406 (2004).
32. K. Sandig, H. Figger, T. W. Hansch, Phys. Rev. Lett. **85**, 4876 (2000).
33. A. S. Alnaser, *et al.*, Phys. Rev. A **71**, 031403 (2005).

This page intentionally left blank

2

GENERALIZATION AND APPLICATION TO MOLECULAR SYSTEMS OF KELDYSH'S ATOMIC PHOTOIONIZATION THEORY

K. MISHIMA[‡], K. NAGAYA*, M. HAYASHI[†], S. H. LIN*
and E. W. SCHLAG[§]

**Institute of Atomic and Molecular Sciences, Academia Sinica,
P. O. Box 23-166, Taipei 10764, Taiwan, ROC.*

[†]*Center for Condensed Matter Sciences, National Taiwan University,
Taipei 106, Taiwan, ROC.*

[‡]*CREST, Japan Science and Technology Agency, 4-1-8 Honcho,
Kawaguchi-shi, Saitama 332-0012, Japan.*

[§]*Institute of Physical and Theoretical Chemistry,
Technical University of Munich, Garching, Germany.*

We present the review of our recent progress of generalization and application to molecular systems of Keldysh's atomic tunneling photoionization theory. The original Keldysh's theory can only treat the photoionization rate of hydrogen-like atoms whereas the theories developed by the present authors are more general. The prominent progresses are (1) the inclusion of the long-range Coulomb potential effect and (2) the inclusion of the Franck–Condon factors and application of the linear combination of atomic orbitals and molecular orbitals for the appropriate treatment of the molecular photoionization rate. These improvements lead to the quite accurate reproduction of the experimental and elaborate numerical results. The physical mechanism of the tunneling photoionization can also be deduced easily and discussed in detail.

2.1. General Introduction

Recently, the physical and chemical phenomena triggered by high power lasers have attracted much attention of many physicists and chemists. This is owing to the recent rapid experimental advancement of tailoring routinely intense ultrashort laser pulses in laboratories. If the laser intensity is very high, the strength of laser-atom/molecule interaction and

electron-nucleus binding energy are comparable, which leads to the phenomena unobservable using the low intensity lasers. In molecules, phenomena more intriguing than those of atoms can be observed due to the additional degrees of freedom induced by many-body particle interactions. In atomic and molecular systems, above threshold ionization and dissociation,^{1,2} bond softening,³ vibrational population trapping,^{4,5} and charge-resonance-enhanced ionization (CREI)⁶ have been predicted theoretically and verified experimentally.

In the atomic systems, multiphoton ionization was observed in the low laser intensity region. In the high laser intensity regime, tunneling photoionization and barrier suppression ionization (BSI) have been predicted theoretically and observed experimentally. For the details, the readers should refer to Ref. 7.

On the other hand, in the molecular systems, multiphoton ionization was predicted and verified in the low laser intensity regime experimentally as well. However, the phenomena by the molecular photoionization in intense laser fields exhibit interesting and novel features where the atomic theories are not adequate; for example, the enhancement of the molecular photoionization rate at some critical distance of the atoms was theoretically predicted by Bandrauk and coworkers,⁸ in addition to the intriguing phenomena mentioned above. For the most part, these molecular phenomena stem from the molecular multi-dimensional nature of constituent atoms. That is, in the high intensity laser fields, the potential barrier width which the electrons feel becomes thinner and the height lower at the outermost atoms, while the complicated behavior takes place in the inner potential barriers. In principle, this leads to the molecule-specific tunneling photoionization or the barrier suppression photoionization that is more difficult to explain than that of atoms.

For the short overview of the actual situation and the prospects for the future of the intense/superintense laser-matter science, the readers should refer to Ref. 9.

If we restrict ourselves to the theoretical developments of formulating the photoionization processes, we notice that many attempts have been made so far by using both the analytical and numerical methods. In this article, for the most part we are interested in the analytical theories that can predict and reproduce the experimental results reasonably.

For example, as for the atomic tunneling photoionization theory, Keldysh–Faisal–Reiss (KFR)^{10–12} and Ammosov–Delone–Krainov (ADK) theories¹³ are very popular in order to account for the photoionization experimental data. Generally speaking, these theories are accurate enough

to reproduce the experimental data of the atomic photoionization rates. In particular, ADK theory has found widespread use in recent years.¹³ This is due to the fact that ADK theory predicts and reproduces the experimental results much better than the KFR theory. In addition, the ADK formula is much simpler and easy to estimate the photoionization rates than the KFR formula. Since there had been no molecular ADK theory, the atomic ADK theory was applied to simple molecular systems such as H_2 , O_2 , N_2 , and so on. In general, the atomic ADK theory reproduced the experimental data very well. However, it should be noticed that the original atomic ADK theory is the atomic theory, not the molecular theory. It can be assumed that the atomic ADK theory was successful simply because the molecules of interest were very small molecules.

Although the original atomic ADK theory has been extensively improved and extended to molecules, no attempt has been made to generalize the original atomic Keldysh theory and extend it to molecules. The present article reviews our generalization and application to molecular systems of the original atomic Keldysh theory.

In this article, we will emphasize that in order to calculate the molecular photoionization rates, the molecular orbital (MO) has to be introduced. In particular, we will adopt the linear combination of atomic orbitals and molecular orbitals (LCAO-MO) in a similar way as Faisal and coworkers.¹⁴

From the numerical results calculated by our extended Keldysh theory, we will find that the original atomic Keldysh theory is not only appropriate to the tunneling photoionization of one-electron hydrogen-like atoms but also to more complicated systems, e.g. single photoionizations of correlated electrons and of molecular systems.

The present article is organized as follows. In Sec. 2.3, we generalize and improve the derivation of photoionization rate formula for one-electron atoms proposed by Keldysh. More exact expressions of the photoionization rate in the tunneling regime have been obtained. In addition, we extend the derivation to photoionization rates of randomly oriented diatomic molecules.

In Sec. 2.4, using the second order Coulomb corrected Volkov function as a continuum state, we quantum-mechanically derive new analytical formulas for photoionization rate of hydrogen-like atoms irradiated by the linearly polarized electric field in the tunneling regime. From our analytical formula is directly drawn an important conclusion that the role of the *first* order Coulomb correction is to lower the ionization potential and enhances the photoionization rates compared with that in the absence of the Coulomb

correction. In addition, the *second* order correction modifies the Keldysh parameter, decreases the binding energy, and increases the photoionization rates relative to that of the *first* order Coulomb correction. We estimate the effects of the respective Coulomb correction on resonance structure of the photoionization rate, Keldysh parameter, ponderomotive energy.

In Sec. 2.5, we demonstrate a detailed derivation of general analytical expressions of photoionization rates of spatially aligned large polyatomic molecules in the tunneling photoionization region. Firstly, *molecular* Coulomb-corrected Volkov function is derived for determining the continuum state and the position dependence of atoms forming the molecule is explicitly included in it. Secondly, using the molecular Coulomb-corrected Volkov function, Keldysh-type photoionization rate formula is derived. For this purpose, LCAO will be used for the initial state. The obtained photoionization rate formula shows that the molecular photoionization rate is the sum of the photoionization rates of the individual occupied orbitals of the atoms forming the molecule that are modified by the position dependence of the atoms, and the quantum interference terms arising from respective occupied orbitals of the constituent identical and different atoms. The formula explicitly indicates that the photoionization rate sensitively depends on the angle between the molecular axis and polarization vector of the linearly polarized laser field, the internuclear distance, and the atomic ionization potential I by the expression $\exp(2\sqrt{2mI\vec{F}} \cdot \vec{R}_j/\hbar F)$. This is a clear indication of the appropriateness of the formulas derived in this article since this is consistent with the experimental and numerical results obtained so far. Using the formula, we show numerical results of photoionization rates of all-*trans* polyacetylene radicals. In addition, from the formula is directly drawn a conclusion that the photoionization rate corresponding to the quantum interference terms is smaller when the distance between the atoms is longer in the case of the laser polarization parallel to the molecular backbone.

In Sec. 2.6, we take into account the Franck–Condon factors and the electron correlations in molecular photoionization processes. We will treat two cases:

(i) H_2 molecules: we extend our previous works on the generalization of Keldysh’s theory to the photoionization processes of molecules. In particular, we include the Franck–Condon factors into our photoionization rate formulas that are based on the use of the molecular orbital theory to describe the electronic degrees of freedom. Inclusion of Franck–Condon factors leads to the proper treatment of the molecular vibrational degrees of freedom. All our formulas consist of the pre-exponential and exponential factors,

and have explicit laser frequency dependence in the same manner as the original atomic Keldysh theory. The latter fact facilitates the exploration of the laser frequency dependence of the photoionization rate, which is more advantageous than the popular ADK formulas. As a consequence, our analytical expressions turn out to be quite instructive to deduce physical meanings of the photoionization processes of molecules. As an example, we have applied our formulas to the photoionization process of H_2 molecule and found that our formulas reproduce the numerical results reported in the literature quite well. Without the Franck–Condon factors our formulas cannot fit the numerical results well, which implies the importance of including properly the Franck–Condon factors for the tunneling photoionization processes of molecules. The results also indicate that the exponential factors which depend on the nuclear equilibrium state play a key role in determining the photoionization rates of the spatially aligned molecules. Comparing the Condon and non-Condon approximations shows that the Condon approximation is usually appropriate for the case of the laser polarization perpendicular to the molecular axis while it is not necessarily true for the parallel case. Our theoretical results are also applied to analyze the experimental data of Urbain *et al.* (2004) for the photoionization process of H_2 molecule.

(ii) Comparison between photoionization processes of N_2 and O_2 molecules: we reexamine the photoionization rates of N_2 and O_2 molecules using our molecular Keldysh theory. We have found that the constructive quantum interference takes place for N_2 molecule while the destructive quantum interference plays an important role for O_2 molecule. This is consistent with the experimental and theoretical results reported in the literature. The formulas derived in this article clearly shows that this is due to the different symmetries of the valence orbitals of N_2 and O_2 molecules.

In Sec. 2.7, based on Keldysh's theory, we theoretically investigate the possibility to use the molecular orbital (MO) theoretic approach for calculating the tunneling photoionization rates of atoms and molecules. As a first step, we shall concentrate on the $1s$ state of the hydrogen atom as the initial state. We decompose the initial Slater-type ($1s$) orbital (STO) into the linear combination of Gaussian-type orbitals (GTO) in the same manner as quantum chemistry calculations. In particular, STO-NG ($N = 1 \sim 4$) basis sets are investigated. It has been found that if the primitive GTOs are more diffuse, its contribution to the total tunneling photoionization rate becomes more predominant. This derives from the fact that the exponential factors in the tunneling rate formulas linearly depend on the inverse of the exponents of the primitives. In addition, we have found that increasing N

counterintuitively does not necessarily improve the photoionization rate. This is because the primitive dominating the photoionization rate fits the STO much worse as N increases. This work is the first step towards the realization of quantum chemistry approach of tunneling photoionization processes in strong laser fields.

In Sec. 2.8, a brief account of *ab initio*/RRKM approach for investigating more elaborately the processes of molecules in strong laser fields will be given.

Finally, Sec. 2.9 is devoted to the concluding remarks.

2.2. Original Atomic Keldysh Theory

The first theoretical treatment of atomic tunneling photoionization in intense laser fields was performed by Keldysh.¹⁰ Using the first-order perturbation theory, he systematically derived the photoionization rate formula for the direct transition between the electronic ground state and the Volkov continuum state that includes the oscillatory motion of the freely ionizing electron in the time-dependent linearly polarized electric field. One of the remarkable features of Keldysh theory is that the so-called Keldysh parameter γ is useful to distinguish between the multiphoton and tunneling photoionization regions,

$$\gamma = \omega\sqrt{2mI_0}/eF. \quad (1)$$

Here, ω is the laser frequency, m the mass of electron, I_0 the ionization potential, e the unit charge of the electron, and F the laser amplitude. Qualitatively, multiphoton ionization takes place when $\gamma \gg 1$ while tunneling ionization does when $\gamma \ll 1$. The Keldysh parameter can also be interpreted as the ratio of the characteristic time that the electron takes to pass through the barrier formed by the electric field and static atomic potential to the cycle time of the oscillating electric field. This is expressed as

$$t_t = \sqrt{mI_0}/\sqrt{2eF}, \quad (2)$$

which is the mean tunneling time of the electron passing through the potential barrier formed by the electric field and the static atomic potential. Actually, this can be recognized using Eqs. (1) and (2),

$$\gamma = 2\omega t_t. \quad (3)$$

In the tunneling limit $\gamma \rightarrow 0$, Keldysh formula reduces to the well-known ionization rate formula in a static electric field.¹⁵

Next, let us review the derivation of the original atomic Keldysh theory in the following since the derivation in the original paper¹⁰ is too insufficient to understand in detail. In addition, if we follow the original atomic Keldysh

theory, we can clearly find out the problems in the theory. As far as we know, the detailed derivation of the original atomic Keldysh theory has not been reported elsewhere.

First, we have to define the freely ionizing electron wavefunction in the electric field. The time-dependent Schrödinger equation for the electron in the velocity gauge is expressed as

$$i\hbar \frac{\partial}{\partial t} \psi_A(\vec{r}, t) = \left\{ \frac{1}{2m} [-i\hbar \vec{\nabla}_r - e\vec{A}(t)]^2 + V(\vec{r}) \right\} \psi_A(\vec{r}, t), \quad (4)$$

where m is the mass of the electron, $V(\vec{r})$ the Coulomb potential between the ionizing electron and the remaining atom, which is usually given by

$$V(\vec{r}) = -Ze^2/r, \quad (5)$$

and $\vec{A}(t)$ the vector potential written as

$$\vec{A}(t) = -(\vec{F}/\omega) \sin \omega t. \quad (6)$$

If we neglect $V(\vec{r})$, Eq. (4) can be solved easily and $\psi_A(\vec{r}, t)$ is given by

$$\psi_A(\vec{r}, t) = \exp \left[\frac{i}{\hbar} \left\{ \vec{p} \cdot \vec{r} - \frac{1}{2m} \int_0^t dt' [\vec{p} - e\vec{A}(t')]^2 \right\} \right], \quad (7)$$

where \vec{p} is some fixed momentum of the electron. The wavefunction, $\psi_A(\vec{r}, t)$, is usually called Volkov function in the velocity gauge.

On the other hand, in the length gauge, the total Hamiltonian in the length gauge, $\hat{H}_F(t)$, is given by

$$\hat{H}_F(\vec{r}, t) = -\frac{\hbar^2}{2m} + V(\vec{r}) - \vec{d} \cdot \vec{F}(t), \quad (8)$$

where \vec{d} is the dipole transition moment and $\vec{F}(t)$ is the electric field written as

$$\vec{F}(t) = \vec{F} \cos \omega t \quad (9)$$

Therefore, the time-dependent Schrödinger equation in the length gauge is written as

$$i\hbar \frac{\partial}{\partial t} \Psi(\vec{r}, t) = \hat{H}_F(\vec{r}, t) \Psi(\vec{r}, t). \quad (10)$$

Here also, if we neglect $V(\vec{r})$, the solution of Eq. (10) is given by

$$\psi_{\vec{p}}(\vec{r}, t) = \exp \left[\frac{i}{\hbar} \left\{ [\vec{p} - e\vec{A}(t)] \cdot \vec{r} - \frac{1}{2m} \int_0^t dt' [\vec{p} - e\vec{A}(t')]^2 \right\} \right], \quad (11)$$

which is called the Volkov function in the length gauge.

Let us assume that the electron wavefunction, $\Psi(\vec{r}, t)$, is expressed as

$$\Psi(\vec{r}, t) = \psi_g(\vec{r}) \exp(-iE_g t/\hbar) + \int d^3 p c_{\vec{p}}(t) \psi_{\vec{p}}(\vec{r}, t), \quad (12)$$

where $\psi_g(\vec{r})$ is the ground state electron wavefunction, E_g the eigenenergy of the ground state, and $c_{\vec{p}}(t)$ the wavefunction amplitude of the freely ionizing electron, which is the main physical quantity we want to solve in the following. Since the wavefunction amplitude for $\psi_g(\vec{r})$ is fixed and unity, Eq. (12) assumes the first-order perturbation theory.

Substituting Eq. (12) into Eq. (10) and noting that

$$\left\{ -\frac{\hbar^2}{2m} \nabla_r^2 + V(\vec{r}) \right\} \psi_g(\vec{r}) = E_g \psi_g(\vec{r}) \quad (13)$$

and

$$\begin{aligned} i\hbar \frac{\partial}{\partial t} \psi_{\vec{p}}(\vec{r}, t) &= \left\{ -\frac{\hbar^2}{2m} \nabla_r^2 - \vec{d} \cdot \vec{F}(t) \right\} \psi_{\vec{p}}(\vec{r}, t) \\ &= \left\{ \frac{[\vec{p} - eA(t)]^2}{2m} - \vec{d} \cdot \vec{F}(t) \right\} \psi_{\vec{p}}(\vec{r}, t) \end{aligned} \quad (14)$$

yield

$$\begin{aligned} i\hbar \int d^3p' \dot{c}_{\vec{p}'}(t) \psi_{\vec{p}'}(\vec{r}, t) &= -\vec{d} \cdot \vec{F}(t) \psi_g(\vec{r}) \exp(-iE_g t/\hbar) \\ &\quad + \int d^3p' c_{\vec{p}'}(t) V(\vec{r}) \psi_{\vec{p}'}(\vec{r}, t). \end{aligned} \quad (15)$$

Multiplying $\int d^3r \psi_{\vec{p}}^*(\vec{r}, t)$ from the left hand side of Eq. (15), using Eq. (11), and using the orthonormality of the Volkov function,

$$\int d^3r \psi_{\vec{p}}^*(\vec{r}, t) \psi_{\vec{p}'}(\vec{r}, t) = \delta(\vec{p} - \vec{p}'), \quad (16)$$

we obtain

$$\begin{aligned} i\hbar \dot{c}_{\vec{p}}(t) &= -\langle \psi_{\vec{p}}(\vec{r}, t) | \vec{d} \cdot \vec{F} | \psi_g(\vec{r}) \rangle \exp(-iE_g t/\hbar) \cos \omega t \\ &\quad + \int d^3p' c_{\vec{p}'}(t) \langle \psi_{\vec{p}}(\vec{r}, t) | V(\vec{r}) | \psi_{\vec{p}'}(\vec{r}, t) \rangle. \end{aligned} \quad (17)$$

In the original atomic Keldysh theory, the second term of the right hand side of Eq. (17) is assumed to be neglected: the Coulomb interaction between the ionizing electron and the remaining atom is totally ignored. This is a very crude approximation and it is easy to understand that if the Coulomb interaction and the interaction between the electron and the laser field compete, this approximation will pose a serious problem. Under this assumption, Eq. (17) becomes

$$c_{\vec{p}}(t) = \frac{i}{\hbar} \int_0^t \langle \psi_{\vec{p}}(\vec{r}, t') | \vec{d} \cdot \vec{F} | \psi_g(\vec{r}) \rangle \exp(-iE_g t'/\hbar) \cos \omega t' dt'. \quad (18)$$

The total photoionization probability, W , is defined by

$$W = \int \frac{d^3p}{(2\pi\hbar)^3} |c_{\vec{p}}(T)|^2 \Big|_{T \rightarrow \infty}. \quad (19)$$

Therefore, the photoionization rate, w_0 , is given by

$$w_0 = \frac{d}{dT} \int \frac{d^3p}{(2\pi\hbar)^3} |c_{\vec{p}}(T)|^2 \Big|_{T \rightarrow \infty} = 2 \operatorname{Re} \int \frac{d^3p}{(2\pi\hbar)^3} \dot{c}_{\vec{p}}^*(T) c_{\vec{p}}(T) \Big|_{T \rightarrow \infty} \quad (20)$$

Substituting Eq. (18) into Eq. (20), we obtain

$$\begin{aligned} w_0 &= \frac{2}{\hbar^2} \lim_{T \rightarrow \infty} \operatorname{Re} \int \frac{d^3p}{(2\pi\hbar)^3} \int_0^T dt \cos(\omega t) \cos(\omega T) V_0^* \\ &\quad \times \left(\vec{p} + \frac{e\vec{F}}{\omega} \sin \omega T \right) V_0 \left(\vec{p} + \frac{e\vec{F}}{\omega} \sin \omega t \right) \\ &\quad \times \exp \left[\frac{i}{\hbar} \int_T^t dt \left\{ I_0 + \frac{1}{2m} \left(\vec{p} + \frac{e\vec{F}}{\omega} \sin \omega \tau \right)^2 \right\} \right], \end{aligned} \quad (21)$$

where

$$V_0(\vec{p}) = \int \exp(-i\vec{p} \cdot \vec{r}/\hbar) e\vec{F} \cdot \vec{r} \frac{1}{\sqrt{\pi a_0^3}} \exp(-r/a_0) d^3r, \quad (22)$$

and

$I_0 = -E_g$: ionization potential of 1s orbital of hydrogen atom, if the target system is hydrogen atom and the initial state is 1s energy level.

Next, we define

$$\begin{aligned} L(\vec{p}, t) &= V_0 \left(\vec{p} + \frac{e\vec{F}}{\omega} \sin \omega t \right) \exp \left[\frac{i}{\hbar} \int_0^t dt \left\{ I_0 + \frac{1}{2m} \left(\vec{p} + \frac{e\vec{F}}{\omega} \sin \omega \tau \right)^2 \right\} \right] \\ &= \exp \left[\frac{i}{\hbar} \left(\tilde{I}_0 + \frac{p^2}{2m} \right) t + \frac{i e \vec{p} \cdot \vec{F}}{\hbar m \omega^2} \right] \\ &\quad \times V_0 \left(\vec{p} + \frac{e\vec{F}}{\omega} \sin \omega t \right) \exp \left\{ -\frac{i}{\hbar} \left(\frac{e \vec{p} \cdot \vec{F}}{m \omega^2} \cos \omega t + \frac{e^2 F^2}{8m \omega^3} \sin 2\omega t \right) \right\}, \end{aligned} \quad (23)$$

where

$$\tilde{I}_0 = I_0 + \frac{e^2 F^2}{4m \omega^2}, \quad (24)$$

and $e^2 F^2 / 4m \omega^2$ is called the ponderomotive energy.

Using the Fourier expansion in t in the last term in Eq. (23), we obtain

$$L(\vec{p}, t) = \sum_{n=-\infty}^{\infty} \exp \left\{ \frac{i}{\hbar} \left(\tilde{I}_0 + \frac{p^2}{2m} - n\hbar\omega \right) t + \right\} L_n(\vec{p}), \quad (25)$$

where

$$\begin{aligned} L_n(\vec{p}) &= \frac{1}{2\pi} \int_{-\pi}^{\pi} dx V_0 \left(\vec{p} + \frac{e\vec{F}}{\omega} \sin x \right) \\ &\times \exp \left[\frac{i}{\hbar\omega} \left\{ n\hbar\omega x + \frac{2e\vec{p} \cdot \vec{F}}{m\omega} \sin^2(x/2) - \frac{e^2 F^2}{8m\omega^2} \sin 2x \right\} \right]. \end{aligned} \quad (26)$$

It follows that

$$\begin{aligned} w_0 &= \frac{2}{\hbar^2} \lim_{T \rightarrow \infty} \operatorname{Re} \int \frac{d^3 p}{(2\pi\hbar)^3} \cos(\omega T) \\ &\times \sum_{n'=-\infty}^{\infty} \exp \left\{ -\frac{i}{\hbar} \left(\tilde{I}_0 + \frac{p^2}{2m} - n'\hbar\omega \right) T \right\} L_{n'}^*(\vec{p}) \int_0^T dt \cos(\omega t) \\ &\times \sum_{n=-\infty}^{\infty} \exp \left\{ \frac{i}{\hbar} \left(\tilde{I}_0 + \frac{p^2}{2m} - n\hbar\omega \right) t \right\} L_n(\vec{p}). \end{aligned} \quad (27)$$

Taking the limit of T in Eq. (27), we obtain

$$w_0 = \frac{\pi}{2\hbar} \int \frac{d^3 p}{(2\pi\hbar)^3} \sum_{n=-\infty}^{\infty} |L_{n-1}(\vec{p}) + L_{n+1}(\vec{p})|^2 \delta \left(\tilde{I}_0 + \frac{p^2}{2m} - n\hbar\omega \right). \quad (28)$$

Here, we find

$$\begin{aligned} L_{n-1}(\vec{p}) + L_{n+1}(\vec{p}) &= \frac{1}{\pi} \oint V_0 \left(\vec{p} + \frac{e\vec{F}}{\omega} u \right) \\ &\times \exp \left[\frac{i}{\hbar\omega} \int_0^u \left\{ I_0 + \frac{1}{2m} \left(\vec{p} + \frac{e\vec{F}}{\omega} v \right)^2 \right\} \frac{dv}{\sqrt{1-v^2}} \right] du. \end{aligned} \quad (29)$$

Substituting Eq. (29) into Eq. (28) yields

$$w_0 = \frac{2\pi}{\hbar} \int \frac{d^3 p}{(2\pi\hbar)^3} |L(\vec{p})|^2 \sum_{n=-\infty}^{\infty} \delta \left(\tilde{I}_0 + \frac{p^2}{2m} - n\hbar\omega \right), \quad (30)$$

where

$$\begin{aligned} L(\vec{p}) &= \frac{1}{2\pi} \oint V_0 \left(\vec{p} + \frac{e\vec{F}}{\omega} u \right) \\ &\times \exp \left[\frac{i}{\hbar\omega} \int_0^u \left\{ I_0 + \frac{1}{2m} \left(\vec{p} + \frac{e\vec{F}}{\omega} v \right)^2 \right\} \frac{dv}{\sqrt{1-v^2}} \right] du. \end{aligned} \quad (31)$$

The exponential part of Eq. (31) is oscillating rapidly so that the integral can be calculated by the saddle-point method. At the saddle-point, V_0 is singular. In such a case, we can apply the saddle-point method for integrals with a singularity mentioned in Appendix A.

Assuming that \vec{F} is parallel with z -axis and taking into account the fact that

$$2mI_0 = \hbar^2/a_0^2 \quad (32)$$

for the 1s orbital of hydrogen atoms, we find

$$\begin{aligned} L(\vec{p}) = & -\frac{1}{2\pi} \cdot \frac{8eF\sqrt{\pi a_0^7}}{\hbar} \cdot 4I_0^3 \oint \frac{|\vec{p} + \frac{e\vec{F}}{\omega}u|}{\left\{I_0 + \frac{1}{2m} \left(\vec{p} + \frac{e\vec{F}}{\omega}u\right)^2\right\}^3} \\ & \times \exp\left[\frac{i}{\hbar\omega} \int_0^u \left\{I_0 + \frac{1}{2m} \left(\vec{p} + \frac{e\vec{F}}{\omega}v\right)^2\right\} \frac{dv}{\sqrt{1-v^2}}\right] du. \end{aligned} \quad (33)$$

Next, we define

$$j(u) = \int_0^u \left\{I_0 + \frac{1}{2m} \left(\vec{p} + \frac{e\vec{F}}{\omega}v\right)^2\right\} \frac{dv}{\sqrt{1-v^2}}. \quad (34)$$

Then,

$$j'(u) = \left\{I_0 + \frac{1}{2m} \left(\vec{p} + \frac{e\vec{F}}{\omega}u\right)^2\right\} \frac{1}{\sqrt{1-u^2}}. \quad (35)$$

If we define the saddle-point as u_s , it follows that $j'(u_s) = 0$. Therefore,

$$\left|\vec{p} + \frac{e\vec{F}}{\omega}u_s\right| = \pm i\sqrt{2mI_0}, \quad (36)$$

which implies that we have two different saddle-points. We calculate the contributions of both the saddle-points. From Eq. (34), we find

$$j''(u_s) = \frac{e\vec{F}}{m\omega} \cdot \left(\vec{p} + \frac{e\vec{F}}{\omega}u_s\right) \frac{1}{\sqrt{1-u_s^2}}. \quad (37)$$

If we expand $j'(u)$ around u_s , we obtain

$$j'(u_s) = j''(u_s)(u - u_s). \quad (38)$$

As a consequence, we find

$$I_0 + \frac{1}{2m} \left(\vec{p} + \frac{e\vec{F}}{\omega} u \right)^2 = j'(u)\sqrt{1-u^2} = j''(u_s)(u-u_s)\sqrt{1-u^2}. \quad (39)$$

Using the above results yields

$$L(\vec{p}) = -\frac{1}{2\pi} \cdot \frac{8eF\sqrt{\pi a_0^7}}{\hbar} \cdot 4I_0^3 \cdot \frac{1}{j''(u_s)^3} \oint \frac{\left| \vec{p} + \frac{e\vec{F}}{\omega} u \right|}{(u-u_s)^3(1-u^2)^{3/2}} \times \exp \left[\frac{i}{\hbar\omega} \int_0^u \left\{ I_0 + \frac{1}{2m} \left(\vec{p} + \frac{e\vec{F}}{\omega} v \right)^2 \right\} \frac{dv}{\sqrt{1-v^2}} \right] du. \quad (40)$$

In Eq. (A13) of Appendix A, we make the following substitution:

$$g(x) \rightarrow \frac{\left| \vec{p} + \frac{e\vec{F}}{\omega} u \right|}{(1-u^2)^{3/2}}, \quad v \rightarrow 3, \quad \text{and} \quad \lambda \rightarrow -\frac{i}{\hbar\omega}. \quad (41)$$

After some manipulation of Eq. (40), we obtain

$$L(\vec{p}) = \mp 2i\sqrt{\pi a_0^3} \cdot \frac{I_0}{eFa_0} \cdot \frac{\hbar\omega}{(1-u_s^2)^{1/2}} \times \exp \left[\frac{i}{\hbar\omega} \int_0^{u_s} \left\{ I_0 + \frac{1}{2m} \left(\vec{p} + \frac{e\vec{F}}{\omega} v \right)^2 \right\} \frac{dv}{\sqrt{1-v^2}} \right] \quad (42)$$

for each saddle-point.

The positions of the saddle-points depend on \vec{p} . However, Keldysh assumed that the contributions to the total photoionization probability are dominant only for small \vec{p} , which satisfies the following condition:

$$p^2 \ll 2mI_0. \quad (43)$$

As a consequence, we can assume that $\vec{p} = \vec{0}$ in the pre-exponential factors of Eq. (42) and expand in the exponential factors in powers of p up to second order inclusively.

The explicit expressions of the saddle-points are obtained by Eq. (36):

$$u_s = \gamma \left(-\frac{p}{\sqrt{2mI_0}} \cos \theta \pm i\sqrt{\frac{p^2}{2mI_0} \sin^2 \theta + 1} \right), \quad (44)$$

where γ is the Keldysh parameter defined by Eq. (1) and θ is the angle between \vec{p} and \vec{F} . In Keldysh's derivation, γ appears here for the first time. Noting Eq. (43), we find the following expansion:

$$\begin{aligned} & \int_0^{u_s} \left\{ I_0 + \frac{1}{2m} \left(\vec{p} + \frac{e\vec{F}}{\omega} v \right)^2 \right\} \frac{dv}{\sqrt{1-v^2}} \\ &= \pm i\tilde{I}_0 \left(\sinh^{-1} \gamma - \frac{\gamma\sqrt{1+\gamma^2}}{1+2\gamma^2} \right) \\ &+ \frac{epF \cos \theta}{m\omega} (1 - \sqrt{1+\gamma^2}) + iC_{\pm}(\theta)p^2, \end{aligned} \quad (45)$$

where

$$C_{\pm}(\theta) = \pm \frac{1}{2m} \left(\sinh^{-1} \gamma - \frac{\gamma \cos^2 \theta}{\sqrt{1+\gamma^2}} \right). \quad (46)$$

One notices that $C_{-}(\theta)$ causes exponential increase as $p \rightarrow \infty$ in Eq. (30) so that w_0 will not converge and it is unphysical. Therefore, we adopt the saddle-point with $C_{+}(\theta)$. Consequently, it follows that

$$\begin{aligned} w_0 &= \frac{2\pi}{\hbar} \cdot 4\pi a_0^3 \cdot \frac{I_0^2}{e^2 F^2 a_0^2} \cdot \hbar^2 \omega^2 \\ &\cdot \frac{1}{1+\gamma^2} \int \frac{d^3 p}{(2\pi\hbar)^3} \left| \exp \left[\frac{1}{\hbar\omega} \left\{ -\tilde{I}_0 \left(\sinh^{-1} \gamma - \frac{\gamma\sqrt{1+\gamma^2}}{1+2\gamma^2} \right) \right. \right. \right. \\ &\left. \left. \left. + i \frac{epF \cos \theta}{m\omega} (1 - \sqrt{1+\gamma^2}) - C_{+}(\theta)p^2 \right\} \right] \right|^2 \sum_{n=-\infty}^{\infty} \delta \left(\tilde{I}_0 + \frac{p^2}{2m} - n\hbar\omega \right) \\ &= \frac{2\pi}{\hbar} \cdot 4\pi a_0^3 \cdot \frac{I_0^2}{e^2 F^2 a_0^2} \cdot \hbar^2 \omega^2 \cdot \frac{1}{1+\gamma^2} \\ &\cdot \frac{1}{(2\pi\hbar)^3} \int_{p=0}^{\infty} \int_{\theta=0}^{\pi} \int_{\varphi=0}^{2\pi} p^2 \sin \theta dp d\theta d\varphi \\ &\times \exp \left[\frac{2}{\hbar\omega} \left\{ -\tilde{I}_0 \left(\sinh^{-1} \gamma - \frac{\gamma\sqrt{1+\gamma^2}}{1+2\gamma^2} \right) - C_{+}(\theta)p^2 \right\} \right] \\ &\times \sum_{n=-\infty}^{\infty} \delta \left(\tilde{I}_0 + \frac{p^2}{2m} - n\hbar\omega \right). \end{aligned} \quad (47)$$

If we let

$$\begin{aligned}
 U &= \int_{p=0}^{\infty} \int_{\theta=0}^{\pi} \int_{\varphi=0}^{2\pi} p^2 \sin \theta \, dp \, d\theta \, d\varphi \\
 &\times \exp \left\{ -\frac{p^2}{m\hbar\omega} \left(\sinh^{-1} \gamma - \frac{\gamma}{\sqrt{1+\gamma^2}} \cos^2 \theta \right) \right\} \\
 &\times \sum_{n=-\infty}^{\infty} \delta \left(\tilde{I}_0 + \frac{p^2}{2m} - n\hbar\omega \right), \tag{48}
 \end{aligned}$$

notice that

$$\begin{aligned}
 &\int_0^{\pi} d\theta \sin \theta \exp \left(\frac{\gamma}{m\hbar\omega\sqrt{1+\gamma^2}} p^2 \cos^2 \theta \right) \\
 &= \int_{-1}^1 \exp \left(\frac{\gamma}{m\hbar\omega\sqrt{1+\gamma^2}} p^2 y^2 \right) dy, \tag{49}
 \end{aligned}$$

and use the formula

$$\int_0^{\infty} dp p^2 \exp(-Qp^2) \delta(p^2/2m - B) = \sqrt{2Bm}^{3/2} \exp(-2mQB) \quad (B > 0), \tag{50}$$

we obtain

$$\begin{aligned}
 U &= 4\sqrt{2\hbar\omega\pi} m^{3/2} \int_0^1 d\xi \sum_{n=0}^{\infty} \sqrt{\langle x+1 \rangle - x + n} \\
 &\cdot \exp \left\{ -2(\langle x+1 \rangle - x + n) \left(\sinh^{-1} \gamma - \frac{\gamma}{\sqrt{1+\gamma^2}} \right) \right. \\
 &\left. + 2(\langle x+1 \rangle - x + n) \frac{\gamma}{\sqrt{1+\gamma^2}} (-1 + \xi^2) \right\}, \tag{51}
 \end{aligned}$$

where $x = \tilde{I}_0/\hbar\omega$ and the symbol $\langle x \rangle$ denotes the integer part of the number x . If we transform the variables

$$\left\{ \frac{2\gamma}{\sqrt{1+\gamma^2}} (\langle x+1 \rangle - x + n) \right\}^{1/2} \xi = z\xi = y, \tag{52}$$

we obtain

$$\begin{aligned}
 U &= 4\sqrt{2\hbar\omega\pi} m^{3/2} \left(\frac{\sqrt{1+\gamma^2}}{2\gamma} \right)^{1/2} \\
 &\times \sum_{n=0}^{\infty} \exp \left\{ -2(\langle x+1 \rangle - x + n) \left(\sinh^{-1} \gamma - \frac{\gamma}{\sqrt{1+\gamma^2}} \right) \right\} \\
 &\times \exp(-z^2) \int_0^z \exp(y^2) dy. \tag{53}
 \end{aligned}$$

Substituting Eq. (53) into Eq. (47), we obtain

$$w_0 = \sqrt{\frac{2I_0\omega}{\hbar}} \left(\frac{\gamma}{\sqrt{1+\gamma^2}} \right)^{3/2} S(\gamma, \tilde{I}_0/\hbar\omega) \times \exp \left\{ -\frac{2\tilde{I}_0}{\hbar\omega} \left(\sinh^{-1} \gamma - \gamma \frac{\sqrt{1+\gamma^2}}{1+2\gamma^2} \right) \right\}, \quad (54)$$

where we have defined

$$S(\gamma, x) = \sum_{n=0}^{\infty} \exp \left\{ -2(\langle x+1 \rangle - x+n) \left(\sinh^{-1} \gamma - \frac{\gamma}{\sqrt{1+\gamma^2}} \right) \right\} \times \Theta \left[\left\{ \frac{2\gamma}{\sqrt{1+\gamma^2}} (\langle x+1 \rangle - x+n) \right\}^{1/2} \right], \quad (55)$$

and

$$\Theta(z) = \exp(-z^2) \int_0^z \exp(y^2) dy. \quad (56)$$

In the formulation mentioned above, Coulomb interaction in the final state was completely neglected. Keldysh proposed that if this interaction is included, the general formula for the photoionization rate is given by

$$w_0 = A\omega \left(\frac{\tilde{I}_0}{\hbar\omega} \right)^{3/2} \left(\frac{\gamma}{\sqrt{1+\gamma^2}} \right)^{5/2} S(\gamma, \tilde{I}_0/\hbar\omega) \times \exp \left\{ -\frac{2\tilde{I}_0}{\hbar\omega} \left(\sinh^{-1} \gamma - \gamma \frac{\sqrt{1+\gamma^2}}{1+2\gamma^2} \right) \right\}, \quad (57)$$

where A is a numerical coefficient of the order of unity.

2.3. Generalization of the Original Atomic Keldysh Theory

2.3.1. Introduction

The purpose of this section is to improve the original atomic Keldysh theory mentioned in Sec. 2.2 and to extend it to diatomic molecular photoionization processes in the tunneling regime. In accordance with the original theory, we will use Volkov function as a final continuum spectrum. We avoid using the saddle-point method to the integration of Eq. (33); instead, we use the residue theorem for its evaluation. The dependence of the pre-exponential factor on the electron momentum \vec{p} is ignored in Ref. 10, which

is given by the following expression,

$$2\sqrt{\pi a_0^3} \frac{I_0}{eFa_0} \frac{\hbar\omega}{(1-u_s^2)^{1/2}} \times \exp \left[\frac{i}{\hbar\omega} \int_0^{u_s} \left\{ I_0 + \frac{1}{2m} \left(\vec{p} + \frac{e\vec{F}}{\omega} v \right)^2 \right\} \frac{dv}{(1-v^2)^{1/2}} \right], \quad (58)$$

will be incorporated in this work. It will be shown that such modifications allow us to obtain more exact expressions for the photoionization rate and to treat analytically the photoionization phenomenon for the molecular system.

In Sec. 2.3.2, following Ref. 10, we show a new derivation of photoionization rate formulas for hydrogen-like one-electron atoms. Our derivation is different from that of Ref. 10 in the respect mentioned above. Our new formulas work quite well in the tunneling ionization regime, which was assumed in the derivation of Ref. 10 and confirmed experimentally as well.¹⁶ In Sec. 2.3.3, based on the development made in Sec. 2.3.2, we extend the derivation to the simple molecular systems: randomly oriented diatomic molecules. As an example, the photoionization formula for N₂ molecules is reported. In Sec. 2.3.4, we compare Keldysh's or other photoionization rates with our new results numerically and discuss the validity of our formulas. For the atomic case, we focus on 1s state of hydrogen atom as the initial state. For the molecular case, our attention is directed to the photoionization pathway to remove $\sigma_g 2p$ electron of N₂ molecule and to produce N₂⁺ in its ground electronic state X²Σ_g⁺.¹⁷⁻¹⁹

2.3.2. Theory-atomic case

In this sub-section, we concentrate on the photoionization of hydrogen-like atoms. The initial wave function, $\psi_g(\vec{r})$, is given by

$$\psi_g(\vec{r}) = \sqrt{\frac{1}{\pi a^3}} \exp\left(-\frac{r}{a}\right), \quad a = \frac{a_0}{Z}, \quad (59)$$

where Z represents the effective nuclear charge and $I_0 = -E_g = \frac{Z^2 e^2}{2a_0}$ (ionization potential).

Unlike the original atomic Keldysh theory, we expand the exponent and the denominator of the integrand of Eq. (33), which leads to

$$L(\vec{p}) = -\frac{16ieI_0^3\sqrt{\pi a^7}}{\pi\hbar} \oint du \frac{\vec{F} \cdot \left(\vec{p} + \frac{e\vec{F}}{\omega}u\right)}{j''(u_s)^3 (u - u_s)^3 (1 - u^2)^{3/2}} \times \exp\left[\frac{i}{\hbar\omega} \left\{j(u_s) + \frac{1}{2}j''(u_s)(u - u_s)^2 + \dots\right\}\right]. \quad (60)$$

Carrying out the contour integration in Eq. (60) using the residue theorem yields

$$L(\vec{p}) = \frac{16ieI_0^3\sqrt{\pi a^7}\vec{F} \cdot \left(\vec{p} + \frac{e\vec{F}}{\omega}u_s\right)}{\hbar^2\omega j''(u_s)^2 (1 - u_s^2)^{3/2}} \exp\left[\frac{i}{\hbar\omega}j(u_s)\right], \quad (61)$$

where

$$j''(u_s) = \frac{e}{m\omega\sqrt{1 - u_s^2}} \vec{F} \cdot \left(\vec{p} + \frac{e\vec{F}}{\omega}u_s\right) \quad (62)$$

and

$$j(u_s) = \left(\tilde{I}_0 + \frac{p^2}{2m}\right) \sin^{-1} u_s - \frac{e^2 F^2}{4m\omega^2} u_s \sqrt{1 - u_s^2} - \frac{e\vec{F} \cdot \vec{p}}{m\omega} \left(\sqrt{1 - u_s^2} - 1\right). \quad (63)$$

Notice that the denominator of the integrand of Eq. (60), $(1 - u^2)^{3/2}$, is approximated by $(1 + \gamma^2)^{3/2}$ due to the assumption of small Keldysh parameter γ and low kinetic momentum p (cf. Appendix B).

A remarkable advantage of our method is that the singular point of the integrand and the zero point of $j'(u)$ do not necessarily have to coincide in Eq. (60).^{10,20} As a result, extension can be easily made when the Volkov function is replaced by Coulomb–Volkov function in which case the saddle-point is different from the zero point of $j'(u)$.^{21,22}

The quantity $L(\vec{p})$ can be written as

$$L(\vec{p}) = \frac{4\hbar\omega I_0\sqrt{\pi a}}{eF \cos \theta_{pF} \sqrt{1 - u_s^2}} \exp\left[\frac{i}{\hbar\omega}j(u_s)\right], \quad (64)$$

where $\cos \theta_{pF}$ is defined by

$$\vec{F} \cdot \left(\vec{p} + \frac{e\vec{F}}{\omega}u_s\right) = F \left| \vec{p} + \frac{e\vec{F}}{\omega}u_s \right| \cos \theta_{pF}. \quad (65)$$

Notice that at this point, our expression for $L(\vec{p})$ [Eq. (64)] is larger than that of Keldysh [Eq. (58)] by a factor of two, which arises from the contour

integration made for evaluating Eq. (60), unlike the saddle-point method utilized in Ref. 10.

In Ref. 10, the dependence of $\cos \theta_{pF}$ and $\sqrt{1 - u_s^2}$ on the electron momentum \vec{p} in Eq. (64) has been ignored, that is, $\cos \theta_{pF} = 1$ and $\sqrt{1 - u_s^2} = \sqrt{1 + \gamma^2}$ were assumed. In the present article, we shall take into account the \vec{p} dependence of these pre-exponential factors and examine what role they will play. For that purpose, we reduce $L(\vec{p})$ defined by Eq. (64) into the form being easily integrated with respect to \vec{p} in Eq. (30). The derivation is shown in Appendix B.

Substituting Eq. (B8) into Eq. (30) and integration with respect to \vec{p} leads to

$$w_0 = 4\sqrt{\frac{2I_0\omega}{\hbar}} \left(\frac{\gamma}{\sqrt{1 + \gamma^2}} \right)^{3/2} N(\gamma, \omega, I_0, \tilde{I}_0, B, C) \\ \times \exp \left[-\frac{2\tilde{I}_0}{\hbar\omega} \left(\sinh^{-1} \gamma - \frac{\gamma\sqrt{1 + \gamma^2}}{1 + 2\gamma^2} \right) \right]. \quad (66)$$

Equation (66) is a new atomic photoionization formula including the \vec{p} dependence of the pre-exponential factors in Eq. (64).

The pre-exponential factor of Eq. (66) is slightly complicated due to the \vec{p} dependence of Eq. (64). It is essential to verify the effect of the pre-exponential factors on the photoionization rate. The pre-exponential factor $N(\gamma, \omega, I_0, \tilde{I}_0)$ in Eq. (66) and the photoionization rate formulas derived on the basis of different treatments for the pre-exponential factors are given in Appendix C.

2.3.3. Theory-diatomic molecule case

In this sub-section, based on the approach introduced in the previous sub-section, we show that the *molecular* photoionization rates can be derived analytically as well.

In general, as is clear from the derivation shown in the following, one can arbitrarily choose any molecular systems and their initial electronic bound states. In the present article, we focus on N_2 molecules as an example. Particularly, we consider the case of the molecular photoionization from the $\sigma 2p_z$ orbital of the N_2 molecules. In this case, the initial molecular state ψ_g is given by

$$\psi_g = N_{2p}[(2p_z)_1 + (2p_z)_2], \quad (67)$$

where $(2p_z)_1$ and $(2p_z)_2$ represent the atomic orbitals, and N_{2p} denotes the normalization constant. Here for simplicity of estimation, we use the simple molecular orbital theory, that is, LCAO-MO.

For the case of randomly oriented molecules, the photoionization rate w_0 is given by

$$w_0 = \frac{1}{3} \frac{2}{\hbar^2} \lim_{T \rightarrow \infty} \operatorname{Re} \int \frac{d^3p}{(2\pi\hbar)^3} \int_0^T dt \cos(\omega T) \cos(\omega t) \vec{V}_0^* \left(\vec{p} + \frac{e\vec{F}}{\omega} \sin(\omega T) \right) \cdot \vec{V}_0 \left(\vec{p} + \frac{e\vec{F}}{\omega} \sin(\omega t) \right) \times \exp \left[\frac{i}{\hbar} \int_T^t d\tau \left\{ I_0 + \frac{1}{2m} \left(\vec{p} + \frac{e\vec{F}}{\omega} \sin(\omega\tau) \right)^2 \right\} \right], \quad (68)$$

where for the N_2 molecules

$$\vec{V}_0(\vec{p}) = \sqrt{2}eF \langle \exp(i\vec{p} \cdot \vec{r}/\hbar) | \vec{r} | N_{2p} [(2p_z)_1 + (2p_z)_2] \rangle, \quad (69)$$

using Eq. (67). Note that in the atomic case, $V_0(\vec{p})$ was a scalar as indicated by Eq. (22), while in the molecular case, its counterpart, $\vec{V}_0(\vec{p})$, is a vector owing to the directional nature of the molecular bond. The factor $1/3$ in Eq. (68) is introduced for the orientational average of the photoionization rate.

In the one-center approximation,²³ Eq. (69) reduces to

$$\vec{V}_0(\vec{p}) = 2eF \langle \exp(i\vec{p} \cdot \vec{r}/\hbar) | \vec{r} | \psi_{2p_z} \rangle, \quad (70)$$

where

$$\psi_{2p_z} = \sqrt{\frac{1}{\pi a_2^5}} z \exp\left(-\frac{r}{a_2}\right). \quad (71)$$

Using the molecular-fixed coordinates, Eq. (70) leads to

$$\vec{V}_0(\vec{p}) = (2ie\hbar F) \vec{\nabla}_p \int d\vec{r} \exp\left(-\frac{i}{\hbar} \vec{p} \cdot \vec{r}\right) \psi_{2p_z}, \quad (72)$$

which after some algebra renders

$$\vec{V}_0(\vec{p}) = 64\pi e F a_2^5 N_{2p} \left[\frac{\hat{k}}{(1+k^2 a_2^2)^3} - \frac{6a_2^2 p_z \vec{p}}{\hbar^2 (1+k^2 a_2^2)^4} \right]. \quad (73)$$

Here, \hat{k} denotes the unit vector along the z-direction, i.e. the molecular axis.

Repeating the derivation shown in the previous sub-section, we obtain

$$w_0 = \frac{2\pi}{3\hbar} \int \frac{d^3p}{(2\pi\hbar)^3} |\vec{L}(\vec{p})|^2 \sum_{n=-\infty}^{\infty} \delta\left(\tilde{I}_0 + \frac{p^2}{2m} - n\hbar\omega\right), \quad (74)$$

where

$$\begin{aligned} \bar{L}(\vec{p}) = & \frac{1}{2\pi} \oint du \bar{V}_0 \left(\vec{p} + \frac{e\vec{F}}{\omega} u \right) \\ & \times \exp \left[\frac{i}{\hbar\omega} \int_0^u \frac{dv}{\sqrt{1-v^2}} \left\{ I_0 + \frac{1}{2m} \left(\vec{p} + \frac{e\vec{F}}{\omega} v \right)^2 \right\} \right]. \end{aligned} \quad (75)$$

Notice that the relation of $\frac{\hbar^2}{a_2^2} = 2mI_0$ still holds for the molecular system as in the case for hydrogen-like atoms. After the contour integration as was done in Sec. 2.3.2, we obtain

$$\begin{aligned} \bar{L}(\vec{p}) = & -\frac{2^5 \pi^{1/2} a_2^{5/2} I_0^3 eF}{\hbar\omega} \exp \left[\frac{i}{\hbar\omega} j(u_s) \right] \left[\frac{\hat{k}}{j''(u_s)^2 (1-u_s^2)^{3/2}} \right. \\ & - \frac{3eF}{m\omega j''(u_s)^3 (1-u_s^2)^2} \left\{ \left(\vec{p} + \frac{e\vec{F}}{\omega} u_s \right) + \left(p_z + \frac{eF}{\omega} u_s \right) \hat{k} \right\} \\ & \left. - \frac{(p_z + \frac{eF}{\omega} u_s) \left(\vec{p} + \frac{e\vec{F}}{\omega} u_s \right)}{mj''(u_s)^4 (1-u_s^2)^2} j'''(u_s) \right], \end{aligned} \quad (76)$$

where

$$j'(u_s) = \frac{i\sqrt{2mI_0}}{\sqrt{1-u_s^2}} \frac{eF}{m\omega} \cos \theta_{pF} \quad (77)$$

and

$$j'''(u_s) = \frac{e^2 F^2}{m\omega^2} \frac{1}{\sqrt{1-u_s^2}} + \frac{2i\sqrt{2mI_0} u_s}{(1-u_s^2)^{3/2}} \frac{eF}{m\omega} \cos \theta_{pF}. \quad (78)$$

Using the same procedure adopted in Sec. 2.3.2, the photoionization rate for the system of randomly oriented molecules is finally given by

$$\begin{aligned} w_0 = & \frac{2^6}{3} \sqrt{\frac{2I_0\omega}{\hbar}} \frac{\gamma^{3/2} (2\gamma^2 + 3)^2}{(1+\gamma^2)^{5/2}} N(\gamma, \omega, I_0, \tilde{I}_0, 1, 0) \\ & \times \exp \left[-\frac{2\tilde{I}_0}{\hbar\omega} \left(\sinh^{-1} \gamma - \frac{\gamma\sqrt{1+\gamma^2}}{1+2\gamma^2} \right) \right]. \end{aligned} \quad (79)$$

In Eq. (79), the pre-exponential factor $N(\gamma, \omega, I_0, \tilde{I}_0, 1, 0)$ is given by Eq. (C1). Note that in Eq. (79) the \vec{p} dependence of the pre-exponential factors is ignored.

It should be noted that the exponential factor for the randomly oriented molecular case [Eq. (79)] is completely the same as that for the atomic case [Eq. (66)]. This indicates that ionization mechanisms of atomic and randomly oriented molecular systems are essentially the same because the

ionization rate is essentially determined by the exponential factors. The difference between atomic and molecular systems arises only from the pre-exponential factors. In addition, it is important to note that in the case of the molecules, the Keldysh parameter γ can be defined in the same way as in the atomic system, Eq. (66).

It should be noted that in the tunneling limit ($\gamma \rightarrow 0$), comparing Eq. (79) for the molecular system and Eq. (66) with $B = 1$ and $C = 0$, we find that the photoionization rate is 48 times larger for the molecular system than for the atomic system. This is due to the different orbitals for the initial state and to the directional nature of the molecular bond.

The photoionization rates from σ_{2s} and π_{2p} states for the N_2 molecules can be evaluated in similar manners and will not be presented in the present article. In addition, application of the present method to other diatomic molecules is straightforward.

2.3.4. Results and discussion

In this sub-section, we demonstrate numerical results by using our analytical formulas (Eq. (66) for the atomic system and Eq. (79) for the molecular system) and compare them with those calculated by the Keldysh theory or other authors' numerical results.

In Fig. 1, we show the atomic ionization rate w_0 calculated by the Keldysh theory [Eq. (54)] and our theory [Eq. (66)] for hydrogen atom with $Z = 1$. For the estimation by the Keldysh theory, we have checked that sufficient convergence has been attained in the summation over n [Eq. (C1)]. Notice that our results for w_0 agree very well with that of Keldysh, although the latter underestimates than the former by a few factors. If we include whole pre-exponential factors, w_0 becomes smallest [solid line in Fig. 1(b)]. According to Ref. 16, the widely used Reiss and Keldysh methods underestimate the experimentally observed photoionization rates to a large extent. Therefore, Fig. 1 indicates that our new formulas ameliorate the Keldysh's original formulas.

In the range of tunneling limit ($\gamma \ll 1$), the photoionization rates w_0 obtained by the different approaches can be approximated as

$$w_0 = \frac{\sqrt{6\pi}}{4} \frac{I_0}{\hbar} \left(\frac{eF\hbar}{m^{1/2}I_0^{3/2}} \right)^{1/2} \exp \left\{ -\frac{4}{3} \frac{\sqrt{2m}I_0^{3/2}}{e\hbar F} \left(1 - \frac{\gamma^2}{10} \right) \right\} \quad (\text{Keldysh}),$$

$$w_0 = \frac{\sqrt{4\sqrt{2\pi}}}{3} \frac{I_0}{\hbar} \left(\frac{eF\hbar}{m^{1/2}I_0^{3/2}} \right)^{1/2} \exp \left\{ -\frac{4}{3} \frac{\sqrt{2m}I_0^{3/2}}{e\hbar F} \left(1 - \frac{\gamma^2}{10} \right) \right\}$$

[for the case Eq. (C4)],

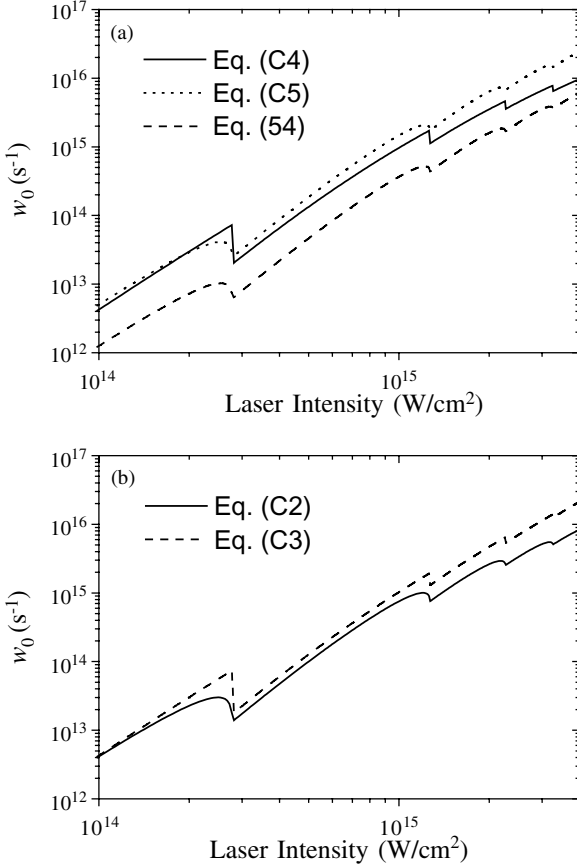


Fig. 1. Log-log plot of the calculated atomic photoionization rate w_0 . The calculation is performed using Keldysh theory [Eq. (54), broken line in panel (a)] and our theory [Eq. (75), solid and dotted lines in panel (a) and solid and broken lines in panel (b) using Eqs. (C4), (C5), (C2), and (C3), respectively]. The wave length of the incident light is 248.0 (nm) ($\hbar\omega = 5.0$ (eV)). In order to ensure the convergence, the summation upper limit of Eq. (C1) was 500 for the higher intensity region. [Reprinted with permission from Mishima *et al.*, Phys. Rev. A, 66, 033401 (2002). Copyright (2002) by the American Physical Society.]

and

$$w_0 = \sqrt{3\sqrt{2}\pi} \frac{I_0}{\hbar} \left(\frac{eF\hbar}{m^{1/2}I_0^{3/2}} \right)^{1/2} \exp \left\{ -\frac{4}{3} \frac{\sqrt{2m}I_0^{3/2}}{e\hbar F} \left(1 - \frac{\gamma^2}{10} \right) \right\} \quad \text{[for the case Eq. (C5)].} \quad (80)$$

In Eq. (80), $\gamma \approx \hbar\omega/I_0$ is assumed, except for the Keldysh's tunneling formula. We notice that only the pre-exponential factors are different from

each other and we can predict the magnitude of the difference of the pre-exponential constants. For instance, near the tunneling limit at the field intensity 4×10^{15} (W/cm²), the photoionization rate w_0 calculated by Keldysh's formula [broken line in Fig. 1(a)] is the smallest and that estimated by Eq. (C4) [solid line in Fig. 1(a)] is smaller than that calculated by Eq. (C5) [dotted line in Fig. 1(a)]. This is consistent with Eq. (80).

From Fig. 1, we also notice that $d \log_{10}(w_0)/d_{10} \log(I)$ (I : laser intensity) is almost constant in the tunneling region, which is evident from Eq. (80). This indicates that the ionization potential I_0 or the effective nuclear charge Z can be estimated by measuring the slope $d \log_{10}(w_0)/d \log_{10}(I)$ using Eq. (80).

Now, let us compare our results and that calculated numerically based on the time-dependent Schrödinger equation by LaGattuta.²⁴ Our results including pre-exponential factors are quite similar to that obtained by LaGattuta, especially in the high intensity range (around 1×10^{15} W/cm² or higher). In the low intensity regime, large discrepancy is found. This tendency has already been pointed out by LaGattuta. This can be attributed to the fact that Keldysh and our theories cannot be applied to the multiphoton regime.

Figure 2 presents dependence of the atomic ionization rate w_0 on the effective charge Z . In the low field intensity range, Keldysh's and our results agree very well. However, in the high field intensity range, large discrepancy is found. Figure 2 shows that the ionization rate varies significantly with ionization energy. The lower the ionization energy is, the larger the ionization rate is. In other words, using Fig. 2, we can estimate the ionization rate as a function of laser intensity and ionization potential.

Next, we consider the molecular photoionization rates. Apart from the atomic photoionization, detailed studies of molecular photoionization will provide additional insights into the dynamics of photoionization processes in general.^{25,26} Therefore, it is important to explore the molecular photoionization in more detail.

It is known that the Keldysh theory can also predict diatomic molecular photoionization rate to a certain extent. However, in order to estimate accurately diatomic or polyatomic molecular photoionization rates, it will be necessary to describe molecular states by including the directional nature of the molecular bond which is the most distinct characteristics from atoms. Along this line, DeWitt *et al.*²⁷ conducted a time-of-flight mass spectrum experiment for benzene, naphthalene, and anthracene, and calculated their photoionization and dissociation probabilities in intense laser fields. From the theoretical or experimental interest, there are several investigations

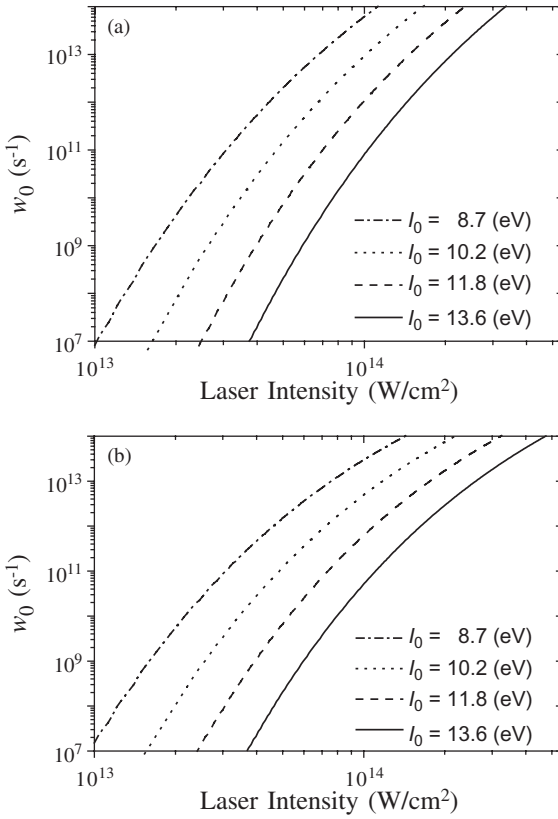


Fig. 2. Log-log plot of the dependence of the atomic ionization rate w_0 on the effective nuclear charge Z . The wave length of the incident laser is 3000.0 (nm) (laser frequency $\omega = 0.413$ eV). The ionization potentials I_0 are 8.7, 10.2, 11.8, and 13.6 eV for $Z = 0.80, 0.87, 0.93$, and 1.0, respectively. Panel (a) was calculated by Keldysh theory [Eq. (54)] and (b), by Eq. (66) with (C2). In order to ensure the convergence, in the highest intensity region, the upper limits of summation with regard to n in Eq. (C1) and the counterpart of Keldysh [Eq. (54)] were $n = 5 \times 10^4, 1 \times 10^5, 6 \times 10^6$, and 7×10^6 for $I_0 = 8.7, 10.2, 11.8$, and 13.6 eV, respectively. [Reprinted with permission from Mishima *et al.*, Phys. Rev. A, 66, 033401 (2002). Copyright (2002) by the American Physical Society.]

concerning photoionization rates or cross sections of N_2 molecule in recent years.^{28–31} In connection with these works, we shall compare numerical results estimated by Eq. (79) and show its validity, which include the effect of the molecular bond to the photoionization rate.

The molecular ionization rates w_0 of N_2 molecule calculated by our theory [Eq. (79)] for various ionization potentials I_0 are demonstrated in Fig. 3. From He I photoelectron spectrum of N_2 , it is known that the minimum energy necessary to remove $\sigma_g 2p$ electron to produce N_2^+ in its ground electronic state $X^2\Sigma_g^+$ is 15.58 eV³²: $I_0 = 15.58$ (eV).

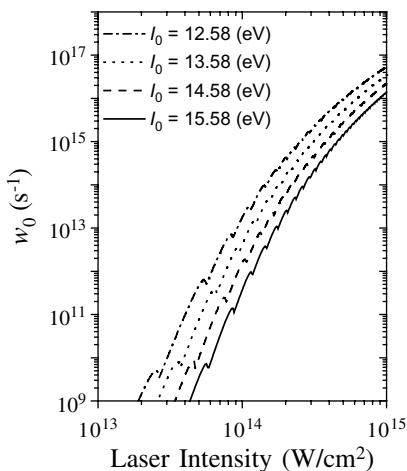


Fig. 3. Log-log plot of the calculated molecular photoionization rate w_0 . The calculation is performed using our theory [Eq. (79)] for $I_0 = 12.58, 13.58, 14.58,$ and 15.58 eV for $Z = 0.80, 0.85, 0.92,$ and 1.00 , respectively. The wave length of the incident laser is 800.0 nm (laser frequency $\omega = 1.55$ eV). The solid line in the figure is compared with those calculated by Guo *et al.*²⁹ and by DeWitt *et al.*³¹ [Reprinted with permission from Mishima *et al.*, Phys. Rev. A, 66, 033401 (2002). Copyright (2002) by the American Physical Society.]

Let us compare our result with those calculated by Guo *et al.* by use of Ammosov-Delone-Krainov (ADK) model¹³ (Fig. 3 of Ref. 29) and those estimated by DeWitt *et al.* by use of the orientationally averaged tunneling theory appropriate for diatomic molecules (Fig. 4 of Ref. 31). In the whole range of the figure, our prediction agrees very well with that of ADK²⁹ and the orientationally averaged tunneling theory.³¹ Lower than the laser intensity 10^{13} (W/cm^2), a minor discrepancy is found between our result and that of the orientationally averaged tunneling theory.³¹ As mentioned in Fig. 2, we can estimate the ionization rate as a function of laser intensity and ionization potential, which is demonstrated in Fig. 3 with various ionization potentials I_0 .

From Figs. 2 and 3, we can see that the photoionization rate increases very rapidly with decreasing ionization potential in the whole range of the laser intensity. This is due to the fact that under the condition of the same laser intensity, the potential barrier height and width are smaller for the system with smaller ionization potential. This suggests that there will be a case where the indirect tunneling ionization process through an excited intermediate state (resonant tunneling ionization) may be more effective than (or at least comparable to) the direct tunneling ionization. In Fig. 4, we investigate the laser intensity and frequency regions where this is the case.

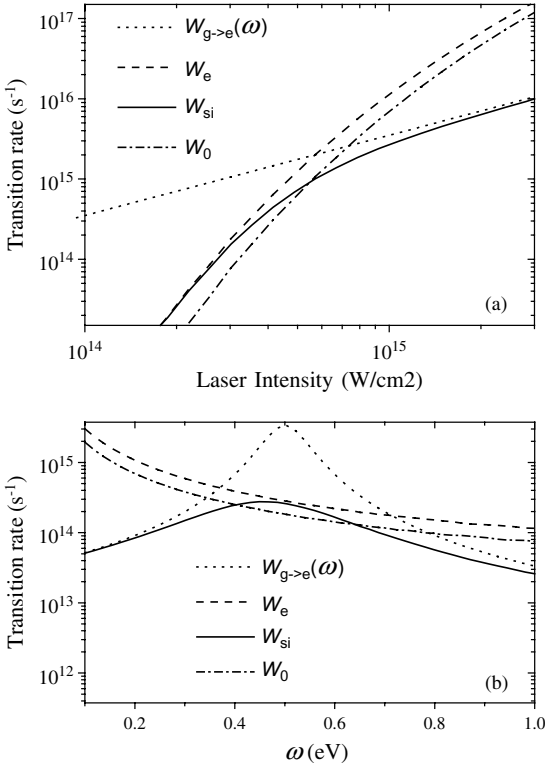


Fig. 4. Optical absorption rate $W_{g \rightarrow e}(\omega)$, ionization rate of the intermediate e -state w_e , indirect photoionization rate w_{si} , and direct photoionization rate w_0 . The calculation is performed using Eqs. (81) and (82). The energy gaps ω_{eg} are 1.0 eV and 0.5 eV for Figs. 4(a) and 4(b), respectively. The laser intensity is 3×10^{14} (W/cm^2) for Fig. 4(b). The ionization potential from the ground state to the ionization threshold is 13.6 eV. The indirect ionization rate w_e in Eq. (81) is estimated by using Eq. (66) with Eq. (C5). The magnitudes of the transition dipole moment \vec{d}_{eg} are set to be 1.0 (a.u.) and 0.2 (a.u.) for Figs. 4(a) and 4(b), respectively. The direction of the transition dipole moment is assumed to be along the laser polarization. The dephasing constants of the e -state, γ_{eg} , are 4 times and 0.1 times of ω_{eg} for Figs. 4(a) and 4(b), respectively. The relaxation decay rate of the e -state corresponds to 100 (ps). Figure (a) shows laser intensity dependence of the transition rates for the fixed photon frequency ω resonant with the energy gap ω_{eg} [1.0 (eV)]. Figure (b) shows laser frequency dependence of the transition rates for the fixed laser intensity [3×10^{14} (W/cm^2)]. [Reprinted with permission from Mishima *et al.*, Phys. Rev. A, 66, 033401 (2002). Copyright (2002) by the American Physical Society.]

For estimation, we shall consider the indirect tunneling ionization from the ground g -state to the ionization continuum via the intermediate state e . In this case, the indirect tunneling ionization rate w_{si} can be estimated from

$$w_{si} = \frac{W_{g \rightarrow e}(\omega)}{W_{g \rightarrow e}(\omega) + \gamma_e + w_e} w_e, \quad (81)$$

where w_e , $W_{g \rightarrow e}(\omega)$, and γ_e denote the tunneling ionization rate for the e -state, optical absorption rate for $g \rightarrow e$, and the relaxation decay rate of the e -state, respectively. Notice that

$$W_{g \rightarrow e}(\omega) = \frac{1}{2\hbar^2} \frac{\gamma_{eg} |\vec{d}_{eg} \cdot \vec{F}|^2}{\left(\omega_{eg} + \frac{|\vec{d}_{ee} - \vec{d}_{gg}| \cdot \vec{F}|^2}{4\hbar^2 \omega_{eg}} - \omega \right)^2 + \gamma_{eg}^2}, \quad (82)$$

where γ_{eg} represents the dephasing constant, and \vec{d}_{ee} and \vec{d}_{gg} denote the permanent dipole moments.

Figure 4 demonstrates laser intensity dependence of $W_{g \rightarrow e}(\omega)$, w_e , w_{si} , and direct tunneling ionization rate w_0 for the fixed photon frequency ω resonant with the energy gap ω_{eg} [1.0 eV for Fig. 4(a)]. Here for simplicity, we assume that the permanent dipole moments can be neglected: $\vec{d}_{ee} = \vec{d}_{gg} = \vec{0}$. In addition, we have used Eq. (C5) in order to calculate w_e and w_0 : we assume the tunneling ionization process of hydrogen atoms.

Now, let us concentrate on Fig. 4(a). From Eq. (81), it is expected that for the first absorption resonance, w_{si} would be negligibly small until a certain intensity of laser power is reached so that w_e and $W_{g \rightarrow e}(\omega)$ are comparable [at the field intensity 5×10^{14} (W/cm²)]. In the case of Fig. 4(a), $W_{g \rightarrow e}(\omega)$ is large due to the resonance transition between g - and e -states, while w_e is much smaller due to the small tunneling probability in the low laser intensity range [$< 5 \times 10^{14}$ (W/cm²)] and slightly larger than w_0 due to the larger tunneling probability. Therefore, w_{si} and w_e are comparable in the low intensity regime. Beyond this limit [around 5×10^{14} (W/cm²)], w_{si} behaves like $W_{g \rightarrow e}(\omega)$ which is much smaller than w_e and w_0 ; the indirect tunneling ionization is less effective than the direct tunneling ionization. In this high-intensity range, the potential barrier is highly transparent, which leads to indistinguishably high ionization probability for the g - and e -states (note that the energy gap ω_{eg} is quite small). Thus, we have found that the indirect tunneling ionization is more effective than the direct tunneling ionization in the low laser intensity region.

Figure 4(b) demonstrates that if the photon frequency ω is in resonance with the intermediate bound state (0.5 eV), $W_{g \rightarrow e}(\omega)$ is quite large, and w_e and w_0 are smaller due to the fact that the potential barrier is not transparent enough for the electron to penetrate through it. Therefore, the resonant ionization rate w_{si} behaves like w_e and is more enhanced than the direct ionization rate w_0 . In addition, we can see that when the photon frequency ω is smaller or larger than the energy gap ω_{eg} (0.5 eV), w_{si} behaves like $W_{g \rightarrow e}(\omega)$ due to the fact that in the off-resonance case $W_{g \rightarrow e}(\omega)$ is much smaller than w_e .

2.4. Coulomb Correction of the Atomic Keldysh Theory

2.4.1. Introduction

In the KFR theory, due to the fact that it presumes photoionization from a short-range potential, whereas the real potential exerts a long-range Coulomb force between the residual core and the ionizing electron, one would not expect good agreement between experiments and theoretical predictions. However, at relatively high intensities and high orders, where external electromagnetic field effects on the electron become dominant, good agreement can be expected. The principal cause of the problem mentioned above is that Keldysh used the Gordon–Volkov function^{33,34} as the final state of the photoionized electron. This normal Volkov function is an exact solution of the quantum-mechanical equations of motion for a free electron in a plane-wave electromagnetic field. However, in the presence of the atomic potential among particles, Volkov function is not necessarily exact in order to describe motion of the photoionizing electron properly. In order to incorporate appropriately the effect of the atomic potential into the Volkov function, there have been many efforts so far^{21,35–44} and the revised Volkov function is usually called “Coulomb–Volkov function.”

Therefore, it is essential to construct a theory to bridge the large discrepancy between the results based on normal Volkov function and Coulomb-corrected Volkov function.

For this purpose, Reiss *et al.*²¹ have improved free-electron Volkov function and obtained *first* order Coulomb corrected Volkov function for the electron irradiated by the circularly polarized electric field. In addition, they demonstrated numerically that the time-dependent phase shift included in the Coulomb–Volkov function leads to much more enhanced photoionization rate compared to that calculated by using the free-electron Volkov function.

Later, based on the development made by Reiss *et al.*, Bauer²² has introduced one more unitary transformation for the Hamiltonian and the Coulomb–Volkov function and succeeded in deriving the *second* order Coulomb corrected Volkov function for the electron irradiated by circularly polarized electric field. However, in his paper, it was not clarified what kind of effect would be introduced to the photoionization rate formulas by such an improvement for the Volkov function.

Based on their ideas, we derive the analytical photoionization rate formulas for the hydrogen atoms irradiated by the linearly polarized electric field in the presence of Coulomb interaction.

Our strategy is as follows. We express the final ionized state by the Coulomb–Volkov function instead of the normal Volkov function utilized by Keldysh. As was done in Sec. 2.3, we avoid using the saddle-point method for the integration of $L(\vec{p})$ of Eq. (33). Instead, we use the residue theorem for its evaluation. Dependence of the pre-exponential factors on \vec{p} ignored by Keldysh (Eq. (58)) will be incorporated in our derivation. In addition, we change the summation of $S(\gamma, x)$ in Eq. (55) into integration with respect to n . It will be shown that such modifications allow us to obtain insightful analytical expressions for the photoionization rate in the simultaneous presence of the electric field and Coulomb potential.

In Sec. 2.4.2, we show a new derivation of Keldysh-like photoionization rate formulas for hydrogen-like atoms, taking into account the main influence of the long-range Coulomb potential on the Volkov function. As for the initial state, we focus on 1s state of hydrogen-like atoms. In Sec. 2.4.3, we numerically show the validity of performing the integration over n for $S(\gamma, x)$ and discuss the features of our formulas.

2.4.2. Theory

First of all, we have to define the wave function of the continuum state in such a way that it involves the effect of the long-range Coulomb potential (Coulomb–Volkov function). To this end, we transform the wave function in Eq. (4), $\psi_A(\vec{r}, t)$, to $\Phi(\vec{r}, t)$ by the following relation:

$$\psi_A(\vec{r}, t) = \exp\left(-\frac{ie^2}{2m\hbar} \int_{-\infty}^t \vec{A}^2(\tau) d\tau\right) \exp(\vec{\alpha} \cdot \vec{\nabla}) \Phi(\vec{r}, t), \quad (83)$$

where

$$\vec{\alpha}(t) = \frac{e}{m} \int_{-\infty}^t \vec{A}(\tau) d\tau. \quad (84)$$

Here, it is assumed that the laser field is adiabatically turned on at $t = -\infty$. Note that the phase-factor transformation is not applied.⁷ The quantity $\vec{\alpha}(t)$ denotes that the classical electron driven by the laser field $\vec{A}(\tau)$ has a quiver motion of vector radius.

Using the Kramers–Henneberger transformation,⁴⁵ it is shown that the wave function $\Phi(\vec{r}, t)$ satisfies the following Schrödinger equation:

$$i\hbar \frac{\partial \Phi(\vec{r}, t)}{\partial t} = \left\{ -\frac{\hbar^2 \vec{\nabla}^2}{2m} + V(|\vec{r} - \vec{\alpha}(t)|) \right\} \Phi(\vec{r}, t). \quad (85)$$

Equation (85) is the space-translated version of the Schrödinger equation. In the special case of the Coulomb potential $V(\vec{r}) = -Ze^2/r$ where Z is the

nuclear charge, V in Eq. (85) is given by

$$V(|\vec{r} - \vec{\alpha}(t)|) = -\frac{Ze^2}{|\vec{r} - \vec{\alpha}(t)|}. \quad (86)$$

Equation (85) cannot be solved in a simple closed form owing to the presence of the term of Eq. (86).

We assume that

$$\alpha_0 \gg a_0/Z, \quad (87)$$

where α_0 is the radius of the quiver motion of a classical electron in the laser field. In the case of the linearly polarized laser field, the maximum quiver radius α_0 can be determined by^{46,47}

$$\alpha_0 = \frac{eF}{m\omega^2}. \quad (88)$$

Because we are interested in the tunneling process, the assumption (87) is valid in most of the cases.

In this approximation, we obtain in the *second* order Coulomb correction

$$V(|\vec{r} - \vec{\alpha}(t)|) \approx -Ze^2 \left\{ \frac{1}{\alpha_0} + \frac{\vec{r} \cdot \vec{\alpha}(t)}{\alpha_0^3} + O(\alpha_0^{-3}) \right\}. \quad (89)$$

For the Taylor expansion similar to that in Eq. (89), Reiss *et al.* and Bauer assumed that the incident laser is *circularly* polarized. In that case, the absolute value of $\vec{\alpha}(t)$ is constant so that the expansion (89) is valid for any time t . However, we are interested in the *linearly* polarized electric field. In this case, the absolute value of $\vec{\alpha}(t)$ varies with time so that the Taylor expansion (89) is not necessarily adequate.

Based on a rough estimation, let us discuss the condition of the validity of using the approximation Eq. (89) in the case of the *linearly* polarized electric field. The mean tunneling time t_t is given by Eq. (2). Usually, tunneling can take place when t_t is less than half the period of the incident laser. Therefore, until the tunneling is almost over, the phase of the laser field will roughly change from zero to ωt_t which is of a small magnitude. In this case, $\vec{\alpha}(t)$ will hardly change. Within this restriction, we can apply the approximation of Eq. (89).

Substituting Eq. (89) into Eq. (85), the approximate Schrödinger equation is of the form

$$i\hbar \frac{\partial \Phi(\vec{r}, t)}{\partial t} = \left[-\frac{\hbar^2 \nabla^2}{2m} - Ze^2 \left\{ \frac{1}{\alpha_0} + \frac{\vec{r} \cdot \vec{\alpha}(t)}{\alpha_0^3} \right\} \right] \Phi(\vec{r}, t). \quad (90)$$

Let us transform the wave function in Eq. (90), $\Phi(\vec{r}, t)$, into $\Phi'(\vec{r}, t)$ by the following unitary transformation,

$$\Phi'(\vec{r}, t) = \exp\{i\beta\vec{A}(t) \cdot \vec{r}\} \Phi(\vec{r}, t), \quad (91)$$

where

$$\beta = \frac{Ze^3}{\hbar m \omega^2 \alpha_0^3}. \quad (92)$$

Then, the wave function $\Phi'(\vec{r}, t)$ satisfies

$$i\hbar \frac{\partial \Phi'(\vec{r}, t)}{\partial t} = \left[\frac{\hbar^2}{2m} \left\{ -i\vec{\nabla} - \beta\vec{A}(t) \right\}^2 - \frac{Ze^2}{\alpha_0} \right] \Phi'(\vec{r}, t). \quad (93)$$

The wave function $\Phi'(\vec{r}, t)$ can be directly obtained from Eq. (93):

$$\begin{aligned} \Phi'(\vec{r}, t) = \exp \left[\frac{i}{\hbar} \left\{ \vec{p} \cdot \vec{r} - \frac{p^2}{2m} t - \frac{1}{2m} \int_{-\infty}^t d\tau (-2\hbar\beta\vec{p} \cdot \vec{A}(\tau) \right. \right. \\ \left. \left. + \hbar^2\beta^2\vec{A}^2(\tau)) + \frac{Ze^2}{\alpha_0} t \right\} \right]. \end{aligned} \quad (94)$$

The wave function $\Phi(\vec{r}, t)$ is easily obtained from the transformation of Eq. (91). Therefore, the *second* order Coulomb-corrected Volkov function in the velocity gauge $\psi_A(\vec{r}, t)$ is obtained from the transformation of Eq. (83):

$$\begin{aligned} \psi_A(\vec{r}, t) = \exp \left[\frac{i}{\hbar} \left\{ \vec{p} \cdot \vec{r} - \frac{p^2}{2m} t - \frac{1}{2m} \int_{-\infty}^t d\tau (-2e\vec{p} \cdot \vec{A}(\tau) + e^2\vec{A}^2(\tau)) + \frac{Ze^2}{\alpha_0} t \right. \right. \\ \left. \left. - \frac{1}{2m} \int_{-\infty}^t d\tau (-2\hbar\beta\vec{p} \cdot \vec{A}(\tau) + \hbar^2\beta^2\vec{A}^2(\tau)) - \hbar\beta\vec{A}(t) \cdot (\vec{r} + \vec{\alpha}(t)) \right\} \right]. \end{aligned} \quad (95)$$

Equation (95) can be further transformed into the length-gauge:

$$\begin{aligned} \psi_{\vec{p}}(\vec{r}, t) = \exp \left[\frac{i}{\hbar} \left\{ (\vec{p} - e\vec{A}(t)) \cdot \vec{r} - \frac{p^2}{2m} t - \frac{1}{2m} \int_{-\infty}^t d\tau (-2e\vec{p} \cdot \vec{A}(\tau) + e^2\vec{A}^2(\tau)) \right. \right. \\ \left. \left. + \frac{Ze^2}{\alpha_0} t - \frac{1}{2m} \int_{-\infty}^t d\tau (-2\hbar\beta\vec{p} \cdot \vec{A}(\tau) + \hbar^2\beta^2\vec{A}^2(\tau)) \right. \right. \\ \left. \left. - \hbar\beta\vec{A}(t) \cdot (\vec{r} + \vec{\alpha}(t)) \right\} \right]. \end{aligned} \quad (96)$$

In Eq. (96), the term containing α_0 is the *first* order and those involving β are the *second* order Coulomb corrections. Note that if the second order Coulomb correction is neglected ($\beta = 0$), the Coulomb-Volkov function utilized in Ref. 21 is recovered. The above mentioned derivation is essentially the same as that done by Bauer.²² As was pointed out above, however, Bauer did not derive the photoionization rate in his paper.²² In the following, we

show the derivation of analytical formulas using the *second* order corrected Coulomb–Volkov function defined by Eq. (96).

To be specific, we consider a hydrogen-like one-electron atom in the presence of a monochromatic electric field. The rate of photoionization w_0 for direct transition from the ground bound state to the continuum state is given by

$$\begin{aligned}
 w_0 = & \frac{2}{\hbar^2} \lim_{T \rightarrow \infty} \operatorname{Re} \int \frac{d^3 p}{(2\pi\hbar)^3} \int_{-\infty}^T dt \cos(\omega T) \cos(\omega t) V_0^* \left(\vec{p} + \frac{\vec{e}\vec{F}}{\omega} \sin(\omega T) \right) V_0 \\
 & \times \left(\vec{p} + \frac{\vec{e}\vec{F}}{\omega} \sin(\omega t) \right) \exp \left[\frac{i}{\hbar} \int_T^t d\tau \left\{ I'_0 + \frac{1}{2m} \left(\vec{p} + \frac{\vec{e}\vec{F}}{\omega} \sin(\omega\tau) \right)^2 \right. \right. \\
 & \left. \left. + \frac{1}{2m} \left(\frac{2\hbar\beta}{\omega} \vec{p} \cdot \vec{F} \sin(\omega\tau) + \frac{\hbar^2\beta^2\vec{F}^2}{\omega^2} \sin^2(\omega\tau) \right) + 2\tilde{B} \cos(2\omega\tau) \right\} \right], \quad (97)
 \end{aligned}$$

where

$$I'_0 = I_0 + \tilde{A}, \quad (98)$$

$$\tilde{A} = -\frac{Ze^2}{\alpha_0}, \quad (99)$$

$$I_0 = -E_g = \frac{Z^2 e^2}{2a_0} \quad (\text{ionization potential}), \quad (100)$$

$$\vec{e} = e + \hbar\beta, \quad (101)$$

$$\tilde{B} = -\frac{\hbar\beta e F^2}{2m\omega^2} = \frac{\tilde{A}}{2}, \quad (102)$$

and

$$V_0(\vec{p}) = \langle \exp(i\vec{p} \cdot \vec{r}/\hbar) | e^{i(\vec{F} \cdot \vec{r})} | \psi_g(\vec{r}) \rangle. \quad (103)$$

At this point, it should be noted that the essential difference between this section and Sec. 2.3 is that the effective ionization potential I'_0 is smaller than that when the usual Volkov function is used (I_0) by the term \tilde{A} ($= -\frac{Ze^2}{\alpha_0}$). The role of this phase shift term is of course the decrease of the binding energy. Notice that in the calculation the quiver radius α_0 cannot be too small, in which case the effective binding energy I'_0 in Eq. (97) will be negative, which is unphysical.

Carrying out the integration over t and taking the infinity of T yield

$$w_0 = \frac{2\pi}{\hbar} \int \frac{d^3 p}{(2\pi\hbar)^3} |L(\vec{p})|^2 \sum_{n=-\infty}^{\infty} \delta \left(\tilde{I}'_0 + \frac{p^2}{2m} - n\hbar\omega \right), \quad (104)$$

where

$$\tilde{I}_0'' = I_0' + \frac{E^2 F^2}{4m\omega^2} = I_0 + \frac{E^2 F^2}{4m\omega^2} + \tilde{A}, \quad (105)$$

$$E = \sqrt{e^2 + \hbar^2 \beta^2}, \quad (106)$$

and

$$L(\vec{p}) = \frac{16ieI_0^3 \sqrt{\pi a_0^7}}{\pi \hbar} \oint du \frac{\vec{F} \cdot \left(\vec{p} + \frac{\vec{e}\vec{F}}{\omega} u \right)}{\left\{ I_0 + \frac{1}{2m} \left(\vec{p} + \frac{\vec{e}\vec{F}}{\omega} u \right)^2 \right\}^3} \times \exp \left[\frac{i}{\hbar\omega} \int_0^u \frac{dv}{\sqrt{1-v^2}} \left\{ I_0' + \frac{1}{2m} \left(\vec{p} + \frac{\vec{e}\vec{F}}{\omega} v \right)^2 + 2\tilde{B}(1-v^2) \right\} \right]. \quad (107)$$

Notice that the singular point of the integrand in Eq. (107) is different from the zero point of the time derivative of the exponent. This is the most different point from Keldysh's theory, in which case they coincide.

One of the singularity points of $L(\vec{p})$, u_s , reads

$$u_s = \bar{\gamma} \left(-\frac{p}{\sqrt{2mI_0}} \cos \theta + i \sqrt{\frac{p^2 \sin^2 \theta}{2mI_0} + 1} \right), \quad (108)$$

where

$$\vec{p} \cdot \vec{F} = pF \cos \theta \quad (109)$$

and "modified" Keldysh parameter:

$$\bar{\gamma} = \frac{\omega \sqrt{2mI_0}}{\bar{e}F}. \quad (110)$$

Note that the *second* order Coulomb correction of the Volkov function β is introduced to the Keldysh parameter, while the *first* order correction does not affect the adiabatic parameter. In addition, we can see that the new Keldysh parameter $\bar{\gamma}$ is always smaller than the original Keldysh parameter,

$$\gamma = \frac{\omega \sqrt{2mI_0}}{eF}, \quad (111)$$

on condition that the laser amplitude F and the frequency ω are the same: the photoionization rate tends towards the tunneling ionization region in the presence of the Coulomb potential.

To evaluate $L(\vec{p})$, we let

$$\begin{aligned}
 j(u) &= \int_0^u \frac{dv}{\sqrt{1-v^2}} \left\{ I'_0 + \frac{1}{2m} \left(\vec{p} + \frac{\vec{e}\vec{F}}{\omega} v \right)^2 + 2\tilde{B}(1-v^2) \right\} \\
 &= \int_0^u \frac{dv}{\sqrt{1-v^2}} \left\{ I_0 + \frac{1}{2m} \left(\vec{p} + \frac{\vec{e}\vec{F}}{\omega} v \right)^2 \right\} \\
 &\quad + \{(\tilde{A} + \tilde{B}) \sin^{-1} u + \tilde{B}u\sqrt{1-u^2}\} \\
 &\equiv j_1(u) + j_2(u).
 \end{aligned} \tag{112}$$

Expanding $j_1(u)$ and $j_2(u)$ in the power series of $(u - u_s)$ leads to

$$\begin{aligned}
 L(\vec{p}) &= \frac{16ieI_0^3 \sqrt{\pi a_0^7}}{\pi \hbar} \oint du \frac{\vec{F} \cdot \left(\vec{p} + \frac{\vec{e}\vec{F}}{\omega} u \right)}{j_1''(u_s)^3 (u - u_s)^3 (1 - u^2)^{3/2}} \\
 &\quad \times \exp \left[\frac{i}{\hbar\omega} \left\{ j_1(u_s) + \frac{1}{2} j_1''(u_s) (u - u_s)^2 + \dots + j_2(u_s) + j_2'(u_s) (u - u_s) \right. \right. \\
 &\quad \left. \left. + \frac{1}{2} j_2''(u_s) (u - u_s)^2 \dots \right\} \right].
 \end{aligned} \tag{113}$$

Carrying out the contour integral in Eq. (113) using the residue theorem yields

$$\begin{aligned}
 L(\vec{p}) &= -\frac{32eI_0^3 \sqrt{\pi a_0^7}}{\hbar^2 \omega} \frac{\exp \left[\frac{i}{\hbar\omega} \{j_1(u_s) + j_2(u_s)\} \right]}{j_1''(u_s)^3 (1 - u_s^2)^{3/2}} \\
 &\quad \times \left[\vec{F} \cdot \left(\vec{p} + \frac{\vec{e}\vec{F}}{\omega} u_s \right) \left\{ \frac{i}{2} j_1''(u_s) + \frac{i}{2} j_2''(u_s) - \frac{1}{2\hbar\omega} j_2'^2(u_s) \right\} + i \frac{\vec{e}\vec{F}^2}{\omega} j_2'(u_s) \right],
 \end{aligned} \tag{114}$$

where

$$\begin{aligned}
 j_1(u_s) &= \left(\tilde{I}_0 + \frac{p^2}{2m} \right) \sin^{-1} u_s - \frac{\vec{e}^2 F^2}{4m\omega^2} u_s \sqrt{1 - u_s^2} \\
 &\quad - \frac{\vec{e}\vec{F} \cdot \vec{p}}{m\omega} \left(\sqrt{1 - u_s^2} - 1 \right),
 \end{aligned} \tag{115}$$

$$j_1''(u_s) = \frac{1}{\sqrt{1 - u_s^2}} \frac{\vec{e}}{m\omega} \vec{F} \cdot \left(\vec{p} + \frac{\vec{e}\vec{F}}{\omega} u_s \right), \tag{116}$$

$$j_2(u_s) = (\tilde{A} + \tilde{B}) \sin^{-1} u_s + \tilde{B}u_s \sqrt{1 - u_s^2}, \tag{117}$$

$$j_2'(u_s) = \frac{1}{\sqrt{1 - u_s^2}} \{ \tilde{A} + 2\tilde{B}(1 - u_s^2) \}, \tag{118}$$

$$j_2''(u_s) = \frac{u_s}{(1 - u_s^2)^{3/2}} \{ \tilde{A} - 2\tilde{B}(1 - u_s^2) \}, \tag{119}$$

and

$$\tilde{I}_0 = I_0 + \frac{\tilde{e}^2 F^2}{4m\omega^2} = I_0 \left(1 + \frac{1}{2\tilde{\gamma}^2} \right). \quad (120)$$

In principle, the integration of Eq. (104) including the \vec{p} -dependence of all the pre-exponential factors can be done, which leads to the most accurate formula. However it is sometimes quite cumbersome and insightful. Therefore, in this sub-section, the simplest expression will be presented. When the Coulomb correction up to second order is included and all the pre-exponential factors of Eq. (104) are \vec{p} -independent, we have

$$w_0 = N(\gamma, \tilde{\gamma}, \omega, I_0, \tilde{A}, \tilde{B}) \exp \left[-\frac{2}{\hbar\omega} \left\{ \tilde{I}_0 \left(\sinh^{-1} \tilde{\gamma} - \frac{\tilde{\gamma}\sqrt{1+\tilde{\gamma}^2}}{1+2\tilde{\gamma}^2} \right) + \tilde{A} \sinh^{-1} \tilde{\gamma} + \tilde{B} (\sinh^{-1} \tilde{\gamma} + \tilde{\gamma}\sqrt{1+\tilde{\gamma}^2}) \right\} \right], \quad (121)$$

where the definition of $N(\gamma, \tilde{\gamma}, \omega, I_0, \tilde{A}, \tilde{B})$ is shown in Appendix D. However, it should be noted that sometimes it happens that the behaviors of the photoionization rates at the tunneling limit are quite different depending on the various treatments of the pre-exponential factors (see Sec. 2.4.3).

In Appendix E, the photoionization rates for different treatments of the pre-exponential factors are reported in the first order Coulomb correction ($\beta = 0$) for comparison.

As mentioned above, the main role of the *first* order Coulomb correction is to lower the ionization potential [see Eq. (98)]. Here, let us discuss the effect of the *second* order Coulomb correction.

In fact, by comparing the *first* order Coulomb corrected Volkov function,

$$\psi_{\vec{p}}(\vec{r}, t) = \exp \left[\frac{i}{\hbar} \left\{ (\vec{p} - e\vec{A}(t)) \cdot \vec{r} - \frac{p^2}{2m}t - \frac{1}{2m} \int_{-\infty}^t d\tau (-2e\vec{p} \cdot \vec{A}(\tau) + e^2\vec{A}^2(\tau)) - \vec{A}t \right\} \right], \quad (122)$$

and the *second* order corrected function of Eq. (96) whose order of the terms in the exponent is changed,

$$\psi_{\vec{p}}(\vec{r}, t) = \exp \left[\frac{i}{\hbar} \left\{ (\vec{p} - (e + \hbar\beta)\vec{A}(t)) \cdot \vec{r} - \frac{p^2}{2m}t - \frac{1}{2m} \int_{-\infty}^t d\tau (-2(e + \hbar\beta)\vec{p} \cdot \vec{A}(\tau) + (e^2 + \hbar^2\beta^2)\vec{A}^2(\tau)) - \vec{A}t - \hbar\beta\vec{A}(t) \cdot \vec{\alpha}(t) \right\} \right], \quad (123)$$

we could have easily obtained some hint about what kind of photoionization rate formulas should be finally derived. Firstly, it is apparent that when we include the second order correction, the following transformations have to be performed:

$$e \rightarrow e + \hbar\beta \quad (124)$$

and

$$e^2 \rightarrow e^2 + \hbar^2\beta^2. \quad (125)$$

In Eqs. (121) and (D5), the electron charge e is included in the Keldysh parameter and the effective ionization potential. However, it would not necessarily have been apparent which transformation [Eq. (124) or (125)] would affect Keldysh parameter or ionization potential without careful derivation. Notwithstanding, it can be qualitatively concluded that the second order correction β lowers the Keldysh parameter and enhances the effective ionization potential.

Secondly, it is noted that the extra term $-\hbar\beta\vec{A}(t) \cdot \vec{\alpha}(t)$ in Eq. (123) is not involved in Eq. (122). The main role of this term is to add an extra term of $\tilde{B}(\sinh^{-1}\tilde{\gamma} + \tilde{\gamma}\sqrt{1 + \tilde{\gamma}^2})$ in the exponents of Eqs. (121) and (D5), and to lower the effective ionization potential (note that \tilde{B} defined by Eq. (102) is negative).

Notice that our expression is almost the same as that of Keldysh if $\vec{A} = \vec{B} = 0$ (no Coulomb effect), although ours is larger than that of Keldysh's by a factor of four. This is due to the fact that we have utilized the residue theorem in order to go from Eq. (113) to Eq. (114), whereas Keldysh used the saddle-point method for that purpose.

An important conclusion can be drawn from Eq. (E3) with the assumption of Eqs. (E10) and (E11), and that with the assumption $\vec{A} = 0$ (no Coulomb effect). By comparing these, one notices that the pre-exponential factors and the exponents of the former are always larger than those of the latter [note that \tilde{A} is negative and that \tilde{I}'_0 of Eq. (E3) is defined by Eq. (E2)]. Therefore, we can predict that the photoionization rate in the presence of Coulomb potential is always larger than that in its absence. This tendency has already been reported in several papers.^{21,44} Intuitively, one can easily suppose that reducing the binding energy gives rise to the increase of the photoionization rate. However, from our formula, one can understand this tendency in a more insightful form and interpret the phenomenon analytically.

2.4.3. Results and discussion

In this sub-section, we show numerically the validity of the approximation (D13) for Eq. (D10). Next, we demonstrate the procedure to obtain the

photoionization rates by our formulas and compare some physical quantities in the first and second order Coulomb corrections.

Figure 5 compares S calculated by summation [Eq. (D10)] and that by integration [Eq. (D13)]. The ordinate y^2 corresponds to $\cos^2 \theta$ where θ is the angle between \vec{p} and \vec{F} . Note that $\ln(S)$ is plotted in the direction of z-axis. It is evident that both of them agree quite well over the wide range of laser intensity. It shows that the simple integration can be used for calculating the ionization rate; in this case, our formulation is much easier than that of Keldysh.

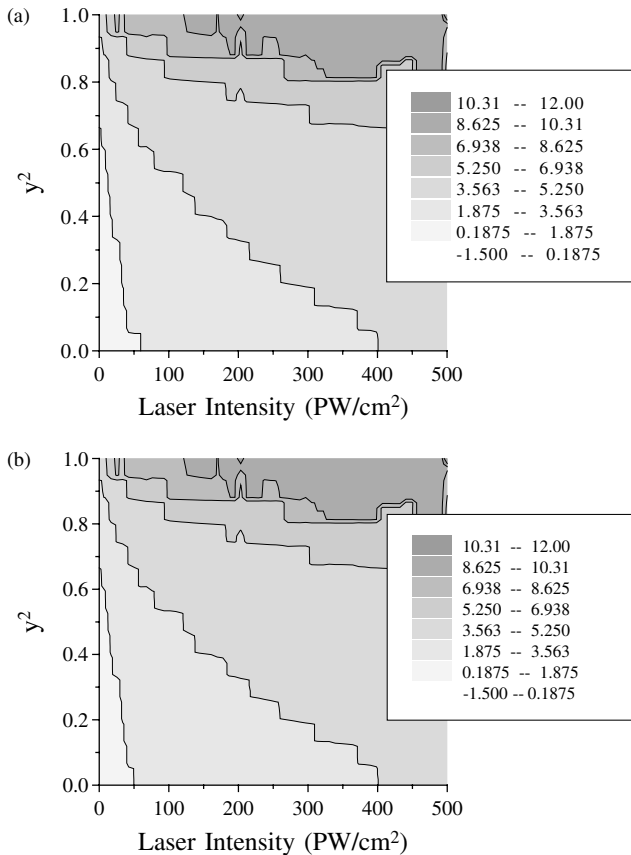


Fig. 5. Comparison of S calculated by (a) summation (Eq. (D10)) and by (b) integration [Eq. (D13)]. The ordinate y^2 is $\cos^2 \theta$ where θ is the angle between \vec{p} and \vec{F} . In this figure, $\ln(S)$ is plotted. The wave length of the incident laser is assumed to be $10 \mu\text{m}$. For the summation in Eq. (D1), 500 000 terms from the lowest limit were summed up. Notice the quite good agreement between them. [Reprinted with permission from Mishima *et al.*, Phys. Rev. A, 66, 053408 (2002). Copyright (2002) by the American Physical Society.]

If the field intensity is small, that is, δ in Eq. (D11) is small, it might be conjectured that the summation in Eq. (D10) and the integration in Eq. (D13) may be quite different. However, in such a case, γ becomes large and K in Eq. (D12) may be a large positive number in the exponent, since K is a monotonically increasing positive function regarding γ for whatever γ values changing between -1 and 1 in the tunneling regime. Therefore, in the low field intensity range, S is quite small as can be seen in the figure.

On the other hand, when the field intensity is large, that is, δ in Eq. (D11) is large, it is conjectured that the summation in Eq. (D10) and the integration in Eq. (D13) may be of almost the same magnitude. We have confirmed that $\ln(S)$ is actually of the same magnitude down to two places of decimals at high field intensity. Although we do not show other calculations for various laser frequencies ω , the above argument holds in a wide range of ω .

According to Keldysh, neglecting the Coulomb interaction in the final state, which is well known, changes the power of F in the pre-exponential expression, without changing the exponential itself. However, our formulas that include \vec{p} -dependence of the pre-exponential factors show such a tendency even if the Coulomb effect vanishes in the tunneling limit. For instance, in the tunneling limit ($\gamma = 0$) for the cases (i) and (iii) in Appendix E, we have

$$w_0 = 2^{3/4} \sqrt{3\pi} \frac{I_0}{\hbar} \left(\frac{m^{1/2} I_0^{3/2}}{\hbar e F} \right)^{1/2} \frac{1}{1 + \frac{\sqrt{2mI_0^3}}{\hbar e F}} \exp \left(-\frac{4\sqrt{2mI_0^3}}{3\hbar e F} \right). \quad (126)$$

On the other hand, for the cases (ii) and (iv) in Appendix E, we obtain

$$w_0 = 2^{1/4} \sqrt{3\pi} \frac{I_0}{\hbar} \left(\frac{\hbar e F}{m^{1/2} I_0^{3/2}} \right)^{1/2} \exp \left(-\frac{4\sqrt{2mI_0^3}}{3\hbar e F} \right). \quad (127)$$

In comparison, we show the Keldysh formula in the tunneling limit,

$$w_0 = \frac{\sqrt{3\pi}}{2} \frac{I_0}{\hbar} \left(\frac{m^{1/2} I_0^{3/2}}{e F \hbar} \right)^{1/2} \exp \left(-\frac{4\sqrt{2mI_0^3}}{3\hbar e F} \right). \quad (128)$$

Equation (126) shows that the photoionization rate increases, saturates, and decreases to zero eventually, while Eq. (127) has a tendency to increase unilaterally to the infinity. This is the same tendency as that of Keldysh and ADK models.⁴⁸ Note that \hat{A} vanishes in the tunneling limit in our approximation. The remarkable point to note is that in Eq. (126) the factor

$1 + \frac{\sqrt{2mI_0^3}}{\hbar eF}$ is relatively large in the tunneling limit below the BSI region. This kind of factor was not found in the theories of Keldysh and ADK. It should be noted that this factor may amount to two or more. This suggests that this term is not negligible.

Next, we show how to estimate the photoionization rate in the tunneling regime. The procedure is as follows. For the approximation of Eq. (89) to be valid, we have to check that

$$\cos(\omega/w_0) \sim 1, \quad (129)$$

where the photoionization rate w_0 is calculated by Eqs. (121), (D5), (E1), or (E3). Equation (129) indicates that the photoionization process should terminate much more rapidly than the laser cycle.

To assure that the we are in the tunneling region,

$$F < \frac{Z^3 e^5 m^2}{16\hbar^4} \quad (130)$$

and

$$\gamma < 0.5. \quad (131)$$

Equation (130) ensures that the photoionization is not within the BSI region.^{48–51} On the other hand, Eq. (131) prohibits the photoionization process from lying in the multiphoton regime. The value 0.5 was adopted on the assumption of Ref. 49. If Eqs. (129)–(131) are satisfied at the same time, the most exact photoionization rate will be obtained.

As was pointed out in Sec. 2.4.2, our formulas show that the photoionization rate is larger in the presence of the Coulomb potential than that in its absence. This can be roughly explained as follows. In its absence, the barrier width is $I_0/(eF)$ and the barrier height, I_0 . On the other hand, in its presence, the barrier width is $\sqrt{I_0^2 - 4Ze^3F/(eF)}$ and the barrier height, $I_0 - \sqrt{(Ze/F)}$. It is evident that the barrier width and height are smaller when the Coulomb potential is present than when it is absent so that the tunneling rate in the presence of the Coulomb potential is larger than that in its absence. Our formula (E3) with (E10) and (E11) reflects this fact. It should be noted that in the high intensity limit the effect of the Coulomb potential is negligibly small.

The second order Coulomb correction is less significant than the first correction in the tunneling regime. Let us compare some physical quantities in the first and second order corrections.

Firstly, because $I_0 = Z^2 e^4 m / (2\hbar^2)$, $\tilde{A} = -2\hbar^3 \omega \gamma / (Z^2 m e^4)$ and $\tilde{L} \equiv \hbar^2 F^2 \beta^2 / (4m\omega^2) = \hbar^6 \omega^2 \gamma^4 / (2Z^4 m^2 e^8)$. The former is the contribution of the

first order Coulomb correction to the shift of the resonance structure of the photoionization rate versus laser intensity and the latter, that of the second order correction. Due to the assumption that

$$\gamma \ll 1 \quad \text{and} \quad \hbar\omega/I_0 = 2\hbar^3\omega/(Z^2me^4) \ll 1, \quad (132)$$

\tilde{L} is much smaller than \tilde{A} . Therefore, it can be seen that the contribution from the second order Coulomb correction is much smaller than that from the first order correction.

Secondly, Keldysh parameter is only affected by the second order Coulomb correction. From Eq. (110),

$$\tilde{\gamma} = \frac{\gamma}{1 + \hbar^3\omega\gamma^3/(Z^2me^4)}. \quad (133)$$

The part $\hbar^3\omega\gamma^3/(Z^2me^4)$ is the contribution from the second order correction. If we compare this with \tilde{A} , it is evident that the second order correction is smaller by many orders of magnitude than the first order correction.

Thirdly, the ‘‘modified’’ ponderomotive energies $\tilde{e}^2F^2/(4m\omega^2)$ and $E^2F^2/(4m\omega^2)$ are introduced by including the second order Coulomb correction. The contribution of the second order correction $\hbar\beta = Zm^2\omega^4/F^3$ is also much smaller than the elementary electron charge e .

From the above arguments, it is concluded that the second order Coulomb correction is negligibly small compared with the first order correction in the tunneling limit.

2.5. Application to Large Polyatomic Molecules

2.5.1. Introduction

Recently, the atomic ADK formula has been developed for the description of the molecular ionization rate.⁵² As indicated in,⁵² it should be stressed that molecules have additional dimensions that atoms do not have: internuclear distance and the incident direction of the laser with respect to the molecule’s alignment. From the theoretical investigations, it has been already found that the internuclear distance and the incident orientation of the laser may be crucial for determining the photoionization rate [8] or the effect may still be uncertain.^{53,54} Recently, a strong molecular alignment dependence of photoionization rate has been observed for the N₂ molecule experimentally.⁵⁵ In Ref. 8, by solving the three-dimensional time-dependent Schrödinger equation, anomalously enhanced ionization was observed for H₂⁺ molecule at large internuclear separation in the linearly polarized electric field. In Refs. 53, 54, the same conclusion was deduced for H₂ molecule by using a nonperturbative *ab initio* calculation.

In order to settle this controversy, many researches are devoted to clarifying this problem.^{56–65} Therefore, one is naturally led to ask, “With what kind of relations does the photoionization rate depend on the characteristics of the incident laser and the molecule?” However, convenient formulas for describing the dependence of the internuclear distance on the photoionization rate have not yet been found; therefore, this question may be still open.

At present, after the work,⁸ many numerical results are reported by directly solving the Schrödinger equation,^{66–75} but unfortunately it is tractable only for small molecules consisting of two or three atoms because of the heavy computational cost for polyatomic molecules. For example, H_2^+ and H_2 molecules are extensively studied, but it is too difficult to analyze theoretically fundamental polyatomic molecules, e.g. CH_4 , C_2H_6 , so that we have not yet witnessed insightful theoretical researches on these kinds of elementary molecules. However, even for these small molecules, it seems to be impossible to obtain analytical expressions to describe the photoionization processes, much less to estimate photoionization rates of large polyatomic molecules such as polyacetylene radicals. Therefore, it is highly required to construct a theory to express the photoionization rates of large molecules.

Polyacetylene molecules attract much attention as the first conducting organic polymer.⁷⁶ In particular, the electronic spectrum and ionized states have been investigated experimentally^{77–79} and theoretically.^{80,81} As we will see in Sec. 2.5.4, the series of polyacetylene molecules or radicals (C_nH_{n+2}) have the structure of a long chain in one direction and a short length perpendicular to the chain direction. In this respect, by changing n , we can systematically investigate the chain length and direction dependence of the photoionization probability. In other words, polyacetylene molecules or radicals can be considered to be a paradigm for the investigation of molecular photoionization processes. Therefore, we adopt polyacetylene radicals for numerical calculations in the present article.

Levis *et al.* estimated intense-laser photoionization probabilities by the structure-based quasistatic tunneling model.^{82,83} Their numerical method is essentially based on WKB tunneling theory. They suggested that large polyatomic molecules would have much higher photoionization rates than small molecules at an intensity level of $\sim 1 \times 10^{13}$ (W/cm^2).^{82,83} In this series of works, they modeled a rectangular potential well with a depth equal to the ionization potential. For example, the width of the potential well has been chosen to be equivalent to the length of a line containing para-hydrogen atoms for the case of benzene, 11.96 bohrs. Their conclusion is that the structure-based model well explains the relative yield of

a variety of hydrocarbons. They have predicted that the ionization efficiency is enhanced strongly when the long axis of the molecular potential is aligned along the polarization direction of the laser field. Although accurate results may be evaluated by using their method, it will not be possible to obtain clear physical insight.

The basic concept of the present article can be explained by CREI. In short, as the molecular bond length increases, the symmetric well structure is broken by the simultaneous presence of the external laser field and the other ions to lower the potential barrier and to allow the electron to escape. As we shall see later, this phenomenon can nicely be explained by our formula.

The purpose of this section is to develop a photoionization rate theory for molecules that can be applied to large polyatomic molecules. As far as we know, this kind of formula has not yet been obtained except for Ref. 52. We investigate the possibility of applying the original atomic Keldysh theory to a molecular system, which is essentially different from molecular ADK theory.⁵²

In this section, we shall explicitly include the position dependence of the constituent atoms in the formulas. Only the molecular orbital of the initial state in the presence of the external electromagnetic field in terms of LCAO, ionization potential of the molecule, the positions of the atoms, and the laser intensity and frequency are required for the calculations. From our analytical expressions, it will be concluded that the photoionization rates depend on $\exp(2\sqrt{2m\bar{I}\bar{F}} \cdot \bar{R}_j/\hbar F)$, where I is the ionization potential for the atomic orbital, \bar{F} the time-independent part of the linearly polarized electric field, \bar{R}_j the position of the atom from the center of mass of the molecule, and m the electron mass. This indicates that the atoms lying in the opposite direction from the polarization vector of the laser field have the lowest ionization rate and those lying along the polarization direction the highest ionization rate. This is consistent with the previous findings.⁸ We perform numerical calculations and systematically estimate photoionization rates of polyacetylene radicals by changing the molecular size.

In Sec. 2.5.2, we show a derivation of the *molecular* Coulomb-corrected Volkov function and a general Keldysh-type photoionization rate formula for spatially aligned molecules in a linearly polarized electric field. For the derivation of the molecular Coulomb-corrected Volkov function, we shall take into account the main influence of the long-range Coulomb potential on the Gordon–Volkov function. In Sec. 2.5.3, the details of *ab initio* calculations are described. In Sec. 2.5.4, we demonstrate numerical results of all-*trans* polyacetylene radicals using the formula derived in Sec. 2.5.2

where the importance of the exponential factor $\exp(2\sqrt{2mI}\vec{F} \cdot \vec{R}_j/\hbar F)$ will be stressed. In addition, we shall examine the quantum interference terms which are not investigated in detail elsewhere.

2.5.2. Theory

Unlike the usual time-dependent perturbation theory of light absorption,⁸⁴ the Coulomb-corrected Volkov function will be used for the electronic part of the ionized electron in order to incorporate the evolution of the ionizing electron subjected to the simultaneous presence of the laser field and the Coulomb interactions. This is essential because the electron is required to gain extra energy (ponderomotive energy) from the laser field to propagate in the free volume. This leads to a shift of ionization threshold energy, which has already been confirmed by experiments. Therefore, we first derive the Volkov function for the electron in the next sub-section.

2.5.2.1. Molecular Coulomb-corrected Volkov function of electron

In this sub-section, we demonstrate the derivation of the molecular Coulomb-corrected Volkov function of one active electron of large polyatomic molecules. Our target systems are all-*trans* polyacetylene radicals, but the molecular Coulomb-corrected Volkov function obtained below is general enough to be applied to any one-active-electron molecules.

In the following derivation, we consider a single active electron in HOMO state of the molecule that is excited directly to the continuum state by a linearly polarized electric field. To derive the photoionization rate formula as exactly as possible, it is necessary to define the wave function of the continuum state in such a way that it involves the effect of the long-range Coulomb potential exerted by the atomic nuclei.

The exact nonrelativistic Schrödinger equation for the continuum state of one valence electron $\psi_A(\vec{r}, t; \{\vec{R}_j\})$ in the velocity gauge is expressed as

$$i\hbar \frac{\partial}{\partial t} \psi_A(\vec{r}, t; \{\vec{R}_j\}) = \left\{ \frac{1}{2m} (-i\hbar \vec{\nabla}_r - e\vec{A}(t))^2 + V(\vec{r}; \{\vec{R}_j\}) \right\} \psi_A(\vec{r}, t; \{\vec{R}_j\}) \quad (134)$$

where

$$V(\vec{r}; \{\vec{R}_j\}) = - \sum_{k=1}^N \frac{Z_k e^2}{|\vec{r} - \vec{R}_k|} + \frac{1}{2} \sum_{l \neq k}^N \frac{Z_l Z_k e^2}{|\vec{R}_l - \vec{R}_k|}. \quad (135)$$

Here, $\{\vec{R}_j\}$ collectively represents the positions of the N atoms, and $V(\vec{r}; \{\vec{R}_j\})$ is the attractive potential between the nuclei and the electrons plus the repulsive ones among the nuclei.

Let us transform the wave function in Eq. (134), $\psi_A(\vec{r}, t; \{\vec{R}_j\})$, to $\Phi(\vec{r}, t; \{\vec{R}_j\})$ by the following relation:

$$\psi_A(\vec{r}, t; \{\vec{R}_j\}) = \exp\left\{-\frac{ie^2}{2m\hbar} \int_{-\infty}^t \vec{A}^2(\tau) d\tau\right\} \exp(\vec{\alpha} \cdot \vec{\nabla}_r) \Phi(\vec{r}, t; \{\vec{R}_j\}), \quad (136)$$

where

$$\vec{\alpha}(t) = \frac{e}{m} \int_{-\infty}^t \vec{A}(\tau) d\tau. \quad (137)$$

Here, it is assumed that the laser field is turned on adiabatically at $t = -\infty$. That is, the laser field is turned on slowly compared with the electron motion, but too fast for the nuclei to move. Therefore, the nuclei can be regarded as being frozen.

The Kramers–Henneberger transformation⁴⁵ will be used to show that the wave function $\Phi(\vec{r}, t; \{\vec{R}_j\})$ satisfies the following Schrödinger equation:

$$i\hbar \frac{\partial}{\partial t} \Phi(\vec{r}, t; \{\vec{R}_j\}) = \left\{ -\frac{\hbar^2 \vec{\nabla}_r^2}{2m} + V(\vec{r} - \vec{\alpha}(t); \{\vec{R}_j\}) \right\} \Phi(\vec{r}, t; \{\vec{R}_j\}). \quad (138)$$

Using the approximation of Eq. (87) and the quiver radius of Eq. (88), we obtain

$$\begin{aligned} V(\vec{r} - \vec{\alpha}(t); \{\vec{R}_j\}) \approx & -\sum_{k=1}^N Z_k e^2 \left\{ \frac{1}{\alpha_0} + \frac{\vec{\alpha}(t) \cdot (\vec{r} - \vec{R}_k)}{\alpha_0^3} + O(\alpha_0^{-3}) \right\} \\ & + \frac{1}{2} \sum_{l \neq k}^N \frac{Z_l Z_k e^2}{|\vec{R}_l - \vec{R}_k|}. \end{aligned} \quad (139)$$

Substituting Eq. (139) into Eq. (138), we have

$$\begin{aligned} i\hbar \frac{\partial}{\partial t} \Phi(\vec{r}, t; \{\vec{R}_j\}) = & \left\{ -\frac{\hbar^2 \vec{\nabla}_r^2}{2m} - \sum_{k=1}^N Z_k e^2 \left\{ \frac{1}{\alpha_0} + \frac{\vec{\alpha}(t) \cdot (\vec{r} - \vec{R}_k)}{\alpha_0^3} \right\} \right. \\ & \left. + \frac{1}{2} \sum_{l \neq k}^N \frac{Z_l Z_k e^2}{|\vec{R}_l - \vec{R}_k|} \right\} \Phi(\vec{r}, t; \{\vec{R}_j\}). \end{aligned} \quad (140)$$

We transform $\Phi(\vec{r}, t; \{\vec{R}_j\})$ into a new wavefunction $\Psi(\vec{r}, t; \{\vec{R}_j\})$ by the following unitary transformation,

$$\Psi(\vec{r}, t; \{\vec{R}_j\}) = \exp\left\{i\vec{A}(t) \cdot \sum_{k=1}^N a_k(\vec{r} - \vec{R}_k)\right\} \Phi(\vec{r}, t; \{\vec{R}_j\}), \quad (141)$$

where

$$a_k = m^2 \omega^4 Z_k / \hbar F^3. \quad (142)$$

Therefore, $\Psi(\vec{r}, t; \{\vec{R}_j\})$ satisfies

$$\begin{aligned} \Psi(\vec{r}, t; \{\vec{R}_j\}) = \exp\left[\frac{i}{\hbar} \left\{ \vec{p} \cdot \vec{r} - \frac{1}{2m} \int_{-\infty}^t d\tau (\vec{p} - \hbar b \vec{A}(t))^2 + \sum_{k=1}^N Z_k e^2 t / \alpha_0 \right. \right. \\ \left. \left. - \frac{1}{2} \sum_{l \neq k}^N Z_l Z_k e^2 t / |\vec{R}_l - \vec{R}_k| \right\} \right]. \end{aligned} \quad (143)$$

Transforming Eq. (143) into the length gauge, we obtain the Coulomb-corrected Volkov function of the molecular system,

$$\begin{aligned} \psi_{\vec{p}}(\vec{r}, t; \{\vec{R}_j\}) = \exp\left[\frac{i}{\hbar} \left\{ (\vec{p} - e\vec{A}(t)) \cdot \vec{r} - \frac{p^2}{2m} t - \frac{1}{2m} \int_{-\infty}^t d\tau (-2\vec{e}\vec{p} \cdot \vec{A}(\tau) \right. \right. \\ \left. \left. + E^2 A(\tau)^2 - \hbar \vec{A}(t) \cdot \sum_{k=1}^N a_k(\vec{r} + \vec{\alpha}(t) - \vec{R}_k) + \sum_{k=1}^N Z_k e^2 t / \alpha_0 \right. \right. \\ \left. \left. - \frac{1}{2} \sum_{l \neq k}^N Z_l Z_k e^2 t / |\vec{R}_l - \vec{R}_k| \right\} \right] \end{aligned} \quad (144)$$

where

$$\vec{e} = e + \hbar b, \quad b = \sum_{j=1}^N a_j, \quad \text{and} \quad E = \sqrt{e^2 + \hbar^2 b^2}. \quad (145)$$

The characteristic of the molecular Coulomb-corrected Volkov function most different from the atomic counterpart is that the total Coulomb correction manifests itself as the sum of those affecting the respective atoms and the nuclear-site-dependent part of a second-order Coulomb correction: $\hbar \vec{A}(t) \cdot \sum_{k=1}^N a_k \vec{R}_k$. The nuclear repulsion term $\frac{1}{2} \sum_{l \neq k}^N Z_l Z_k e^2 t / |\vec{R}_l - \vec{R}_k|$ will be cancelled out to be included in the molecular ionization potential I_0 .

2.5.2.2. Photoionization rate of spatially aligned molecules in the linearly polarized electric field

In the following, we consider the situation where the molecule is under the influence of a monochromatic linearly polarized electric field with its polarization direction along the z -axis. The rate of photoionization w_0 for direct transition from the HOMO to the continuum Coulomb-corrected Volkov state can be obtained by Eq. (20); however, $c_{\vec{p}}$ is given by

$$c_{\vec{p}}(T) = \frac{i}{\hbar} \int_{-\infty}^T dt \cos(\omega t) e^{-\frac{i}{\hbar} E_{\text{HOMO}} t} \langle \psi_{\vec{p}}(\vec{r}, t; \{\vec{R}_j\}) | \vec{d} \cdot \vec{F} | \Psi_{\text{HOMO}}(\vec{r}; \{\vec{R}_j\}) \rangle, \quad (146)$$

instead of Eq. (18) for the atomic case.

For the ground state wave function, we generally have

$$\Psi_{\text{HOMO}}(\vec{r}; \{\vec{R}_j\}) = \sum_{j=1}^N \sum_{k_j=1}^{n_j} s_{k_j,j} \psi_{k_j}(\vec{r} - \vec{R}_j). \quad (147)$$

Here, k_j means the k_j -th atomic orbital of the j -th atom, n_j is the number of atomic orbitals included in the j -th atom, $s_{k_j,j}$ is the molecular orbital coefficient of the k_j -th atomic orbital of the j -th atom, ψ_{k_j} is the normalized atomic wavefunction of the k_j -th atomic orbital of the j -th atom, and N is the number of nuclei. For example, we utilize a LCAO of the ground state of all-*trans* polyacetylene radicals consisting of $2p_x$ orbitals on carbon atoms in the presence of the electric field,

$$\Psi_{\text{HOMO}}(\vec{r}; \{\vec{R}_j\}) = \sum_{j=1}^N s_{2p_x,j} \psi_{2p_x}(\vec{r} - \vec{R}_j), \quad (148)$$

$$\psi_{2p_x}(\vec{r}) = \frac{\Omega_{2p_x}^{5/2}}{\sqrt{\pi}} r \exp(-\Omega_{2p_x} r) \sin \theta \cos \phi \quad (149)$$

where N is the total number of carbon atoms.

Therefore, substituting Eqs. (146) and (147) into Eq. (20) yields

$$w_0 = \frac{2}{\hbar^2} \lim_{T \rightarrow \infty} \text{Re} \int \frac{d^3 p}{(2\pi\hbar)^3} \int_{-\infty}^T dt \cos(\omega T) \cos(\omega t) V_0^* \left(\vec{p} + \frac{\vec{e}\vec{F}}{\omega} \sin(\omega T); \{\vec{R}_j\} \right) \\ \times V_0 \left(\vec{p} + \frac{\vec{e}\vec{F}}{\omega} \sin(\omega t); \{\vec{R}_j\} \right)$$

$$\begin{aligned} & \times \exp \left[\frac{i}{\hbar} \int_T^t d\tau \left\{ I'_0 + \frac{1}{2m} \left(\vec{p} + \frac{e\vec{F}}{\omega} \sin(\omega\tau) \right)^2 + \frac{1}{2m} \left(\frac{2\hbar b}{\omega} \vec{p} \cdot \vec{F} \sin(\omega\tau) \right. \right. \right. \\ & \left. \left. \left. + \frac{\hbar^2 b^2 F^2}{\omega^2} \sin^2(\omega\tau) \right) - \hbar b \frac{eF^2}{m\omega^2} \cos(2\omega\tau) + Y(\{\vec{R}_j\}) \cos(\omega\tau) \right\} \right], \end{aligned} \quad (150)$$

where

$$I'_0 = I_0 + \tilde{A}, \quad (151)$$

$$\tilde{A} = - \sum_{j=1}^N Z_j e^2 / \alpha_0, \quad (152)$$

$$Y(\{\vec{R}_j\}) = \sum_{k=1}^N (Z_k e + \hbar a_k) \vec{R}_k \cdot \vec{F}, \quad (153)$$

and I_0 is the ionization potential of the molecule.

In Eq. (150), we define

$$V_0(\vec{p}; \{\vec{R}_j\}) = \sum_{j=1}^N \sum_{AO(j)} V_{0,AO(j)}(\vec{p}, \vec{R}_j), \quad (154)$$

where $\sum_{AO(j)}$ means the summation over the atomic orbitals of the j -th atom participating in the LCAO; $AO(j)$ represents $1s, 2s, 2p_x$, etc. of the j -th atom.

The important integral, the transition dipole matrix element between the atomic state ψ_{AO} and the plane wave, $V_{0,AO}(\vec{p}, \vec{R}_j)$, is given by

$$V_{0,AO}(\vec{p}, \vec{R}_j) = \int d^3r \exp(-\vec{p} \cdot \vec{r} / \hbar) (e\vec{F} \cdot \vec{r}) \psi_{AO}(\vec{r} - \vec{R}_j). \quad (155)$$

For example, for the $2p_x$ orbital (e.g. the HOMO state of all-*trans* polyacetylene radicals with the laser field polarization vector perpendicular and parallel to the carbon backbone), we have

$$\begin{aligned} & V_{0,2px}(\vec{p}, \vec{R}_j) \\ & = -\zeta_{2px,j} \frac{4\sqrt{2}\pi\hbar^4 \sqrt{I_{2px}} p_x}{m^{5/2}} \left\{ \frac{3\hbar e F p_z}{m(I_{2px} + p^2/2m)^4} + \frac{i(e\vec{F} \cdot \vec{R}_j)}{(I_{2px} + p^2/2m)^3} \right\} \\ & \quad \times \exp(-i\vec{p} \cdot \vec{R}_j / \hbar). \end{aligned} \quad (156)$$

One of the most important features of this equation is that $\exp(-i\vec{p} \cdot \vec{R}_j / \hbar)$ induces \vec{R}_j dependence in the exponential factors of the photoionization rate. In Eqs. (155) and (156), the $\zeta_{AO,j}$'s are determined by the normalization

condition. For other atomic orbitals, $V_{0,AO}(\vec{p}, \vec{R}_j)$ are given in Appendix F for comparison. Here, we define the binding energies for the $2p_x$ orbital by

$$I_{2px} = \hbar^2 \Omega_{2px}^2 / 2m. \quad (157)$$

Next, we define $L(\vec{p}, t; \{\vec{R}_j\})$ by

$$\begin{aligned} L(\vec{p}, t; \{\vec{R}_j\}) = & V_0 \left(\vec{p} + \frac{\vec{e}\vec{F}}{\omega} \sin(\omega t); \{\vec{R}_j\} \right) \\ & \times \exp \left[\frac{i}{\hbar} \int_0^t d\tau \left\{ I'_0 + \frac{1}{2m} \left(\vec{p} + \frac{b\vec{F}}{\omega} \sin(\omega\tau) \right)^2 \right. \right. \\ & + \frac{e\vec{p} \cdot \vec{F}}{m\omega} \sin(\omega\tau) + \frac{e^2 F^2}{2m\omega^2} \sin^2(\omega\tau) + Y(\{\vec{R}_j\}) \cos(\omega\tau) \\ & \left. \left. - \frac{\hbar b e F^2}{m\omega^2} \cos(2\omega\tau) \right\} \right]. \quad (158) \end{aligned}$$

Equation (158) is periodic in time so that $L(\vec{p}, t; \{\vec{R}_j\})$ can be expanded in a Fourier series,

$$L(\vec{p}, t; \{\vec{R}_j\}) = \sum_{n=-\infty}^{\infty} \exp \left\{ \frac{it}{\hbar} \left(\tilde{I}'_0 + \frac{p^2}{2m} - n\hbar\omega \right) \right\} L_n(\vec{p}; \{\vec{R}_j\}), \quad (159)$$

where

$$\tilde{I}'_0 = I'_0 + \frac{E^2 F^2}{4m\omega^2} \quad (160)$$

and

$$\begin{aligned} L_n(\vec{p}; \{\vec{R}_j\}) = & \frac{1}{2\pi} \int_{-\pi}^{\pi} dx V_0 \left(\vec{p} + \frac{\vec{e}\vec{F}}{\omega} \sin x; \{\vec{R}_j\} \right) \\ & \times \exp \left\{ \frac{i}{\hbar\omega} \left(n\hbar\omega x + \frac{2\vec{e}\vec{p} \cdot \vec{F}}{m\omega} \sin^2(x/2) \right. \right. \\ & \left. \left. - \frac{F^2}{8m\omega^3} (E^2 + 4\hbar b e) \sin(2x) + Y(\{\vec{R}_j\}) \omega \sin x \right) \right\}. \quad (161) \end{aligned}$$

The main difference between the atomic and molecular cases is that $Y(\{\vec{R}_j\})$, the effect of the long-tail Coulomb potential associated with the interatomic vector, is introduced in the latter case.

Substituting Eq. (158) into Eq. (150) yields

$$w_0 = \frac{2\pi}{\hbar} \int \frac{d^3p}{(2\pi\hbar)^3} |L(\vec{p}; \{\vec{R}_j\})|^2 \sum_{n=-\infty}^{\infty} \delta \left(\tilde{I}'_0 + \frac{p^2}{2m} - n\hbar\omega \right), \quad (162)$$

where

$$L(\vec{p}; \{\vec{R}_j\}) = \frac{1}{2\pi} \oint du V_0\left(\vec{p} + \frac{\vec{e}\vec{F}}{\omega}u; \{\vec{R}_j\}\right) \exp\{iM_0(u, \vec{p}; \{\vec{R}_j\})\}. \quad (163)$$

In Eq. (163), we define

$$M_0(u, \vec{p}; \{\vec{R}_j\}) = \frac{1}{\hbar\omega} \int_0^u \frac{dv}{\sqrt{1-v^2}} \left\{ \vec{I}'_0 + \frac{1}{2m} \left(\vec{p} + \frac{\vec{e}\vec{F}}{\omega}v\right)^2 - \frac{\vec{e}^2 F^2}{2m\omega^2} v^2 \right. \\ \left. + Y(\{\vec{R}_j\})\omega\sqrt{1-v^2} - \frac{F^2}{4m\omega^2} (E^2 + 4\hbar b e)(1-2v^2) \right\}. \quad (164)$$

Substituting Eq. (164) into Eq. (163), we obtain

$$L(\vec{p}; \{\vec{R}_j\}) = \sum_{j=1}^N \sum_{AO(j)} \bar{N}(\vec{p}, \vec{R}_j, AO(j); \{\vec{R}_k\}). \quad (165)$$

Here, we define

$$\bar{N}(\vec{p}, \vec{R}_j, AO(j); \{\vec{R}_k\}) = \frac{1}{2\pi} \oint du V_{0,AO(j)}\left(\vec{p} + \frac{\vec{e}\vec{F}}{\omega}u, \vec{R}_j\right) \exp\left\{iM_0(u, \vec{p}; \{\vec{R}_k\})\right\}. \quad (166)$$

Carrying out the contour integration in Eq. (163) is the most formidable task. The most important point to note is that the \vec{R}_j 's ($j = 1, 2, \dots, N$) in the pre-exponential factors are contained only in the form $\vec{R}_j \cdot \vec{F}$. Following the same procedure as that in Secs. 2.3 and 2.4, we can obtain $\bar{N}(\vec{p}, \vec{R}_j, AO(j); \{\vec{R}_k\})$. The detailed derivation is reported in Appendix G. Finally, the detailed derivation of w_0 is shown in Appendix H.

If we rewrite Eq. (H1) more compactly, the most general molecular photoionization rate for the spatially aligned molecules is given by

$$w_0 = \sum_{l=1}^N \sum_{k_l=1}^{n_l} S(l, k_l) \exp\{h(l, k_l)\} \\ + \sum_{l \geq m=1}^N \sum_{k_l=1}^{n_l} \sum_{k_m=1}^{n_m} \quad (\text{quantum interference term}), \quad (167)$$

where the prime on the second term of the right hand side of Eq. (167) means that the terms satisfying $l = m$ and $k_l = k_m$ are excluded. Here, k_l means the k_l -th atomic orbital of the l -th atom and so on. The exponential

factor of the first term on the right hand side of Eq. (167) is of the form

$$h(l, k_l) = -\frac{2}{\hbar\omega} \left[\tilde{I}'_0 \sinh^{-1} \bar{\gamma}_{k_l} - \frac{F^2}{4m\omega^2} (E^2 + 4\hbar be) \bar{\gamma}_{k_l} \sqrt{1 + \bar{\gamma}_{k_l}^2} + \{Y(\{\bar{R}_j\})\omega - \bar{e}\bar{R}_l \cdot \bar{F}\} \bar{\gamma}_{k_l} \right]. \quad (168)$$

Here, $\bar{\gamma}_{k_l}$ is the “modified” Keldysh parameter for each atomic orbital k_l defined by

$$\bar{\gamma}_{k_l} = \frac{\omega \sqrt{2mI_{k_l}}}{\bar{e}F}. \quad (169)$$

Another factor in Eq. (168) is

$$\tilde{I}'_0 = I_0 - \sum_{j=1}^N Z_j e^2 / \alpha_0 + \frac{E^2 F^2}{4m\omega^2}. \quad (170)$$

In Eqs. (167) and (168), N is the number of atoms of the molecule and n_l the number of atomic orbitals constituting the initial molecular state of the l -th atom. For example, in the case of HOMO of all-*trans* polyacetylene radicals $C_n H_{n+2}$, $N = n$ and $n_l = 2$ ($l = 1, 2, \dots, n$). Note that the exponential part of Eq. (168) is the same as that of the atomic case when $\bar{R}_j = \vec{0}$ (see Secs. 2.3 and 2.4).

Equation (167) consists of a simple summation of the ionization rates from each atom and orbital as predominant terms. As additional terms, the quantum interference manifests itself as coherent sums of transition amplitudes of the respective constituent atoms and their atomic orbitals. This fact seems to be closely related to the finding deduced using the intense-field many-body S -matrix theory.^{14,85–88} Equation (167) is suggestive of phase interference effect ubiquitous in quantum mechanics, e.g. double-slit experiment. The interference terms arise from the fact that $L(\vec{p})$ defined by Eq. (165) has V_0 which is the sum of contributions from each atom and orbital as can be seen from Eq. (154). The interference terms cannot be obtained in an analytical form. These terms are obtained by numerical calculations as shown in Appendix H.

It should be noted that the quantum interference terms in Eq. (167) are a consequence of the overlaps of the tails of the wave functions in the potential barriers among the nuclei. Therefore, the influence of the forms of the interstitial potential barriers is included in these terms. As is well known, this effect is crucial for determining the photoionization rates of molecules. In particular, this effect is most evidently recognized when the photoionization rates are calculated while the internuclear distances are changed as mentioned in Sec. 2.5.1.

In addition, it should be noted that the exponential parts $\exp(-i\vec{p} \cdot \vec{R}_j/\hbar)$ in Eqs. (156) and (F1)–(F6) play a significant role for the photoionization rate formula because the exponent $e\vec{F} \cdot \vec{R}_l$ in Eq. (168) arises from this part. These exponentials $\exp(-i\vec{p} \cdot \vec{R}_j/\hbar)$ essentially arise from the displacement of the atom from the center of mass of the molecule. On the other hand, the terms $e\vec{F} \cdot \vec{R}_j$ in Eqs. (156) and (F1)–(F6) affect only the pre-exponential parts so that their contribution to the photoionization rate is presumably small. Note that the atomic site \vec{R}_j is included only in the form $\vec{F} \cdot \vec{R}_j$ in Eq. (167).

From Eqs. (167) and (168), it is clear that the molecular photoionization rate strongly depends on the exponential factor $\exp(2\sqrt{2mI}\vec{F} \cdot \vec{R}_l/\hbar F)$, where I is the ionization potential for the atomic orbital [e.g. $I = I_{2p_x}$ for the HOMO of all-*trans* polyacetylene radicals as defined by Eq. (157)]. This indicates that the atoms lying downstream along the polarization vector of the laser field have the lowest ionization rate and those lying upstream along it the highest ionization rate. Roughly speaking, if we can neglect the position dependence of the pre-exponential terms, the photoionization rate depends exponentially on the cosine of the position direction of the atoms and the polarization direction of the laser pulse. This tendency has been found qualitatively so far, but the quantitative relation has not been reported. In addition, it should be noted that the photoionization rate is sensitive to the ionization potential of the atom due to the factor \sqrt{I} in the exponent. As shown in the next sub-section, the interference terms are comparable to or smaller than the total photoionization rate so that the total photoionization rate is roughly the sum of the contributions from the respective occupied orbitals of the atoms of the molecule in many cases.

In the low frequency limit ($\omega \rightarrow 0$), we have

$$h(l, k_l) \rightarrow -\frac{4\sqrt{2mI_{k_l}}}{3\hbar eF} + \frac{2\sqrt{2mI_{k_l}}\vec{R}_l \cdot \vec{F}}{\hbar F}. \quad (171)$$

The first term on the right hand side of Eq. (171) is the same as that of the atomic Keldysh theory. This term indicates that the slope of the photoionization rate versus laser intensity decreases as the laser intensity increases. However, for the spatially oriented molecules, we have an additional term: the second term on the right hand side of Eq. (171). It should be noted that this exponential term does not affect the slope of the photoionization rate versus laser intensity. This discussion indicates that the slope of each constituent atom has the same tendency as that of the atoms. However, for the molecules, because the total photoionization rate consists of those of the constituent atoms, it may happen that the total photoionization rate does not have a simple exponential increase versus laser intensity.

2.5.3. Computational method — *ab initio* calculation

Ab initio quantum chemistry calculations are performed for open-shell polyacetylene radicals C_nH_{n+2} ($n = 3, 5, 7, 9, 13, 27$) in the all-*trans* configuration. The geometries of each polyacetylene radical are completely optimized with C_{2v} symmetry using the hybrid density functional method B3LYP/6-31G, and the corresponding harmonic frequencies are characterized at the same level of theory. By the geometry optimization, we assume the planarity of the molecules. From the force-constant matrix calculation, no vibrational modes with imaginary frequencies are found, which means that truly local minima are obtained. In order to obtain reliable values, the energies are obtained with the G2M(cc, MP2) method,⁸⁹ a modification of the Gaussian-2 (G2) method proposed by Pople and co-workers.⁹⁰ The basis sets for C2M(cc, MP2) calculations are 6-311G** for CCSD(T) and 6-311+G(3df, 2p) and 6-311G** for MP2 calculations.

The ionization potentials are obtained by the outer valence Green's function (propagator) calculations.⁹¹ The inner shells are excluded from the correlation function calculation. The molecular orbital coefficient $\zeta_{2px,j}$ included in Eq. (147) is obtained at the time-dependent Hartree-Fock level by *ab initio* calculations. In this article, we have chosen this level of theory since the theoretical structure does not alter because of the calculation method. In addition, we have not taken into account the local modification of the external laser field by the constituent atoms of the molecular chain (i.e. their cooperative effects, each acting as an individual oscillator, changing thus the electric polarizability).

The package of GAUSSIAN 98 is employed for all the *ab initio* calculations performed in this article.⁹²

2.5.4. Numerical results and discussion

2.5.4.1. *Ab initio* calculation

The motivation of choosing all-*trans* polyacetylene radicals in the calculations is that so far there are no experimental or numerical results to compare with, especially large polyatomic molecules. Therefore, in this sub-section, we show model calculations and systematically investigate some general features deduced from the analyses of the analytical expressions and the numerical results.

Figure 6 demonstrates the structures optimized by *ab initio* calculations at the B3LYP/6-31G level of theory. All of them have C_{2v} symmetry and planar geometries. According to Suhai,⁷⁶ it is recognized that the extension

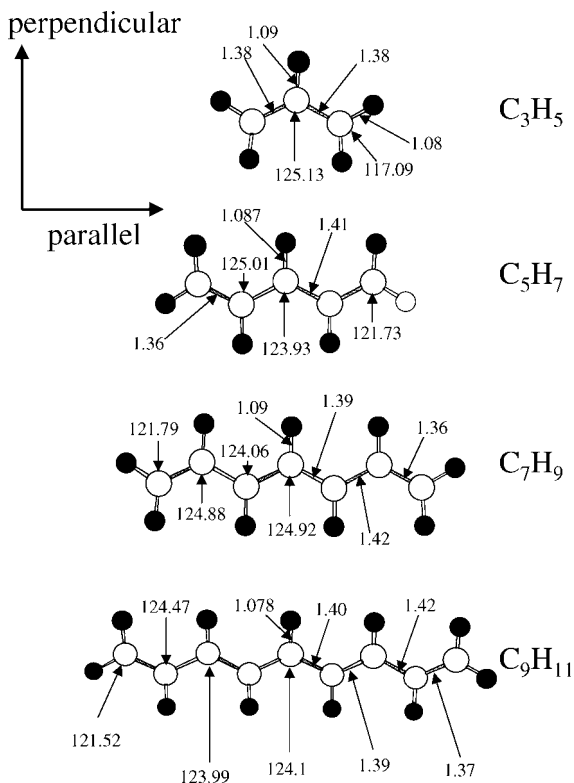


Fig. 6. Structures of all-*trans* polyacetylene radicals obtained by *ab initio* calculations. Black and white circles represent hydrogen and carbon atoms, respectively. Bond lengths are in the unit of Å and angles in the unit of degree. By the arrows shown in the upper left side in the figure, the parallel and perpendicular directions of the polarization vectors of the incident laser pulses are indicated. [Reprinted with permission from Mishima *et al.*, Phys. Rev. A, 71, 053411 (2005). Copyright (2005) by the American Physical Society.]

of the basis sets beyond the STO-3G level will not change the obtained results fundamentally. Therefore, the basis set employed in this article, 6-31G, seems to be enough for us to investigate the photoionization rates later using the results obtained by *ab initio* calculation.

In Table 1, we demonstrate the ionization potentials obtained by an outer valence Green's function (propagator) calculation. The calculated ionization potential 8.880 eV for the allyl radical agrees very well with the experimental values 8.13 or 8.07 eV.⁷⁷ From this table, we can see that the ionization potentials decrease with the size of the molecule. This tendency also holds for neutral polyacetylene (see Fig. 2 of Ref. 93). Comparing Table 1 and Fig. 2 of Ref. 93, polyacetylene radicals have comparable or

Table 1. Ionization potentials of all-*trans* polyacetylene radicals in the unit of eV.

Species	This Article	Theoretical	Experiment
C ₃ H ₅	8.880	7.57 ^c	8.13, ^a 8.07 ^b
C ₅ H ₇	7.543		7.76 ^d
C ₇ H ₉	6.752		
C ₉ H ₁₁	6.197		
C ₁₁ H ₁₃	5.885		
C ₁₃ H ₁₅	5.751		
C ₂₇ H ₂₉	5.239		

^aRef. 77.^bRef. 78.^cRef. 80.^dRef. 98.Table 2. Examples of energies of all-*trans* polyacetylene radicals in the unit of hartree.

Species	Energy
C ₃ H ₅	-117.024426
C ₅ H ₇	-194.2863222
C ₇ H ₉	-271.5448569

lower potential energies than neutral ones. This is because the valence electron of polyacetylene radicals has single-active-electron nature. The total energies of some of the all-*trans* polyacetylene radicals are shown in Table 2.

From the molecular orbital coefficient analysis, it is found that the valence electron density is concentrated on the carbon backbone and there is no electron density on the hydrogen atoms in all the laser intensity range investigated in this article.

Figure 7 demonstrates the molecular orbital coefficients of the C₂₇H₂₉ molecule in the linearly polarized electric field whose polarization is (a) vertical and (b) parallel to the carbon backbone. Figure 7(a) shows that the molecular orbital coefficients remain almost the same over the laser intensity range shown in the figure. On the other hand, from Fig. 7(b), we can see that when the laser intensity is not so high, the electron population is distributed almost evenly among the nuclear sites. However, when the laser intensity is high, the population tends to concentrate downstream along the carbon backbone due to the polarizability of the molecule.

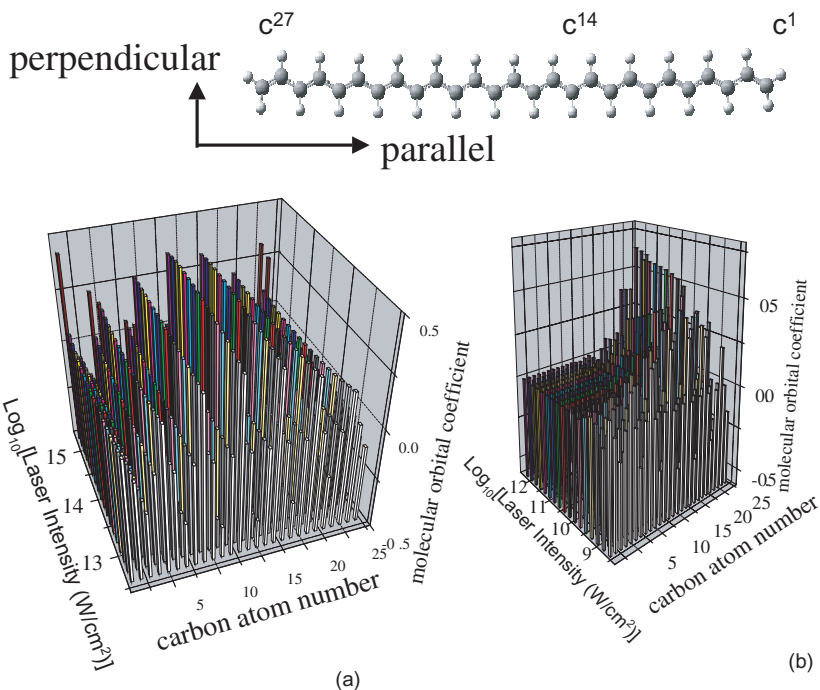


Fig. 7. Molecular orbital coefficients of the $C_{27}H_{29}$ molecule in the linearly polarized electric field whose polarization is (a) vertical and (b) parallel to the carbon backbone. [Reprinted with permission from Mishima *et al.*, Phys. Rev. A, 71, 053411 (2005). Copyright (2005) by the American Physical Society.]

2.5.4.2. Photoionization rates of all-trans polyacetylene radicals (C_nH_{n+2} , $n = 3, 5, 7, 9, 13, 27$)

In the following calculations, we use effective ionization potentials for the binding energies expressed by Eq. (157). This means that the effect of the electrons other than the ionizing electron is taken into account by the static screening potential. The wavelength of the incident laser is assumed to be 1450 nm throughout the following numerical examples. The tunneling ionization criterion $\bar{\gamma}_{\text{korb}} \leq 0.5$ is satisfied in almost all the figures presented in this article⁹⁴ so that the molecular Keldysh theory derived in the preceding sub-section is valid over the laser intensity region investigated in the present article. In the extreme case [e.g. laser intensity $3.6 \times 10^{11} \text{ W/cm}^2$ in Fig. 11(b)], $\bar{\gamma}_{\text{korb}}$ of the 1s orbital of the hydrogen atom amounts to 0.2.

Before proceeding to the numerical calculation of the photoionization rates, the dipole approximation assumed in the calculations should be justified. The laser wavelength (or frequency) of interest in the tunneling

region lies in the range 800 nm and more (or less than 1.55 eV). For example, the length between C^1 and C^{27} of the largest all-*trans* polyacetylene radical treated in this article (namely, $C_{27}H_{29}$ in Fig. 7) is 32 Å. The ratio of this length and the laser wavelength 1450 nm amounts only to 0.0022. Clearly, this ratio is quite small so that it is legitimate to apply the dipole approximation.

In Fig. 8, we demonstrate the photoionization rates versus incident laser intensity calculated by Eq. (167) for two of the all-*trans* polyacetylene radicals, C_3H_5 and $C_{13}H_{15}$. One can see that the total photoionization rates w_0 when the polarization of the laser pulse is parallel to the molecular axis are always larger than those when it is perpendicular to the molecular axis. If the polarization of the laser field lies between these two directions, w_0 will fall between these two extrema.

In addition, it is apparent from these figures that w_0 is essentially the sum of the photoionization rates of the almost identical atoms in Figs. 8(a) and 8(c), while in Figs. 8(b) and 8(d), only one of the carbon atoms predominates in the total photoionization rate w_0 . In the former case, the molecular orbital coefficients determine the relative magnitude of photoionization

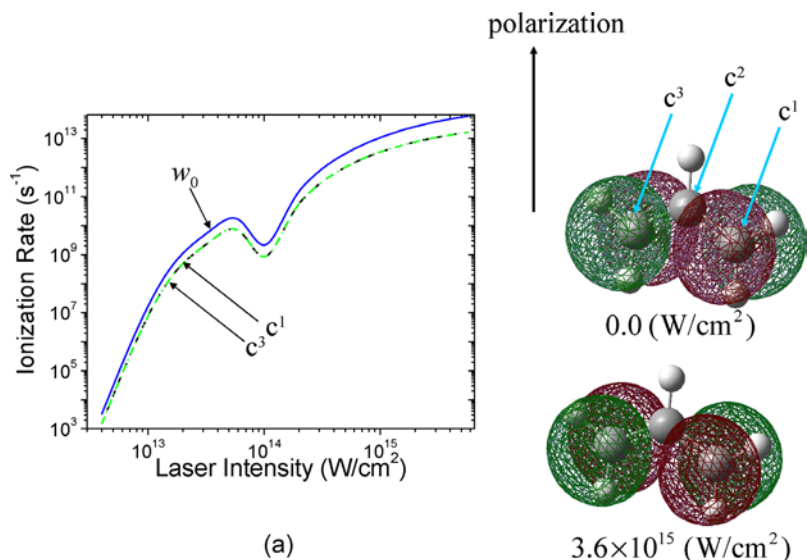
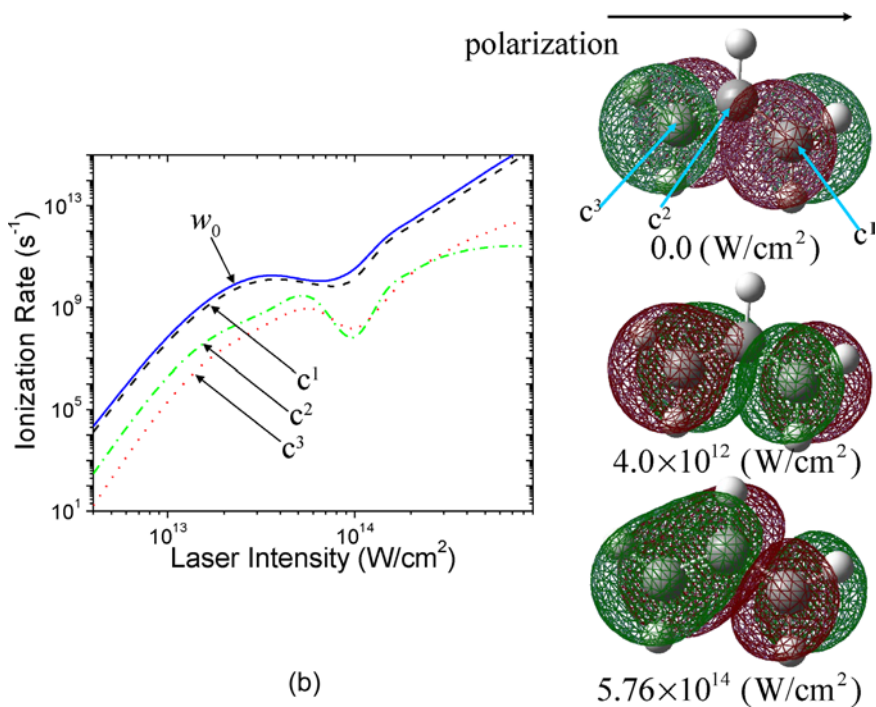
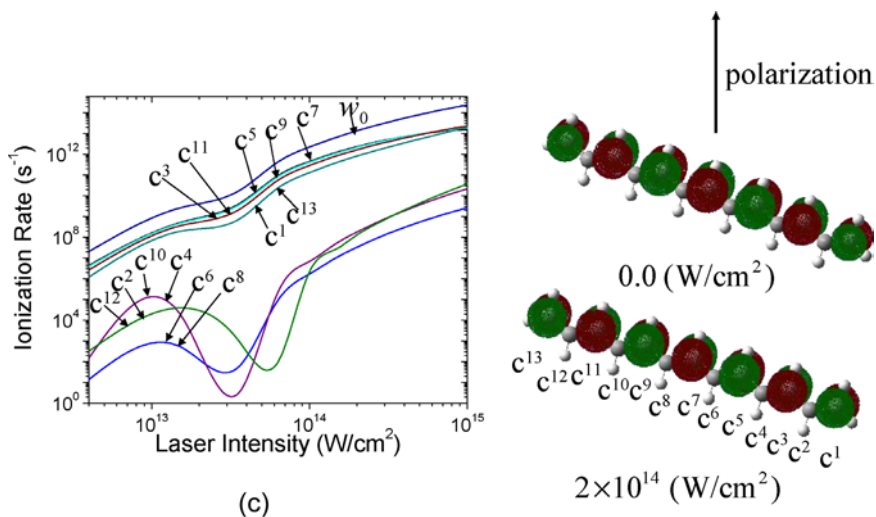


Fig. 8. Photoionization rates versus laser intensity for C_3H_5 (a, b) and $C_{13}H_{15}$ (c, d), radicals. In panels (a) and (c), the laser polarization is perpendicular to the molecular axis, and in panels (b) and (d), parallel to it. The photoionization rate w_0 is the total rate defined by Eq. (167). In panel (a), the molecular orbital coefficient of C^2 is zero so that there is no line for C^2 in the figure. [Reprinted with permission from Mishima *et al.*, Phys. Rev. A, 71, 053411 (2005). Copyright (2005) by the American Physical Society.]



(b)



(c)

Fig. 8. (Continued)

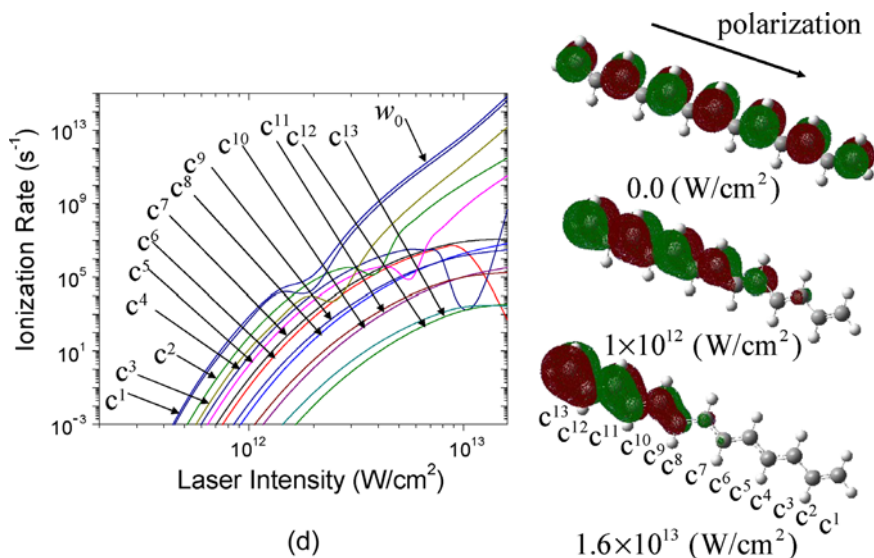


Fig. 8. (Continued)

rates. That is, for example, in Fig. 8(c), at almost all the laser intensities, the absolute values of $\zeta_{2px,j}$ are either 3×10^{-3} or 5×10^{-4} . On the other hand, in the latter case, again at almost all the laser intensities, they are either 1×10^{-2} or 1×10^{-4} . In other words, in the latter case, we cannot predict the photoionization rates shown in Fig. 8(d) only from the molecular orbital coefficients. In this case, \bar{R}_j in Eq. (168) plays an important role for determining the photoionization rate in Figs. 8(b) and 8(d).

By careful examination, we can see from Fig. 8(b) that the photoionization rate from C^2 is larger than from C^3 below the laser intensity about 1×10^{14} (W/cm^2). This is due to the fact that the exponential factor of C^2 is larger than that of C^3 . However, over the laser intensity around 1×10^{14} (W/cm^2), we notice that the photoionization rates from C^2 and C^3 are comparable. This is because the pre-exponential factor of C^3 is larger than that of C^2 .

From inspection of Fig. 8, we can conclude the followings. The directional dependence of the photoionization rate is prominent in the molecules, in particular, those that have directional anisotropy, such as polyacetylene. For example, it is found that when the polarization direction of the laser field is parallel with the carbon backbone of the polyacetylene radical, the photoionization rates show a maximum; if it is perpendicular, a minimum. Increasing the molecular size further will incline the electron

density to be concentrated in the opposite direction to the laser polarization direction and decrease the photoionization rate.

Figure 9 demonstrates the photoionization rate versus laser intensity under the assumption $\vec{R}_j = \vec{0}$ for all j for the polarization direction (a) vertical and (b) parallel to the carbon backbone. Comparing Figs. 9(a) and 8(c) leads to the conclusion that the nuclear-site dependence is not so important for the vertical polarization direction case. On the other hand, for the parallel polarization direction case (b), we can see that because of the smaller exponential factors for the atoms upstream along the polarization direction and the larger ones for those downstream, the individual photoionization rates are much more similar than when \vec{R}_j dependence is included properly [compare Fig. 8(d) and Fig. 9(a)]. This indicates the importance of the

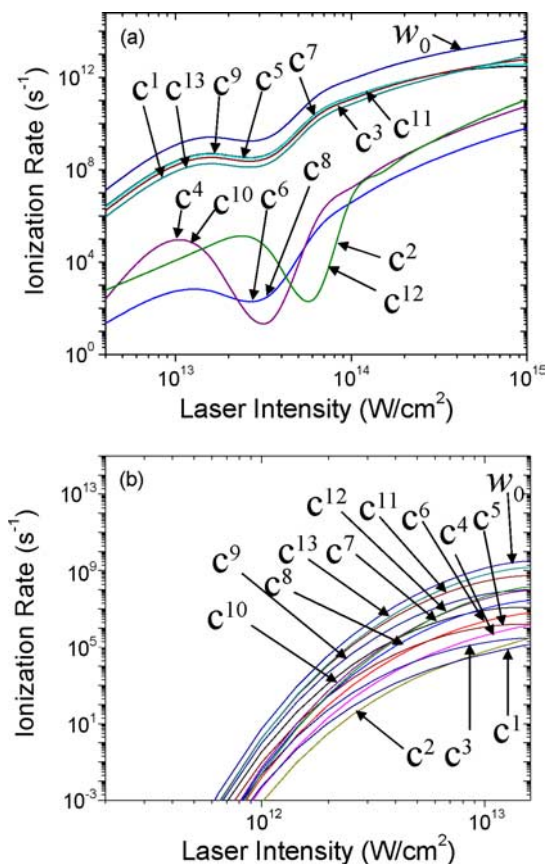


Fig. 9. Photoionization rates versus laser intensity under the assumption $\vec{R}_j = \vec{0}$ for all j (a) for Figs. 8(c) and 8(b) for Fig. 8(d). [Reprinted with permission from Mishima *et al.*, *Phys. Rev. A*, 71, 053411 (2005). Copyright (2005) by the American Physical Society.]

nuclear-site dependence of the exponential factor of Eq. (167) for the parallel polarization direction case. In addition, if only the molecular orbital coefficients are taken into account as in Fig. 9(b), the contributions from each atom would be predicted in reverse order from those calculated by properly including \vec{R}_j dependence in Eq. (167) [compare Fig. 8(d) and Fig. 9(a)].

Next, it may be necessary to investigate the role of the factors $\vec{F} \cdot \vec{R}_j$ in the pre-exponential and exponential factors of Eq. (167). This is due to that fact that this term is one of the characteristics most different from those of atoms. Figure 10(a) demonstrates the photoionization rate under the assumption that only the factors $\vec{F} \cdot \vec{R}_l$ in Eq. (168) are set to be zero in Eq. (167). Comparing this with Fig. 8(d) indicates that the factors $\vec{F} \cdot \vec{R}_l$ in Eq. (168) play an important role in the high intensity region. This factor

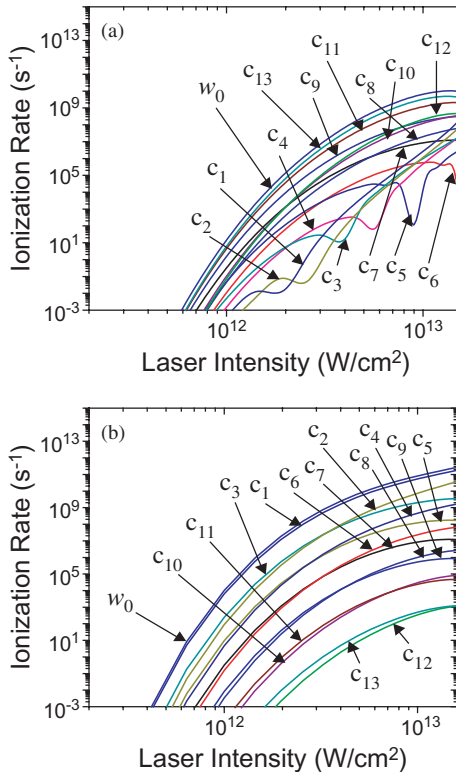


Fig. 10. Demonstration of the predominance of the factor $\vec{F} \cdot \vec{R}_l$ in the exponential part defined by Eq. (168) in the photoionization rates. In Fig. 10(a), only the factors $\vec{F} \cdot \vec{R}_j$ in Eq. (168) are set to be zero in Eq. (167) while in Fig. 10(b), the factors $\vec{F} \cdot \vec{R}_l$ other than those in Eq. (168) are set to be zero in Eq. (167). These figures are compared with Fig. 8(d). [Reprinted with permission from Mishima *et al.*, Phys. Rev. A, 71, 053411 (2005). Copyright (2005) by the American Physical Society.]

serves to increase photoionization rates in the high intensity range. On the other hand, in Fig. 10(b), factors $\vec{F} \cdot \vec{R}_i$ other than those in Eq. (168) are set to be zero in Eq. (167). In this case, due to the presence of the factors $\vec{F} \cdot \vec{R}_i$ in the exponent of Eq. (168), the order of magnitude is the same as for the correct photoionization rates Fig. 8(d). In addition, it should be noted that neglecting only the pre-exponential parts is not so harmful in the low intensity region. In particular, it is remarkable to note that, comparing Figs. 8(d) and 10(b), the anomalous decrease of the photoionization rate with increasing laser intensity is due to the pre-exponential factors.

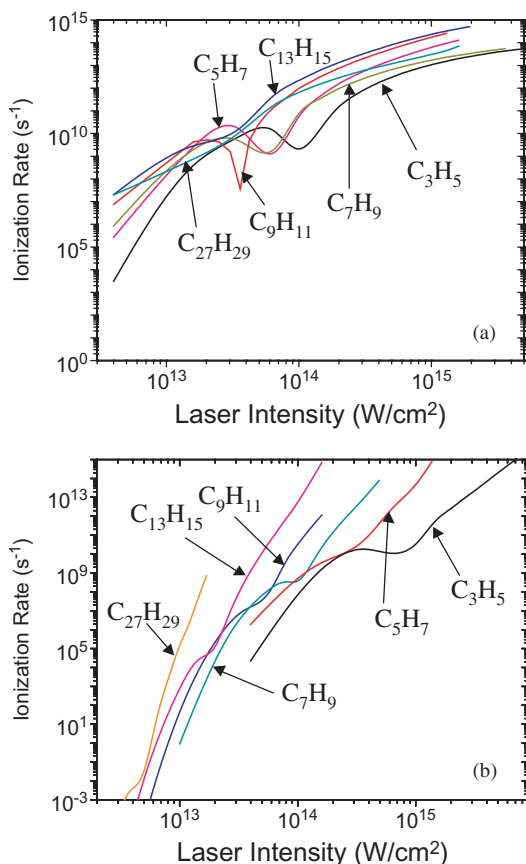


Fig. 11. Total photoionization rates w_0 versus laser intensity for all-*trans* polyacetylene radicals C_nH_{n+2} ($n = 3, 5, 7, 9, 13, \text{ and } 27$) calculated by Eq. (167). Panel (a) is for the perpendicular and (b) for the parallel polarization direction, respectively. [Reprinted with permission from Mishima *et al.*, Phys. Rev. A, 71, 053411 (2005). Copyright (2005) by the American Physical Society.]

In Fig. 11, the total photoionization rates w_0 in Fig. 8 for the cases of the laser polarization vectors parallel and perpendicular to the molecular axes of C_3H_5 , C_5H_7 , C_7H_9 , C_9H_{11} , $C_{13}H_{15}$, and $C_{27}H_{29}$ are shown at the same time. From Fig. 11(a), in the case of the laser polarization perpendicular to the carbon backbone, it is found that the molecular size does not play any role in determining the photoionization rate. On the other hand, in the case of the laser polarization parallel to the carbon backbone [Fig. 11(b)], we can see that by increasing the molecular size, the photoionization rate reaches a given value at the lower laser intensity. In addition, note that the slope of the photoionization rate versus laser intensity increases with molecular size. This is consistent with the fact that in the small molecules, a large variation of the laser field strength is necessary for the photoionization rate to reach a given value, while in the large molecules, a small change of the laser intensity drastically changes the tunneling probability of the electron.

From the figures, we notice that in general the photoionization rates are remarkably not a monotonic function of the laser intensity. This has already been observed in several experiments, although the authors do not point it out clearly (see, e.g. the data of D_2^+ in Fig. 5 of Ref. 95) and numerically (see, e.g. the data of H_2^+ in Fig. 1 of Ref. 96). But theoretically this has been clearly pointed out by Barnett *et al.*⁶⁵ They calculated the photoionization rate versus laser intensity of H_2^+ molecule, the calculation of which is one-dimensional tunneling ionization model based on the Weyl–Titchmarsh–Kodaira spectral theorem. They found that the photoionization rate is not a monotonic function of the laser intensity. They attributed this anomalous behavior to the significant difference of the shape of the wave function of the initial state at the minimum and maximum photoionization rates. This leads to an interference effect between the inner and outer barriers of the H_2^+ molecule. Although it is difficult to perform similar estimations for large polyatomic molecules such as those studied in this article, the above discussion may be applied to them as well. In our opinion, this may be due to the fact that we still have scarce experimental and theoretical data on spatially fixed molecules. This remains to be explored in detail in the future.

In summary, Fig. 12 schematically demonstrates the results or predictions deduced from the present analyses. In panel (a), the molecular axis is perpendicular to the polarization direction of the linearly polarized laser field. In the low laser intensity region, the photoionization rates from the respective atoms are almost equally probable, mostly proportional to the electron density on the atom. On the other hand in the strong laser intensity range, the electron cloud will be deformed by the polarizability induced by the laser field. However, if the chain length of the molecule is much shorter

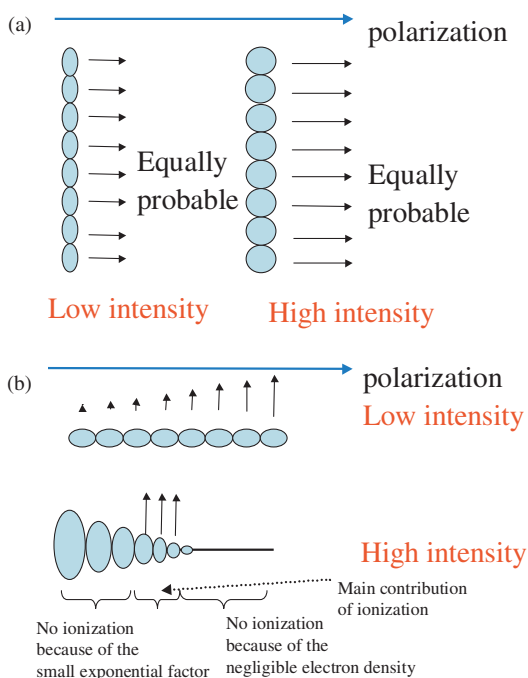


Fig. 12. Schematic representation of photoionization of large polyatomic molecules in the low and high intensity linearly polarized lasers for the polarizations (a) perpendicular to and (b) parallel with the molecular axis. [Reprinted with permission from Mishima *et al.*, Phys. Rev. A, 71, 053411 (2005). Copyright (2005) by the American Physical Society.]

than the molecular axis, the photoionization rates from each atom increase only proportionally.

In Fig. 12(b), the molecular axis is parallel to the polarization direction of the linearly polarized electric field. In the low laser intensity region, the contribution from the exponential factor $\exp(2\sqrt{2mI\vec{F}} \cdot \vec{R}_j/\hbar F)$ overwhelms that from the molecular orbital coefficient, and the photoionization rate increases gradually as one goes down along the laser polarization direction. On the other hand, in the strong laser intensity regime, the electron density tends to concentrate on the upstream of the laser polarization direction and there is almost no electron density on the downstream. Because of the small exponential factor $\exp(2\sqrt{2mI\vec{F}} \cdot \vec{R}_j/\hbar F)$ for the upstream atoms and negligible electron density for the downstream atoms, the contribution from the atoms of both ends is very small. Therefore, it is predicted that if the laser intensity is very strong, photoionization takes place only from the vicinity of the center of the molecule.

Because the quantum interference terms are comparable with or smaller than the photoionization rates of the individual atoms, it is important to investigate the quantum interference terms in detail. Figure 13 demonstrates the photoionization rates for each two atoms arising from the quantum interference terms. In all the figures, the bars on the diagonal line represent the photoionization rates of each atom and those on the off-diagonal lines, those of quantum interference. The bars are symmetric with respect to the diagonal line. The photoionization rates are positive when the molecular orbital coefficients have the same sign for two atoms while those

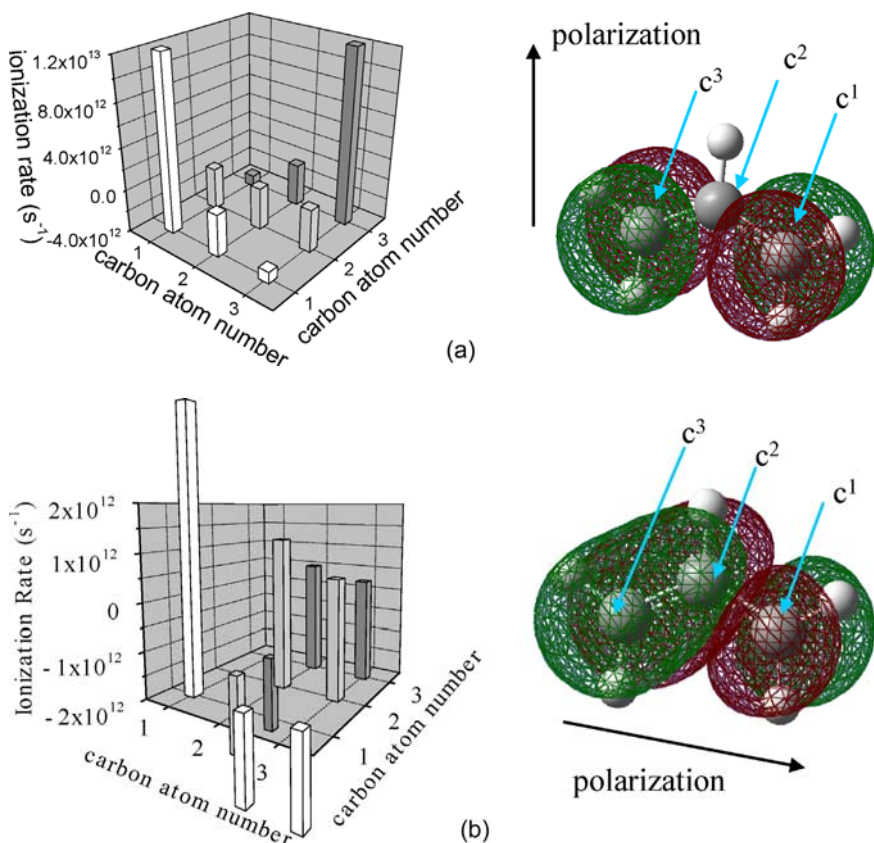


Fig. 13. Quantum interference terms calculated by Eq. (167) for (a) C_3H_5 at 3.6×10^{15} (W/cm^2), (b) C_3H_5 at 5.76×10^{14} (W/cm^2), (c) $C_{27}H_{29}$ at 4.0×10^{14} (W/cm^2), and (d) $C_{27}H_{29}$ at 1.69×10^{12} (W/cm^2). In panels (a) and (c), the polarization of the incident linearly polarized laser field is perpendicular to the carbon backbone while in panels (b) and (d), it is parallel to the carbon backbone. [Reprinted with permission from Mishima *et al.*, Phys. Rev. A, 71, 053411 (2005). Copyright (2005) by the American Physical Society.]

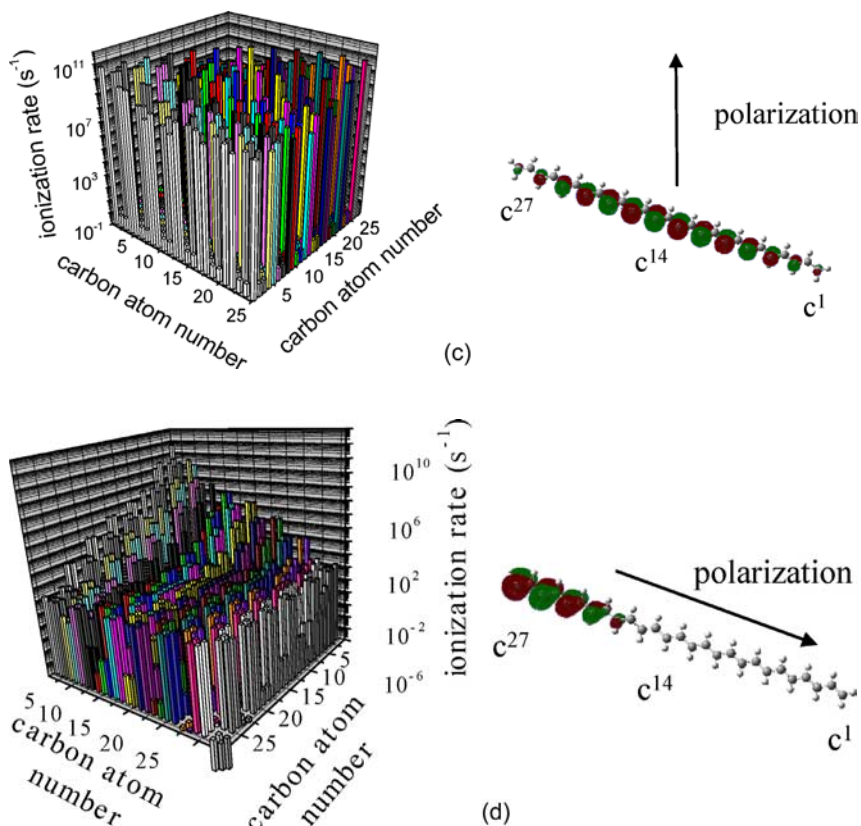


Fig. 13. (Continued)

are negative when they have the opposite sign for two atoms. In the smallest molecule case (C_3H_5), the diagonal terms decrease with increasing carbon atom numbers as we saw in Fig. 8 [compare Fig. 13(b) and Fig. 8(b)]. From Figs. 13(a) and 13(b), we can see that the individual quantum interference terms are smaller than the photoionization rates of the individual atoms. Nothing very remarkable can be obtained from the observation of this small molecule. However, in the largest molecule case ($C_{27}H_{29}$), we can clearly recognize something quite remarkable. We notice that the quantum interference terms are largest when the distances between the two atoms are shortest while they are smallest when they are longest. In addition, as the partners go up along the polarization direction, the photoionization rate tends to decrease. This phenomenon is clearly understood by Eqs. (G29), (H9), and (H10). For a given carbon atom, if the partner goes up along the

polarization direction, the exponential factor of Eq. (H10) decreases predominantly, which leads to a significant decrease of the photoionization rate. This is peculiar to large polyatomic molecules, which cannot clearly be realized by the small molecules.

Finally, we show that these features are really due to the exponential factor of Eq. (H10). Figures 14(a) and 14(b) are obtained by letting $\vec{F} \cdot \vec{R}_j = 0$ in Eq. (G29) for Figs. 13(b) and 13(d), respectively. Comparing Fig. 13(b) and Fig. 14(a), we actually notice the important role of the exponential factor of Eq. (H10) even for the small molecules. In the absolute value, the

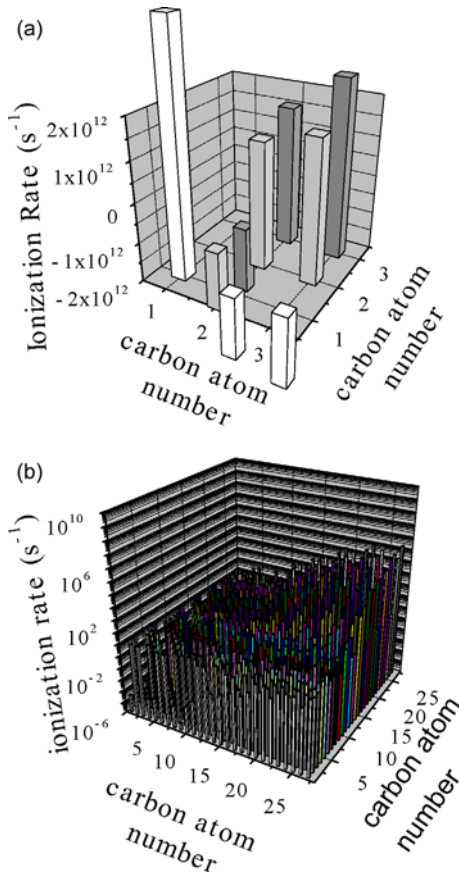


Fig. 14. Quantum interference terms calculated by Eq. (167) for (a) C_3H_5 at 5.76×10^{14} (W/cm^2) and (b) $C_{27}H_{29}$ at 1.69×10^{12} (W/cm^2) when the polarization of the laser field is parallel to the carbon backbone. In these figures, the factor $\vec{F} \cdot \vec{R}_j$ in the exponential part defined by Eq. (G29) is set to be zero. Compare (a) with Figs. 13(b) and 13(b) with Fig. 13(d). [Reprinted with permission from Mishima *et al.*, Phys. Rev. A, 71, 053411 (2005). Copyright (2005) by the American Physical Society.]

quantum interference terms between C^1 and C^2 become smaller if we let $\vec{F} \cdot \vec{R}_j = 0$. This is because $\vec{F} \cdot \vec{R}_1$ becomes very small in Eq. (G29). However, the quantum interference term between C^1 and C^3 does not change because $\vec{F} \cdot \vec{R}_j$ is canceled out due to the symmetry of C^1 and C^3 from the center of the molecule. On the other hand, the quantum interference term C^2 and C^3 becomes very large if we let $\vec{F} \cdot \vec{R}_j = 0$ since $\vec{F} \cdot \vec{R}_3$ is larger than that of Fig. 13(b).

If we compare Fig. 13(d) and Fig. 14(b) for large molecule $C_{27}H_{29}$, the importance of the exponential factor of Eq. (H10) is much clearer. Actually, if we neglected $\vec{F} \cdot \vec{R}_j$ in Eq. (H10), we might make the wrong prediction that the quantum interference terms among the atoms upstream along the polarization direction are bigger than those downstream. This wrong tendency is only due to the larger electron density for the atoms upstream. From this comparison, it becomes clear that the terms $\vec{F} \cdot \vec{R}_j$ in the exponent of Eq. (H10) also play an important role in determining the quantum interference terms.

The prediction of these peculiar behaviors of large molecules has been made in,¹⁴ although detailed discussion has not been made. Their prediction can be easily verified by our formula as mentioned above.

Recently, molecular ADK theory has been proposed, extending atomic ADK theory.⁵² Our molecular Keldysh theory is different from it with regard to the following points.

- (1) As in the atomic ADK theory, the molecular ADK theory assumes that the electron goes out only along the polarization direction. However, in the molecular Keldysh theory, the three-dimensional nature of the electron momentum \vec{p} is appropriately taken into account as is shown in Appendix H.
- (2) The nuclear-site dependence is explicitly taken into account in the present theory while in the molecular ADK theory it is not the case. Therefore, in the present theory, several features of molecular photoionization can be easily deduced from the formula.
- (3) The present molecular theory can be applied to any kinds of molecules while in the molecular ADK theory it will be difficult.
- (4) In our theory, we have developed the molecular Coulomb–Volkov function for the final continuum state that includes the free electron motion in the free volume while in the molecular ADK theory it is not included properly.

Finally, a remark is in order. Our formula derived for the molecular system has the feature different from that for the atomic system that in the

former case only the atomic-site dependence is included in the form $\vec{F} \cdot \vec{R}_j$, whereas in the latter case it is absent. One should not confuse the “modified” Keldysh parameter defined by Eq. (169) with the modified adiabatic parameter $\gamma(\psi)$ used in Ref. 97. Our “modified” Keldysh parameter pertains to the constituent atoms while $\gamma(\psi)$ pertains to the overall molecular characteristics, the molecular wavefunction ψ .

2.6. Extension of the Atomic Keldysh Theory to Molecular Photoionization Processes

(i) H₂ molecule

2.6.1. Introduction

In this section, we will extend our previous formulations of the photoionization of molecules by introducing the Born–Oppenheimer approximation to properly take into consideration of the electronic and nuclear degrees of freedom. The new formulation can treat the photoionization of not only diatomic molecules, but also polyatomic molecules, and as application and illustration, it will be applied to calculate the photoionization rate of H₂. Our computed results will be compared with experimental data.

In Sec. 2.6.2, we derive the theoretical aspects of our method in detail. In Sec. 2.6.3, the details of the *ab initio* calculation of H₂, the calculation of potential energy curves (PECs) of H₂⁺ deformed by the laser field, and the calculation of Franck–Condon factors are described. In Sec. 2.6.4, we demonstrate our numerical photoionization rates of H₂ using the formula derived in Sec. 2.6.2. We investigate two cases where the laser polarization direction is parallel and perpendicular to the molecular axis. The behaviors of the two cases are quite different, which agrees with the previously reported work.⁸ In addition, we compare Condon and non-Condon approximations. This comparison shows that the more accurate molecular photoionization rate can be obtained by taking into account the relative geometries between the neutral and ionic potential energy surfaces and the characteristics of the ionic potential itself in addition to the equilibrium neutral state.

2.6.2. Theory

According to the time-dependent perturbation theory, we have

$$i\hbar \frac{\partial \Psi}{\partial t} = \hat{H} \Psi, \quad (172)$$

where

$$\hat{H} = \hat{H}_0 + \hat{H}' \quad (173)$$

and

$$i\hbar \frac{\partial}{\partial t} \Psi_n^0(q, t) = \hat{H}_0 \Psi_n^0(q, t), \quad (174)$$

where \hat{H}_0 is the zero-order Hamiltonian and \hat{H}' the perturbation. If the system is initially in the k -th state, then from

$$\Psi(q, t) = \sum_n c_n(t) \Psi_n^0(q, t) \quad (175)$$

we obtain

$$i\hbar \frac{dc_m(t)}{dt} = \langle \Psi_m^0(q, t) | \hat{H}' | \Psi_k^0(q, t) \rangle. \quad (176)$$

In the dipole approximation, \hat{H}' is given by

$$\hat{H}' = -\vec{M} \cdot \vec{F}(t), \quad (177)$$

where

$$\vec{M} = -e \sum_{i=1}^{N_e} \vec{r}_i \quad (178)$$

is the dipole operator. Here, N_e represents the number of the electrons in the system, \vec{r}_i the position of the i -th electron.

For molecular systems, the Born–Oppenheimer approximation is commonly used; thus for the photoionization from the initial rovibronic state av to the ionized rovibronic state pv' , we find

$$i\hbar \frac{dc_{pv'}(t)}{dt} = \langle \Psi_{pv'}^0(q, t) | \hat{H}' | \Psi_{av}^0(q, t) \rangle, \quad (179)$$

where a and p denote the initial bound electronic state and the final ionized electronic state, respectively, while v and v' represent their corresponding ro-vibrational states. For example, for the case of diatomic molecules, if the molecular ion is a stable species, then we have the Franck–Condon transition between the discrete ro-vibrational states.

If we let $\Theta_{pv'}$ and Θ_{av} represent the ro-vibrational wavefunctions with energies $E_{pv'}$ and E_{av} , then Eq. (179) can be written as

$$i\hbar \frac{dc_{pv'}(t)}{dt} = \langle \Theta_{pv'} | H'_{pa}(t) | \Theta_{av} \rangle \exp \left\{ \frac{it}{\hbar} (E_{pv'} - E_{av}) \right\}, \quad (180)$$

where $H'_{pa}(t)$ denotes the electronic matrix element of the dipole interaction. If the molecule is initially in a closed-shell bound state a , then for the case

of one-electron ionization, $H'_{pa}(t)$ can be written as

$$H'_{pa}(t) = -\sqrt{2}\langle\phi_{\bar{p}}|\bar{\mu}\cdot\vec{F}(t)|\phi_a\rangle, \quad (181)$$

where ϕ_a denotes the HOMO while $\phi_{\bar{p}}$ represents the Volkov function.

In this section, we shall concentrate on the derivation and calculation of the following process:



In this case, $\phi_a = \phi_{\sigma 1s}$ and using the LCAO-MO theory,

$$\phi_{\sigma 1s} = b_1\chi_{1,1s} + b_2\chi_{2,1s}, \quad (183)$$

where $\chi_{1,1s}$ and $\chi_{2,1s}$ represent the 1s orbitals of nuclei 1 and 2, respectively, and b_1 and b_2 are the molecular orbital coefficients for nuclei 1 and 2, respectively. If the laser intensity is not so strong or the molecular axis is perpendicular to the direction of the laser polarization, we can simply write

$$\phi_{\sigma 1s} = \frac{\chi_{1,1s} + \chi_{2,1s}}{\sqrt{2 + 2S_{12}}}, \quad (184)$$

where S_{12} denotes the overlap integral. It should be noted that a better basis set than the simple LCAO-MO theory can be used. For polyatomic molecules, ϕ_a will be much more complicated than that used in Eq. (183).

Using Eq. (11), we obtain

$$\begin{aligned} H'_{pa}(t) &= -\sqrt{2} \sum_{j=1}^2 b_{j,1s} \langle \phi_{\bar{p}}(\vec{r}, t) | \bar{\mu}_j(\vec{r}) \cdot \vec{F}(t) | \chi_{j,1s}(\vec{r}_j) \rangle \\ &= -\sqrt{2} \sum_{j=1}^2 b_{j,1s} \langle \phi_{\bar{p}}(\vec{r}_j, t) | \bar{\mu}_j(\vec{r}_j) \cdot \vec{F}(t) | \chi_{j,1s}(\vec{r}_j) \rangle \exp \left\{ -\frac{i}{\hbar} (\vec{p} - e\vec{A}(t)) \cdot \vec{R}_j \right\}, \end{aligned} \quad (185)$$

where we have defined

$$\vec{R}_1 = \frac{\vec{R}_{0a}}{2} \quad \text{and} \quad \vec{R}_2 = -\frac{\vec{R}_{0a}}{2}. \quad (186)$$

The vector \vec{R}_{0a} is the instantaneous internuclear vector of H_2 . In deriving this equation, we have used the notation defined in Fig. 15.

In the Keldysh notation, we have

$$\begin{aligned} V_{0,1s}(\vec{p} - e\vec{A}(t)) &= \langle \phi_{\bar{p}}(\vec{r}_j, t) | \bar{\mu}_j(\vec{r}_j) \cdot \vec{F} | \chi_{j,1s}(\vec{r}_j) \rangle \\ &\quad \times \exp \left\{ -\frac{i}{2m\hbar} \int_0^t dt' (\vec{p} - e\vec{A}(t'))^2 \right\}. \end{aligned} \quad (187)$$

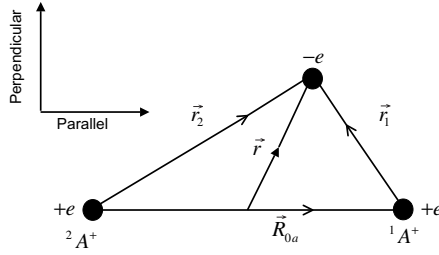


Fig. 15. Configuration of the molecular ion A_2^+ composed of two atomic ions $^1A^+$ and $^2A^+$, and one electron e^- ($A = \text{H, N, or O}$). The vector \vec{R} denotes the internuclear distance directing from $^2A^+$ to $^1A^+$, \vec{r} , the position of the electron from the center of mass of the molecule, \vec{r}_1 and \vec{r}_2 , the positions of the electron measured from $^1A^+$ and $^2A^+$, respectively. On the upper left-hand side, the polarization direction of the linearly polarized electric field is indicated by the arrows. [Reprinted with permission from Mishima *et al.*, Phys. Rev. A, 70, 063414 (2004). Copyright (2004) by the American Physical Society.]

Therefore, we obtain

$$H'_{pa}(t) = -\sqrt{2} \sum_{j=1}^2 b_{j,1s} V_{0,1s} (\vec{p} - e\vec{A}(t)) \cos \omega t \\ \times \exp \left[\frac{i}{\hbar} \left\{ \frac{1}{2m} \int_0^t dt' (\vec{p} - e\vec{A}(t'))^2 - (\vec{p} - e\vec{A}(t)) \cdot \vec{R}_j \right\} \right]. \quad (188)$$

For the photoionization process of H_2 , if $H'_{pa}(t)$ does not change significantly with vibration, we can use the so-called Condon approximation in Eq. (180) to obtain

$$i\hbar \frac{dc_{pv'}(t)}{dt} = -\sqrt{2} \langle \Theta_{pv'} | \Theta_{av} \rangle \sum_{j=1}^2 b_{j,1s} V_{0,1s} (\vec{p} - e\vec{A}(t)) \cos \omega t \\ \times \exp \left[\frac{i}{\hbar} \left\{ (E_{pv'} - E_{av})t \right. \right. \\ \left. \left. + \frac{1}{2m} \int_0^t dt' (\vec{p} - e\vec{A}(t'))^2 - (\vec{p} - e\vec{A}(t)) \cdot \vec{R}_j \right\} \right]. \quad (189)$$

Finally, the photoionization rate can be written as

$$w_{av \rightarrow pv'} = 2 \lim_{T \rightarrow \infty} \int \frac{d^3p}{(2\pi\hbar)^3} \text{Re} [\dot{c}_{pv'}^*(T) c_{pv'}(T)] \\ = \frac{4}{\hbar^2} \lim_{T \rightarrow \infty} \text{Re} \int \frac{d^3p}{(2\pi\hbar)^3} |\langle \Theta_{pv'} | \Theta_{av} \rangle|^2 \sum_{j=1}^2 \sum_{j'=1}^2 b_{j,1s}^* b_{j',1s} \\ \times \int_0^T dt \cos \omega T \cos \omega t V_{0,1s}^* (\vec{p} - e\vec{A}(T)) V_{0,1s} (\vec{p} - e\vec{A}(t))$$

$$\begin{aligned} & \times \exp \left[\frac{i}{\hbar} \left\{ \int_T^t dt' \left(I_{av,pv'} + \frac{1}{2m} (\vec{p} - e\vec{A}(t'))^2 \right) \right. \right. \\ & \left. \left. + (\vec{p} - e\vec{A}(T)) \cdot \vec{R}_j - (\vec{p} - e\vec{A}(t)) \cdot \vec{R}_j \right\} \right], \end{aligned} \quad (190)$$

where $|\langle \Theta_{pv'} | \Theta_{av} \rangle|^2$ is the Franck–Condon factor, and we define

$$I_{av,pv'} = E_{pv'} - E_{av}, \quad (191)$$

and the transition dipole matrix element between the plane wave and 1s atomic orbital is given by

$$V_{0,1s}(\vec{p}) = \langle \exp(i\vec{p} \cdot \vec{r}/\hbar) | e\vec{F} \cdot \vec{r} | \chi_{1s}(\vec{r}) \rangle = -\frac{2^{13/4} \sqrt{\pi} i e F p_z \hbar^{5/2} I_{1s}^{5/4}}{m^{7/4} (I_{1s} + p^2/2m)^3}. \quad (192)$$

Performing the integration over t and taking the limit $T \rightarrow \infty$ render

$$\begin{aligned} w_{av \rightarrow pv'} &= \frac{4\pi}{\hbar} \text{Re} \sum_{j=1}^2 \sum_{j'=1}^2 b_{j,1s}^* b_{j',1s} \int \frac{d^3p}{(2\pi\hbar)^3} \\ & \times \sum_{n=-\infty}^{\infty} L_{j,1s}^*(\vec{p}) L_{j',1s}(\vec{p}) \delta \left(I_{av,pv'} + \frac{p^2}{2m} + \frac{e^2 F^2}{4m\omega^2} - n\hbar\omega \right), \end{aligned} \quad (193)$$

where

$$\begin{aligned} L_{j,1s}(\vec{p}) &= \frac{1}{2\pi} \oint du V_{0,1s} \left(\vec{p} + \frac{e\vec{F}}{\omega} u \right) I_C \left(-\frac{1}{\hbar} \left(\vec{p} + \frac{e\vec{F}}{\omega} u \right), \vec{R}_j, v, v' \right) \\ & \times \exp \left[\frac{i}{\hbar\omega} \int_0^u \left\{ I_{av,pv'} + \frac{1}{2m} \left(\vec{p} + \frac{e\vec{F}}{\omega} u' \right)^2 \right\} \frac{du'}{\sqrt{1-u'^2}} \right]. \end{aligned} \quad (194)$$

Here we have defined

$$I_C(\vec{k}, \vec{R}_j, v, v') = \exp(i\vec{k} \cdot \vec{R}_j) \langle \Theta_{pv'} | \Theta_{av} \rangle, \quad (195)$$

where the subscript C denotes the Condon approximation.

Carrying out the contour integration in the above equation and substituting it into Eq. (193), we obtain the general expression for the total photoionization rate of H₂ molecule from state av to pv' under the Condon approximation, which consists of the individual rates and those from the quantum interference effect.^{85,86,88} The individual photoionization rate can

be expressed as

$$w_{av \rightarrow pv', C}^{j, 1s, j, 1s} = \frac{E_{1s} |b_{j, 1s}|^2 |D_{j, 1s, C}(I_{av, pv'})|^2 |(\Theta_{pv'} | \Theta_{av})|^2 \exp \{-2g_{j, 1s, C}^{(1)}(I_{av, pv'}, \vec{R}_j)\}}{B_{j, 1s, C}(I_{av, pv'}, \vec{R}_j)} \quad (196)$$

for the individual atoms $j = 1$ or $j = 2$, where the definitions of the terms here are

$$B_{j, 1s, C}(I_{av, pv'}, \vec{R}_j) = \left(\sinh^{-1} \gamma_{1s} + \frac{I_{av, pv'} - I_{1s}}{2I_{1s}} \frac{\gamma_{1s}}{\sqrt{1 + \gamma_{1s}^2}} - \frac{\gamma_{1s} e\vec{F} \cdot \vec{R}_j}{2I_{1s}} \right) \times \left\{ \sinh^{-1} \gamma_{1s} - \frac{\gamma_{1s}}{\sqrt{1 + \gamma_{1s}^2}} + \frac{I_{av, pv'} - I_{1s}}{2I_{1s}} \frac{\gamma_{1s}^3}{(1 + \gamma_{1s}^2)^{3/2}} \right\}^{1/2}, \quad (197)$$

$$D_{j, 1s, C}(I_{av, pv'}) = \frac{1}{I_{1s} \gamma_{1s}} \left(\frac{I_{av, pv'} - I_{1s}}{\sqrt{1 + \gamma_{1s}^2}} - e\vec{F} \cdot \vec{R}_j \right) - \left\{ \frac{1}{\gamma_{1s} \sqrt{1 + \gamma_{1s}^2}} + \frac{I_{av, pv'} - I_{1s}}{2I_{1s}} \frac{\gamma_{1s}}{(1 + \gamma_{1s}^2)^{3/2}} \right\} - \frac{1}{2\hbar\omega I_{1s}} \left(\frac{I_{av, pv'} - I_{1s}}{\sqrt{1 + \gamma_{1s}^2}} - e\vec{F} \cdot \vec{R}_j \right)^2, \quad (198)$$

$$E_{1s} = 2\sqrt{2\pi} \gamma_{1s}^4 \sqrt{\frac{\omega I_{1s}}{\hbar}}, \quad (199)$$

$$g_{j, 1s, C}^{(1)}(I_{av, pv'}, \vec{R}_j) = \frac{1}{\hbar\omega} \left(\tilde{I}_{av, pv'} \sinh^{-1} \gamma_{1s} - \tilde{I}_{1s} \frac{\gamma_{1s} \sqrt{1 + \gamma_{1s}^2}}{1 + 2\gamma_{1s}^2} - e\vec{F} \cdot \vec{R}_j \gamma_{1s} \right), \quad (200)$$

$$\tilde{I}_{av, pv'} = I_{av, pv'} + \frac{e^2 F^2}{4m\omega^2} \quad (\text{effective ionization potential of the molecule}), \quad (201)$$

$$\tilde{I}_{1s} = I_{1s} + \frac{e^2 F^2}{4m\omega^2} \quad (\text{effective ionization potential of the atomic } 1s \text{ orbital}), \quad (202)$$

and

$$\gamma_{1s} = \frac{\omega\sqrt{2mI_{1s}}}{eF} \quad (\text{Keldysh parameter of the atomic } 1s \text{ orbital}). \quad (203)$$

Equation (196) is general in that it can be applied to any fixed molecular geometries with respect to the laser polarization direction. From Eq. (196), we notice that the individual photoionization rates depend on the molecular geometry with respect to the laser polarization, which is different from atoms. They depend on the angle between the laser polarization direction and the vector of the molecular axis (due to the terms $\vec{F} \cdot \vec{R}_j$).

The quantum interference term for the transition from av to pv' under the Condon approximation $w_{av \rightarrow pv', C}^{j, 1s, j', 1s}$ ($j \neq j'$) is given in Appendix I. It should be noted that the individual photoionization rate and the quantum interference term depend on the molecular geometry in a different way. Unlike the individual ones, the quantum interference terms depend not only on the angle between the laser polarization direction and the vector of the molecular axis by the relation $\vec{F} \cdot \vec{R}_j$ but also by the angle between the molecular axis and the direction of the emitted electron [due to the term $(\vec{R}_j - \vec{R}_{j'}) \cdot \hat{p}$ in Eq. (I9)]. Since we integrate over the solid angle $\Omega_{\hat{p}}$ to obtain the total photoionization rate, the relation between the quantum interference term and the molecular geometry is not so obvious. However, we can predict that when the different nuclei lie very far from each other, the term $(\vec{R}_j - \vec{R}_{j'}) \cdot \hat{p}$ in Eq. (I9) will contribute to a significant extent. Therefore, the quantum interference terms are expected to be very different for small and large internuclear separations if other parameters are identical. In addition, it is likely that the angular dependence of the photoemitted electron in the quantum interference terms will be quite sensitive to the angle between the molecular axis and the direction of emitted electron in the case of a large separation of the nuclei.

Mathematically speaking, $w_{av \rightarrow pv', C}^{j, 1s, j, 1s}$ and $w_{av \rightarrow pv', C}^{j, 1s, j', 1s}$ ($j \neq j'$) are quite different. The former can always be obtained in a closed form (no numerical integration is needed) as is the case for the original atomic Keldysh theory, while in general the latter contains the numerical integration over the solid angle of the emitted electron and thus for simple molecules, $w_{av \rightarrow pv', C}^{j, 1s, j', 1s}$ ($j \neq j'$) can sometimes be obtained in a closed form.

In summary, the total photoionization rate of the transition $av \rightarrow pv'$ under the Condon approximation, $w_{av \rightarrow pv', C}$, is given by

$$w_{av \rightarrow pv', C} = \sum_{j=1}^2 w_{av \rightarrow pv', C}^{j, 1s, j, 1s} + \sum_{j=1}^2 \sum_{j'=1 (j \neq j')}^2 w_{av \rightarrow pv', C}^{j, 1s, j', 1s}. \quad (204)$$

Using the individual ionization rates and the quantum interference terms, the total photoionization rate from the initial state av under the Condon approximation is given by

$$w_{av,C} = \sum_{v'} w_{av \rightarrow pv',C}. \quad (205)$$

Next, we derive the photoionization formulas in the tunneling limit. These can be obtained by taking the limit $\omega \rightarrow 0$ in the equations shown above. Thus, Eq. (196) reduces to

$$w_{av \rightarrow pv',C.Tun}^{j,1s,j,1s} = \frac{E'_{1s} |b_{j,1s}|^2 |D'_{j,1s,C}(I_{av,pv'})|^2 |\langle \Theta_{pv'} | \Theta_{av} \rangle|^2}{B'_{j,1s,C}(I_{av,pv'})} \times \exp\{-2h_{j,1s,C}(I_{av,pv'})\}. \quad (206)$$

The definitions of the terms in Eq. (206) are given by

$$B'_{j,1s,C}(I_{av,pv'}) = \frac{I_{av,pv'} + I_{1s} - e\vec{F} \cdot \vec{R}_j}{I_{1s}} \left(\frac{3I_{av,pv'}}{I_{1s}} - 1 \right)^{1/2}, \quad (207)$$

$$D'_{j,1s,C}(I_{av,pv'}) = \frac{\hbar e F}{I_{1s}^2 \sqrt{2mI_{1s}}} (I_{av,pv'} - I_{1s} - e\vec{F} \cdot \vec{R}_j) - \frac{\hbar e F}{I_{1s} \sqrt{2mI_{1s}}} - \frac{1}{2I_{1s}^2} (I_{av,pv'} - I_{1s} - e\vec{F} \cdot \vec{R}_j)^2, \quad (208)$$

and

$$h_{j,1s,C}(I_{av,pv'}) = \frac{\sqrt{2mI_{1s}}}{\hbar e F} \left(I_{av,pv'} - \frac{I_{1s}}{3} - e\vec{F} \cdot \vec{R}_j \right). \quad (209)$$

Next, it will be necessary to check the validity of the Condon approximation in deriving the above formulas. To this end, we consider the following simplest model system. The system considered here is depicted in Fig. 16, where two identical harmonic oscillators for the neutral and ionized states are displaced from each other by ΔR . Under the Condon approximation, we have

$$|\langle \Theta_{pv'} | \Theta_{av} \rangle|^2 |_{v=0} = \frac{S^{v'} e^{-S}}{v'!}, \quad (210)$$

where

$$S = \beta \Delta R^2 / 2, \quad \beta = \mu_{H_2} \omega_h / \hbar, \quad \text{and} \quad \omega_h = \sqrt{k_f / \mu_{H_2}} \quad (211)$$

for the transition from the vibrational state $v = 0$ to the vibrational state v' . Here, S is the Huang-Rhys factor, μ_{H_2} the reduced mass of H_2 , and k_f the force constant. The above formulas, Eqs. (196), (I6), and (206), using

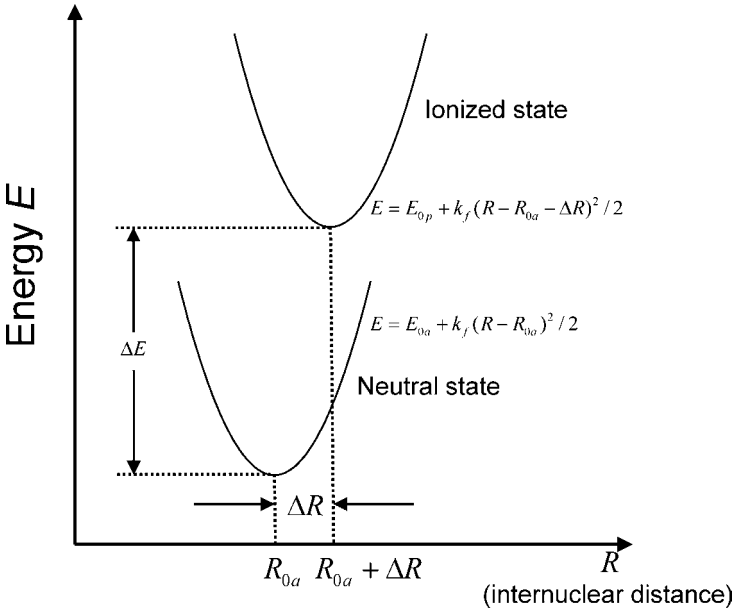


Fig. 16. Pictorial representation of the harmonic oscillator model system used for the comparison between the Condon and non-Condon approximations. The neutral and ionic PECs are identical except that the latter is displaced from the former by distance ΔR , and the energy minimum of the latter is larger than that of the former by ΔE . [Reprinted with permission from Mishima *et al.*, Phys. Rev. A, 70, 063414 (2004). Copyright (2004) by the American Physical Society.]

Eq. (210) are applicable for both the parallel and perpendicular laser polarization cases.

For the derivation of the ionization rate under the non-Condon approximation, we have only to change Eq. (195) to the following form,

$$\begin{aligned}
 I_{NC}(\vec{k}, \vec{R}_j, v=0, v') &= \langle \Theta_{pv'} | e^{i\vec{k} \cdot \vec{R}_j} | \Theta_{av} \rangle |_{v=0} \\
 &= \frac{1}{\sqrt{v'}} \left(\frac{\beta}{2} \right)^{v'/2} \left(\Delta R - \frac{i(-1)^j \vec{k} \cdot \hat{R}}{\beta} \right)^{v'} \\
 &\quad \times \exp \left[-\frac{\beta}{4} \left\{ \Delta R^2 + \left(\frac{\vec{k} \cdot \hat{R}}{2\beta} \right)^2 \right\} + \frac{i}{2} (-1)^j \vec{k} \right. \\
 &\quad \left. \cdot (\vec{R}_{0a} + \Delta R \hat{R} / 2) \right], \tag{212}
 \end{aligned}$$

where \hat{R} denotes the unit vector along \vec{R}_{0a} and it is also assumed that the initial vibrational state is $v = 0$. On the other hand, under the Condon

approximation, we have

$$I_C(\vec{k}, \vec{R}_j, v = 0, v') = \frac{1}{\sqrt{v'}} \left(\frac{\beta}{2} \right)^{v'/2} (\Delta R)^{v'} \exp \left\{ -\frac{\beta}{4} \Delta R^2 + \frac{i}{2} (-1)^j \vec{k} \cdot \vec{R}_{0a} \right\}. \quad (213)$$

The difference between $I_C(\vec{k}, \vec{R}_j, v, v')$ and $I_{NC}(\vec{k}, \vec{R}_j, v, v')$ is that the latter contains extra terms $-\frac{i(-1)^j \vec{k} \cdot \vec{R}}{2\beta}$ in the pre-exponential factor, and $-\frac{\beta}{4} \left(\frac{\vec{k} \cdot \vec{R}}{2\beta} \right)^2$ and $+\frac{i}{4} (-1)^j \Delta R \vec{k} \cdot \vec{R}$ in the exponent.

Under the non-Condon approximation with the molecular axis parallel to the laser polarization, the individual photoionization rate $w_{av \rightarrow pv', NC, par}^{j, 1s, j, 1s}$ is given by

$$w_{av \rightarrow pv', NC, par}^{j, 1s, j, 1s} = \frac{(2^{v'}/v'!) E_{1s} |b_{j, 1s}|^2 |D_{j, 1s, NC, par}(I_{av, pv'})|^2 \exp \{ -2g_{har, j, 1s}^{(1)}(I_{av, pv'}) \}}{B_{j, 1s, NC, par}(I_{av, pv'})}. \quad (214)$$

The definitions of the terms are given in Appendix J.

In Eq. (J9), the term $+\frac{\beta}{4} \Delta R^2$ is nothing but one of the factors of the Franck–Condon factor, e^{-S} in the Condon approximation, while the term $+\frac{(-1)^j \sqrt{2mI_{1s}}}{4\hbar} \Delta R - \frac{mI_{1s}}{8\hbar^2\beta}$ purely stems from the non-Condon approximation. The first term on the right hand side of Eq. (J9) is the same as that in the absence of the vibrational degrees of freedom. From this, we notice that including vibrational motion in molecules under the Condon approximation decreases photoionization rate by the Huang-Rhys factor $\frac{S}{2} = \frac{\beta}{4} \Delta R^2$, the inclusion of the vibrational motion under the non-Condon approximation further changes it by the factor $\frac{(-1)^j \sqrt{2mI_{1s}}}{4\hbar} \Delta R - \frac{mI_{1s}}{8\hbar^2\beta}$. Therefore, while keeping S constant, an increase of ΔR will bring about significant change of the photoionization rate in the non-Condon approximation using this factor; particularly for $j = 2$, ionization rate will decrease significantly.

In the pre-exponential factors defined by Eqs. (J1)–(J8), the terms $\frac{(-1)^j m\omega}{4\sqrt{2mI_{1s}}} \left\{ \Delta R - \frac{(-1)^j \sqrt{2mI_{1s}}}{2\hbar\beta} \right\}$ in Eq. (J1), $-\frac{\gamma_{1s}(eF)^2}{8\beta\hbar\omega} + (-1)^j eF \frac{\Delta R}{4}$ in Eq. (J5), and $+\frac{m\omega}{8\beta\hbar\gamma_{1s}^2}$ in Eq. (J6), $-\frac{(-1)^j \gamma_{1s}(eF)}{2\beta\hbar\omega}$ in Eq. (J7), and $-\frac{(-1)^j \gamma_{1s}(eF)}{4\beta\hbar\omega}$ in Eq. (J8) also originate purely from the non-Condon approximation. Note that the term on the third line of right hand side of Eq. (J1) is independent of the Franck–Condon factor, and Condon and non-Condon approximations.

For v' larger than zero, we can compare Condon and non-Condon approximations. In the Condon approximation limit, $D_{j, 1s, NC}(I_{av, pv'})$ reduces to

$$D_{j, 1s, NC}(I_{av, pv'}) \rightarrow \frac{(-1)^{v'}}{2^{v'/2}} S^{v'/2} D_{j, 1s, C}(I_{av, pv'}), \quad (215)$$

which means that the pre-exponential factors in the Condon approximation limit also reproduce those of the Condon approximation.

The quantum interference term under the non-Condon approximation with molecular axis parallel to the laser polarization, $w_{av \rightarrow pv', NC, par}^{j, 1s, j', 1s}$ is given by

$$w_{av \rightarrow pv', NC, par}^{j, 1s, j', 1s} = \frac{(2^{v'}/v') E_{1s} b_{j, 1s} b_{j', 1s} D_{j, 1s, NC, par}(I_{av, pv'}) D_{j', 1s, NC, par}(I_{av, pv'}) \exp\{-2g_{har, 1s}^{(1)}(I_{av, pv'})\}}{B_{1s, NC, par}(I_{av, pv'})}, \quad (216)$$

where

$$B_{1s, NC, par}(I_{av, pv'}) = \left(\sinh^{-1} \gamma_{1s} + \frac{I_{av, pv'} - I_{1s}}{2I_{1s}} \frac{\gamma_{1s}}{\sqrt{1 + \gamma_{1s}^2}} - \frac{m\omega}{8\hbar\beta} \right) \times \left\{ \sinh^{-1} \gamma_{1s} - \frac{\gamma_{1s}}{\sqrt{1 + \gamma_{1s}^2}} + \frac{I_{av, pv'} - I_{1s}}{2I_{1s}} \frac{\gamma_{1s}^3}{(1 + \gamma_{1s}^2)^{3/2}} \right\}^{1/2} \quad (217)$$

and

$$g_{har, 1s}^{(1)}(I_{av, pv'}) = \frac{1}{\hbar\omega} \left(\tilde{I}_{av, pv'} \sinh^{-1} \gamma_{1s} - \tilde{I}_{1s} \frac{\gamma_{1s} \sqrt{1 + \gamma_{1s}^2}}{1 + 2\gamma_{1s}^2} \right) + \frac{\beta}{4} \Delta R^2 - \frac{mI_{1s}}{8\hbar^2\beta'}, \quad (218)$$

where $j = 1$ and $j' = 2$, or $j = 2$ and $j' = 1$. Here, it should be noticed that in the quantum interference term the factor $\frac{(-1)^j \sqrt{2mI_{1s}}}{4\hbar} \Delta R$, which is present in the individual photoionization rate, is absent so that the quantum interference term will not be affected significantly by the drastic change of ΔR . The factors pertaining to the non-Condon approximation, especially those of the pre-exponential factors, Eqs. (J2)–(J4), are difficult to analyze so that we shall numerically investigate them later. In any case, it clearly shows that the displacement ΔR has to be included properly for the accurate calculation of the molecular ionization rate.

For the case in which the molecular axis is perpendicular to the laser polarization (the molecular axis is parallel to the y -axis), the individual photoionization rate and quantum interference terms under the non-Condon approximation, $w_{av \rightarrow pv', NC, per}^{1s, 1s}$ and $w_{av \rightarrow pv', NC, per}^{j, 1s, j', 1s}$, are presented

in Appendix K. The total photoionization rates under the non-Condon approximation are given by simply replacing C in Eqs. (204) and (205) with NC .

In all the formulas presented above, it should be noted that the slopes in the log-log plot of the molecular photoionization rates versus laser intensity are not the same as those of the atomic photoionization rates or those of the molecular photoionization rates with the ionization potential being substituted by the molecular ionization potential in the atomic photoionization formulas. This is most easily recognized, for example, by inspection of Eq. (209):

$$h_{j,1s}(I_{av,pv'}) = \frac{\sqrt{2mI_{1s}}}{\hbar eF} \left(I_{av,pv'} - \frac{I_{1s}}{3} - e\vec{F} \cdot \vec{R}_j \right). \quad (219)$$

If it happens that $I_{av,pv'}$ is equal to I_{1s} and $\vec{F} \cdot \vec{R}_j$ is equal to zero (e.g. the molecular axis is perpendicular to the laser polarization) at the same time, Eq. (219) becomes

$$h_{j,1s} = \frac{2\sqrt{2mI_{1s}}}{3\hbar eF} I_0. \quad (220)$$

This is the same exponent as that of the hypothetical atom having the atomic ionization potential I_0 which is equal to $I_{av,pv'}$ or I_{1s} . In this case, we can also see that the pre-exponential factor is also almost the same as that of this hypothetical atom and we will observe a good agreement between the photoionization rates of the molecule of interest and the hypothetical atom. However, in the actual molecules, this will hardly happen. In reality, $I_{av,pv'}$ is not equal to I_{1s} , $\vec{F} \cdot \vec{R}_j$ is not equal to zero, and much worse, $I_{av,pv'}$ is not a fixed parameter. Instead, we have to sum up the photoionization rates from each ionization potential $I_{av,pv'}$ as is shown in Eq. (205). This implies that great caution must be taken when applying the atomic photoionization rate formulas to the real molecules as was done in previous investigations.

In the numerical calculations shown below, we include the semiclassical Coulomb correction for the pre-exponential factors as was suggested by Keldysh,¹⁰

$$\frac{I_{av,pv'} \gamma_{av,pv'}}{\hbar\omega \sqrt{1 + \gamma_{av,pv'}^2}}, \quad (221)$$

for each vibrational excitation. In this case, we have different pre-exponential factors as shown in the following. That is, we have to substitute

$E_{1s}(I_{av,pv'})$ and $E'_{1s}(I_{av,pv'})$ for E_{1s} and E'_{1s} ,

$$E_{1s}(I_{av,pv'}) = \frac{2\sqrt{2\pi}\gamma_{1s}^4\gamma_{av,pv'}}{\sqrt{1 + \gamma_{av,pv'}^2}} \sqrt{\frac{I_{1s}I_{av,pv'}^2}{\hbar^3\omega}}, \quad (222)$$

$$E'_{1s}(I_{av,pv'}) = \frac{2^{17/4}\sqrt{3\pi}m^{5/4}I_{1s}^{13/4}I_{av,pv'}^{3/2}}{(eF)^{5/2}\hbar^{7/2}}, \quad (223)$$

and

$$\gamma_{av,pv'} = \frac{\omega\sqrt{2mI_{av,pv'}}}{eF} \quad (\text{Keldysh parameter of the molecule}). \quad (224)$$

Here we have explicitly shown that these factors depend on the vibrational excitations considered.

2.6.3. Computational methods

2.6.3.1. *Ab initio* calculation

Ab initio quantum chemistry calculations are performed for the ground state of H_2 molecule. Its geometry is optimized using the hybrid density functional method B3LYP with the 6-31G basis set and the corresponding harmonic frequencies are characterized at the same level of theory. From the force-constant matrix calculation, no vibrational modes with imaginary frequencies are found, which means that the truly local minimum has been obtained.

Using the optimized geometry calculated above, the molecular orbital coefficients $b_{j,1s}$ ($j = 1, 2$) are obtained by the HF method with the STO-3G basis set. The package of GAUSSIAN 98 is employed for all the *ab initio* calculations performed in this work.⁹² In this preliminary work, higher levels of *ab initio* calculations will not be carried out.

2.6.3.2. Calculation of Franck–Condon factors

The potential energy of the H_2 ground electronic state can analytically be represented by the following Morse potential:

$$V_a(R) = D_a [\exp\{-2\beta_a(R - R_{0a})\} - 2\exp\{-\beta_a(R - R_{0a})\}] - \Delta V_{ap}, \quad (225)$$

where $D_a = 4.7$ eV, $\beta_a = 1.0338$ bohr⁻¹, $R_{0a} = 0.74168$ Å, and $V_{ap} = 15.427$ eV. On the other hand, σ_g and σ_u states of H_2^+ molecule are

given by⁹⁹

$$V_{p,\varepsilon}(R) = D_p [\exp\{-2\beta_p(R - R_{0p})\} - 2t_\varepsilon \exp\{-\beta_p(R - R_{0p})\}], \quad (226)$$

where $D_p = 2.7925$ eV, $\beta_p = 0.72$ bohr⁻¹, $R_{0p} = 2.0$ bohr, and

$$t_\varepsilon = \begin{cases} 1.0 & \text{for } \varepsilon = \sigma_g \\ -1.1 & \text{for } \varepsilon = \sigma_u \end{cases}. \quad (227)$$

The PECs are depicted in Fig. 17(a).

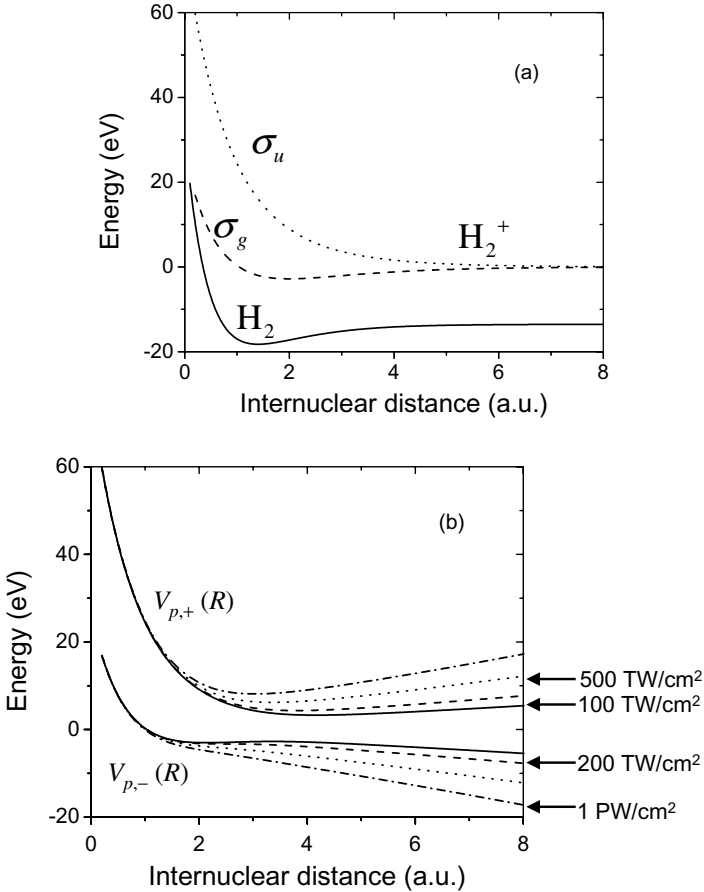


Fig. 17. Calculation results of PECs of H_2 and H_2^+ molecules relevant to this section. Panel (a): PECs of H_2 and H_2^+ molecules relevant to the tunneling ionization of H_2 molecule. Panel (b): field-modified PECs $V_{p,\pm}(R)$ of H_2^+ molecule. Panel (c): artificially cut PECs $\tilde{V}_{p,-}(R)$ and $V_{p,-}(R)$ of H_2^+ molecule. The laser intensity is 100 TW/cm^2 . [Reprinted with permission from Mishima *et al.*, Phys. Rev. A, 70, 063414 (2004). Copyright (2004) by the American Physical Society.]

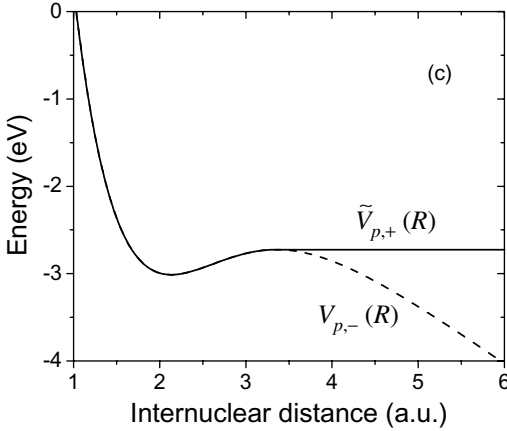


Fig. 17. (Continued)

The transition dipole moments between the σ_g and σ_u states of H_2^+ molecules are calculated to obtain the field-modified PECs of H_2^+ . The analytical expression is given by⁹⁹

$$\mu(R) = \begin{cases} \mu + \frac{\mu'}{\beta_\varepsilon y} [1 - \exp\{-\beta_\varepsilon y(R - R_{0p})\}] & \text{for } R \leq 12 \text{ bohr} \\ R/2 & \text{for } R > 12 \text{ bohr} \end{cases}, \quad (228)$$

where $\mu = 1.07$ (a.u.), $\mu' = 0.396$ (a.u.), and $y = -0.055$.

The vibrational wave function ($v = 0$) of the ground electronic state of H_2 is given by the analytical eigenfunction of the Morse potential of $V_a(R)$. In addition, analytical eigenfunctions of Morse potential $V_{p,\sigma_g}(R)$ are used. For the dissociative potential $V_{p,\sigma_u}(R)$, we only have continuum states: $\Theta_{p,E}(R)$. In order to obtain $\Theta_{p,E}(R)$, we numerically solve the following time-independent Schrödinger equation,

$$\left\{ -\frac{\hbar^2}{2\mu_{\text{H}_2}} \frac{d^2}{dR^2} + V_{p,\sigma_u}(R) \right\} \Theta_{p,E}(R) = E \Theta_{p,E}(R) \quad (229)$$

using the shooting method.¹⁰⁰ We normalize the continuum eigenfunctions to satisfy

$$\int \Theta_{p,E'}^*(R) \Theta_{p,E}(R) dR = \delta(E - E'). \quad (230)$$

This normalization is done by ensuring that $\Theta_{p,E}(R)$ is equal to the JWKB wave function $\left(\frac{2\mu_{\text{H}_2}}{\pi\hbar^2}\right)^{1/2} \frac{1}{k(x)^{1/2}} \sin\left(\int_{a_t}^x k(x) dx + \frac{\pi}{4}\right)$ at some point far from the classical turning point $x = a_t$ where $k(x) = [2\mu_{\text{H}_2}\{E - V_{p,\sigma_u}(R)\}]^{1/2}/\hbar$.¹⁰¹

In the parallel laser polarization case, the PECs of H_2^+ are significantly modified by the laser field. In order to take into account this Stark shift, we have to diagonalize the following matrix:

$$\begin{bmatrix} V_{p,\sigma_g}(R) & -\mu(R)F \\ -\mu(R)F & V_{p,\sigma_u}(R) \end{bmatrix}. \quad (231)$$

Then we can obtain the field-modified adiabatic PECs $V_{p,-}(R)$ and $V_{p,+}(R)$:

$$V_{p,\pm}(R) = \frac{V_{p,\sigma_g}(R) + V_{p,\sigma_u}(R)}{2} \pm \sqrt{\left\{ \frac{V_{p,\sigma_g}(R) - V_{p,\sigma_u}(R)}{2} \right\}^2 + \{\mu(R)F\}^2}. \quad (232)$$

These adiabatic potentials are depicted in Fig. 17(b).

When the laser intensity exceeds $200 \text{ TW}/\text{cm}^2$, $V_{p,-}(R)$ becomes completely dissociative and does not have any discrete vibrational states. In this case, we calculate the continuum states $\Theta_{p,E}(R)$ in the same way as described above.

On the other hand, when the laser intensity is smaller than $200 \text{ TW}/\text{cm}^2$, $V_{p,-}(R)$ has several quasi-bound vibrational states. For the quasi-bound states with short life-time, it is easy to obtain $\Theta_{p,E}(R)$ and to calculate $|\langle \Theta_{pv'} | \Theta_{av} \rangle|^2$ which shows a broad profile, while for those with very long life-time, $|\langle \Theta_{pv'} | \Theta_{av} \rangle|^2$ shows a very steep and large peak, so that we require very small energy steps and much more computational time. To avoid this, we numerically calculate the discrete vibrational eigenstates for the potential cutoff artificially: $\tilde{V}_{p,-}(R)$ [see Fig. 17(c)]. It is numerically assured that $\sum_{v'} |\langle \tilde{\Theta}_{pv'} | \Theta_{av} \rangle|^2 + \int dE |\langle \tilde{\Theta}_{p,E} | \Theta_{av} \rangle|^2$ is almost equal to unity (the percentage of the numerical errors is of the order of 0.1% for any laser intensities used here).

When the laser intensity becomes very large, $V_{p,+}(R)$ becomes a steep potential well and has dense discrete eigenstates. In this case, we calculate them numerically with the method described above. We can then determine the Franck–Condon factor $|\langle \Theta_{pv'} | \Theta_{av} \rangle|^2$. Strictly speaking, even when the laser intensity is low, $V_{p,+}(R)$ forms a bound PEC. Since this potential well is very shallow, we approximately regard the eigenstate as a continuum and calculate the Franck–Condon factor $|\langle \Theta_{p,E} | \Theta_{av} \rangle|^2$ accordingly.

Although we did not take into account the field distortion of the ground state PEC of H_2 molecules, it is a reasonable first order approximation.¹⁰²

2.6.4. Numerical results and discussion

Next, we show numerical results of the tunneling single-photoionization rate of a H_2 molecule calculated by using the formulas derived in Sec. 2.6.2.

The other factors, for example, the molecular orbital coefficients $b_{j,1s}$ and the quantities associated with PECs (the ionization potential $I_{av,pv'}$, the internuclear distance $R_1 - R_2$, etc.) can only be obtained numerically so that the numerical values obtained in Sec. 2.6.3 will be used. In the numerical calculations for the comparison between the Condon and non-Condon approximations, the molecular orbital coefficients are assumed to be constant even if we are working with the parallel polarization case. In all of the calculations shown below, we assume that the initial vibrational state v is equal to zero. In addition, the semi-classical corrections, Eqs. (222) and (223), are used except for Fig. 20.

Figure 18 shows the molecular orbital coefficients $b_{j,1s}$ ($j = 1, 2$) for the case of the parallel laser polarization. We can clearly see that $b_{1,1s}$ increases while $b_{2,1s}$ decreases with laser intensity due to the polarizability of the molecule. This is characteristic of the molecules in intense laser fields.

On the other hand, the molecular orbital coefficients $b_{j,1s}$ ($j = 1, 2$) for the case of the perpendicular laser polarization are 0.54836 in any laser field amplitudes. This value agrees with the analytical value very well.

Figure 19(a) shows the photoionization rate versus laser intensity in the tunneling limit when the laser polarization is parallel to the molecular axis. In this figure, we compare our results with those of Saenz calculated in *ab initio* fashion (Fig. 3(a) of Ref. 54). The comparison shows that the numerical results calculated seem to be reliable so that we can carry out benchmark tests. Another reason is that we do not yet have experimental

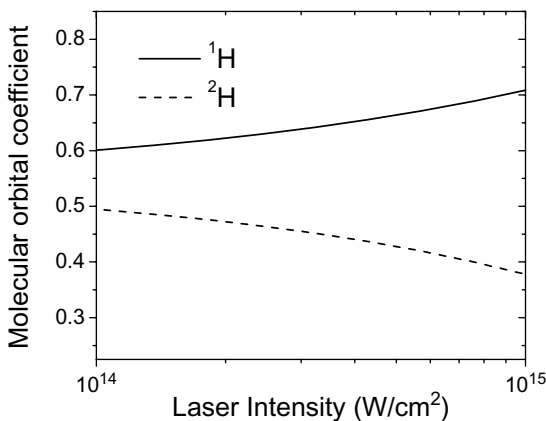


Fig. 18. Laser intensity dependence of the molecular orbital coefficients $b_{j,1s}$ ($j = 1, 2$) of the ground electronic state of H_2 molecule calculated at the HF/STO-3G level of theory. The laser polarization is parallel to the molecular axis. [Reprinted with permission from Mishima *et al.*, Phys. Rev. A, 70, 063414 (2004). Copyright (2004) by the American Physical Society.]

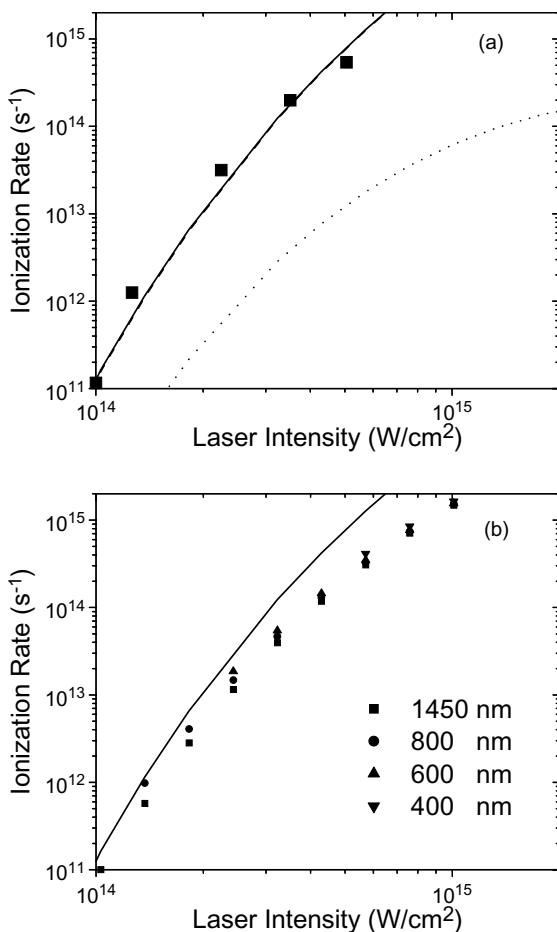


Fig. 19. Photoionization rates versus laser intensity of H₂ molecule in the tunneling limit with the laser polarization parallel to the molecular axis, calculated by using Eq. (206) [panel (a)] and quantum interference terms for the laser wavelengths 1450, 800, 600, and 400 nm calculated by Eq. (16) [panel (b)]. Panel (a) is compared with that calculated by the *ab initio* method (Fig. 3(a) of Ref. 54). In this panel, the solid squares stand for the results taken from Fig. 3(a) of Ref. 54, the solid line for the total photoionization rate calculated by Eq. (206), the broken line for the partial contribution from ¹H, and dotted line for that from ²H of Fig. 15. Note that the solid and broken lines are superimposed in panel (a). This means that the total photoionization rate is dominated by that of ¹H in the parallel laser polarization case. [Reprinted with permission from Mishima *et al.*, Phys. Rev. A, 70, 063414 (2004). Copyright (2004) by the American Physical Society.]

data to compare with our calculation quantitatively (i.e. absolute value of the photoionization rate). From the figure, we can see that our results reproduce Saenz's results well. In addition, we notice that the hydrogen atom ¹H which is upstream along the laser polarization direction contributes to

the total photoionization predominantly. This is due to the fact that the exponential factor $\exp(2\sqrt{2mI_s}\vec{F} \cdot \vec{R}_j/\hbar F)$ of ^1H is much larger than that of ^2H . This is consistent with the results reported so far.⁶⁴

As mentioned in Sec. 2.6.2, Eq. (206) does not include the quantum interference terms appropriately. We have to check if the total photoionization rate demonstrated in panel (a) (solid line) is reliable. Figure 19(b) shows the quantum interference terms for the laser wavelengths 1450, 800, 600, and 400 nm calculated by using Eq. (I6). It is found that as the laser wavelength increases, the quantum interference terms decrease. This tendency indicates that it is reasonable to assume that the quantum interference terms in the tunneling limit are smaller at least than those with the laser wavelength 1450 nm. Comparing panels (a) and (b), we can see that the quantum interference terms are several factors smaller than the individual and total photoionization rates. This fact leads to the conclusion that the quantum interference terms are negligibly smaller than the individual or total photoionization rates in the tunneling limit.

Figure 20 compares the total photoionization rates with and without the quasi-classical correction of the long-range Coulomb potential effect in the tunneling limit. We can see that if the correction is not included, the photoionization rate becomes about ten times smaller than that with

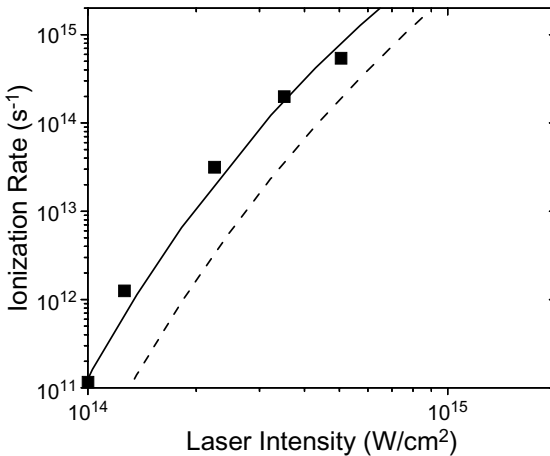


Fig. 20. Comparison of the photoionization rates versus laser intensity of H_2 molecule in the tunneling limit with semi-classical correction and without it. Solid line and the squares are the same as those in Fig. 19 while the broken line is calculated under the assumption of no correction. This figure indicates the importance of the Coulomb correction for the accurate calculation of the photoionization rates. [Reprinted with permission from Mishima *et al.*, Phys. Rev. A, 70, 063414 (2004). Copyright (2004) by the American Physical Society.]

the correction. In general, the order of this difference becomes larger as the laser intensity decreases or $I_{av,pv'}$ increases since in the tunneling limit we have the semiclassical Coulomb correction $\frac{I_{av,pv'}\sqrt{2mI_{av,pv'}}}{\hbar eF}$ from Eq. (221).

Figure 21 compares the total photoionization rates with and without the Franck–Condon factors. The difference between these two cases is not negligible, twice or thrice larger for the case without Franck–Condon factor. However, we can see a slight tendency that the inclusion of the Franck–Condon factors decreases the photoionization rate, which is consistent with that calculated by the ADK formula.¹⁰²

Figure 22 shows the photoionization rate versus laser intensity when the laser polarization is perpendicular to the molecular axis. Comparing Figs. 19 and 22, we can see that the photoionization rate with the perpendicular laser polarization is much smaller than that with the parallel laser polarization. In addition, we notice that the partial contributions from ^1H and ^2H hydrogen atoms are of the same magnitude. This can be easily understood by inspection of Eqs. (206)–(209). In the perpendicular laser polarization, $\vec{F} \cdot \vec{R}_j$ for both $j = 1$ and $j = 2$ is zero so that $w_{av \rightarrow pv',C,Tun}^{j,1s,j,1s}$ is identical for both $j = 1$ and $j = 2$. This comparison between the parallel and perpendicular laser polarization cases actually indicates the importance of the site-dependent exponential factor of $\exp(2\sqrt{2mI_s}\vec{F} \cdot \vec{R}_j/\hbar F)$.

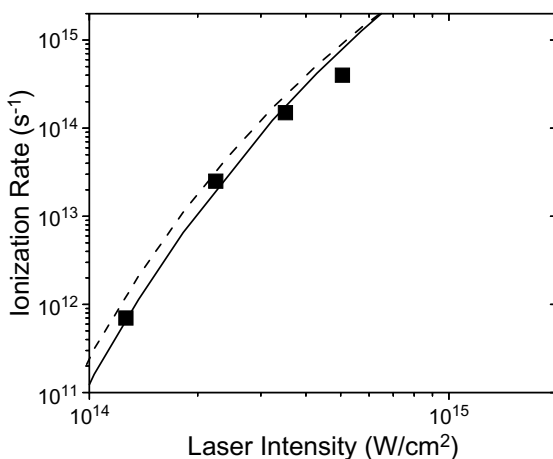


Fig. 21. Comparison between the molecular photoionization rates including the Franck–Condon factor and those in its absence (i.e. only the photoionization rate of the transition to the vibrational level $v' = 0$ is considered). Solid line and squares are the same as those in Fig. 19 while the broken line is calculated under the assumption of no Franck–Condon factors. [Reprinted with permission from Mishima *et al.*, Phys. Rev. A, 70, 063414 (2004). Copyright (2004) by the American Physical Society.]

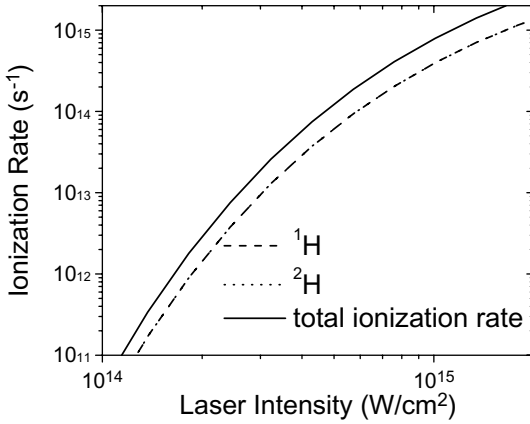


Fig. 22. Photoionization rates versus laser intensity of H₂ molecule in the tunneling limit, with the laser polarization perpendicular to the molecular axis, calculated by using Eq. (206). The broken and dotted lines are the partial photoionization rates from ¹H and ²H, respectively. The solid line is for the total photoionization rate. Note that the broken and dotted lines are superimposed. [Reprinted with permission from Mishima et al., Phys. Rev. A, 70, 063414 (2004). Copyright (2004) by the American Physical Society.]

In Table 3, we show the laser frequency dependence of the total photoionization rates $w_{av,C}$ with the parallel laser polarization under the Condon approximation. We can see that increasing the laser frequency leads to the enhancement of the total photoionization rate provided that the

Table 3. Total photoionization rate (s⁻¹) of H₂ to H₂⁺ for various laser wavelengths when the laser polarization is parallel to the molecular axis.

Wavelength λ (nm)	Tunneling Laser intensity (W/cm ²)	1450	γ_{1s}	800	γ_{1s}	600	γ_{1s}	400	γ_{1s}
1.03×10^{14}	1.62×10^{11}	3.58×10^{11}	0.58						
1.37×10^{14}	1.14×10^{12}	2.13×10^{12}	0.50	3.74×10^{12}	0.91				
1.82×10^{14}	6.57×10^{12}	1.09×10^{13}	0.44	1.62×10^{13}	0.79				
2.43×10^{14}	3.21×10^{13}	4.74×10^{13}	0.38	6.21×10^{13}	0.68	8.03×10^{13}	0.91		
3.23×10^{14}	1.23×10^{14}	1.74×10^{14}	0.33	2.10×10^{14}	0.59	2.51×10^{14}	0.79		
4.29×10^{14}	4.20×10^{14}	5.64×10^{14}	0.28	6.39×10^{14}	0.51	7.25×10^{14}	0.69		
5.71×10^{14}	1.27×10^{15}	1.63×10^{15}	0.25	1.78×10^{15}	0.45	1.94×10^{15}	0.60	2.40×10^{15}	0.89
7.60×10^{14}	3.49×10^{15}	4.29×10^{15}	0.21	4.53×10^{15}	0.39	4.81×10^{15}	0.52	5.59×10^{15}	0.77
1.01×10^{15}	8.84×10^{15}	1.05×10^{16}	0.19	1.09×10^{16}	0.34	1.13×10^{16}	0.45	1.25×10^{16}	0.67
1.34×10^{15}	2.12×10^{16}	2.43×10^{16}	0.16	2.48×10^{16}	0.29	2.55×10^{16}	0.39	2.72×10^{16}	0.58

laser intensities are identical. The frequency dependence of the photoionization rates can be analyzed more conveniently by the Keldysh type of theories than by ADK theory since the laser frequency dependence cannot be included in an explicit fashion in the latter case.

So far, the Condon approximation was assumed. Below, we shall investigate the validity of the Condon approximations made in the above discussion. In the following calculations for the comparison between the Condon and non-Condon approximations, the parameters are chosen to be laser intensity 7.59×10^{14} (W/cm²), $\omega = 1.55$ eV [or wavelength = 800 (nm)], $R_{0a} = 0.735$ (Å) (very close to the equilibrium distance of the H₂ molecule in the electronic ground state), and $\Delta E = 17.33$ eV.

Figure 23 shows that Huang-Rhys factor S defined by Eq. (211) with the parameters defined above. We can see that as far as both parameters β and ΔR are very small, the Huang-Rhys factor is very small, which is reasonable in real systems. However, if these parameters are very large, the most probable vibrational excitation is to the higher vibrational states of the ionic potential.

Figures 24 and 25 compare the molecular ionization rates under the Condon and non-Condon approximations for the cases of the parallel and perpendicular polarizations, respectively. In the case of the perpendicular polarization, we can see the good agreement between the results under the Condon and non-Condon approximations; in particular, the

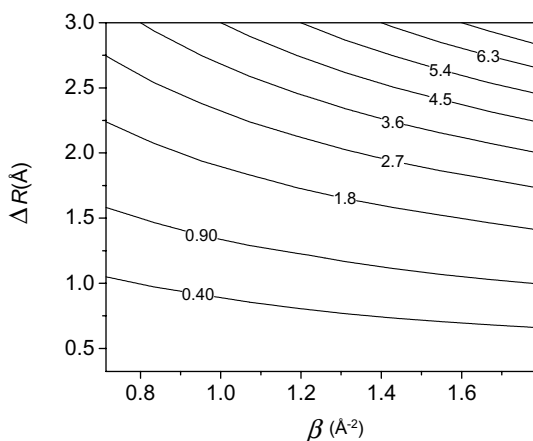


Fig. 23. Huang-Rhys factor S defined by Eq. (211) when the laser intensity is equal to 7.59×10^{14} (W/cm²), $\omega = 1.55$ (eV) [or wavelength = 800 (nm)], $R_{0a} = 0.735$ (Å), and $\Delta E = 17.33$ (eV). The value on each curve represents S . [Reprinted with permission from Mishima *et al.*, Phys. Rev. A, 70, 063414 (2004). Copyright (2004) by the American Physical Society.]

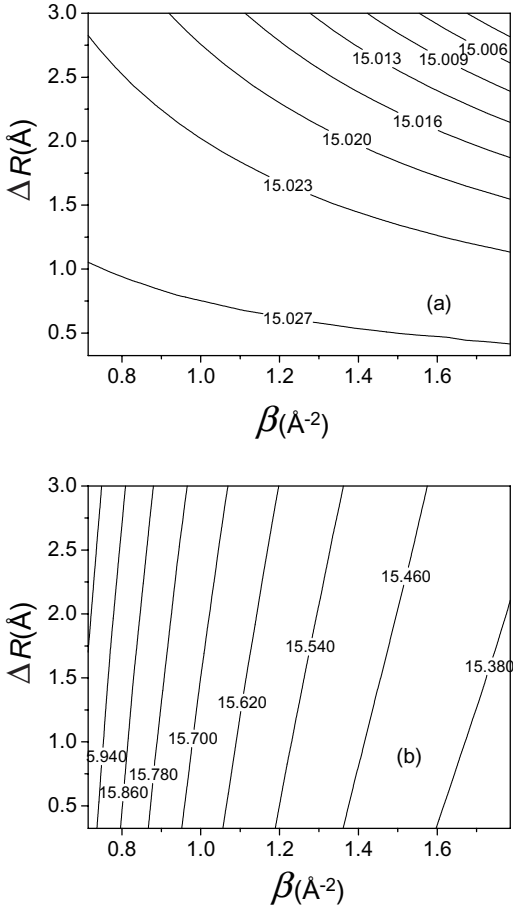


Fig. 24. Dependence of the total photoionization rates on β and ΔR with the same parameters used in Fig. 23 in the case of the parallel laser polarization. The value on each curve represents \log_{10} (total ionization rate in W/cm^2). In panels (a) and (b), the Condon and non-Condon approximations are assumed, respectively. [Reprinted with permission from Mishima *et al.*, Phys. Rev. A, 70, 063414 (2004). Copyright (2004) by the American Physical Society.]

photoionization rate with the perpendicular laser polarization is much more insensitive to the Condon approximation. In the linear laser polarization case, we can see around a ten times difference between the Condon and non-Condon approximations (from Fig. 24). In addition, we notice that as β or ΔR becomes smaller, the total photoionization rate becomes larger. This is due to that fact that in this case the quantum number of the vibrational state of the ionic state with the largest Franck–Condon factor is $v' = 0$. In addition, the transition to the state $v' = 0$ has the smallest ionization

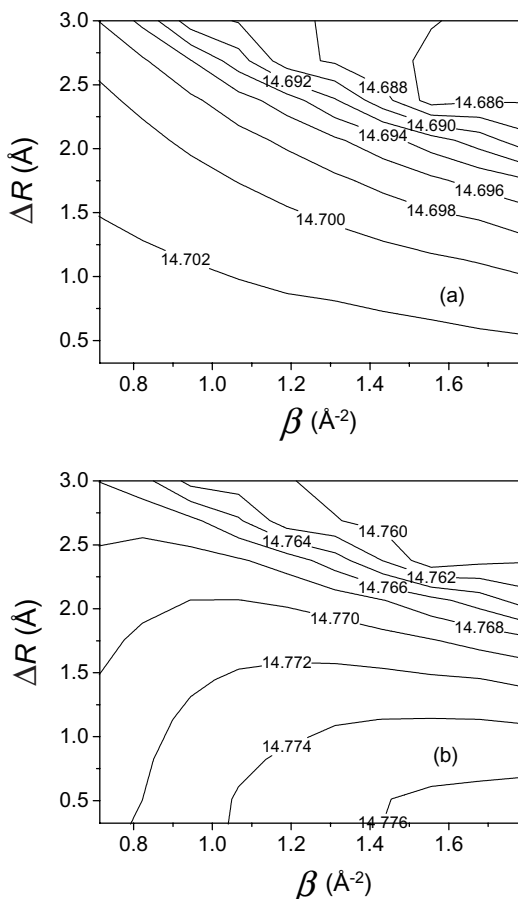


Fig. 25. Dependence of the total photoionization rates on β and ΔR with the same parameters used in Fig. 23 in the case of the perpendicular laser polarization. The value on each curve represents \log_{10} (total ionization rate in W/cm^2). In panels (a) and (b), the Condon and non-Condon approximations are assumed, respectively. [Reprinted with permission from Mishima *et al.*, Phys. Rev. A, 70, 063414 (2004). Copyright (2004) by the American Physical Society.]

potential $I_{av,pv'}$. Since the photoionization rate is very sensitive to the value of $I_{av,pv'}$ but less sensitive to the Franck–Condon factor, the transition to the state $v' = 0$, which has the largest Franck–Condon factor, has the largest photoionization rate in all the situations. From the figures, we can see that the photoionization rates seem to be more sensitive to β than to ΔR .

In the area where the Condon and non-Condon approximations do not agree well, the photoionization rates under the non-Condon approximation are larger than those under the Condon approximation because of the

several times difference of the exponential and pre-exponential factors. In addition, due to the lack of the term $\frac{\sqrt{2mI_{ls}}}{2\hbar}(-1)^j R_{0a}$ in the exponent in the quantum interference terms, the contribution from the quantum interference term is smaller by one or three orders of magnitude than the individual photoionization rate contributed from ^1H .

Finally, we note the recently published work concerning the experimental results of vibrational distribution of H_2^+ molecule in the tunneling photoionization of the process of Eq. (182).¹⁰³ This study has clearly demonstrated the importance of including the vibrational degrees of freedom for the molecular tunneling photoionization. They have found that the relative populations of the vibrational states of H_2^+ molecule after the tunneling photoionization of H_2 molecule do not follow the conventional Franck–Condon principle. The reason for this is the rapid variation of the photoionization rate with the internuclear distance. They used the following formula to calculate the transition rates to the individual field-modified vibrational levels of H_2^+ molecule,

$$\Gamma(v') = \left| \int \Gamma^{1/2}(R) \chi_{v'}(R) \chi_0(R) dR \right|^2, \quad (233)$$

where $\chi_{v'}(R)$ and $\chi_0(R)$ are the vibrational wave functions of H_2^+ and H_2 molecules, respectively, and $\Gamma(R)$ is the photionization rate dependent on the internuclear distance R . The R -dependent photoionization rate $\Gamma(R)$ is calculated by the ADK formula.¹³

We compare their results to those obtained by our formulas. The relative population $p_{rel}(v')$ in the vibrational state v' is given by

$$p_{rel}(v') = \frac{w_{av \rightarrow pv', C}}{w_{av, C}}. \quad (234)$$

Figure 26 shows the relative populations for each vibrational state v' for the parallel and perpendicular laser polarization cases. As in Ref. 103, when the laser intensity is very large, the number of the bound or quasi-bound vibrational states of H_2^+ diminishes so that the total populations of the bound or quasi-bound vibrational states of H_2^+ decrease. For example, the total populations from the bound or quasi-bound states add up to 94, 91, 70% for the figures (a), (b), and (c), respectively. This agrees well with the experimental results reported in the literature.¹⁰³ Contrary to the results obtained by Urbain *et al.*,¹⁰³ the relative populations calculated by our formulas follow the same distributions predicted by Franck–Condon factors, although they claim that the dissociative photoionization does not follow the Franck–Condon principle since the ADK photoionization rate is dependent on R .

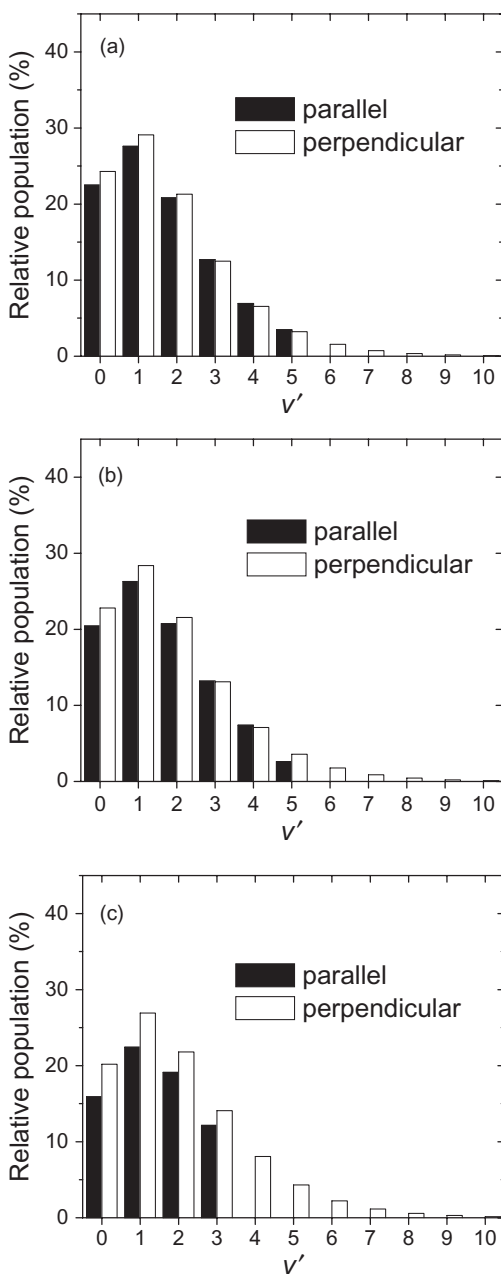


Fig. 26. Vibrational distributions of H_2^+ molecule after the tunneling photoionization of H_2 molecule. The laser intensities are (a) 4.40×10^{13} , (b) 5.84×10^{13} , and (c) $1.03 \times 10^{14} \text{ W/cm}^2$. These figures should be compared with Figs. 2 and 4 of the literature in Ref. 103. [Reprinted with permission from Mishima *et al.*, Phys. Rev. A, 70, 063414 (2004). Copyright (2004) by the American Physical Society.]

Some features are very similar between Fig. 2 of Ref. 103 and Fig. 26 of this section. For example, we notice that as the laser intensity increases, the relative populations of higher vibrational quantum number v' become larger for the perpendicular laser polarization case. This tendency agrees well with that of Figs. 2 and 4 of the literature in Ref. 103.

From the above comparisons, we can conclude that if the laser intensity is very large, the prediction by the ADK theory and that of our theory are very similar. But if the laser intensity is not so large, these two theories yield very different results. The decisive conclusion has to await more experimental studies of intense laser ionization of different molecules.

(ii) Comparison between N_2 and O_2 molecules

2.6.5. Introduction

In early days, it was believed that the atomic photoionization rate is comparable to that of molecules if the ionization potentials (IPs) are identical.^{104–106} However, it has been revealed that this is not necessarily the case. For example, one of the most remarkable features of the molecular photoionization has recently been recognized in the unexpectedly low molecular photoionization rate (or probability) of O_2 . Many experimental and theoretical studies have been devoted to clarify this issue.^{28,107–109} Thereby, N_2 molecule is usually compared, which shows no suppression.

We can find some of the likely explanations for the molecular photoionization suppression in the literature. In Ref. 109, this suppression of O_2 molecule was attributed to the electron rescattering.¹¹⁰ In Ref. 111, Guo introduced a charge-screening correction to the tunneling theory and found that this correction makes it possible to explain the observed suppression of O_2 photoionization when it is used with the appropriate parameters.

Furthermore, Faisal and coworkers^{14,112} emphasized that this difference originates from the differing characters of the valence orbitals of N_2 and O_2 . The former has a bonding symmetry character (σ_g symmetry) while the latter an antibonding symmetry character (π_g symmetry).

In addition to the suppressed photoionization of O_2 , D_2 molecules also exhibit similar suppressed photoionization.¹¹² In Ref. 112, Chin and coworkers have found this experimentally and attributed this to the creation of the barrier for tunneling, which in turn originates from the two-center nature of the potential. In addition, they found that this suppression take place in C_6H_6 and CO molecules. Faisal and coworkers also found the suppression for C_2H_2 , C_2H_4 , and C_6H_6 molecules theoretically.¹⁴

In addition to the suppression of O_2 molecule, the comparison between the molecule of interest and the “companion” atom (which has almost the same IP as the molecule of interest) has frequently been undertaken in order to reveal the mechanism pertinent only to the molecules. For example, the partners, N_2 and Ar ($IP_{N_2} = 15.58$ eV and $IP_{Ar} = 15.76$ eV), O_2 and Xe ($IP_{O_2} = 12.06$ eV and $IP_{Xe} = 12.13$ eV), F_2 and Ar ($IP_{N_2} = 15.70$ eV and $IP_{Ar} = 15.76$ eV), CO and Kr ($IP_{CO} = 14.01$ eV and $IP_{Kr} = 14.00$ eV), and D_2 and Ar ($IP_{D_2} = 15.47$ eV and $IP_{Ar} = 15.76$ eV), etc. have been investigated. In Ref. 95, the ionization yields of the partners including these examples were experimentally explored. From the comparison between the experimental data and the theoretical calculations using the atomic ADK theory,¹³ they found that the photoionization rate (or probability) of these partners do not agree well. They concluded that in general molecules in singlet configurations display more atomlike ionization properties, while doublet or triplet configurations appear to have suppressed ionization rates relative to an atomic target of similar IP.

In this section, we theoretically reexamine the photoionization rates of the companion groups N_2/Ar and O_2/Xe by developing our molecular Keldysh theory. The investigation of N_2 and O_2 molecules is also very important in that it is necessary to examine if the atomic orbitals other than $1s$ can be used for the original Keldysh theory. The success will be an evidence of the possibility to extend our molecular Keldysh theory to large polyatomic molecules.

In Sec. 2.6.6, we derive the photoionization rate formulas of diatomic molecules consisting of $2px$ and $2py$ atomic orbitals for MO with molecular axis chosen to be along the z -axis. Here, it should be emphasized that the vibrational motion pertinent to molecular systems is adequately incorporated. In Sec. 2.6.7, calculation methods are described. In Sec. 2.6.8, numerical results calculated by the formulas derived in Sec. 2.6.6 are demonstrated and compared with the experimental and theoretical results already published in the literature.

2.6.6. Theory

In this sub-section, we shall derive the photoionization rate formulas of N_2 and O_2 molecules within the Born–Oppenheimer and the Condon approximations. Here, we shall concentrate on the derivation and calculation of the following processes:



and



Similar to Eq. (190), the photoionization rate from the initial rovibronic state av to the ionized rovibronic state pv' for the processes of Eqs. (235) and (236) is given by

$$\begin{aligned} w_{av \rightarrow pv'} &= \frac{4}{\hbar^2} \lim_{T \rightarrow \infty} \text{Re} \int \frac{d^3 p}{(2\pi\hbar)^3} |\langle \Theta_{pv'} | \Theta_{av} \rangle|^2 \sum_{j,j'=1}^2 \sum_{k_j, k_{j'}=2px, 2py} b_{j,k_j}^* b_{j',k_{j'}} \\ &\times \int_0^T dt \cos \omega T \cos \omega t V_{0,k_j}^* (\vec{p} - e\vec{A}(T)) V_{0,k_{j'}} (\vec{p} - e\vec{A}(t)) \\ &\times \exp \left[\frac{i}{\hbar} \left\{ \int_T^t dt' \left(I_{av,pv'} + \frac{1}{2m} (\vec{p} - e\vec{A}(t'))^2 \right) \right. \right. \\ &\left. \left. + (\vec{p} - e\vec{A}(T)) \cdot \vec{R}_j - (\vec{p} - e\vec{A}(t)) \cdot \vec{R}_{j'} \right\} \right]. \quad (237) \end{aligned}$$

Here, the subscripts j and j' denote the numbering of the nuclei and k_j and $k_{j'}$, 2px or 2py orbitals of which the HOMOs of N_2 and O_2 molecules consist.

For the photoionization processes of Eqs. (235) and (236), the molecular wavefunction of the ground electronic state ϕ_a , when using the LCAO-MO, is given by

$$\phi_a = \sum_{j=1}^2 \sum_{k_j=2px, 2py} b_{j,k_j} \chi_{j,k_j} \quad (238)$$

where b_{j,k_j} and χ_{j,k_j} represent the molecular orbital coefficients and the atomic orbitals, respectively. Here, $k_j = 2px$ or $2py$ and $j = 1$ or 2 . If the molecular axis is perpendicular to the direction of the laser polarization, the molecular orbital coefficients b_{j,k_j} can be written as

$$b_{1,k_1} = b_{2,k_2} = \frac{1}{\sqrt{2 + 2S_{12}}} \quad \text{for bonding case} \quad (239)$$

and

$$b_{1,k_1} = -b_{2,k_2} = \frac{1}{\sqrt{2 - 2S_{12}}} \quad \text{for anti-bonding case,} \quad (240)$$

where S_{12} denotes the overlap integral. We will use Eq. (239) for the initial state $(\sigma_g 2p)^2$ of the N_2 molecule, while Eq. (240) for the initial state $(\pi_g^* 2p)^2$ of the O_2 molecule when the molecular axis is perpendicular to the laser polarization. In other cases, we have to calculate b_{j,k_j} using the quantum chemistry calculation package (see Sec. 2.6.7).

The transition dipole matrix element between the plane wave and 2px or 2py atomic orbitals is given by

$$\begin{aligned}
 V_{0,k_j}(\vec{p}) &= \langle \exp(i\vec{p} \cdot \vec{r}/\hbar) | e\vec{F} \cdot \vec{r} | \chi_{k_j}(\vec{r}) \rangle \\
 &= -\frac{3 \times 2^{15/4} \sqrt{\pi} eF \hbar^{5/2} I_{k_j}^{7/4} p^2 \sin \theta \cos \theta \Phi_{k_j}(\phi)}{m^{9/4} (I_{k_j} + p^2/2m)^4}. \quad (241)
 \end{aligned}$$

In Eq. (241), we define

$$\Phi_{k_j}(\phi) = \begin{cases} \cos \phi & \text{for } k_j = 2\text{px} \\ \sin \phi & \text{for } k_j = 2\text{py} \end{cases}. \quad (242)$$

The remarkable difference between $V_{0,1s}(\vec{p})$ defined by Eq. (192) and $V_{0,k_j}(\vec{p})$ is that the former depends only on θ while the latter on both θ and ϕ . This stems from the difference of the angular dependence of 1s and 2px or 2py orbitals. Furthermore, $V_{0,1s}(\vec{p})$ depends on the third power of $I_{1s} + p^2/2m$ while $V_{0,k_j}(\vec{p})$ on the fourth power of $I_{k_j} + p^2/2m$. This fact leads to the formula more complicated for 2px and 2py orbitals than for 1s orbital.

Performing the integration over t and taking the limit $T \rightarrow \infty$ in Eq. (237) yield

$$\begin{aligned}
 w_{av \rightarrow pv'} &= \frac{4\pi}{\hbar} \text{Re} \sum_{j,j'=1}^2 \sum_{k_j,k'_j=2\text{px},2\text{py}} b_{j,k_j}^* b_{j',k'_j} \int \frac{d^3p}{(2\pi\hbar)^3} \\
 &\times \sum_{n=-\infty}^{\infty} L_{j,2\text{py}}^*(\vec{p}) L_{j',2\text{py}}(\vec{p}) \delta \left(I_{av,pv'} + \frac{p^2}{2m} + \frac{e^2 F^2}{4m\omega^2} - n\hbar\omega \right), \quad (243)
 \end{aligned}$$

where

$$\begin{aligned}
 L_{j,k_j}(\vec{p}) &= \frac{1}{2\pi} \oint du V_{0,k_j} \left(\vec{p} + \frac{e\vec{F}}{\omega} u \right) I \left(-\frac{1}{\hbar} \left(\vec{p} + \frac{e\vec{F}}{\omega} u \right), \vec{R}_j, v, v' \right) \\
 &\times \exp \left[\frac{i}{\hbar\omega} \int_0^u \left\{ I_{av,pv'} + \frac{1}{2m} \left(\vec{p} + \frac{e\vec{F}}{\omega} u' \right)^2 \right\} \frac{du'}{\sqrt{1-u'^2}} \right]. \quad (244)
 \end{aligned}$$

Here we have defined

$$I(\vec{k}, \vec{R}_j, v, v') = \exp(i\vec{k} \cdot \vec{R}_j) \langle \Theta_{pv'} | \Theta_{av} \rangle. \quad (245)$$

Carrying out the contour integration in the above equation and substituting it into Eq. (243), we obtain the general expressions for the total photoionization rates of N_2 and O_2 molecules from state av to pv' under the Born–Oppenheimer and the Condon approximations. They consist of

the individual rates and those from the quantum interference effect. The individual photoionization rate can be expressed as

$$w_{av \rightarrow pv'}^{j,k_j,j,k_j} = E_{k_j} b_{j,k_j}^2 D_{j,k_j}(I_{av,pv'}, \vec{R}_j)^2 |\langle \Theta_{pv'} | \Theta_{av} \rangle|^2 B_{j,k_j}(I_{av,pv'}, \vec{R}_j)^{-1} \times \exp\left\{-2g_{j,k_j}^{(1)}(I_{av,pv'}, \vec{R}_j)\right\}, \quad (246)$$

for the individual atoms $j = 1$ and $j = 2$ and the individual atomic orbitals $k_j = 2px$ and $k_j = 2py$. The definitions of the terms here are

$$B_{j,k_j}(I_{av,pv'}, \vec{R}_j) = \left(\sinh^{-1} \gamma_{k_j} + \frac{\gamma_{k_j}}{2I_{k_j}} M_1(I_{av,pv'}, \vec{R}_j) \right)^2 \times \left\{ \sinh^{-1} \gamma_{k_j} - \frac{\gamma_{k_j}}{\sqrt{1 + \gamma_{k_j}^2}} + \frac{I_{av,pv'} - I_{k_j}}{2I_{k_j}} \frac{\gamma_{k_j}^3}{(1 + \gamma_{k_j}^2)^{3/2}} \right\}^{1/2}, \quad (247)$$

$$D_{j,k_j}(I_{av,pv'}, \vec{R}_j) = \frac{\gamma_{k_j}^2}{12I_{k_j} \hbar^2 \omega^2} M_1(I_{av,pv'}, \vec{R}_j)^3 + \frac{\gamma_{k_j}}{4I_{k_j} \hbar \omega} M_1(I_{av,pv'}, \vec{R}_j) M_2(I_{av,pv'}) - I_{k_j} (3\gamma_{k_j}^4 + 8\gamma_{k_j}^2 + 8) - I_{av,pv'} \gamma_{k_j}^2 (\gamma_{k_j}^2 + 4), \quad (248)$$

$$M_1(I_{av,pv'}, \vec{R}_j) = \frac{I_{av,pv'} - I_{k_j}}{\sqrt{1 + \gamma_{k_j}^2}} - e\vec{F} \cdot \vec{R}_j, \quad (249)$$

$$M_2(I_{av,pv'}) = \frac{\gamma_{k_j}^2 (I_{av,pv'} - I_{k_j})}{(1 + \gamma_{k_j}^2)^{3/2}} + \frac{2I_{k_j}}{\sqrt{1 + \gamma_{k_j}^2}} \quad (250)$$

$$E_{k_j} = 3^2 2^{3/2} \pi^{1/2} \gamma_{k_j}^2 \sqrt{\frac{\hbar \omega^3}{I_{k_j}}}, \quad (251)$$

$$g_{j,k_j}^{(1)}(I_{av,pv'}, \vec{R}_j) = \frac{1}{\hbar \omega} \left(\tilde{I}_{av,pv'} \sinh^{-1} \gamma_{k_j} - \tilde{I}_{k_j} \frac{\gamma_{k_j} \sqrt{1 + \gamma_{k_j}^2}}{1 + 2\gamma_{k_j}^2} - e\vec{F} \cdot \vec{R}_j \gamma_{k_j} \right), \quad (252)$$

$$\tilde{I}_{k_j} = I_{k_j} + \frac{e^2 F^2}{4m\omega^2} \quad \left(\begin{array}{l} \text{effective ionization potential} \\ \text{of the atomic } k_j \text{ orbital}, \end{array} \right) \quad (253)$$

and

$$\gamma_{2py} = \frac{\omega \sqrt{2mI_{2py}}}{eF} \quad \left(\text{Keldysh parameter of the atomic } 2py \text{ orbital} \right). \quad (254)$$

On the other hand, the quantum interference term for the transition from av to pv' under the Born–Oppenheimer and the Condon approximations $w_{av \rightarrow pv'}^{j,k_j,j',k'_j}$ ($j \neq j'$) is given by

$$\begin{aligned}
 w_{av \rightarrow pv'}^{j,k_j,j',k'_j} &= \frac{9\omega}{27/4} \sqrt{\frac{\hbar\omega}{\pi I_{k_j}}} \gamma_{k_j}^2 b_{j,k_j} b_{j',k'_j} D_{j,k_j}(I_{av,pv'}) D_{j',k'_j}(I_{av,pv'}) |\langle \Theta_{pv'} | \Theta_{av} \rangle|^2 \\
 &\times \exp \left\{ -g_{j,k_j}^{(1)}(I_{av,pv'}, \vec{R}_j) - g_{j',k'_j}^{(1)}(I_{av,pv'}, \vec{R}_{j'}) \right\} \\
 &\times \int d\Omega_{\vec{p}} \sin^2 \theta_p \Upsilon_{k_j,k'_j}(\phi_p) \{ 12G_{k_j,k'_j}(I_{av,pv'}, \theta_p)^2 \\
 &- 12J_{j,k_j,j',k'_j}(I_{av,pv'}, \hat{\vec{p}})^2 G_{k_j,k'_j}(I_{av,pv'}, \theta_p) + J_{j,k_j,j',k'_j}(I_{av,pv'}, \hat{\vec{p}})^4 \} \\
 &\times G_{k_j,k'_j}(I_{av,pv'}, \theta_p)^{-9/2} \exp \left\{ -\frac{J_{j,k_j,j',k'_j}(I_{av,pv'}, \hat{\vec{p}})^2}{4G_{k_j,k'_j}(I_{av,pv'}, \theta_p)} \right\}. \quad (255)
 \end{aligned}$$

The detailed definitions of $g_{j,k_j}^{(1)}(I_{av,pv'}, \vec{R}_j)$, $\Upsilon_{k_j,k'_j}(\phi_p)$, $G_{k_j,k'_j}(I_{av,pv'}, \theta_p)$, and $J_{j,k_j,j',k'_j}(I_{av,pv'}, \hat{\vec{p}})$ are given in Appendix L.

In summary, for N_2 and O_2 molecules (or any diatomic molecules whose molecular orbitals consist of $2p_x$ and $2p_y$ atomic orbitals), the total photoionization rate of the transition $av \rightarrow pv'$ under the Condon approximation, $w_{av \rightarrow pv'}$, is given by

$$w_{av \rightarrow pv'} = \sum_{j=1}^2 \sum_{k_j=2p_x, 2p_y} w_{av \rightarrow pv'}^{j,k_j,j,k_j} + \sum_{j=1}^2 \sum_{j'=1}^2 \sum_{(j \neq j')} \sum_{k_j,k'_j=2p_x, 2p_y} w_{av \rightarrow pv'}^{j,k_j,j',k'_j}. \quad (256)$$

Using the individual ionization rates and the quantum interference terms, the total photoionization rate from the initial state av under the Born–Oppenheimer and the Condon approximations is given by

$$w_{av} = \sum_{v'} w_{av \rightarrow pv'}. \quad (257)$$

Next, we derive the photoionization formulas in the tunneling limit. These can be obtained by taking the limit $\omega \rightarrow 0$ in the equations demonstrated above. In this case, Eq. (246) reduces to

$$\begin{aligned}
 w_{av \rightarrow pv', Tun}^{j,k_j,j,k_j} &= E_{k_j}^{\prime} b_{j,k_j}^2 D_{j,k_j}'(I_{av,pv'}, \vec{R}_j)^2 |\langle \Theta_{pv'} | \Theta_{av} \rangle|^2 B_{j,k_j}'(I_{av,pv'}, \vec{R}_j)^{-1} \\
 &\times \exp \{ -2I_{j,k_j}(I_{av,pv'}, \vec{R}_j) \}. \quad (258)
 \end{aligned}$$

The definitions of the terms in Eq. (258) are given by

$$B'_{j,k_j}(I_{av,pv'}, \vec{R}_j) = \left(\frac{I_{av,pv'} + I_{k_j} - e\vec{F} \cdot \vec{R}_j}{I_{k_j}} \right)^2 \left(\frac{3I_{av,pv'}}{I_{k_j}} - 1 \right)^{1/2}, \quad (259)$$

$$D'_{j,k_j}(I_{av,pv'}, \vec{R}_j) = \frac{m}{6(\hbar eF)^2} K'(I_{av,pv'}, \vec{R}_j)^3 - \frac{m^{1/2}}{2^{3/2} \hbar eF I_{k_j}^{1/2}} K'(I_{av,pv'}, \vec{R}_j)^2 \\ + \frac{m^{1/2} I_{k_j}^{1/2}}{2^{1/2} \hbar eF} K'(I_{av,pv'}, \vec{R}_j) - \frac{2}{3}, \quad (260)$$

$$K'(I_{av,pv'}, \vec{R}_j) = I_{av,pv'} - I_{k_j} - e\vec{F} \cdot \vec{R}_j, \quad (261)$$

$$E'_{k_j} = \frac{2^{9/4} 3^{5/2} \pi^{1/2} \hbar^{1/2} (eF)^{3/2}}{m^{3/4} I_{k_j}^{5/4}}, \quad (262)$$

and

$$h_{j,k_j}(I_{av,pv'}) = \frac{\sqrt{2mI_{k_j}}}{\hbar eF} (I_{av,pv'} - \frac{I_{k_j}}{3} - e\vec{F} \cdot \vec{R}_j). \quad (263)$$

As for the quantum interference term defined by Eq. (255), a closed-form solution cannot be obtained as mentioned in Sec. 2.6.2.

Again, in the numerical calculations demonstrated in Sec. 2.6.8, we will include the semiclassical Coulomb correction for the pre-exponential factors suggested by Keldysh: Eq. (221). In this case, we have to substitute $E_{k_j}(I_{av,pv'})$ and $E'_{k_j}(I_{av,pv'})$ for E_{k_j} and E'_{k_j} in Eqs. (251) and (262)

$$E_{k_j} = \frac{3^2 2^{3/2} \pi^{1/2} \gamma_{k_j}^2 \gamma_{av,pv'}}{\sqrt{1 + \gamma_{av,pv'}^2}} \sqrt{\frac{I_{av,pv'}^2 \omega}{\hbar I_{k_j}}} \quad (264)$$

and

$$E'_{k_j}(I_{av,pv'}) = \frac{2^{11/4} 3^{5/2} \pi^{1/2} (eF)^{1/2} I_{av,pv'}^{3/2}}{m^{1/4} \hbar^{1/2} I_{k_j}^{5/4}}. \quad (265)$$

2.6.7. Computational methods

2.6.7.1. *Ab initio* calculation

We have performed *ab initio* quantum chemistry calculations for the ground states of N₂ and O₂ molecules. Their geometries have been optimized using the hybrid density functional method, B3LYP/6-31G, and the corresponding harmonic frequencies have been characterized at the same level of theory. From the force-constant matrix calculation, we have found no vibrational modes with imaginary frequencies. This clearly indicates that the truly local minima have been achieved.

Table 4. Experimentally obtained spectroscopic data of N_2 .¹¹³

State	Re (Å)	ω_e (cm ⁻¹)	$\omega_e x_e$ (cm ⁻¹)
$N_2(X^1\Sigma_g^+)$	1.0977	2358	14.1
$N_2^+(X^2\Sigma_g^+)$	1.116	2207	16.1

Table 5. Experimentally obtained spectroscopic data of O_2 .¹¹⁴

State	Re (Å)	ω_e (cm ⁻¹)	$\omega_e x_e$ (cm ⁻¹)
$O_2(X^3\Sigma_g^-)$	1.20739	1580.361	12.0730
$O_2^+(X^2\Pi_g)$	1.1227	1876.4	16.53

From these calculations, it was found that the equilibrium bond lengths of N_2 and O_2 molecules in the ground electronic state are 1.118 and 1.255 Å, respectively. These results agree very well with the experimental data (see Tables 4 and 5).

Using the optimized geometries calculated above, the molecular orbital coefficients $b_{j,k}$ ($j = 1, 2, k_j = 2px, 2py$) have been obtained at the HF/STO-3G level of theory. The package of GAUSSIAN 98 has been employed for all the *ab initio* calculations.⁹²

2.6.7.2. Calculation of potential energy curves and Franck–Condon factors

The PECs of the N_2 ground electronic state $X^1\Sigma_g^+$ and the N_2^+ ground electronic state $X^2\Sigma_g^+$ are depicted in Fig. 27(a). On the other hand, PECs of the O_2 ground electronic state $X^3\Sigma_g^-$ and the O_2^+ ground electronic state $X^2\Pi_g$ are depicted in Fig. 27(b). For calculating these PECs, we have used the parameters of the Morse potentials shown in Tables 4 and 5. These parameters have the usual meanings in the spectroscopy.

The Franck–Condon factors calculated by using these PECs are shown in Fig. 28. From this figure, we can predict that for N_2 molecule the vibrational state $v' = 0$ of the molecular ion dominates the total photoionization rate while for O_2 molecule the vibrational state $v' = 1$ of the molecular ion has the most probable photoionization rate.

Although we did not take the field distortion of the PECs of N_2 and O_2 molecules into consideration, it is a reasonably good first order approximation.¹⁰² Furthermore, in spite of the fact that the Franck–Condon

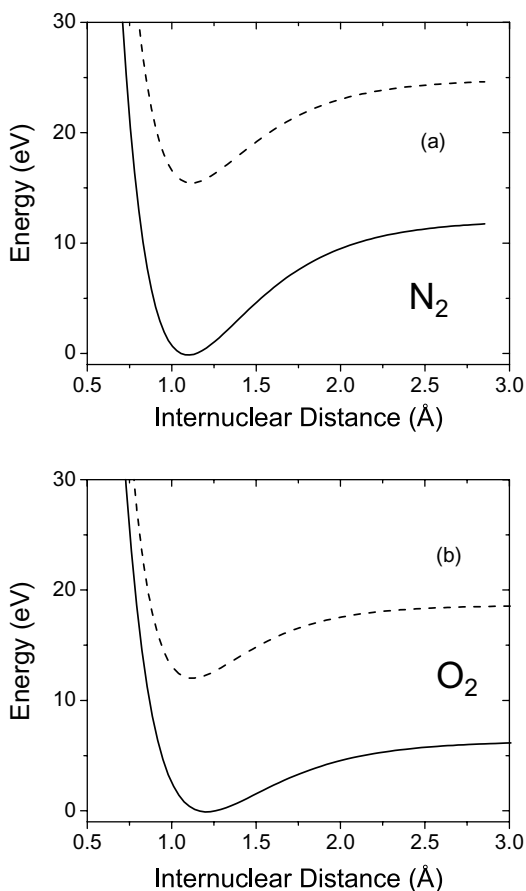


Fig. 27. PECs relevant to this section. Panel (a) shows $X^1\Sigma_g^+$ state of N_2 (solid line) and $X^2\Sigma_g^+$ state of N_2^+ (broken line). Panel (b) shows $X^3\Sigma_g^-$ state of O_2 (solid line) and $X^2\Pi_g$ state of O_2^+ (broken line). [Reused with permission from K. Mishima, K. Nagaya, M. Hayashi and S.H. Lin, *Journal of Chemical Physics*, 122, 104312 (2005). Copyright (2005) American Institute of Physics.]

factors depend on the internuclear distance, we will assume that it is given by the equilibrium bond length within the frozen core approximation (that is, the electron motion is much more rapid than the nuclear motion).

2.6.8. Numerical results and discussion

In this section, we shall use the formulas derived in Sec. 2.6.6 to check the validity of our theory by performing the numerical computations. Thereby, the orientational average originating from the random orientation of the

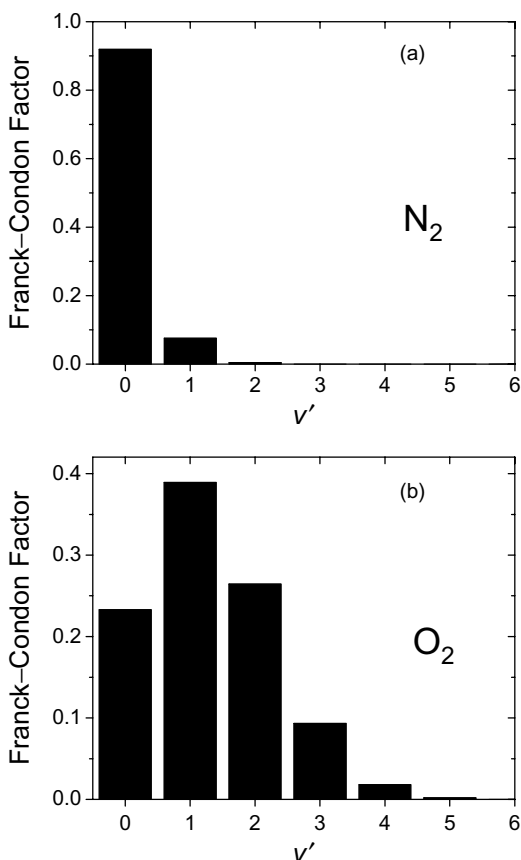


Fig. 28. Franck–Condon factors for (a) N_2 and (b) O_2 molecules using the PECs of Fig. 27. [Reused with permission from K. Mishima, K. Nagaya, M. Hayashi and S.H. Lin, *Journal of Chemical Physics*, 122, 104312 (2005). Copyright (2005) American Institute of Physics.]

molecules with respect to the laser polarization direction in the actual experiments is taken into account. This can be carried out as follows.

Let us assume that the laser polarization is directed along the z -axis in the polar coordinate. We define θ_{or} as the angle between the molecular axis and the laser polarization direction. The spatial symmetry of the molecular orbitals in the laser field leads to the fact that the photoionization rates do not depend on the angle ϕ . In addition, the photoionization rates for θ_{or} and $\pi - \theta_{or}$ are identical since the molecule of interest is a homonuclear diatomic. Therefore, we can restrict ourselves to the range $0 \leq \theta_{or} \leq \pi/2$ for the numerical calculations and the total photoionization rate can be

obtained by doubling the partial photoionization rate obtained in the range $0 \leq \theta_{or} \leq \pi/2$. When we divide this domain into the segments with a small solid angle element $2\pi\Delta\theta_{or}$, the partial contribution from this solid angle element is given by

$$\Delta w_{av}(\theta_{or}) = \frac{1}{2} \{ \cos(\theta_{or} - \Delta\theta_{or}/2) - \cos(\theta_{or} + \Delta\theta_{or}/2) \} w_{av}(\theta_{or}). \quad (266)$$

Therefore, the total photoionization rate of the randomly oriented molecules, w_{ran} , is expressed as

$$w_{ran} = 2 \sum_{j=1}^{[\pi/\Delta\theta_{or}]} \Delta w_{av}(\theta_{or,j}) \Delta\theta_{or}, \quad (267)$$

where

$$\theta_{or,j} = (j - 1)\Delta\theta_{or}. \quad (268)$$

In the following numerical calculations, we set $\Delta\theta_{or} = 0.064$ rad. We have checked that this grid size is sufficient to obtain the converged numerical results.

For the atomic ionization potentials, I_{2px} and I_{2py} , we have used the realistic values: $I_{2px} = I_{2py} = 14.53$ eV for N_2 and $I_{2px} = I_{2py} = 13.61$ eV for O_2 .

Figure 29 shows the total photoionization rates versus laser intensity for (a) N_2 and (b) O_2 molecules. From panel (a), we can see that both the ADK (Ar) and our calculations (N_2) show good agreements. From panel (b), it can be seen that both the ADK (Xe) and our calculations (O_2) also agree very well. At 10^{14} (W/cm^2), the ratio of photoionization rates of O_2 and Xe is 0.8:1.0 (compare with 0.67:1.0 obtained by DeWitt *et al.*³¹ As a general trend, our numerical results are qualitatively similar to the experimental results (see, e.g. Figs. 1 and 2 of Ref. 28) in that the slopes of the photoionization curves are increasing slowly with the laser intensity in the low laser intensity region. The ADK formula cannot reproduce this trend in the low laser intensity regime. In addition, we should note that the ADK and the static tunneling models (e.g. WKB method) seem to produce the same order of magnitude of difference in the log-log plot of the ionization rate and the laser intensity (this can typically be seen from Figs. 4 and 5 of Ref. 31) for the molecule of interest and the companion atom. This feature was also be reported by other researches (e.g. Fig. 1 of Ref. 109).

The fact that in the high intensity range our results do not show a prominent difference between ADK and our theory for O_2 may be attributed to the following reasons.

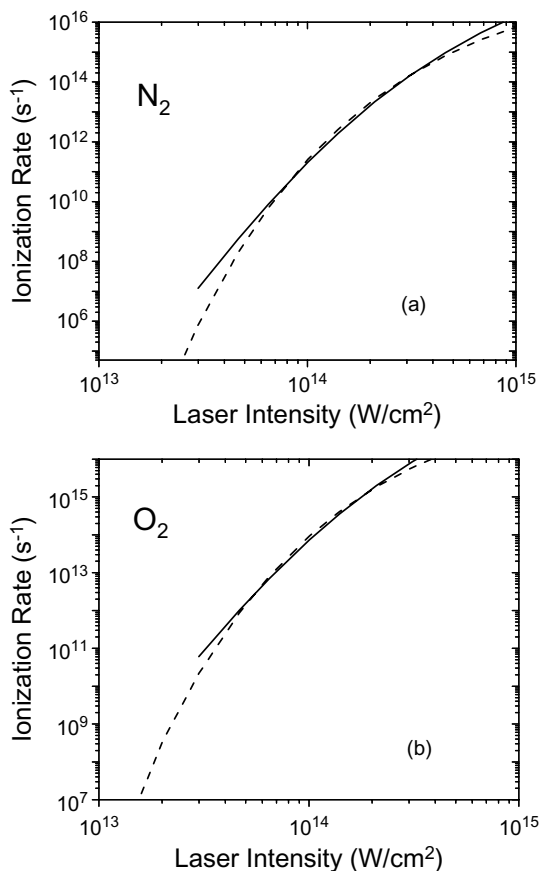


Fig. 29. Total photoionization rates versus laser intensity for (a) N_2 (solid line) and Ar (broken line), and (b) O_2 (solid line) and Xe (broken line). The broken lines were calculated by the ADK formula while the solid lines were evaluated by Eqs. (246) and (255). [Reused with permission from K. Mishima, K. Nagaya, M. Hayashi and S.H. Lin, *Journal of Chemical Physics*, 122, 104312 (2005). Copyright (2005) American Institute of Physics.]

The first one is the neglect of the distortions of the PECs due to the intense laser fields. This can substantially lead to large errors, as pointed out by Saenz.¹⁰² This is one of the advantages of our theory in that the ADK theory and WKB method cannot incorporate the Franck–Condon factors in an explicit fashion.

The second one is that the molecules in these experiments were not completely randomly oriented. If there are many more molecules oriented along the vertical laser polarization than those along the parallel laser polarization, the total photoionization rate will be much reduced for O_2

molecule. It may be possible to rationalize this by examining Fig. 5 of Ref. 31. DeWitt *et al.* also used the approximation similar to Eq. (267). That is, under the assumption of complete random orientation of O₂ molecule, Fig. 5 of Ref. 31 also shows a very similar, yet slight suppression of the total photoionization rate of O₂ molecule. The same assumption, complete random orientation of O₂ molecule in both Ref. 31 and our work may lead to comparable photoionization rate of O₂ molecule.

The third one is that our numerical results are the photoionization *rate*, not the photoionization *yield*. It should be noted that Fig. 5 of Ref. 31 is also the photoionization *rate*, which clearly shows that there is only a slight suppression of the photoionization rate of O₂ molecule compared to Xe atom.

The fourth one is that we did not take into account the effects of the laser pulse shape, the finite duration of the laser pulse, and the focal volume.

Finally, it should be noted that the calculated photoionization rates in Fig. 29 is the *absolute* value for both ADK theory and ours. We have not shifted these curves to compare the shape as was done, e.g. in Ref. 86.

It should be noted (see Fig. 29), however, that in the lower laser intensity range, the discrepancy between the ADK theory and ours increases. This indicates the “atomic” description of molecules is no longer valid.

In Fig. 30, we show the overall individual photoionization rates, the total quantum interference terms, and the total photoionization rates for (a) N₂ and (b) O₂ at 1.0×10^{14} (W/cm²). Notice that the quantum interference terms change sign from negative to positive at $\theta_{or} = 1.1$ rad for N₂ while they remain negative for O₂. In the small θ_{or} range, the quantum interference terms are negligibly small for both N₂ and O₂ although they commonly affect the total photoionization rate destructively. In the large θ_{or} range, however, the mechanisms of N₂ and O₂ are essentially different. In both molecules, the total individual photoionization rates are comparable to the quantum interference terms in terms of the magnitude. However, it should be noted that the quantum interference terms affect the overall photoionization rates constructively for N₂ while destructively for O₂. Therefore, we can see that the overall photoionization rate is surprisingly reduced for O₂ in the perpendicular laser polarization case.

Furthermore, it should be noted that from Fig. 30 we can see that not only the constructive interference but also the destructive interference exists for N₂ molecule. The individual photoionization rates are quite large and the quantum interference terms are smaller in several orders of magnitude than the individual photoionization rates so that the role of quantum interference terms is negligibly small.

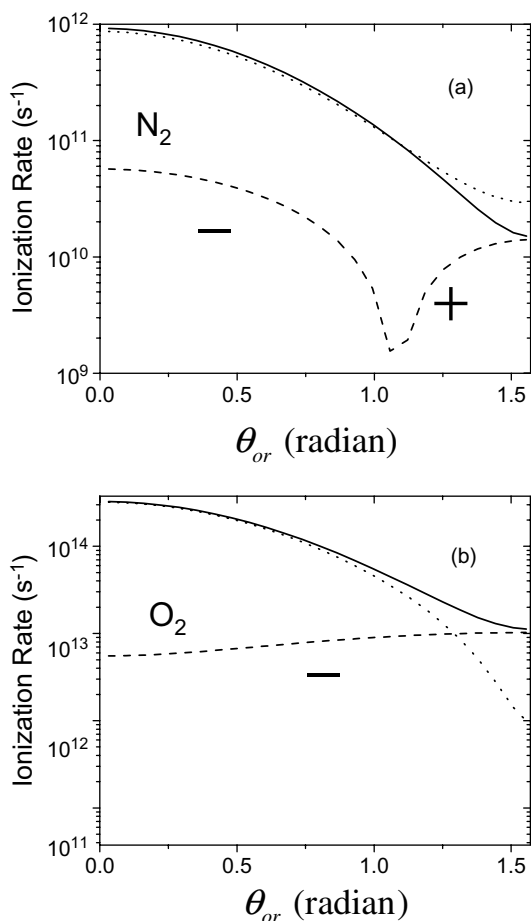


Fig. 30. Total individual photoionization rates (solid line), total quantum interference terms (broken line), and overall photoionization rates (dotted line) for (a) N_2 and (b) O_2 at the laser intensity 1.0×10^{14} (W/cm^2). The abscissa θ_{or} represents $\theta_{or,j}$ defined by Eq. (268) for $j = 1, 2, \dots, 24$ from left to right. [Reused with permission from K. Mishima, K. Nagaya, M. Hayashi and S.H. Lin, *Journal of Chemical Physics*, 122, 104312 (2005). Copyright (2005) American Institute of Physics.]

Figure 31 displays the total photoionization rates integrated over the solid angles $\Delta\theta_{or} = 0.064$ rad at the angle θ_{or} at the laser intensity 1.0×10^{14} (W/cm^2). The sum of the peak values of each bar is equal to the overall photoionization rate. We can see that even if the total photoionization rate at the specific solid angle θ_{or} is very large, its contribution to the total photoionization rate of the randomly oriented molecules is not necessarily significant. This is due to the fact that small surface area for the parallel laser

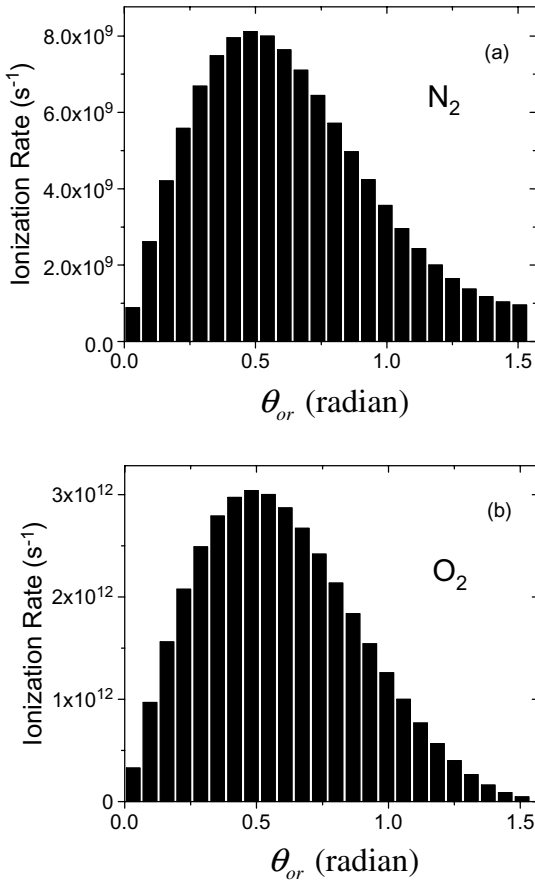


Fig. 31. Total photoionization rates integrated over the solid angles $\Delta\theta_{or} = 0.064$ rad at the angle θ_{or} at the laser intensity 1.0×10^{14} (W/cm²) for (a) N₂ and (b) O₂ molecules. Note that the sum of the peak values of each bar is equal to the overall photoionization rate. The abscissa θ_{or} represents $\theta_{or,j}$ defined by Eq. (268) for $j = 1, 2, \dots, 24$ from left to right. [Reused with permission from K. Mishima, K. Nagaya, M. Hayashi and S.H. Lin, *Journal of Chemical Physics*, 122, 104312 (2005). Copyright (2005) American Institute of Physics.]

polarization case leads to a small partial photoionization rate. The remarkable feature of Fig. 31 is that the partial photoionization rate of O₂ in the vicinity of the perpendicular laser polarization is extremely small compared with that of N₂. This is consistent with the fact that the destructive interference is the strongest for the perpendicular laser polarization, as was shown in Fig. 30. From Fig. 31, it can be concluded that the contribution from $\theta_{or} = 0.5$ rad is the largest in most of the cases.

Figure 32 is the ratios of the photoionization signal of N₂ versus Ar and (b) O₂ versus Xe. For Ar and Xe, we employ the ADK theory¹³ and

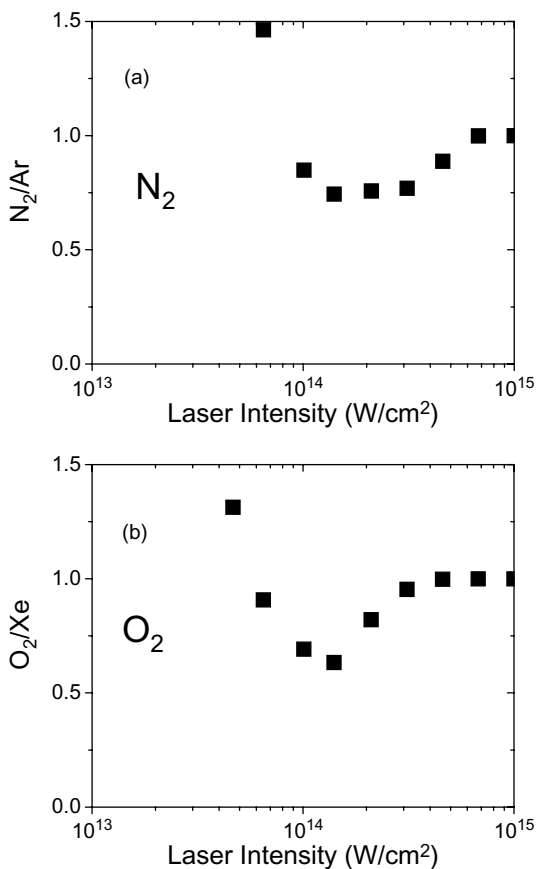


Fig. 32. Ratios of photoionization signal of (a) N₂ versus Ar and (b) O₂ versus Xe calculated by Eq. (271). Figure 32 is compared with Figs. 1 and 2 obtained experimentally and calculated by the atomic ADK theory of Ref. 13. [Reused with permission from K. Mishima, K. Nagaya, M. Hayashi and S.H. Lin, *Journal of Chemical Physics*, 122, 104312 (2005). Copyright (2005) American Institute of Physics.]

for N₂ and O₂, Eqs. (246) and (255) are used. The photoionization signal is calculated as follows. In order to include the effect of the Gaussian pulse shape of the incident laser, we have to replace \vec{F} in Eq. (9) as

$$\vec{F} \rightarrow \vec{F}'(t) = \exp\{-4 \ln(2)/w_{FWHM}(t - t_0)^2\}, \quad (269)$$

where w_{FWHM} is the full width at half maximum. The laser amplitude F in the formulas derived in Sec. 2.6.6 should be replaced with $F'(t)$. We shall compare our numerical results with those of Ref. 28, in which case the laser pulse duration is 30 fs and the laser wavelength is 800 nm. Since the laser

amplitude $\vec{F}'(t)$ is time-dependent, $\Delta w_{av}(\theta_{or})$ of Eq. (266) also has a time-dependence. The photoionization probability into the small solid angle element $2\pi\Delta\theta_{or}$ is given by

$$\Delta P(\theta_{or,j}) = 1 - \exp\left\{-\int_0^\infty dt \Delta w_{av}(\theta_{or,j})\right\}. \quad (270)$$

Then we calculate the summation of $\Delta P(\theta_{or,j})$ over the solid angle,

$$P_{ran} = 2 \sum_{j=1}^{[\pi/\Delta\theta_{or}]} \Delta P(\theta_{or,j}) \Delta\theta_{or}. \quad (271)$$

The ratios of P_{ran} of the molecule of interest and the ‘‘companion’’ atom are compared in Fig. 32.

In Fig. 32, the ratios of P_{ran} are compared for each partner. From Fig. 32, we can see that when the laser intensity is small (below 7×10^{13} W/cm²), the ratios calculated by our theory are more than unity for both of the groups N₂/Ar and O₂/Xe. This agrees with Figs. 1 and 2 of Ref. 28 qualitatively. For N₂/Ar system, the experimentally observed photoionization yield of N₂ is always larger than that calculated by the ADK theory (see Fig. 1 of Ref. 28). Figure 32(a) shows that our result has a minimum around 2×10^{14} W/cm², while this is not the case for Fig. 1 of Ref. 28. However, in both cases, the ratio approaches unity in the high laser intensity limit (1.0×10^{15} W/cm²).

On the other hand, in the O₂/Xe system, if the laser intensity increases, there is a crossing between the photoionization yield of Xe (calculated by the ADK theory) and that of O₂ (obtained experimentally) (see Fig. 2 of Ref. 28). This also holds for Fig. 32(b). In the much higher intensity region ($1 \times 10^{14} \sim 1 \times 10^{15}$ W/cm²), the photoionization field of Xe is larger than that of O₂. The same tendency is shown in Fig. 2 of Ref. 28 and our result. Again, in the high laser intensity limit, the ratio approaches unity for both Fig. 32(b) and Fig. 2 of Ref. 28.

From the above discussions, it is concluded that our molecular theory can predict the molecular photoionization rate reasonably well.

2.7. Towards the Realization of the Quantum Chemistry Approach to Tunneling Photoionization Processes in Strong Laser Fields

Taking into account the importance of the MO theoretic approach to the molecular tunneling photoionization processes as was emphasized in previous sections, we will bridge one of the potential gaps between the MO

and tunneling photoionization theories. As is well-known, the Slater-type atomic orbitals (STOs) are realistic functions but they require a heavy computational effort in quantum chemistry calculations, e.g. the computation of two-electron integrals. To overcome this difficulty, Gaussian-type orbitals (GTOs) are commonly used. In this section, we reconsider the Keldysh theory for its efficient application to molecular systems, e.g. by replacing the initial STO bound state with a linear combination of the GTOs as a first step.

In the quantum chemistry calculations, one usually decomposes the STO $\psi_{1s}(r)$ into the sum of GTOs $\phi_{1s,k}(r)$,

$$\psi_{1s}(r) \cong \sum_{k=1}^N c_k \phi_{1s,k}(r), \quad (272)$$

where c_k is the contraction coefficient, α_k the exponent of each contracted GTO, and

$$\phi_{1s,k}(r) = \left(\frac{2\alpha_k}{\pi} \right)^{3/4} \exp(-\alpha_k r^2). \quad (273)$$

Here, we have assumed that we are interested in 1s orbital. The basis set for N is usually called STO-NG basis set.

The Keldysh theory yields the following total tunneling photoionization rate w_{total} ,

$$w_{\text{total}} = \sum_{k=1}^N \sum_{l=1}^N c_k c_l w_{k,l}, \quad (274)$$

for 1s STO-NG basis set. Here, we have defined

$$w_{k,l} = D_{k,l} \exp(g_{k,l}), \quad (275)$$

where

$$D_{k,l} = \frac{m^{7/2} I_{1s}^2 \omega^{5/2}}{2^{5/2} \hbar^{11/2} (\alpha_k \alpha_l)^{7/4} \sinh^{-1} \gamma_{1s} \sqrt{\sinh^{-1} \gamma_{1s} - \frac{\gamma_{1s}}{\sqrt{1+\gamma_{1s}^2}}}}, \quad (276)$$

and

$$g_{k,l} = -\frac{2\tilde{I}_{1s}}{\hbar\omega} \left(\sinh^{-1} \gamma_{1s} - \frac{\gamma_{1s} \sqrt{1+\gamma_{1s}^2}}{1+2\gamma_{1s}^2} \right) + \frac{m I_{1s}}{2\hbar^2} \left(\frac{1}{\alpha_k} + \frac{1}{\alpha_l} \right). \quad (277)$$

Note that the exponents of the primitive Gaussian functions are included in the exponent: $\frac{m I_{1s}}{2\hbar^2} \left(\frac{1}{\alpha_k} + \frac{1}{\alpha_l} \right)$. As we know that the exponential factors play a significant role, Eq. (274) clearly shows that the diffuse primitives play a more dominant role for determining the total photoionization rate.

First, let us review STO-NG originally proposed by Pople and coworkers.^{115,116} Table 6 shows the contraction coefficients c_k and the

Table 6. Contraction coefficients c_k and exponents α_k for each contracted GTO $\phi_{1s,k}(r)$ using the scaling factor $\zeta = 1.24$.^{115,116}

	STO-1G	STO-2G	STO-3G	STO-4G
α_1	2.830×10^{-1}	2.332×10^{-1}	1.689×10^{-1}	1.353×10^{-1}
c_1	1.000	0.679	0.445	0.292
α_2		1.309×10^0	6.238×10^{-1}	4.078×10^{-1}
c_2		0.430	0.535	0.533
α_3			3.425×10^0	1.468×10^0
c_3			0.154	0.260
α_4				8.000×10^0
c_4				0.0568

exponents α_k for each contracted GTO $\phi_{1s,k}(r)$ ^{115,116} defined by Eq. (272). As is well known, these parameters were obtained by the least squares method.¹¹⁷ As N increases, STO- N G becomes more similar to the real STO.

From Fig. 33(a), we can see that the total photoionization rates w_{total} calculated by the two methods agree fairly well in the low intensity region (around 1×10^{14} W/cm²), in particular, if N is small. On the other hand, when N becomes larger, the discrepancy between the two methods is more pronounced. This is contradictory to the fact that increasing N produces a more accurate wavefunction.

From Fig. 33(b), we can see that there is a general tendency that $c_k c_l w_{k,l}$ with the combination of the smaller α_k and α_l is much larger than the larger α_k and α_l . Actually, by comparing with Table 6, the combination of $k = 1$ and $l = 1$ is by far the largest than any other combinations. This is due to the fact that the exponential factor $\frac{mI_s}{2\hbar^2} \left(\frac{1}{\alpha_k} + \frac{1}{\alpha_l} \right)$ in Eq. (275) is the largest for the former combination.

In order to make clear the unexpected results obtained in Table 6, we will compute the following quantities:

$$f = \int \left\{ \psi_{1s}(r) - \sum_{k=1}^N c_k \phi_{1s,k,GTO}(r) \right\}^2 d\vec{r}, \quad (278)$$

and

$$f' = \int \left\{ \psi_{1s}(r) - c_{k_{\text{max}}} \phi_{1s,k_{\text{max}},GTO}(r) \right\}^2 d\vec{r}. \quad (279)$$

The quantity f in Eq. (278) was used by the least squares method by Pople and coworkers,^{115,116} which measures the magnitude of difference between the realistic STO and STO- N G. On the other hand, f' in Eq. (279) measures how much different the realistic STO and one of the primitive primitives, $c_{k_{\text{max}}} \phi_{1s,k_{\text{max}},GTO}(r)$, are. In Eq. (279), k_{max} stands for the number of

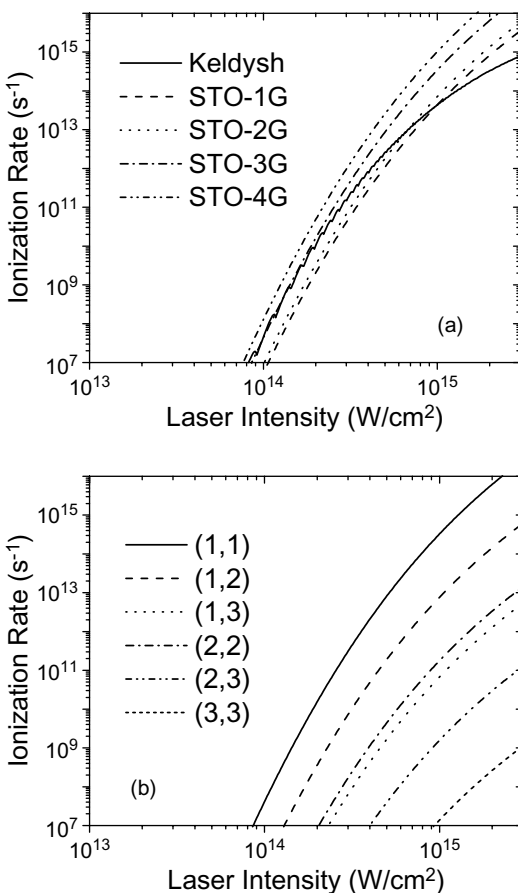


Fig. 33. Photoionization rates versus laser intensity calculated by the Coulomb-corrected Keldysh theory (Eq. (16) in Ref. 10) and those calculated by Eq. (274). Panel (b) shows the individual photoionization rates $c_k c_l w_{k,l}$ defined by Eq. (275) for STO-3G. The combination (k,l) is indicated in the figure. The incident laser frequency ω is 1.55 eV. [Reused with permission from K. Mishima, K. Nagaya, M. Hayashi and S.H. Lin, Journal of chemical physics, 122, 024104 (2005). Copyright (2005) American Institute of Physics.]

the primitive whose exponent is the smallest in the STO-NG; e.g. in Table 6, $k_{\max} = 1$.

Figure 34 shows f and f' at the same time. As expected, f decreases as N increases. However, we can see that f' increases as N increases. This indicates that the primitive most dominant in the photoionization rate formula becomes more different from the real STO as N increases. This is one of the reasons why the Keldysh and our numerical results increasingly differ as N increases as shown in Fig. 33.

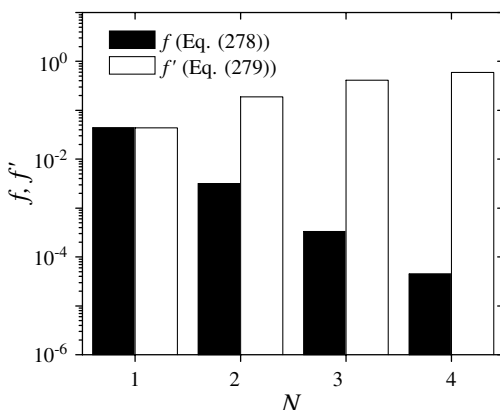


Fig. 34. Bar diagram of f and f' defined by Eqs. (278) and (279) versus N of STO-NG ($N = 1 \sim 4$). [Reused with permission from K. Mishima, K. Nagaya, M. Hayashi and S.H. Lin, Journal of chemical physics, 122, 024104 (2005). Copyright (2005) American Institute of Physics.]

In summary, the emphasis of this section has been placed on the first attempt to adopt the quantum chemistry approach for the efficient calculation of the molecular photoionization rates using the Keldysh theory. As shown above, replacing the initial STO orbital with the STO-NG leads to the unexpected conclusions. In future, one will be able to adopt other quantum chemistry approaches, e.g. use higher levels of MOs.

2.8. *Ab Initio*/RRKM Approach to the Elucidation of the Mechanism of Photoionization and Photodissociation of Molecules in Intense Laser Fields

In this section, we will briefly present the theoretical methods aimed at more elaborate investigations of the processes of molecules in strong laser fields.

So far, we have only concentrated on the photoionization of molecules. However, recent experimental studies have shown that the molecules in intense laser fields (10^{13} – 10^{16} W/cm²) undergo not only photoionization but also isomerization as well as dissociation. In particular, multiple ionization of molecules followed by their decomposition to fragments has been found and the phenomenon is usually called Coulomb explosion.¹¹⁸ For the details of the experimental studies, consult the section of Nakashima and coworkers of this volume.

Coulomb explosion of polyatomic molecules is much more complicated to treat than simple molecules theoretically since it is expected that

numerous molecular fragments, especially ionic molecular fragments can be produced and intertwined isomerization and dissociation channels will be open; for example, the isomerization and dissociation of acetone cation radicals,¹¹⁹ and singly and doubly charged ethanol cations¹²⁰ have been studied by the present authors. One of the excellent theoretical methods to treat Coulomb explosion of polyatomic molecules is to obtain potential energy surfaces (PES) of the parent ions by quantum chemistry *ab initio* calculation as a first step. Then, one calculates the rate constants for each isomerization and dissociation channel using RRKM (Rice–Ramsperger–Kassel–Marcus) theory or quasi-equilibrium theory (QET).^{121–123} From the rate constants, one can predict branching ratios for various products by integrating the kinetic master equation. This *ab initio*/RRKM method has already been applied to various chemical reactions by our group; for example see Ref. 124. In particular, numerical calculations have been performed for investigating isomerization and dissociation of the benzene cation $C_6H_6^{3+}$.¹²⁵ That study is aimed at investigating one of the highly positively charged fragments produced by the Coulomb explosion of polyatomic molecules.

In short, the calculation procedure of *ab initio*/RRKM method is summarized as follows. The reaction rate, $k(E)$, at an internal energy E for a unimolecular reaction $A^* \rightarrow A^\ddagger \rightarrow P$ is given by

$$k(E) = \frac{\sigma W^\ddagger(E - E^\ddagger)}{h \rho(E)}. \quad (280)$$

In Eq. (280), σ is the reaction path degeneracy, h the Planck constant, $W^\ddagger(E - E^\ddagger)$ the total number of states of the transition state (activated complex) A^\ddagger with a barrier E^\ddagger , and $\rho(E)$ the density of states of the energized reactant molecule A^* , P the product(s).

Using the reaction rate $k(E)$ calculated by Eq. (280), the kinetic master equations for unimolecular reactions can be expressed as

$$\frac{d}{dt} C_i(t) = \sum k_n C_j(t) - \sum k_m C_i(t). \quad (281)$$

Here, $C_j(t)$ and $C_i(t)$ are concentrations of various intermediates or products at time t , and k_n and k_m are macrocanonical rate constants obtained by RRKM theory. Taking the steady-state limit in Eq. (281), we can obtain the eventual product branching ratios.

One of the concerns about using the numerical results obtained by quantum chemistry *ab initio* calculations is that the PES'es calculated without the effect of the incident laser fields will be incorrect since the PES'es are deformed by the strong laser fields. However, the PES'es calculated without

the laser fields govern the fragmentation processes if the dissociation of molecules photoionized by the intense laser fields takes place between the laser pulses or after the laser shots. This was clearly pointed out in Ref. 125.

Taking into account the fact that the present computational resources can only treat small molecules, the *ab initio*/RRKM approach introduced in this section will continue to be a powerful tool to investigate the detailed processes of large polyatomic molecules in strong laser fields.

2.9. Conclusion

In Sec. 2.3.2, we have generalized and improved the derivation of photoionization rate of hydrogen-like atoms proposed by Keldysh. We have performed the contour integration of Eq. (60) in a different way from Keldysh or many other authors. In most of the cases, the saddle-point method has been used, while we adopted the residue theorem for the contour integration. In addition, we have taken into account the \vec{p} -dependence of the pre-exponential factor in Eq. (64). Our formulas are more accurate than those derived by Keldysh's theory. The numerical calculations have shown that the photoionization rate for the hydrogen atoms should be more enhanced than Keldysh's, which is in accord with the experimental results.¹⁶

In Sec. 2.3.3, based on our new derivational method, we have extended the Keldysh theory to the photoionization processes of the randomly oriented diatomic molecules: N_2 . The photoionization rates calculated by our formula for the randomly oriented N_2 molecules were in a good agreement with those estimated by the ADK formula.¹³

In Sec. 2.4, by including the principal effect of the long-range Coulomb potential to the Volkov function (approximate Coulomb-Volkov function), we have derived the analytical formulas of photoionization rate for hydrogen-like atoms following the method developed in Sec. 2.3. However, we did not depend on the crude quasi-classical analysis for the pre-exponential factors, which was originally adopted by Keldysh. An important point is that our formulas are quite simple and insightful, do not require a huge computer memory for the calculation, and physical meaning can easily be deduced. For example, comparing Eq. (E3) with the assumption of Eqs. (E10) and (E11), and that with the assumption $\vec{A} = 0$ (no Coulomb effect), one can draw the important conclusion that the photoionization rate in the presence of Coulomb potential is always larger than that in the absence of Coulomb potential.

As for the derivation, we have reduced the infinite summation to integration as shown in Eq. (D7), which renders the final photoionization rate

formula quite simple. Our simple formulas of Eqs. (D5) and (E3) are free from the infinite summation $S(\gamma, \tilde{I}_0/\hbar\omega)$ in Eq. (55) and Dawson's integral of Eq. (56). In summary, we have found that the role of the *first* order Coulomb correction is to lower the ionization potential and enhances the photoionization rates and that of the *second* order correction modifies the Keldysh parameter, decreases the binding energy, and increases the photoionization rates.

In Sec. 2.5, we have analytically derived the tunneling photoionization rate formula for large molecules taking into account the positions of the constituent atoms explicitly. We have clarified the mechanism of molecular size dependence of the photoionization rate by numerical calculations taking all-*trans* polyacetylene radicals as an example. From the derived expressions, we have predicted that the photoionization rate is sensitive to the angle between the polarization vector of the linearly polarized laser field and the molecular axis, and the internuclear distance. In addition, we have found that the photoionization rate strongly depends on the factor $\exp(2\sqrt{2m\tilde{I}\tilde{F}} \cdot \tilde{R}_j/\hbar F)$. It should be noted that it is possible to estimate photoionization rates in a reasonable CPU time although at present the numerical calculations are essentially impossible. Moreover, because we used LCAO for the initial bound state and our equations are analytical, many phenomena peculiar to molecules are understood clearly from our formulas and a lot of useful information that cannot be derived from the numerical calculations (e.g. quantum interference terms, especially *negative* quantum interference terms) can be easily obtained.

As evidenced in Sec. 2.5.4, the photoionization rates induced by the quantum interference terms between distinct constituent atoms are quite characteristic for molecules, which do not exist for atoms. We have found that the quantum interference terms are comparable with the individual terms. More importantly, the contribution of quantum interference terms decreases with increasing distance between the partners parallel to the polarization of the linearly polarized electric field.

In Sec. 2.6. (i), we have obtained the analytical Keldysh-type expressions for the photoionization rates of H_2 molecule in the linearly polarized electric field in the tunneling region. For this purpose, we have extended the Keldysh theory improved by us in the previous sections; especially, we have included Franck–Condon factors to take the molecular vibrational degrees of freedom into consideration. The comparison of the numerical calculations performed by using these formulas with the numerical results calculated by Saenz⁵⁴ has actually shown the validity of our formulas. Clearly, our formulas have more complicated structures than the

ADK theory, but we could obtain physical insights by inspection of the formulas themselves and the numerical results. This feature is due to the simple structure of the formulas derived by the Keldysh-type theory: our formulas are expressed in the form of a combination of the exponential and pre-exponential terms, which is very similar to the original atomic Keldysh theory. However, in the case of molecules, there exists a special feature due to the interferences between different atoms. The explicit dependence of the photoionization rate on the laser frequency is also one of the advantages over other tunneling theories, e.g. the ADK theory.

In Sec. 2.6. (ii), we have derived the molecular Keldysh-type formulas for the photoionization rates of N_2 and O_2 molecules in the linearly polarized electric field in the tunneling region. In the derivation, we have properly incorporated the vibrational degrees of freedom, which is essential for molecular systems. In addition, we have shown the calculation results using these formulas. It was found that the quantum interference terms play an important role to determine the photoionization rates or probabilities for the suppressed photoionization of O_2 and the enhanced photoionization of N_2 molecules. The suppression and the enhancement are particularly important if the molecular axis approaches the perpendicular direction of the laser polarization. We have compared the photoionization rates and yields of the molecules of interest and the “companion” atoms: N_2/Ar and O_2/Xe . From this comparison, we have found that our formulas qualitatively agree with the experimental data. These numerical examples also show that our molecular Keldysh theory is one of the adequate theories.

In Sec. 2.7, we have theoretically investigated the possibility to employ the MO theoretic approach for calculating the tunneling photoionization rates of molecules. As a first step, we have concentrated on the simplest example: 1s state of the hydrogen atom. The issue treated in this section was to investigate the influence on the photoionization rate brought about by expanding the real STO by the STO-NG ($N = 1-4$). The numerical results obtained by our analytical formulas agree well with those by the Keldysh theory in the low intensity region, but they do not agree in the high intensity regime. In particular, we have obtained a quite counterintuitive result that improving the initial wavefunction by increasing N of the STO-NG leads to large deviation of the photoionization rate from that obtained by the real STO. The reason for this result has been attributed to the exponent of the primitives α_k in Eq. (273). Furthermore, it has been found that if the primitive GTOs are more diffuse, its contribution to the

total tunneling photoionization rate becomes more pronounced. This was also the consequence of the exponents of the GTOs. In conclusion, only the most diffuse primitive GTO in the basis function (not the STO-NG itself) should be similar as much as possible to the exact atomic or molecular orbital in the calculations using our formulas. The present work is the first step towards the realization of quantum chemistry approach of photoionization processes.

Finally, in Sec. 2.8, we have pointed out that in the multiphoton processes of molecules, it is necessary to investigate the intermediates and transition states of molecules carefully since the dissociation of the molecules can compete with the photoionization processes. To this end, it was shown that *ab initio*/RRKM approach is one of the promising theoretical methods for treating polyatomic molecules.

The present review has summarized our recent advancement of the original atomic Keldysh theory published in Refs. 126–132.

Acknowledgments

The authors wish to thank Academia Sinica, National Science Council of ROC for supporting this work. One of the authors (K. Mishima) would like to thank Prof. K. Yamashita and JST for the financial support during the preparation of this article.

Appendix

Appendix A. Saddle-Point Method for Integrals with a Singularity

Let us consider the following integral:

$$J_v = \int_C \frac{g(x)}{(x-x_0)^v} \exp\{-\lambda f(x)\} dx. \quad (\text{A1})$$

The function $f(x)$ is assumed to oscillate rapidly at the saddle-point x_0 where

$$f'(x_0) = 0. \quad (\text{A2})$$

The function $g(x)$ is assumed not to be singular at any points x and the integrated function has v -th order singularity at the saddle-point x_0 .

By applying the transformation,

$$\frac{1}{(x-x_0)^v} = \frac{1}{\Gamma(v)} \int_0^\infty d\xi \xi^{v-1} \exp\{-\xi(x-x_0)\}, \quad (\text{A3})$$

to Eq. (A1), we obtain

$$J_v = \frac{1}{\Gamma(v)} \int_0^\infty d\xi \xi^{v-1} \int_C g(x) \exp\left[-\lambda \left\{f(x) + \frac{\xi(x-x_0)}{\lambda}\right\}\right] dx. \quad (\text{A4})$$

Let us evaluate the following:

$$h(\xi) = \int_C g(x) \exp\left[-\lambda \left\{f(x) + \frac{\xi(x-x_0)}{\lambda}\right\}\right] dx. \quad (\text{A5})$$

The saddle-point of $f(x) + \frac{\xi(x-x_0)}{\lambda}$, x_1 , is given by

$$f'(x_1) + \frac{\xi}{\lambda} = 0. \quad (\text{A6})$$

It follows that

$$f'(x_1) = f'(x_0) + f''(x_0)(x_1 - x_0) = f''(x_0)(x_1 - x_0) = -\frac{\xi}{\lambda}. \quad (\text{A7})$$

Therefore, the new saddle-point, x_1 , is explicitly expressed as

$$x_1 = x_0 - \frac{\xi}{\lambda f''(x_0)}. \quad (\text{A8})$$

By using the conventional saddle-point method, we find

$$h(\xi) = \left\{ \frac{2\pi}{\lambda f''(x_1)} \right\}^{1/2} g(x_1) \exp\left[-\lambda \left\{f(x_1) + \frac{\xi(x_1 - x_0)}{\lambda}\right\}\right]. \quad (\text{A9})$$

Expanding $f(x_1)$ around x_0 and using Eqs. (A2) and (A8) in Eq. (A9) yield

$$h(\xi) = \left\{ \frac{2\pi}{\lambda f''(x_0)} \right\}^{1/2} g(x_0) \exp\{-\lambda f(x_0)\} \exp\left\{ \frac{-\xi^2}{-2\lambda f''(x_0)} \right\}. \quad (\text{A10})$$

Substituting Eq. (A10) into Eq. (A4), we obtain

$$J_v = \frac{1}{\Gamma(v)} \left\{ \frac{2\pi}{\lambda f''(x_0)} \right\}^{1/2} g(x_0) \exp\{-\lambda f(x_0)\} \int_0^\infty d\xi \xi^{v-1} \exp\left\{ \frac{-\xi^2}{-2\lambda f''(x_0)} \right\}. \quad (\text{A11})$$

Letting $A = -\{2\lambda f''(x_0)\}^{-1}$ in the following formula

$$\int_0^\infty d\xi \xi^n \exp(-A\xi^2) = \begin{cases} \frac{(n-1)!!}{2^{n/2+1}} \sqrt{\frac{\pi}{A^{n+1}}} & (n : \text{even}) \\ \frac{\{(n-1)/2\}!}{2A^{(n+1)/2}} & (n : \text{odd}) \end{cases}, \quad (\text{A12})$$

we finally obtain

$$J_v \approx i^v \frac{\Gamma(v/2)}{2\Gamma(v)} \left\{ \frac{2\pi}{\lambda f''(x_0)} \right\}^{1/2} g(x_0) \{2\lambda f''(x_0)\}^{v/2} \exp\{-\lambda f(x_0)\}. \quad (\text{A13})$$

Appendix B. Compact Forms of $L(\vec{p})$ Defined by Eq. (64)

To facilitate the integration with respect to \vec{p} in w_0 of Eq. (30), we shall expand the functions included in Eq. (64) in the power series of p up to second order inclusively. This means that the kinetic momentum of the ionizing electron is assumed to be low.

Using the following expression for u_s obtained from Eq. (36),

$$u_s = \gamma \left(i - \frac{p}{\sqrt{2mI_0}} \cos \theta + \frac{ip^2 \sin^2 \theta}{4mI_0} + \dots \right), \quad (\text{B1})$$

it is easy to show that

$$\begin{aligned} j(u_s) &= \tilde{I}_0 \left(\sinh^{-1} \gamma - \frac{\gamma \sqrt{1 + \gamma^2}}{1 + 2\gamma^2} \right) + \frac{eF \cos \theta}{m\omega} (1 - \sqrt{1 + \gamma^2}) p \\ &+ \frac{i}{2m} \left(\sinh^{-1} \gamma - \frac{\gamma \cos^2 \theta}{\sqrt{1 + \gamma^2}} \right) p^2. \end{aligned} \quad (\text{B2})$$

Similarly, from Eq. (65), we find

$$\cos \theta_{pF} = 1 + \frac{p^2 \sin^2 \theta}{4mI_0} + \dots \quad (\text{B3})$$

From Eq. (B1), we obtain

$$\sqrt{1 - u_s^2} = \sqrt{1 + \gamma^2} \left\{ 1 + \frac{i\gamma^2 p \cos \theta}{\sqrt{2mI_0}(1 + \gamma^2)} + \frac{\gamma^2 p^2 (1 - 2 \cos^2 \theta + \gamma^2 \sin^2 \theta)}{4mI_0(1 + \gamma^2)^2} \right\}. \quad (\text{B4})$$

Using the Taylor expansion of $\exp\{f(p)\}$ for an arbitrary function $f(p)$ around $p = 0$,

$$\exp\{f(p)\} = \exp\{f(0)\} + f'(0) \exp\{f(0)\} p + \frac{f''(0) + f'(0)^2}{2} \exp\{f(0)\} p^2, \quad (\text{B5})$$

we find

$$\cos \theta_{pF} = \exp\left(\frac{p^2 \sin^2 \theta}{4mI_0}\right) \quad (\text{B6})$$

and

$$\sqrt{1 - u_s^2} = \sqrt{1 + \gamma^2} \exp\left\{ \frac{i\gamma^2 p \cos \theta}{\sqrt{2mI_0}(1 + \gamma^2)} + \frac{\gamma^2 p^2 (1 + \gamma^2 - 2 \cos^2 \theta)}{4mI_0(1 + \gamma^2)^2} \right\}. \quad (\text{B7})$$

Inserting Eqs. (B2), (B6), and (B7) into (64) yields

$$L(\vec{p}) = \frac{4\hbar\omega I_0 \sqrt{\pi a}}{eF\sqrt{1+\gamma^2}} \exp(A + iB(\theta)p + C(\theta)p^2), \quad (\text{B8})$$

where

$$A = -\frac{\tilde{I}_0}{\hbar\omega} \left(\sinh^{-1} \gamma - \frac{\gamma\sqrt{1+\gamma^2}}{1+2\gamma^2} \right), \quad (\text{B9})$$

$$B(\theta) = \frac{eF \cos \theta}{m\hbar\omega^2} \left(1 - \sqrt{1+\gamma^2} \right) - \frac{\gamma^2 \cos \theta}{\sqrt{2mI_0}(1+\gamma^2)}, \quad (\text{B10})$$

and

$$C(\theta) = \frac{1}{4mI_0} \left[-\frac{1+2\gamma^2}{1+\gamma^2} + \frac{\gamma^4+4\gamma^2+1}{(1+\gamma^2)^2} \cos^2 \theta \right] - \frac{1}{2m\hbar\omega} \left(\sinh^{-1} \gamma - \frac{\gamma \cos^2 \theta}{\sqrt{1+\gamma^2}} \right). \quad (\text{B11})$$

The above procedure can be easily extended to the four cases of (C3)–(C6) in Appendix C.

Appendix C. Definition of $N(\gamma, \omega, I_0, \tilde{I}_0, B, C)$ in Eqs. (66) and (79)

As shown in the text, we have taken into account the \vec{p} dependence of the pre-exponential factors in Eq. (66), which was disregarded in Ref. 10. In order to examine the influence of the \vec{p} dependence on the photoionization rate, we show some formulas depending on various treatments of the pre-exponential factors.

The pre-exponential factor $N(\gamma, \omega, I_0, \tilde{I}_0, B, C)$ in Eq. (66) is given by

$$\begin{aligned} N(\gamma, \omega, I_0, \tilde{I}_0, B, C) &= \frac{1}{\sqrt{B}} \sum_{n=0}^{\infty} \exp \left[-2 \left(\left\langle \frac{\tilde{I}_0}{\hbar\omega} + 1 \right\rangle - \frac{\tilde{I}_0}{\hbar\omega} + n \right) \right. \\ &\quad \times \left. \left\{ \sinh^{-1} \gamma - \frac{\gamma}{\sqrt{1+\gamma^2}} + C \right\} \right] \\ &\quad \times \Theta \left[\left\{ \frac{2\gamma}{\sqrt{1+\gamma^2}} B \left(\left\langle \frac{\tilde{I}_0}{\hbar\omega} + 1 \right\rangle - \frac{\tilde{I}_0}{\hbar\omega} + n \right) \right\}^{1/2} \right]. \end{aligned} \quad (\text{C1})$$

Let us now consider the four cases: (i) $\sqrt{1-u_s^2}$ and $\cos \theta_{pF}$ depend on \vec{p} , (ii) $\sqrt{1-u_s^2}$ depends on \vec{p} and $\cos \theta_{pF} = 1$, (iii) $\sqrt{1-u_s^2} = \sqrt{1+\gamma^2}$ and

$\cos \theta_{pF}$ depends on \vec{p} , and (iv) $\cos \theta_{pF} = 1$ and $\sqrt{1 - u_s^2} = \sqrt{1 + \gamma^2}$. It follows that

$$(i) \quad B = 1 + \frac{\hbar\omega(\gamma^4 + 4\gamma^2 + 1)}{2I_0\gamma(1 + \gamma^2)^{3/2}} \quad \text{and} \quad C = \frac{\hbar\omega\gamma^2(\gamma^2 - 1)}{2I_0(1 + \gamma^2)^2} \quad (C2)$$

$$(ii) \quad B = 1 + \frac{\hbar\omega\gamma}{I_0(1 + \gamma^2)^{3/2}} \quad \text{and} \quad C = \frac{\hbar\omega\gamma^2(\gamma^2 - 1)}{2I_0(1 + \gamma^2)^2} \quad (C3)$$

$$(iii) \quad B = 1 + \frac{\hbar\omega\sqrt{1 + \gamma^2}}{2I_0\gamma} \quad \text{and} \quad C = 0 \quad (C4)$$

$$(iv) \quad B = 1 \quad \text{and} \quad C = 0. \quad (C5)$$

In the case (iv), our formula is four times larger than that of Keldysh for the atomic system. This discrepancy stems from the different methods for the contour integration in Eq. (60).

The numerical results estimated by Eq. (66) for the above four cases and that by Eq. (79) for the case (iv) are compared and discussed in Fig. 1 and Fig. 3, respectively.

Appendix D. Definition of $N(\gamma, \bar{\gamma}, \omega, I_0, \tilde{A}, \tilde{B})$ and Integrated Form of Eq. (121)

The pre-exponential factor $N(\gamma, \bar{\gamma}, \omega, I_0, \tilde{A}, \tilde{B})$ in Eq. (121) is given by

$$\begin{aligned} N(\gamma, \bar{\gamma}, \omega, I_0, \tilde{A}, \tilde{B}) &= 4\sqrt{\frac{2I_0\omega}{\hbar}} \left(\frac{\bar{\gamma}}{\gamma}\right)^2 \left(\frac{\bar{\gamma}}{\sqrt{1 + \bar{\gamma}^2}}\right)^{3/2} \frac{C_1}{C_2} \\ &\times \sum_{n=0}^{\infty} \exp\left[-2\left(\left\langle\frac{\tilde{I}''_0}{\hbar\omega} + 1\right\rangle - \frac{\tilde{I}''_0}{\hbar\omega} + n\right) C_3\right] \\ &\times \Theta\left[\left\{\frac{2\bar{\gamma}}{\sqrt{1 + \bar{\gamma}^2}} C_2 \left(\left\langle\frac{\tilde{I}''_0}{\hbar\omega} + 1\right\rangle - \frac{\tilde{I}''_0}{\hbar\omega} + n\right)\right\}^{1/2}\right]. \end{aligned} \quad (D1)$$

Other quantities in Eq. (D1) are defined by

$$\begin{aligned} C_1 = \left\{ 1 - \frac{\tilde{A}(2 + \bar{\gamma}^2)}{2I_0(1 + \bar{\gamma}^2)} + \frac{\tilde{A}^2}{2I_0\hbar\omega} \frac{\bar{\gamma}}{\sqrt{1 + \bar{\gamma}^2}} + \frac{2\bar{\gamma}\sqrt{1 + \bar{\gamma}^2}}{I_0\hbar\omega} \tilde{A}\tilde{B} \right. \\ \left. - \frac{2 + 3\bar{\gamma}^2}{I_0} \tilde{B} + \frac{2\bar{\gamma}(1 + \bar{\gamma}^2)^{3/2}}{I_0\hbar\omega} \tilde{B}^2 \right\}^2, \end{aligned} \quad (D2)$$

$$C_2 = \sqrt{1 + \frac{\tilde{A}}{2I_0(1 + \tilde{\gamma}^2)} + \tilde{B} \frac{1 + 2\tilde{\gamma}^2}{I_0}}, \quad (\text{D3})$$

$$C_3 = \sinh^{-1} \tilde{\gamma} - \frac{\tilde{\gamma}}{\sqrt{1 + \tilde{\gamma}^2}} + \frac{\tilde{A}\tilde{\gamma}^3}{2I_0(1 + \tilde{\gamma}^2)^{3/2}} - \frac{\tilde{B}\tilde{\gamma}^3}{I_0\sqrt{1 + \tilde{\gamma}^2}}. \quad (\text{D4})$$

Aside from the Keldysh-like form of Eq. (D1), it is insightful to integrate it over n . By so doing, Eq. (121) reduces to

$$\begin{aligned} w_0 = & \sqrt{\frac{2\pi I_0 \omega}{\hbar}} \left(\frac{\tilde{\gamma}}{\gamma}\right)^2 \frac{\tilde{\gamma}^2}{1 + \tilde{\gamma}^2} \frac{C_1}{C_4 \sqrt{C_3}} \\ & \times \exp \left[-\frac{2}{\hbar\omega} \left\{ \tilde{I}_0 \left(\sinh^{-1} \tilde{\gamma} - \frac{\tilde{\gamma}\sqrt{1 + \tilde{\gamma}^2}}{1 + 2\tilde{\gamma}^2} \right) + \tilde{A} \sinh^{-1} \tilde{\gamma} \right. \right. \\ & \left. \left. + \tilde{B} \left(\sinh^{-1} \tilde{\gamma} + \tilde{\gamma}\sqrt{1 + \tilde{\gamma}^2} \right) \right\} \right], \quad (\text{D5}) \end{aligned}$$

where

$$C_4 = \sinh^{-1} \tilde{\gamma} + \frac{\tilde{A}\tilde{\gamma}}{2I_0\sqrt{1 + \tilde{\gamma}^2}} + \frac{\tilde{B}\tilde{\gamma}\sqrt{1 + \tilde{\gamma}^2}}{I_0}. \quad (\text{D6})$$

Note that \tilde{I}_0'' disappears in Eq. (D5), while Eq. (D1) contains this term. The resonance structures detected by using Eq. (D1) are expected to have a shift from the counterpart of Ref. 10 and that of the first order Coulomb correction (see Appendix E).

An important approximation involved in the present theory is to change the summation with respect to n (proportional to excess photon number absorbed above threshold) to integration,

$$\begin{aligned} & \sum_{n > \left\langle \frac{\tilde{I}_0''}{\hbar\omega} \right\rangle}^{\infty} \sqrt{n\hbar\omega - \tilde{I}_0''} \exp \left\{ -\frac{2}{\hbar\omega} (n\hbar\omega - \tilde{I}_0'')(G - Hy^2) \right\} \\ & \approx \int_{\frac{\tilde{I}_0''}{\hbar\omega}}^{\infty} dn \sqrt{n\hbar\omega - \tilde{I}_0''} \exp \left\{ -\frac{2}{\hbar\omega} (n\hbar\omega - \tilde{I}_0'')(G - Hy^2) \right\}, \quad (\text{D7}) \end{aligned}$$

where

$$G = \sinh^{-1} \tilde{\gamma} + \frac{\tilde{A}\tilde{\gamma}}{2I_0\sqrt{1 + \tilde{\gamma}^2}} + \frac{\tilde{B}\tilde{\gamma}\sqrt{1 + \tilde{\gamma}^2}}{I_0} \quad (\text{D8})$$

and

$$H = \frac{\tilde{\gamma}}{\sqrt{1 + \tilde{\gamma}^2}} + \frac{\tilde{A}\tilde{\gamma}}{2I_0(1 + \tilde{\gamma}^2)^{3/2}} + \frac{\tilde{B}\tilde{\gamma}(1 + 2\tilde{\gamma}^2)}{I_0\sqrt{1 + \tilde{\gamma}^2}}. \quad (\text{D9})$$

This approximation needs to be examined. For this purpose, we consider

$$S = \sum_n \sqrt{n - \delta} \exp[-K(n - \delta)] \quad (\text{D10})$$

where

$$\delta = \frac{\tilde{I}'_0}{\hbar\omega} \quad (\text{D11})$$

and

$$K = 2(G - Hy^2). \quad (\text{D12})$$

S in Eq. (D10) should be compared with

$$S = \int_{\delta}^{\infty} dn \sqrt{n - \delta} \exp[-K(n - \delta)] = \frac{1}{2} \sqrt{\frac{\pi}{K^3}}. \quad (\text{D13})$$

An important feature of the approximation (D13) is that it is independent of δ . In Sec. 2.4.3, we show numerically the validity of the approximation Eq. (D13) for Eq. (D10).

The formula Eq. (D5) is quite simple and the infinite summation of Eq. (D1) is unnecessary. By adopting Dawson's integral, as the tunneling limit approaches, the computation time for obtaining converged results becomes quite large because the summation over n requires many iterations. In that case, the above formulas integrated over n such as Eq. (D5) are quite convenient.

Appendix E. Photoionization Rates in the First-Order Coulomb Correction

In this appendix, we show explicitly the terms appearing in Eq. (121) for the different treatments of the pre-exponential factors. Here, we show four cases that we can consider.

Generally, the photoionization rate can be expressed as

$$\begin{aligned} w_0 = & 4\sqrt{\frac{2I_0\omega}{\hbar}} \left(\frac{\gamma}{\sqrt{1+\gamma^2}} \right)^{3/2} \frac{\left(1 - \frac{\tilde{A}(2+\gamma^2)}{2I_0(1+\gamma^2)} + \frac{\tilde{A}^2}{2I_0\hbar\omega} \frac{\gamma}{\sqrt{1+\gamma^2}} \right)^2}{\sqrt{1 + \frac{\tilde{A}}{2I_0(1+\gamma^2)} + B}} \\ & \times \exp \left[-\frac{2}{\hbar\omega} \left\{ \tilde{I}'_0 \left(\sinh^{-1} \gamma - \frac{\gamma\sqrt{1+\gamma^2}}{1+2\gamma^2} \right) + \tilde{A} \sinh^{-1} \gamma \right\} \right] \\ & \times \sum_{n=0}^{\infty} \exp \left[-2 \left(\left\langle \frac{\tilde{I}'_0}{\hbar\omega} + 1 \right\rangle - \frac{\tilde{I}'_0}{\hbar\omega} + n \right) \right] \end{aligned}$$

$$\begin{aligned} & \times \left\{ \sinh^{-1} \gamma - \frac{\gamma}{\sqrt{1+\gamma^2}} + \frac{\tilde{A}\gamma^3}{2I_0(1+\gamma^2)^{3/2}} + C - \frac{\gamma}{\sqrt{1+\gamma^2}} B \right\} \\ & \times \Theta \left[\left\{ \frac{2\gamma}{\sqrt{1+\gamma^2}} B \left(\left\langle \frac{\tilde{I}_0}{\hbar\omega} + 1 \right\rangle - \frac{\tilde{I}_0}{\hbar\omega} + n \right) \right\}^{1/2} \right], \end{aligned} \quad (\text{E1})$$

where

$$\tilde{I}'_0 = I_0 + \frac{e^2 F^2}{4m\omega^2} = I_0 \left(1 + \frac{1}{2\gamma^2} \right). \quad (\text{E2})$$

Furthermore, if we perform summation over n in the above equation, then the following simpler expression is obtained

$$\begin{aligned} \omega_0 = & 2\sqrt{\frac{\pi I_0 \omega}{\hbar}} \frac{\gamma^2}{1+\gamma^2} \left(1 - \frac{\tilde{A}(2+\gamma^2)}{2I_0(1+\gamma^2)} + \frac{\tilde{A}^2}{2I_0 \hbar\omega} \frac{\gamma}{\sqrt{1+\gamma^2}} \right)^2 \\ & \times \frac{\exp \left[-\frac{2}{\hbar\omega} \left\{ \tilde{I}_0 \left(\sinh^{-1} \gamma - \frac{\gamma\sqrt{1+\gamma^2}}{1+2\gamma^2} \right) + \tilde{A} \sinh^{-1} \gamma \right\} \right]}{\left(\sinh^{-1} \gamma + \frac{\tilde{A}}{2I_0} \frac{\gamma}{\sqrt{1+\gamma^2}} + 2C \right) \sqrt{2 \left\{ \sinh^{-1} \gamma - \frac{\gamma}{\sqrt{1+\gamma^2}} + \frac{\tilde{A}}{2I_0} \frac{\gamma^3}{(1+\gamma^2)^{3/2}} + C - \frac{\gamma}{\sqrt{1+\gamma^2}} B \right\}}}. \end{aligned} \quad (\text{E3})$$

(i) If we assume that all of the pre-exponential factors depend on \vec{p} ,

$$\begin{aligned} B = & \frac{\hbar\omega}{2I_0 b_4^2} \frac{\gamma^3}{(1+\gamma^2)^{3/2}} \left\{ 1 - \frac{3\tilde{A}}{2I_0(1+\gamma^2)} + \frac{\tilde{A}^2\gamma}{\hbar\omega I_0 \sqrt{1+\gamma^2}} \right\}^2 \\ & + \frac{\hbar\omega}{2I_0 b_4} \frac{1}{\gamma(1+\gamma^2)^{3/2}} \left\{ -(4\gamma^2 + 1) + \frac{3\tilde{A}(2\gamma^6 + 2\gamma^4 + 7\gamma^2 + 2)}{2I_0(1+\gamma^2)} \right. \\ & \left. + \frac{\tilde{A}^2\gamma(\gamma^4 - 4\gamma^2 - 1)}{\hbar\omega I_0 \sqrt{1+\gamma^2}} \right\} \end{aligned} \quad (\text{E4})$$

and

$$C = -\frac{\hbar\omega}{2(1+\gamma^2)I_0 b_4} \left\{ (1+2\gamma^2) - \frac{\tilde{A}(4\gamma^4 + 13\gamma^2 + 6)}{2I_0(1+\gamma^2)} + \frac{\tilde{A}^2\gamma(1+2\gamma^2)}{\hbar\omega I_0 \sqrt{1+\gamma^2}} \right\}. \quad (\text{E5})$$

(ii) If we assume that u_s depends on \vec{p} but $\cos \theta_{pF}$ does not depend on it ($\cos \theta_{pF} = 1$),

$$\begin{aligned} B = & \frac{\hbar\omega}{2I_0 b_4^2} \frac{\gamma^3}{(1+\gamma^2)^{3/2}} \left\{ 1 - \frac{3\tilde{A}}{2I_0(1+\gamma^2)} + \frac{\tilde{A}^2\gamma}{\hbar\omega I_0 \sqrt{1+\gamma^2}} \right\}^2 \\ & + \frac{\hbar\omega}{2I_0 b_4} \frac{\gamma}{(1+\gamma^2)^{3/2}} \left\{ (\gamma^2 - 2) + \frac{\tilde{A}(2\gamma^4 - 8\gamma^2 + 5)}{2I_0(1+\gamma^2)} + \frac{2\tilde{A}^2}{\hbar\omega I_0} \frac{\gamma(\gamma^2 - 1)}{\sqrt{1+\gamma^2}} \right\} \end{aligned} \quad (\text{E6})$$

and

$$C = -\frac{\hbar\omega\gamma^2}{2(1+\gamma^2)I_0b_4} \left\{ 1 - \frac{3\tilde{A}}{2I_0(1+\gamma^2)} + \frac{\tilde{A}^2\gamma}{\hbar\omega I_0\sqrt{1+\gamma^2}} \right\}. \quad (\text{E7})$$

(iii) If we assume that $\cos\theta_{pF}$ depends on \vec{p} but u_s does not depend on it ($u_s = i\gamma$),

$$B = -\frac{\hbar\omega\sqrt{1+\gamma^2}}{2\gamma I_0b_4} \left\{ 1 + \frac{\tilde{A}\gamma^2}{I_0(1+\gamma^2)} + \frac{\tilde{A}^2\gamma}{\hbar\omega I_0(1+\gamma^2)} - \frac{3\tilde{A}}{I_0\sqrt{1+\gamma^2}} \right\} \quad (\text{E8})$$

and

$$C = -\frac{\hbar\omega}{2I_0b_4} \left\{ 1 - \frac{\tilde{A}(2\gamma^2+3)}{I_0(1+\gamma^2)} + \frac{\tilde{A}^2\gamma}{\hbar\omega I_0\sqrt{1+\gamma^2}} \right\}. \quad (\text{E9})$$

(iv) If we assume that $\cos\theta_{pF}$ and u_s are \vec{p} -independent ($\cos\theta_{pF} = 1$ and $u_s = i\gamma$),

$$B = 0 \quad (\text{E10})$$

and

$$C = 0. \quad (\text{E11})$$

In Eqs. (E4)–(E9), b_4 is defined by

$$b_4 = -1 + \frac{\tilde{A}(2+\gamma^2)}{2I_0(1+\gamma^2)} - \frac{\tilde{A}^2\gamma}{2I_0\hbar\omega\sqrt{1+\gamma^2}}. \quad (\text{E12})$$

Appendix F

Let us consider the significant atomic orbitals of the atoms (carbon, oxygen, or nitrogen, etc.) contributing to the molecular orbitals ($1s, 2s, 2p_x, 2p_y, 2p_z, 3s, 3p_x, 3p_y, 3p_z$) usually found in organic species. The transition dipole matrix elements between the plane wave and the atom situated at \vec{R}_j from the center of mass of the molecule are given by

$$V_{0,1s}(\vec{p}, \vec{R}_j) = \varsigma_{1s,j} \frac{2\sqrt{2}\pi\hbar^3\sqrt{I_{1s}}}{m^{3/2}} \left\{ \frac{-2i\hbar(eF)p_z}{m(I_{1s} + p^2/2m)^3} + \frac{(e\vec{F} \cdot \vec{R}_j)}{(I_{1s} + p^2/2m)^2} \right\} \\ \times \exp(-i\vec{p} \cdot \vec{R}_j/\hbar) \quad (\text{F1})$$

for $1s$ orbital,

$$\begin{aligned}
& V_{0,2s}(\vec{p}, \vec{R}_j) \\
&= S_{2s,j} \frac{2\sqrt{2}\pi\hbar^3\sqrt{I_{2s}}}{m^{5/2}} \left\{ \frac{2i\hbar(eF)p_z(4mI_{2s} - p^2)}{m(I_{2s} + p^2/2m)^4} + \frac{(e\vec{F} \cdot \vec{R}_j)(p^2 - 2mI_{2s})}{(I_{2s} + p^2/2m)^3} \right\} \\
&\quad \times \exp(-i\vec{p} \cdot \vec{R}_j/\hbar) \tag{F2}
\end{aligned}$$

for 2s orbital,

$$\begin{aligned}
& V_{0,2pz}(\vec{p}, \vec{R}_j) \\
&= S_{2pz,j} \frac{4\sqrt{2}\pi\hbar^4\sqrt{I_{2pz}}}{m^{5/2}} \left\{ \frac{\hbar(eF)(2mI_{2pz} + p^2 - 6p_z^2)}{2m(I_{2pz} + p^2/2m)^4} - \frac{i(e\vec{F} \cdot \vec{R}_j)p_z}{(I_{2pz} + p^2/2m)^3} \right\} \\
&\quad \times \exp(-i\vec{p} \cdot \vec{R}_j/\hbar) \tag{F3}
\end{aligned}$$

for 2p_z orbital,

$$\begin{aligned}
V_{0,3s}(\vec{p}, \vec{R}_j) &= S_{3s,j} \frac{\sqrt{2}\pi\hbar^3\sqrt{I_{3s}}}{2m^{7/2}} \left\{ -\frac{2i\hbar(eF)p_z(11p^4 - 36mI_{3s}p^2 + 12m^2I_{3s}^2)}{m(I_{3s} + p^2/2m)^5} \right. \\
&\quad \left. + \frac{(e\vec{F} \cdot \vec{R}_j)(3p^4 - 20mI_{3s}p^2 + 12m^2I_{3s}^2)}{(I_{3s} + p^2/2m)^4} \right\} \exp(-i\vec{p} \cdot \vec{R}_j/\hbar) \tag{F4}
\end{aligned}$$

for 3s orbital,

$$\begin{aligned}
V_{0,3px}(\vec{p}, \vec{R}_j) &= S_{3px,j} \frac{12\sqrt{2}\pi\hbar^4\sqrt{I_{3px}p_x}}{m^{5/2}} \left\{ \frac{-\hbar eFp_z(-5I_{3px} + 3p^2/2m)}{m(I_{3px} + p^2/2m)^5} \right. \\
&\quad \left. + \frac{i(e\vec{F} \cdot \vec{R}_j)(I_{3px} - p^2/2m)}{(I_{3px} + p^2/2m)^4} \right\} \exp(-i\vec{p} \cdot \vec{R}_j/\hbar) \tag{F5}
\end{aligned}$$

for 3p_x orbital,

$$\begin{aligned}
V_{0,3pz}(\vec{p}, \vec{R}_j) &= S_{3pz,j} \frac{6\sqrt{2}\pi\hbar^4\sqrt{I_{3pz}}}{m^{7/2}} \left\{ \frac{\hbar(eF)(p^4 + 20mI_{3pz}p_z^2 - 6p_z^2p^2 - 4m^2I_{3pz}^2)}{2m(I_{3pz} + p^2/2m)^5} \right. \\
&\quad \left. - \frac{i(e\vec{F} \cdot \vec{R}_j)p_z(p^2 - 2mI_{3pz})}{(I_{3pz} + p^2/2m)^4} \right\} \exp(-i\vec{p} \cdot \vec{R}_j/\hbar) \tag{F6}
\end{aligned}$$

for 3p_z orbital.

For 2p_y and 3p_y orbitals, p_x in Eqs. (149) and (F5) should be replaced with p_y . It is important to note that the parts which have \vec{R}_j dependence and contribute to the exponential part of Eq. (168), $\exp(-i\vec{p} \cdot \vec{R}_j/\hbar)$, are common to all the transition dipole matrix elements and the parts $\vec{F} \cdot \vec{R}_j$

only contribute to the pre-exponential factor in the photoionization rate formula.

Appendix G

In this appendix, we show how to obtain $\bar{N}(\vec{p}, \vec{R}_j, AO(j); \{\vec{R}_k\})$ defined by Eq. (166). Equation (166) can be rewritten as

$$\begin{aligned} \bar{N}(\vec{p}, \vec{R}_j, AO(j); \{\vec{R}_k\}) &= \zeta_{AO(j),j} \oint du V_{1,AO(j)} \left(\vec{p} + \frac{\vec{e}\vec{F}}{\omega} u, \vec{R}_j \right) \\ &\quad \times \exp\{iM_0(u, \vec{p}; \{\vec{R}_k\})\}, \end{aligned} \quad (G1)$$

where

$$V_{1,AO(j)} \left(\vec{p} + \frac{\vec{e}\vec{F}}{\omega} u, \vec{R}_j \right) = V_{0,AO(j)} \left(\vec{p} + \frac{\vec{e}\vec{F}}{\omega} u, \vec{R}_j \right) / \zeta_{AO(j),j}. \quad (G2)$$

Rearranging the terms in the integral in Eq. (G1), we find

$$\begin{aligned} \bar{N}(\vec{p}, \vec{R}_j, AO(j); \{\vec{R}_k\}) &= \zeta_{AO(j),j} \oint du V_{2,AO(j)} \left(\vec{p} + \frac{\vec{e}\vec{F}}{\omega} u, \vec{R}_j \right) \\ &\quad \times \exp\{iM_1(u, \vec{p}, \vec{R}_j; \{\vec{R}_k\})\}, \end{aligned} \quad (G3)$$

where

$$V_{2,AO(j)} \left(\vec{p} + \frac{\vec{e}\vec{F}}{\omega} u, \vec{R}_j \right) = V_{1,AO(j)} \left(\vec{p} + \frac{\vec{e}\vec{F}}{\omega} u, \vec{R}_j \right) \exp(i\vec{e}u\vec{R}_j \cdot \vec{F}/\hbar\omega) \quad (G4)$$

and

$$M_1(u, \vec{p}, \vec{R}_j; \{\vec{R}_k\}) = \frac{1}{\hbar\omega} J(u, \vec{p}, \vec{R}_j; \{\vec{R}_k\}). \quad (G5)$$

Here,

$$J(u, \vec{p}, \vec{R}_j; \{\vec{R}_k\}) = J_{1,AO(j)}(u, \vec{p}) + J_{2,AO(j)}(u, \vec{p}, \vec{R}_j; \{\vec{R}_k\}), \quad (G6)$$

$$J_{1,AO(j)}(u, \vec{p}) = \int_0^u \frac{dv}{\sqrt{1-v^2}} \left\{ \frac{1}{2m} \left(\vec{p} + \frac{\vec{e}\vec{F}}{\omega} v \right)^2 + I_{AO(j)} \right\}, \quad (G7)$$

and

$$\begin{aligned} J_{2,AO(j)}(u, \vec{R}_j; \{\vec{R}_k\}) &= \int_0^u \frac{dv}{\sqrt{1-v^2}} \left[\tilde{J}'_0 - I_{AO(j)} - \frac{\vec{e}^2 F^2}{2m\omega^2} v^2 \right. \\ &\quad \left. + \{Y(\{\vec{R}_k\})\omega - \vec{e}\vec{R}_j \cdot \vec{F}\} \sqrt{1-v^2} \right. \\ &\quad \left. - \frac{F^2}{4m\omega^2} (E^2 + 4\hbar b e)(1-2v^2) \right]. \end{aligned} \quad (G8)$$

The singular points of Eq. (G3) $u_{s,AO(j)}$ are given by

$$u_{s,AO(j)} = \bar{\gamma}_{AO(j)} \left(i - \frac{p \cos \theta}{\sqrt{2mI_{AO(j)}}} + \frac{ip^2 \sin^2 \theta}{4mI_{AO(j)}} \right), \quad (\text{G9})$$

where θ is the angle between \vec{p} and \vec{F} .

Using the Taylor expansion for Eq. (G7), we obtain

$$J_{1,AO(j)}(u, \vec{p}) = \sum_{\substack{k=0 \\ k \neq 1}} \frac{1}{k!} J_{1,AO(j)}^{(k)}(u_{s,AO(j)}, \vec{p})(u - u_{s,AO(j)})^k, \quad (\text{G10})$$

where

$$\begin{aligned} J_{1,AO(j)}(u_{s,AO(j)}, \vec{p}) &= \left(I_{AO(j)} + \frac{\bar{e}^2 F^2}{4m\omega^2} + \frac{p^2}{2m} \right) \sin^{-1} u_{s,AO(j)} \\ &\quad + \frac{\bar{e}\vec{p} \cdot \vec{F}}{m\omega} \left(1 - \sqrt{1 - u_{s,AO(j)}^2} \right) \\ &\quad - \frac{\bar{e}^2 F^2}{4m\omega^2} u_{s,AO(j)} \sqrt{1 - u_{s,AO(j)}^2}, \end{aligned} \quad (\text{G11})$$

$$J'_{1,AO(j)}(u_{s,AO(j)}, \vec{p}) = 0, \quad (\text{G12})$$

$$J''_{1,AO(j)}(u_{s,AO(j)}, \vec{p}) = \frac{1}{\sqrt{1 - u_{s,AO(j)}^2}} \frac{\bar{e}\vec{F}}{m\omega} \cdot \left(\vec{p} + \frac{\bar{e}\vec{F}}{\omega} u_{s,AO(j)} \right), \quad (\text{G13})$$

$$\begin{aligned} J'''_{1,AO(j)}(u_{s,AO(j)}, \vec{p}) &= \frac{1}{m} \left(\frac{\bar{e}F}{\omega} \right)^2 \frac{1}{\sqrt{1 - u_{s,AO(j)}^2}} \\ &\quad + 2 \frac{\bar{e}\vec{F}}{m\omega} \cdot \left(\vec{p} + \frac{\bar{e}\vec{F}}{\omega} u_{s,AO(j)} \right) \frac{u_{s,AO(j)}}{(1 - u_{s,AO(j)}^2)^{3/2}}, \end{aligned} \quad (\text{G14})$$

and

$$\begin{aligned} J^{(4)}_{1,AO(j)}(u_{s,AO(j)}, \vec{p}) &= \frac{3}{m} \left(\frac{\bar{e}F}{\omega} \right)^2 \frac{u_{s,AO(j)}}{(1 - u_{s,AO(j)}^2)^{3/2}} \\ &\quad + 3 \frac{\bar{e}\vec{F}}{m\omega} \cdot \left(\vec{p} + \frac{\bar{e}\vec{F}}{\omega} u_{s,AO(j)} \right) \frac{1 + 2u_{s,AO(j)}^2}{(1 - u_{s,AO(j)}^2)^{5/2}}. \end{aligned} \quad (\text{G15})$$

In the same way, we expand Eq. (G8) in Taylor series:

$$J_{2,AO(j)}(u, \vec{R}_j; \{\vec{R}_k\}) = \sum_{l=0} \frac{1}{l!} J_{2,AO(j)}^{(l)}(u_{s,AO(j)}, \vec{R}_j; \{\vec{R}_k\})(u - u_{s,AO(j)})^l, \quad (\text{G16})$$

where

$$J_{2,AO(j)}(u_{s,AO(j)}, \vec{R}_j; \{\vec{R}_k\}) = \left(\tilde{I}'_0 - I_{AO(j)} - \frac{\bar{e}F^2}{4m\omega^2} \right) \sin^{-1} u_{s,AO(j)} \\ - \frac{\hbar b e F^2}{2m\omega^2} u_{s,AO(j)} \sqrt{1 - u_{s,AO(j)}^2} \\ + Y(\{\vec{R}_k\})\omega - \bar{e}\vec{R}_j \cdot \vec{F}, \quad (G17)$$

$$J'_{2,AO(j)}(u_{s,AO(j)}, \vec{R}_j; \{\vec{R}_k\}) \\ = \left(\tilde{I}'_0 - I_{AO(j)} - \frac{\bar{e}F^2}{4m\omega^2} \right) \frac{1}{\sqrt{1 - u_{s,AO(j)}^2}} \\ - \frac{\hbar b e F^2}{2m\omega^2} \frac{1 - 2u_{s,AO(j)}^2}{\sqrt{1 - u_{s,AO(j)}^2}} + Y(\{\vec{R}_k\})\omega - \bar{e}\vec{R}_j \cdot \vec{F}, \quad (G18)$$

$$J''_{2,AO(j)}(u_{s,AO(j)}, \vec{R}_j; \{\vec{R}_k\}) = \left(\tilde{I}'_0 - I_{AO(j)} - \frac{\bar{e}F^2}{4m\omega^2} \right) \frac{u_{s,AO(j)}}{(1 - u_{s,AO(j)}^2)^{3/2}} \\ - \frac{\hbar b e F^2}{2m\omega^2} \frac{u_{s,AO(j)}(2u_{s,AO(j)}^2 - 3)}{(1 - u_{s,AO(j)}^2)^{3/2}}, \quad (G19)$$

$$J'''_{2,AO(j)}(u_{s,AO(j)}, \vec{R}_j; \{\vec{R}_k\}) = \left(\tilde{I}'_0 - I_{AO(j)} - \frac{\bar{e}F^2}{4m\omega^2} \right) \frac{2u_{s,AO(j)}^2 + 1}{(1 - u_{s,AO(j)}^2)^{5/2}} \\ + \frac{3\hbar b e F^2}{2m\omega^2} \frac{1}{(1 - u_{s,AO(j)}^2)^{5/2}}, \quad (G20)$$

$$J^{(4)}_{2,AO(j)}(u_{s,AO(j)}, \vec{R}_j; \{\vec{R}_k\}) = 3 \left(\tilde{I}'_0 - I_{AO(j)} - \frac{\bar{e}F^2}{4m\omega^2} \right) \frac{u_{s,AO(j)}(2u_{s,AO(j)}^2 + 3)}{(1 - u_{s,AO(j)}^2)^{7/2}} \\ + \frac{15\hbar b e F^2}{2m\omega^2} \frac{u_{s,AO(j)}}{(1 - u_{s,AO(j)}^2)^{7/2}}. \quad (G21)$$

Therefore, we have

$$\begin{aligned}
\bar{N}(\vec{p}, \vec{R}_j, AO(j); \{\vec{R}_k\}) &= \zeta_{AO(j),j} \exp \left[\frac{i}{\hbar\omega} K_{0,AO(j)}(u_{s,AO(j)}, \vec{p}, \vec{R}_j; \{\vec{R}_k\}) \right] \\
&\times \oint du V_{2,AO(j)} \left(\vec{p} + \frac{\vec{e}\vec{F}}{\omega} u, \vec{R}_j \right) \\
&\times \exp \left\{ \frac{i}{\hbar\omega} \sum_{l=1} \frac{1}{l!} K_{l,AO(j)}(u_{s,AO(j)}, \vec{p}, \vec{R}_j; \{\vec{R}_k\}) (u - u_{s,AO(j)})^l \right\}, \quad (G22)
\end{aligned}$$

where we define

$$\begin{aligned}
K_{l,AO(j)}(u_{s,AO(j)}, \vec{p}, \vec{R}_j; \{\vec{R}_k\}) &= J_{1,AO(j)}^{(l)}(u_{s,AO(j)}, \vec{p}) \\
&+ J_{2,AO(j)}^{(l)}(u_{s,AO(j)}, \vec{R}_j; \{\vec{R}_k\}) \quad \text{for } l = 0, 2, 3, 4, \dots
\end{aligned}$$

Otherwise,

$$K_{1,AO(j)}(u_{s,AO(j)}, \vec{p}, \vec{R}_j; \{\vec{R}_k\}) = J'_{2,AO(j)}(u_{s,AO(j)}, \vec{R}_j; \{\vec{R}_k\}). \quad (G23)$$

Expanding the exponential factor in the contour integral over u in Eq. (G22) using Eq. (G11) and using the residue theorem at the same time, we have

$$\begin{aligned}
\bar{N}(\vec{p}, \vec{R}_j, AO(j); \{\vec{R}_k\}) &= \zeta_{AO(j),j} C(u_{s,AO(j)}, \vec{p}, \vec{R}_j, AO(j); \{\vec{R}_k\}) \\
&\times \exp \left\{ \frac{i}{\hbar\omega} K_{0,AO(j)}(u_{s,AO(j)}, \vec{p}, \vec{R}_j; \{\vec{R}_k\}) \right\}. \quad (G24)
\end{aligned}$$

For example, for $2p_x$ orbital, we have

$$\begin{aligned}
C(u_{s,2p_x}, \vec{p}, \vec{R}_j, 2p_x; \{\vec{R}_k\}) &= -\frac{3\sqrt{2}\pi i e \hbar^5 \omega^4}{m^{3/2} \bar{e}^4 F^3 I_{2p_x}^{3/2}} \exp \left(-i \frac{\vec{p} \cdot \vec{R}_j}{\hbar} \right) p \sin \theta \cos \phi \\
&\times \left[\left\{ i K_{2,AO(j)}(u_{s,AO(j)}, \vec{p}, \vec{R}_j; \{\vec{R}_k\}) \right. \right. \\
&\quad \left. \left. - \frac{1}{\hbar\omega} K_{1,AO(j)}(u_{s,AO(j)}, \vec{p}, \vec{R}_j; \{\vec{R}_k\})^2 \right\} \frac{\vec{e}\vec{F}}{2\hbar\omega^2} \right. \\
&\quad \left. + \left\{ \frac{i}{6\hbar\omega} K_{3,AO(j)}(u_{s,AO(j)}, \vec{p}, \vec{R}_j; \{\vec{R}_k\}) \right. \right. \\
&\quad \left. \left. - \frac{1}{2\hbar^2\omega^2} J'_{2,AO(j)}(u_{s,AO(j)}, \vec{R}_j; \{\vec{R}_k\}) \right. \right.
\end{aligned}$$

$$\begin{aligned}
& \times K_{2,AO(j)}(u_{s,AO(j)}, \vec{p}, \vec{R}_j; \{\vec{R}_k\}) \\
& - \frac{i}{6\hbar^3\omega^3} K_{1,AO(j)}(u_{s,AO(j)}, \vec{p}, \vec{R}_j; \{\vec{R}_k\})^3 \Big\} \\
& \times \left(p \cos \theta + \frac{\vec{e}\vec{F}}{\omega} u_{s,AO(j)} \right) \Big] \\
& + \frac{2\pi i \hbar^4 \omega^3 (\vec{e}\vec{F} \cdot \vec{R}_j)}{m\bar{e}^3 F^3 I_{2px}} \exp\left(-i \frac{\vec{p} \cdot \vec{R}_j}{\hbar}\right) p \sin \theta \cos \phi \\
& \times \left\{ \frac{i}{2\hbar\omega} K_{2,AO(j)}(u_{s,AO(j)}, \vec{p}, \vec{R}_j; \{\vec{R}_k\}) \right. \\
& \left. - \frac{1}{2\hbar^2\omega^2} K_{1,AO(j)}(u_{s,AO(j)}, \vec{p}, \vec{R}_j; \{\vec{R}_k\})^2 \right\}. \tag{G25}
\end{aligned}$$

For orbitals other than $2p_x$, the derivation is straightforward. From here, we assume that the atomic orbitals of interest are $2p_x$ and $3p_x$ orbitals. Substituting Eq. (G9) into Eq. (G25), from Eq. (G24), we obtain

$$\begin{aligned}
\bar{N}(\vec{p}, \vec{R}_j, AO(j); \{\vec{R}_k\}) &= \zeta_{AO(j),j} p \sin \theta \cos \phi \exp\left(-i \frac{\vec{p} \cdot \vec{R}_j}{\hbar}\right) \\
& \times [U_{1,AO(j)}(\vec{F} \cdot \vec{R}_j; \{\vec{R}_k\}) + iU_{2,AO(j)}(\vec{F} \cdot \vec{R}_j; \{\vec{R}_k\}) p \cos \theta \\
& + U_{3,AO(j)}(\vec{F} \cdot \vec{R}_j; \{\vec{R}_k\}) p^2 \\
& \times U_{4,AO(j)}(\vec{F} \cdot \vec{R}_j; \{\vec{R}_k\}) p^2 \cos^2 \theta] \\
& \times \exp\left\{ \frac{i}{\hbar\omega} K_{0,AO(j)}(u_{s,AO(j)}, \vec{p}, \vec{R}_j; \{\vec{R}_k\}) \right\}, \tag{G26}
\end{aligned}$$

where $U_{l,AO(j)}(\vec{F} \cdot \vec{R}_j; \{\vec{R}_k\})$ ($l = 1, 2, 3, 4$) are real. Using Eqs. (G9) and (G23) into Eq. (G26), we obtain

$$\begin{aligned}
\bar{N}(\vec{p}, \vec{R}_j, AO(j); \{\vec{R}_k\}) &= i\zeta_{AO(j),j} U_{1,AO(j)}(\vec{F} \cdot \vec{R}_j; \{\vec{R}_k\}) p \sin \theta \cos \phi \\
& \times \exp\left(-i \frac{\vec{p} \cdot \vec{R}_j}{\hbar}\right) \exp\left[\frac{i}{\hbar\omega} W_{1,AO(j)}(\vec{F} \cdot \vec{R}_j; \{\vec{R}_k\}) p \cos \theta \right. \\
& - \frac{1}{\hbar\omega} \{W_{2,AO(j)}(\vec{F} \cdot \vec{R}_j; \{\vec{R}_k\}) \\
& + W_{3,AO(j)}(\vec{F} \cdot \vec{R}_j; \{\vec{R}_k\}) p^2 \\
& \left. + W_{4,AO(j)}(\vec{F} \cdot \vec{R}_j; \{\vec{R}_k\}) p^2 \cos^2 \theta\} \right], \tag{G27}
\end{aligned}$$

where

$$\begin{aligned}
W_{1,AO(j)}(\vec{F} \cdot \vec{R}_j; \{\vec{R}_k\}) &= \hbar\omega \frac{U_2(\vec{F} \cdot \vec{R}_j; \{\vec{R}_k\})}{U_1(\vec{F} \cdot \vec{R}_j; \{\vec{R}_k\})} - \tilde{I}'_0 \frac{\omega}{\tilde{e}F\sqrt{1 + \tilde{\gamma}_{AO(j)}^2}} \\
&\quad - 2Y_3(\{\vec{R}_k\})\omega\tilde{\gamma}_{AO(j)} \\
&\quad \times \frac{2\tilde{\gamma}_{AO(j)}^2 + 1}{\sqrt{2mI_{AO(j)}(1 + \tilde{\gamma}_{AO(j)}^2)}} + \frac{\tilde{e}F}{m\omega} \left(1 - \sqrt{1 + \tilde{\gamma}_{AO(j)}^2}\right) \\
&\quad - \{Y(\{\vec{R}_k\})\omega - \tilde{e}\vec{F} \cdot \vec{R}_j\} \frac{\tilde{\gamma}_{AO(j)}}{\sqrt{2mI_{AO(j)}}}, \tag{G28}
\end{aligned}$$

$$\begin{aligned}
W_{2,AO(j)}(\vec{F} \cdot \vec{R}_j; \{\vec{R}_k\}) &= \tilde{I}'_0 \sinh^{-1} \tilde{\gamma}_{AO(j)} + 2Y_3(\{\vec{R}_k\})\omega\tilde{\gamma}_{AO(j)}\sqrt{1 + \tilde{\gamma}_{AO(j)}^2} \\
&\quad + \{Y(\{\vec{R}_k\})\omega - \tilde{e}\vec{F} \cdot \vec{R}_j\}\tilde{\gamma}_{AO(j)}, \tag{G29}
\end{aligned}$$

$$\begin{aligned}
W_{3,AO(j)}(\vec{F} \cdot \vec{R}_j; \{\vec{R}_k\}) &= -\hbar\omega \frac{U_3(\vec{F} \cdot \vec{R}_j; \{\vec{R}_k\})}{U_1(\vec{F} \cdot \vec{R}_j; \{\vec{R}_k\})} + \tilde{I}'_0 \frac{\tilde{\gamma}_{AO(j)}}{4mI_{AO(j)}\sqrt{1 + \tilde{\gamma}_{AO(j)}^2}} \\
&\quad + \frac{1}{2m} \sinh^{-1} \tilde{\gamma}_{AO(j)} \\
&\quad + Y_3(\{\vec{R}_k\})\omega\tilde{\gamma}_{AO(j)} \frac{2\tilde{\gamma}_{AO(j)}^2 + 1}{2mI_{AO(j)}\sqrt{1 + \tilde{\gamma}_{AO(j)}^2}} \\
&\quad + \{Y(\{\vec{R}_k\})\omega - \tilde{e}\vec{F} \cdot \vec{R}_j\} \frac{\tilde{\gamma}_{AO(j)}}{4mI_{AO(j)}}, \tag{G30}
\end{aligned}$$

and

$$\begin{aligned}
W_{4,AO(j)}(\vec{F} \cdot \vec{R}_j; \{\vec{R}_k\}) &= -\hbar\omega \left\{ \frac{U_4(\vec{F} \cdot \vec{R}_j; \{\vec{R}_k\})}{U_1(\vec{F} \cdot \vec{R}_j; \{\vec{R}_k\})} + \frac{1}{2} \frac{U_2(\vec{F} \cdot \vec{R}_j; \{\vec{R}_k\})^2}{U_1(\vec{F} \cdot \vec{R}_j; \{\vec{R}_k\})^2} \right\} \\
&\quad - \tilde{I}'_0 \frac{\tilde{\gamma}_{AO(j)}}{4mI_{AO(j)}(1 + \tilde{\gamma}_{AO(j)}^2)^{3/2}} \\
&\quad - Y_3(\{\vec{R}_k\})\omega\tilde{\gamma}_{AO(j)} \frac{4\tilde{\gamma}_{AO(j)}^4 + 6\tilde{\gamma}_{AO(j)}^2 + 1}{2mI_{AO(j)}(1 + \tilde{\gamma}_{AO(j)}^2)^{3/2}} - \frac{\tilde{e}F}{m\omega} \\
&\quad + \{Y(\{\vec{R}_k\})\omega - \tilde{e}\vec{F} \cdot \vec{R}_j\} \frac{\tilde{\gamma}_{AO(j)}}{4mI_{AO(j)}}, \tag{G31}
\end{aligned}$$

where

$$Y_3(\{\vec{R}_k\}) = -\frac{E^2 F^2}{8m\omega^3} - \frac{\hbar b e F^2}{2m\omega^3}. \quad (\text{G32})$$

Note that $W_{i, AO(j)}(\vec{F} \cdot \vec{R}_j; \{\vec{R}_k\})$ ($i = 1-4$) are real.

Appendix H

Substituting Eq. (165) into Eq. (162), we find

$$\begin{aligned} w_0 = & \sum_{j=1}^N \sum_{AO(j)} \bar{N}_1(\vec{R}_j, AO(j); \{\vec{R}_k\}) \\ & + \sum_{j \geq k=1}^N \sum_{AO(j) \geq AO(k)} \bar{N}'_2(\vec{R}_j, AO(j), \vec{R}_k, AO(k); \{\vec{R}_l\}) \end{aligned} \quad (\text{H1})$$

where

$$\begin{aligned} & \bar{N}_1(\vec{R}_j, AO(j); \{\vec{R}_k\}) \\ & = \frac{2\pi}{\hbar} \int \frac{d^3 p}{(2\pi\hbar)^3} |\bar{N}(\vec{p}, \vec{R}_j, AO(j); \{\vec{R}_k\})|^2 \sum_{n=-\infty}^{\infty} \delta\left(\tilde{I}'_0 + \frac{p^2}{2m} - n\hbar\omega\right), \end{aligned} \quad (\text{H2})$$

and

$$\begin{aligned} & \bar{N}'_2(\vec{R}_j, AO(j), \vec{R}_k, AO(k); \{\vec{R}_l\}) \\ & = \frac{2\pi}{\hbar} \int \frac{d^3 p}{(2\pi\hbar)^3} 2 \operatorname{Re} \{ \bar{N}(\vec{p}, \vec{R}_j, AO(j); \{\vec{R}_l\}) \bar{N}(\vec{p}, \vec{R}_k, AO(k); \{\vec{R}_l\})^* \} \\ & \quad \times \sum_{n=-\infty}^{\infty} \delta\left(\tilde{I}'_0 + \frac{p^2}{2m} - n\hbar\omega\right). \end{aligned} \quad (\text{H3})$$

In Eq. (H1), the prime on the second term of the right hand side indicates that the case where the case $j = k$ and $AO(j) = AO(k)$ is excluded from the summation. From Eq. (H1), we can readily see that the total molecular photoionization rate w_0 consists of two parts. The one is the summation of photoionization rates of each atom and each atomic orbital of the atoms forming the molecule: the first term on the right hand side of Eq. (H1). The other one is the summation of the quantum interference terms of all possible combinations of the transition amplitudes of the atoms and atomic orbitals forming the molecule: the second term of the right hand side of Eq. (H1).

Let us derive $\bar{N}_1(\bar{R}_j, AO(j); \{\bar{R}_k\})$ of Eq. (H2). Substituting Eq. (G27) into Eq. (H2), we obtain

$$\begin{aligned}
& \bar{N}_1(\bar{R}_j, AO(j); \{\bar{R}_k\}) \\
&= \frac{2\pi}{\hbar} |\zeta_{AO(j),j}|^2 U_{1,AO(j)}(\vec{F} \cdot \bar{R}_j; \{\bar{R}_k\})^2 \exp \left\{ -\frac{2}{\hbar\omega} W_{2,AO(j)}(\vec{F} \cdot \bar{R}_j; \{\bar{R}_k\}) \right\} \\
&\quad \times \int \frac{d^3p}{(2\pi\hbar)^3} p^2 \sin^2 \theta \cos^2 \phi \exp \left[-\frac{2}{\hbar\omega} \{ W_{3,AO(j)}(\vec{F} \cdot \bar{R}_j; \{\bar{R}_k\}) p^2 \right. \\
&\quad \left. + W_{4,AO(j)}(\vec{F} \cdot \bar{R}_j; \{\bar{R}_k\}) p^2 \cos^2 \theta \right] \\
&\quad \times \sum_{n=-\infty}^{\infty} \delta \left(\tilde{I}'_0 + \frac{p^2}{2m} - n\hbar\omega \right). \tag{H4}
\end{aligned}$$

Carrying out the integration over \vec{p} and changing the summation over n into the integration over n , we obtain

$$\begin{aligned}
\bar{N}_1(\bar{R}_j, AO(j); \{\bar{R}_k\}) &= |\zeta_{AO(j),j}|^2 s(\vec{F} \cdot \bar{R}_j, AO(j); \{\bar{R}_k\}) \\
&\quad \times \exp \left\{ -\frac{2}{\hbar\omega} W_{2,AO(j)}(\vec{F} \cdot \bar{R}_j; \{\bar{R}_k\}) \right\}, \tag{H5}
\end{aligned}$$

where

$$\begin{aligned}
& s(\vec{F} \cdot \bar{R}_j, AO(j); \{\bar{R}_k\}) \\
&= \frac{\omega^{3/2}}{2^{11/2} \sqrt{\pi} \hbar^{5/2}} U_{1,AO(j)}(\vec{F} \cdot \bar{R}_j; \{\bar{R}_k\})^2 W_{3,AO(j)}(\vec{F} \cdot \bar{R}_j; \{\bar{R}_k\})^{-2} \\
&\quad \times \{ W_{3,AO(j)}(\vec{F} \cdot \bar{R}_j; \{\bar{R}_k\}) + W_{4,AO(j)}(\vec{F} \cdot \bar{R}_j; \{\bar{R}_k\}) \}^{-1/2}. \tag{H6}
\end{aligned}$$

Next, let us derive $\bar{N}_2(\bar{R}_j, AO(j), \bar{R}_k, AO(k); \{\bar{R}_l\})$ of Eq. (H1) (quantum interference term between the atomic orbital $AO(j)$ of the j -th atom and the atomic orbital $AO(k)$ of the k -th atom). Substituting Eq. (G27) into Eq. (H3), we find

$$\begin{aligned}
& \bar{N}_2(\bar{R}_j, AO(j), \bar{R}_k, AO(k); \{\bar{R}_l\}) \\
&= 2 \operatorname{Re} \frac{2\pi}{\hbar} \zeta_{AO(j),j} \zeta_{AO(k),k}^* U_{1,AO(j)}(\vec{F} \cdot \bar{R}_j; \{\bar{R}_l\}) U_{1,AO(k)}(\vec{F} \cdot \bar{R}_k; \{\bar{R}_l\}) \\
&\quad \times \exp \left\{ -\frac{1}{\hbar\omega} \bar{W}_{2,AO(j),AO(k)}(\vec{F} \cdot \bar{R}_j, \vec{F} \cdot \bar{R}_k; \{\bar{R}_l\}) \right\} \\
&\quad \times \int \frac{d^3p}{(2\pi\hbar)^3} p^2 \sin^2 \theta \cos^2 \phi \exp \left\{ -i \frac{\vec{p} \cdot (\bar{R}_j - \bar{R}_k)}{\hbar} \right\}
\end{aligned}$$

$$\begin{aligned}
& \times \exp \left[\frac{i}{\hbar\omega} \bar{W}_{1,AO(j),AO(k)}(\vec{F} \cdot \vec{R}_j, \vec{F} \cdot \vec{R}_k; \{\vec{R}_l\}) p \cos \theta \right. \\
& - \frac{1}{\hbar\omega} \{ \bar{W}_{3,AO(j),AO(k)}(\vec{F} \cdot \vec{R}_j, \vec{F} \cdot \vec{R}_k; \{\vec{R}_l\}) p^2 \\
& \left. + \bar{W}_{4,AO(j),AO(k)}(\vec{F} \cdot \vec{R}_j, \vec{F} \cdot \vec{R}_k; \{\vec{R}_l\}) p^2 \cos^2 \theta \right] \sum_{n=-\infty}^{\infty} \delta \left(\tilde{I}'_0 + \frac{p^2}{2m} - n\hbar\omega \right), \tag{H7}
\end{aligned}$$

where

$$\begin{aligned}
& \bar{W}_{1,AO(j),AO(k)}(\vec{F} \cdot \vec{R}_j, \vec{F} \cdot \vec{R}_k; \{\vec{R}_l\}) \\
& = W_{1,AO(j)}(\vec{F} \cdot \vec{R}_j; \{\vec{R}_l\}) - W_{1,AO(k)}(\vec{F} \cdot \vec{R}_k; \{\vec{R}_l\}), \tag{H8}
\end{aligned}$$

and

$$\begin{aligned}
& \bar{W}_{i,AO(j),AO(k)}(\vec{F} \cdot \vec{R}_j, \vec{F} \cdot \vec{R}_k; \{\vec{R}_l\}) = W_{i,AO(j)}(\vec{F} \cdot \vec{R}_j; \{\vec{R}_l\}) \\
& + W_{i,AO(k)}(\vec{F} \cdot \vec{R}_k; \{\vec{R}_l\}) \quad \text{for } i = 2, 3, 4. \tag{H9}
\end{aligned}$$

Integrating over p and changing the summation over n into the integration over n in Eq. (H7), we obtain

$$\begin{aligned}
& \bar{N}_2(\vec{R}_j, AO(j), \vec{R}_k, AO(k); \{\vec{R}_l\}) \\
& = \text{Re} \left\{ \zeta_{AO(j),j} \zeta_{AO(k),k}^* \bar{U}_{AO(j),AO(k)}(\vec{F} \cdot \vec{R}_j, \vec{F} \cdot \vec{R}_k; \{\vec{R}_l\}) \right\} \\
& \times \exp \left\{ -\frac{1}{\hbar\omega} \bar{W}_{2,AO(j),AO(k)}(\vec{F} \cdot \vec{R}_j, \vec{F} \cdot \vec{R}_k; \{\vec{R}_l\}) \right\}, \tag{H10}
\end{aligned}$$

where

$$\bar{U}_{AO(j),AO(k)}(\vec{F} \cdot \vec{R}_j, \vec{F} \cdot \vec{R}_k; \{\vec{R}_l\}) = \frac{\sqrt{2m}^{5/2} \omega^{3/2}}{\pi^{3/2} \hbar^{5/2}} \int d\theta d\phi d \sin^3 \theta \cos^2 \phi G(\theta, \phi). \tag{H11}$$

Here, we define

$$G(\theta, \phi) = \left\{ \frac{f_1(\theta, \phi)^4}{16f_2(\theta)^{9/2}} - \frac{3f_1(\theta, \phi)^2}{4f_2(\theta)^{7/2}} + \frac{3}{4f_2(\theta)^{5/2}} \right\} \exp \left\{ -\frac{f_1(\theta, \phi)^2}{4f_2(\theta)} \right\}, \tag{H12}$$

where

$$\begin{aligned}
f_1(\theta, \phi) & = -\sqrt{\frac{2m\omega}{\hbar}} \{ (R_j^x - R_k^x) \sin \theta \cos \phi \\
& + (R_j^y - R_k^y) \sin \theta \sin \phi + (R_j^z - R_k^z) \cos \theta \} \\
& + \sqrt{\frac{2m}{\hbar\omega}} \bar{W}_{1,AO(j),AO(k)}(\vec{F} \cdot \vec{R}_j, \vec{F} \cdot \vec{R}_k; \{\vec{R}_l\}) \cos \theta, \tag{H13}
\end{aligned}$$

and

$$f_2(\theta) = 2m \{ \bar{W}_{3,AO(j),AO(k)}(\vec{F} \cdot \vec{R}_j, \vec{F} \cdot \vec{R}_k; \{\vec{R}_l\}) + \bar{W}_{4,AO(j),AO(k)}(\vec{F} \cdot \vec{R}_j, \vec{F} \cdot \vec{R}_k; \{\vec{R}_l\}) \cos^2 \theta \}. \quad (\text{H14})$$

The integration over the electron momentum directions θ and ϕ in Eq. (H11) can be performed numerically.

If the \vec{p} -dependence of the pre-exponential factors is to be used, we can set $U_{l,AO(j)}(\vec{F} \cdot \vec{R}_j; \{\vec{R}_k\}) = 0$ except for the case $l = 1$, which we have assumed in the present calculation.

Appendix I. Derivation of the Quantum Interference Terms

The quantum interference terms are derived as follows: from Eq. (193), we obtain

$$\begin{aligned} w_{av \rightarrow pv', C}^{j,1s,j',1s} &= \frac{4\pi}{\hbar} \text{Re} \left[b_{j,1s}^* b_{j',1s} C_{1s}^* C_{1s} D_{j,1s}^*(I_{av,pv'}) D_{j',1s}(I_{av,pv'}) |\langle \Theta_{pv'} | \Theta_{av} \rangle|^2 \right. \\ &\times \exp \{ -g_{j,1s}^{(1)}(I_{av,pv'}, \vec{R}_j) - g_{j',1s}^{(1)}(I_{av,pv'}, \vec{R}_{j'}) \} \\ &\times \int \frac{d^3 p}{(2\pi\hbar)^3} \exp \left[\frac{i}{\hbar} (\vec{R}_j - \vec{R}_{j'}) \cdot \vec{p} - i \{ g_{j,1s}^{(2)}(I_{av,pv'}) \right. \\ &- g_{j',1s}^{(2)}(I_{av,pv'}) \} p \cos \theta_p - \{ g_{j,1s}^{(3)}(I_{av,pv'}) + g_{j',1s}^{(3)}(I_{av,pv'}) \} p^2 \\ &- \left. \{ g_{j,1s}^{(4)}(I_{av,pv'}) + g_{j',1s}^{(4)}(I_{av,pv'}) \} p^2 \cos^2 \theta_p \right] \\ &\times \sum_{n=-\infty}^{\infty} \delta \left(\tilde{I}_{av,pv'} + \frac{p^2}{2m} - n\hbar\omega \right) \Bigg], \quad (\text{I1}) \end{aligned}$$

where

$$\begin{aligned} g_{j,1s}^{(2)}(I_{av,pv'}) &= \frac{1}{\hbar\omega} \left\{ \frac{eF}{m\omega} (1 - \sqrt{1 + \gamma_{1s}^2}) - (I_{av,pv'} - I_{1s}) \frac{\gamma_{1s}}{\sqrt{2mI_{1s}} \sqrt{1 + \gamma_{1s}^2}} \right. \\ &+ \left. \frac{e\vec{F} \cdot \vec{R}_j \gamma_{1s}}{\sqrt{2mI_{1s}}} \right\}, \quad (\text{I2}) \end{aligned}$$

$$g_{j,1s}^{(3)}(I_{av,pv'}) = \frac{1}{2m\hbar\omega} \left\{ \sinh^{-1} \gamma_{1s} + \frac{I_{av,pv'} - I_{1s}}{2I_{1s}} \frac{\gamma_{1s}}{\sqrt{1 + \gamma_{1s}^2}} - \frac{e\vec{F} \cdot \vec{R}_j \gamma_{1s}}{2I_{1s}} \right\}, \quad (\text{I3})$$

$$g_{j,1s}^{(4)}(I_{av,pv'}) = \frac{1}{2m\hbar\omega} \left\{ -\frac{\gamma_{1s}}{\sqrt{1 + \gamma_{1s}^2}} - \frac{I_{av,pv'} - I_{1s}}{2I_{1s}} \frac{\gamma_{1s}}{(1 + \gamma_{1s}^2)^{3/2}} + \frac{e\vec{F} \cdot \vec{R}_j \gamma_{1s}}{2I_{1s}} \right\}, \quad (\text{I4})$$

and

$$C_{1s} = -\frac{2\sqrt{\pi}(2mI_{1s})^{5/4}\hbar^{3/2}\omega^2}{me^2F^2}. \quad (I5)$$

Integrating over p , we finally obtain the general quantum interference terms for the homonuclear diatomic molecules consisting of only 1s atomic orbitals:

$$\begin{aligned} w_{av \rightarrow pv', C}^{j, 1s, j', 1s} &= -\sqrt{\frac{\omega I_{1s}}{\pi \hbar}} \gamma_{1s}^4 b_{j, 1s} b_{j', 1s} D_{j, 1s, C}(I_{av, pv'}) D_{j', 1s, C}(I_{av, pv'}) \left| \langle \Theta_{pv'} | \Theta_{av} \rangle \right|^2 \\ &\times \exp\left\{-g_{j, 1s, C}^{(1)}(I_{av, pv'}, \vec{R}_j) - g_{j', 1s, C}^{(1)}(I_{av, pv'}, \vec{R}_{j'})\right\} \\ &\times \int d\Omega_{\vec{p}} \frac{J_{j, 1s, j', 1s}^2(I_{av, pv'}, \hat{\vec{p}}) - 2G_{1s, 1s}(I_{av, pv'}, \theta_p)}{G_{1s, 1s}^{5/2}(I_{av, pv'}, \theta_p)} \\ &\times \exp\left\{-\frac{J_{j, 1s, j', 1s}^2(I_{av, pv'}, \hat{\vec{p}})}{4G_{1s, 1s}(I_{av, pv'}, \theta_p)}\right\}, \end{aligned} \quad (I6)$$

where

$$j = 1 \quad \text{and} \quad j' = 2, \quad \text{or} \quad j = 2 \quad \text{and} \quad j' = 1, \quad (I7)$$

$$\begin{aligned} G_{1s, 1s}(I_{av, pv'}, \theta_p) &= 2m\hbar\omega \left[g_{j, 1s}^{(3)}(I_{av, pv'}) + g_{j', 1s}^{(3)}(I_{av, pv'}) \right. \\ &\quad \left. + \{g_{j, 1s}^{(4)}(I_{av, pv'}) + g_{j', 1s}^{(4)}(I_{av, pv'})\} \cos^2 \theta_p \right], \end{aligned} \quad (I8)$$

$$\begin{aligned} J_{j, 1s, j', 1s}(I_{av, pv'}, \hat{\vec{p}}) &= \sqrt{\frac{2m\omega}{\hbar}} (\vec{R}_j - \vec{R}_{j'}) \cdot \hat{\vec{p}} + \cos \theta_p \{K_{j, 1s}(I_{av, pv'}) \\ &\quad - K_{j', 1s}(I_{av, pv'})\}, \end{aligned} \quad (I9)$$

and

$$K_{j, 1s}(I_{av, pv'}) = \frac{\gamma_{1s}}{\sqrt{\hbar\omega I_{1s}}} \left(\frac{I_{av, pv'} - I_{1s}}{\sqrt{1 + \gamma_{1s}^2}} - e\vec{F} \cdot \vec{R}_j \right), \quad (I10)$$

and $\hat{\vec{p}}$ is the unit vector defined by \vec{p} . In this derivation, we have used the fact that $b_{j, 1s}$, C_{1s} , and $D_{j, 1s, C}(I_{av, pv'})$ are real. It is clear from Eqs. (I8)–(I10) that the quantum interference terms arise from the two-center geometry of the nuclear field: only two different j -th and j' -th atoms contribute to each quantum interference term $w_{av \rightarrow pv', C}^{j, 1s, j', 1s}$. In particular, $J_{j, 1s, j', 1s}(I_{av, pv'}, \hat{\vec{p}})$ depends on the distance between j -th and j' -th atoms while $G_{1s, 1s}(I_{av, pv'}, \theta_p)$ on the sum of the distances between j -th and j' -th atoms from the molecular center.

Because many terms which depend on the nuclear position cancel out in Eq. (I8) or completely disappear in the exponent in Eq. (I6) for the homonuclear diatomic molecules the quantum interference terms are less sensitive to molecular geometries than the individual photoionization rates for such a simple diatomic molecule.

Appendix J. Definitions of the Terms in Eq. (214)

The definitions of the terms appearing in Eq. (214) are given by

$$\begin{aligned}
 & B_{j,1s,NC,par}(I_{av,pv'}) \\
 &= \left[\sinh^{-1} \gamma_{1s} + \frac{I_{av,pv'} - I_{1s}}{2I_{1s}} \frac{\gamma_{1s}}{\sqrt{1 + \gamma_{1s}^2}} + (-1)^j eF \frac{R_{0a}}{2} \frac{\gamma_{1s}}{2I_{1s}} \right. \\
 & \quad \left. + \frac{(-1)^j m\omega}{4\sqrt{2mI_{1s}}} \left\{ \Delta R - \frac{(-1)^j \sqrt{2mI_{1s}}}{2\hbar\beta} \right\} \right] \\
 & \quad \times \left\{ \sinh^{-1} \gamma_{1s} - \frac{\gamma_{1s}}{\sqrt{1 + \gamma_{1s}^2}} + \frac{I_{av,pv'} - I_{1s}}{2I_{1s}} \frac{\gamma_{1s}^3}{(1 + \gamma_{1s}^2)^{3/2}} \right\}^{1/2}, \quad (J1)
 \end{aligned}$$

$$D_{j,1s,NC,par}(I_{av,pv'})_{v'=0} = \frac{X_{1,j}(I_{av,pv'})_{v'=0}}{\gamma_{1s}I_{1s}} - X_2(I_{av,pv'})_{v'=0} - \frac{X_{1,j}(I_{av,pv'})_{v'=0}^2}{2\hbar\omega I_{1s}}, \quad (J2)$$

or

$$\begin{aligned}
 D_{j,1s,NC,par}(I_{av,pv'})_{v'=1} &= \frac{(-1)^j eF}{4\gamma_{1s}I_{1s}\sqrt{\beta}} + \frac{\sqrt{\beta}X_{1,j}(I_{av,pv'})_{v'=1}}{\gamma_{1s}I_{1s}} X_{3,j} \\
 & \quad - \left\{ X_2(I_{av,pv'})_{v'=1} + \frac{X_{1,j}(I_{av,pv'})_{v'=1}^2}{2\hbar\omega I_{1s}} \right\} \sqrt{\beta} X_{4,j}, \quad (J3)
 \end{aligned}$$

or

$$\begin{aligned}
 & D_{j,1s,NC,par}(I_{av,pv'})_{v' \geq 2} \\
 &= \frac{v'(-1)^j eF \beta^{v'/2-1}}{4\gamma_{1s}I_{1s}} X_{4,j}^{v'-1} - \frac{v'(v'-1)(eF)^2 \beta^{v'/2-2}}{32\hbar\omega I_{1s}} X_{4,j}^{v'-2} \\
 & \quad + \frac{\beta^{v'/2}(eF)X_{1,j}(I_{av,pv'})}{\omega\gamma_{1s}I_{1s}} \left\{ X_{4,j}^{v'} - \frac{v'(-1)^j (eF)\gamma_{1s}}{4\beta\hbar\omega} X_{4,j}^{v'-1} \right\} \\
 & \quad - \beta^{v'/2} \left\{ X_2(I_{av,pv'}) + \frac{X_{1,j}(I_{av,pv'})^2}{2\hbar\omega I_{1s}} \right\} X_{4,j}^{v'} \quad (J4)
 \end{aligned}$$

$$X_{1,j}(I_{av,pv'}) = \frac{I_{av,pv'} - I_{1s}}{\sqrt{1 + \gamma_{1s}^2}} + (-1)^j eF \frac{R_{0a}}{2} - \frac{\gamma_{1s}(eF)^2}{8\beta\hbar\omega} + (-1)^j eF \frac{\Delta R}{4}, \quad (J5)$$

$$X_{2,j}(I_{av,pv'}) = \frac{1}{\gamma_{1s}\sqrt{1 + \gamma_{1s}^2}} + \frac{(I_{av,pv'} - I_{1s})}{2I_{1s}} \frac{\gamma_{1s}}{(1 + \gamma_{1s}^2)^{3/2}} + \frac{m\omega}{8\beta\hbar\gamma_{1s}^2}, \quad (J6)$$

$$X_{3,j} = -\frac{\Delta R}{2} - \frac{(-1)^j \gamma_{1s}(eF)}{2\beta\hbar\omega}, \quad (J7)$$

$$X_{4,j} = -\frac{\Delta R}{2} - \frac{(-1)^j \gamma_{1s}(eF)}{4\beta\hbar\omega}, \quad (J8)$$

and

$$\begin{aligned} g_{har,j,1s}^{(1)}(I_{av,pv'}) &= \frac{1}{\hbar\omega} \left(\tilde{I}_{av,pv'} \sinh^{-1} \gamma_{1s} - \tilde{I}_{1s} \frac{\gamma_{1s}\sqrt{1 + \gamma_{1s}^2}}{1 + 2\gamma_{1s}^2} \right) + \frac{\sqrt{2mI_{1s}}}{2\hbar} (-1)^j R_{0a} \\ &+ \frac{\beta}{4} \Delta R^2 + \frac{(-1)^j \sqrt{2mI_{1s}}}{4\hbar} \Delta R - \frac{mI_{1s}}{8\hbar^2\beta}, \end{aligned} \quad (J9)$$

for the homonuclear diatomic molecules.

Appendix K. Total Photoionization Rate with the Perpendicular Polarization under the Non-Condon Approximation

The individual photoionization rate with the perpendicular polarization under the non-Condon approximation is given by

$$\begin{aligned} w_{av \rightarrow pv', NC, per}^{j,1s,j,1s} &= E_{1s} |b_{j,1s}|^2 |D_{j,1s,C}(I_{av,pv'})|^2 |\langle \Theta_{pv'} | \Theta_{av} \rangle|^2 \\ &\times \exp\{-2g_{j,1s,C}^{(1)}(I_{av,pv'}, \vec{0})\} \sum_{\lambda=0}^{v'} v' C_{\lambda} \frac{(2\lambda + 1)!!}{2^{3\lambda+3/2}\pi} \left(\frac{m\omega}{\hbar\beta^2 \Delta R^2} \right)^{\lambda} \\ &\times \int_0^{\pi} \sin\theta d\theta \int_0^{2\pi} d\phi \left\{ \eta_1 + \eta_2 \cos^2\theta + \frac{m\omega}{8\hbar\beta} \sin^2\theta \sin^2\phi \right\}^{-(2\lambda+3)/2}, \end{aligned} \quad (K1)$$

while the quantum interference terms are given by

$$\begin{aligned}
w_{av \rightarrow pv', NC, per}^{j, 1s, j', 1s} &= E_{1s} b_{j, 1s} b_{j', 1s} |D_{j, 1s, C}(I_{av, pv'})|^2 | \langle \Theta_{pv'} | \Theta_{av} \rangle |^2 \\
&\times \exp \{ -2g_{j, 1s, C}^{(1)}(I_{av, pv'}, \vec{0}) \} \\
&\times \sum_{\lambda=0}^{v'} \sum_{\lambda'=0}^{v'} v' C_{\lambda v'} C_{\lambda'} (-1)^{j\lambda + j'\lambda' + \lambda'} \frac{1}{2^{\lambda + \lambda'} \pi^{3/2}} \left(\frac{m\omega}{\hbar \beta^2 \Delta R^2} \right)^{(\lambda + \lambda')/2} \\
&\times \int_0^\pi d\theta (\sin \theta)^{\lambda + \lambda' + 1} \\
&\times \int_0^{2\pi} d\phi (\sin \phi)^{\lambda + \lambda'} \text{Re} [i^{\lambda + \lambda'} \Xi_{j, j'}(\lambda + \lambda', \theta, \phi)], \tag{K2}
\end{aligned}$$

where

$$\eta_1 = \sinh^{-1} \gamma_{1s} + \frac{I_{av, pv'} - I_{1s}}{2I_{1s}} \frac{\gamma_{1s}}{\sqrt{1 + \gamma_{1s}^2}}, \tag{K3}$$

$$\eta_2 = -\frac{\gamma_{1s}}{\sqrt{1 + \gamma_{1s}^2}} - \frac{I_{av, pv'} - I_{1s}}{2I_{1s}} \frac{\gamma_{1s}}{(1 + \gamma_{1s}^2)^{3/2}}, \tag{K4}$$

$$\begin{aligned}
&\Xi_{j, j'}(\lambda + \lambda', \theta, \phi) \\
&= \int_0^\infty d\alpha \alpha^{\lambda + \lambda' + 2} \exp \left\{ - \left(\eta_1 + \eta_2 \cos^2 \theta + \frac{m\omega}{8\hbar\beta} \sin^2 \theta \sin^2 \phi \right) \alpha^2 \right. \\
&\quad \left. + i\alpha \eta_3(j, j') \sin \theta \sin \phi \right\}, \tag{K5}
\end{aligned}$$

$$\eta_3(j, j') = \frac{-(-1)^j + (-1)^{j'}}{2} \sqrt{\frac{m\omega}{\hbar}} \left(R_{0a} + \frac{\Delta R}{2} \right), \tag{K6}$$

and

$$j = 1 \quad \text{and} \quad j' = 2, \quad \text{or} \quad j = 2 \quad \text{and} \quad j' = 1.$$

The integrations in Eqs. (K1), (K2), and (K5) have been performed numerically. For the integration over α in Eq. (K5), we have used the following formula,

$$\begin{aligned}
&\int_0^\infty d\alpha \exp(-A\alpha^2 + iB\alpha) \\
&= \frac{1}{2} \sqrt{\frac{\pi}{A}} \exp\left(-\frac{B^2}{4A}\right) + \frac{i}{\sqrt{A}} \exp\left(-\frac{B^2}{4A}\right) \int_0^{\frac{B}{2\sqrt{A}}} \exp(t^2) dt. \tag{K7}
\end{aligned}$$

From the above equations, we notice that the non-Condon approximation does not affect the exponential factor, but the pre-exponential factor is affected in the perpendicular polarization case.

We can see that the terms where $\lambda = 0$ and $\frac{m\omega}{8\hbar\beta} = 0$ on the right hand side of Eq. (K1) for the individual photoionization rate, and $\lambda = \lambda' = 0$ in Eq. (K2), $\frac{m\omega}{8\hbar\beta} \sin^2 \theta \sin^2 \phi = 0$ in Eq. (K5), and $\frac{\Delta R}{2} = 0$ in Eq. (K6) for the quantum interference terms correspond to those under the Condon approximation. The other terms stem purely from the non-Condon approximation. Comparing this with Eq. (214), we notice that under the non-Condon approximation, the parallel polarization case will be affected more than that of perpendicular case because the former contains many more terms.

As has already been shown above, the term $\frac{\Delta R}{2}$ in Eq. (K6) and the summations for $\lambda \neq 0$ or $\lambda' \neq 0$ purely stem from the non-Condon approximation. In their absence, Eq. (K2) reduces to Eq. (I6). $\Xi_{j,j'}(\lambda + \lambda', \theta, \phi)$ in Eq. (K5) can be calculated by using Eq. (K7). We can see that the nuclear distance R_{0a} does not affect the individual photoionization rates but the quantum interference terms are affected.

Appendix L. Quantum Interference Terms

As shown below, the quantum interference terms cannot be obtained in a closed form in general cases. In principle, if the molecular axis is parallel and perpendicular to the laser polarization, even the quantum interference terms can be obtained analytically. However, this is only the special case when we calculate the photoionization rates for the randomly oriented molecules. Therefore, we shall show the most general expressions in this appendix.

The derivation of the quantum interference terms are as follows: from Eq. (243), we find

$$\begin{aligned}
 & w_{av \rightarrow pv}^{j,k_j j',k'_j} \\
 &= \frac{4\pi}{\hbar} \text{Re} \left[b_{j,k_j}^* b_{j',k'_j} C_{k_j}^* C_{k'_j} D_{j,k_j}^* (I_{av,pv'}, \vec{R}_j) D_{j',k'_j} (I_{av,pv'}, \vec{R}_j') |(\Theta_{pv'} | \Theta_{av})|^2 \right. \\
 &\quad \times \exp \left\{ -g_{j,k_j}^{(1)} (I_{av,pv'}, \vec{R}_j) - g_{j',k'_j}^{(1)} (I_{av,pv'}, \vec{R}_j') \right\} \\
 &\quad \times \int \frac{d^3 p}{(2\pi\hbar)^3} p^2 \sin^2 \theta_p \Upsilon_{k_j, k'_j}(\phi_p) \exp \left[\frac{i}{\hbar} (\vec{R}_j - \vec{R}_j') \cdot \vec{p} \right. \\
 &\quad - i \{ g_{j,k_j}^{(2)} (I_{av,pv'}, \vec{R}_j) - g_{j',k'_j}^{(2)} (I_{av,pv'}, \vec{R}_j') \} p \cos \theta_p \\
 &\quad - \{ g_{j,k_j}^{(3)} (I_{av,pv'}, \vec{R}_j) + g_{j',k'_j}^{(3)} (I_{av,pv'}, \vec{R}_j') \} p^2 - \{ g_{j,k_j}^{(4)} (I_{av,pv'}, \vec{R}_j) \\
 &\quad \left. + g_{j',k'_j}^{(4)} (I_{av,pv'}, \vec{R}_j') \} p^2 \cos^2 \theta_p \right] \sum_{n=-\infty}^{\infty} \delta \left(\tilde{I}_{av,pv'} + \frac{p^2}{2m} - n\hbar\omega \right), \quad (L1)
 \end{aligned}$$

where

$$g_{j,k_j}^{(2)}(I_{av,pv'}, \vec{R}_j) = \frac{1}{\hbar\omega} \left\{ \frac{eF}{m\omega} (1 - \sqrt{1 + \gamma_{k_j}^2}) - \frac{\gamma_{k_j}(I_{av,pv'} - I_{k_j})}{\sqrt{2mI_{k_j}}\sqrt{1 + \gamma_{k_j}^2}} + \frac{e\vec{F} \cdot \vec{R}_j \gamma_{k_j}}{\sqrt{2mI_{k_j}}} \right\}, \quad (\text{L2})$$

$$g_{j,k_j}^{(3)}(I_{av,pv'}, \vec{R}_j) = \frac{1}{2m\hbar\omega} \left\{ \sinh^{-1} \gamma_{k_j} + \frac{I_{av,pv'} - I_{k_j}}{2I_{k_j}} \frac{\gamma_{k_j}}{\sqrt{1 + \gamma_{k_j}^2}} - \frac{e\vec{F} \cdot \vec{R}_j \gamma_{k_j}}{2I_{k_j}} \right\}, \quad (\text{L3})$$

$$g_{j,k_j}^{(4)}(I_{av,pv'}, \vec{R}_j) = \frac{1}{2m\hbar\omega} \left\{ -\frac{\gamma_{k_j}}{\sqrt{1 + \gamma_{k_j}^2}} - \frac{I_{av,pv'} - I_{k_j}}{2I_{k_j}} \frac{\gamma_{k_j}}{(1 + \gamma_{k_j}^2)^{3/2}} + \frac{e\vec{F} \cdot \vec{R}_j \gamma_{k_j}}{2I_{k_j}} \right\}, \quad (\text{L4})$$

$$C_{k_j} = -\frac{3 \times 2^{7/4} \sqrt{\pi} \hbar^{3/2} \gamma_{k_j}}{m^{5/4} I_{k_j}^{1/4}}, \quad (\text{L5})$$

and

$$\Upsilon_{k_j, k'_j}(\phi_p) = \begin{cases} \cos^2 \phi_p & \text{for } k_j = 2px \text{ and } k'_j = 2px \\ \sin \phi_p \cos \phi_p & \text{for } k_j = 2px \text{ and } k'_j = 2py \text{ or } k_j = 2py \\ & \text{and } k'_j = 2px \\ \sin^2 \phi_p & \text{for } k_j = 2py \text{ and } k'_j = 2py. \end{cases} \quad (\text{L6})$$

Integrating over p , we finally obtain the general quantum interference terms for the homonuclear diatomic molecules consisting of only 2px and 2py atomic orbitals as shown in Eq. (255). The definitions of the terms in Eq. (255) are

$$G_{k_j, k'_j}(I_{av,pv'}, \theta_p) = 2m\hbar\omega [g_{j,k_j}^{(3)}(I_{av,pv'}) + g_{j',k'_j}^{(3)}(I_{av,pv'}) + \{g_{j,k_j}^{(4)}(I_{av,pv'}) + g_{j',k'_j}^{(4)}(I_{av,pv'})\} \cos^2 \theta_p], \quad (\text{L7})$$

$$J_{j,k_j, j', k'_j}(I_{av,pv'}, \hat{p}) = \sqrt{\frac{2m\omega}{\hbar}} (\vec{R}_j - \vec{R}_{j'}) \cdot \hat{p} + \cos \theta_p \{K_{j,k_j}(I_{av,pv'}, \vec{R}_j) - K_{j',k'_j}(I_{av,pv'}, \vec{R}_{j'})\}, \quad (\text{L8})$$

$$K_{j,k_j}(I_{av,pv'}, \vec{R}_j) = -\frac{\gamma_{k_j} e\vec{F} \cdot \vec{R}_j}{\sqrt{\hbar\omega I_{k_j}}}, \quad (\text{L9})$$

and \hat{p} is the unit vector defined by \vec{p} . In this derivation, we have used the fact that b_{j,k_j} , C_{k_j} , and $D_{j,k_j}(I_{av,pv'})$ are real.

References

1. A. Giusti-Suzor, X. He, O. Atabek, Phys. Rev. Lett. **64**, 515 (1990).
2. A. Zavriyev, P. H. Bucksbaum, H. G. Muller, D. W. Schumacher, Phys. Rev. A **42**, 5500 (1990).
3. G. Jolicard, O. Atabek, Phys. Rev. A **46**, 5845 (1992).
4. A. Giusti-Suzor, F. H. Mies, Phys. Rev. Lett. **68**, 3869 (1992).
5. G. H. Yao, S.-I. Chu, Chem. Phys. Lett. **197**, 413 (1992).
6. A. D. Bandrauk, *Molecules in Laser Fields* (Marcel Dekker, New York, 1994).
7. N. B. Delone, V. P. Krainov, *Multiphoton Processes in Atoms* (Springer-Verlag, Berlin, 1994); S. L. Chin, P. Lambropoulos, *Multiphoton Ionization of Atoms* (Academic, New York, 1984); M. Gavrilu, *Atoms in Intense Laser Fields* (Academic, New York, 1992).
8. T. Zuo, A. D. Bandrauk, Phys. Rev. A **52**, R2511 (1995).
9. K. Yamanouchi, Science **295**, 1659 (2002).
10. L. V. Keldysh, Zh. Eksp. Teor. Fiz. **47**, 1945 (1964) [Sov. Phys. JETP **20**, 1307 (1965)].
11. F. H. M. Faisal, J. Phys. B **6**, L89 (1973).
12. H. R. Reiss, Phys. Rev. A **22**, 1786 (1980).
13. M. V. Ammosov, N. B. Delone, V. P. Krainov, Zh. Eksp. Teor. Fiz. **91**, 2008 (1986) [Sov. Phys. JETP **64**, 1191 (1987)].
14. J. Muth-Böhm, A. Becker, S. L. Chin, F. H. M. Faisal, Chem. Phys. Lett. **337**, 313 (2001).
15. L. D. Landau, E. M. Lifshitz, *Quantum Mechanics: Non-Relativistic Theory*, 3rd ed. (Pergamon, Oxford, 1991).
16. G. A. Kyrala, T. D. Nichols, Phys. Rev. A **44**, R1450 (1991).
17. I. Cacelli, R. Moccia, A. Rizzo, Phys. Rev. A **57**, 1895 (1998).
18. R. R. Lucchese, G. Raseev, V. McKoy, Phys. Rev. A **25**, 2572 (1982).
19. G. S. Ondrey, C. Rose, D. Proch, K. L. Kompa, J. Chem. Phys. **95**, 7823 (1991).
20. G. F. Gribakin, M. Yu. Kuchiev, Phys. Rev. A **55**, 3760 (1997).
21. H. R. Reiss, V. P. Krainov, Phys. Rev. A **50**, R910 (1994).
22. J. Bauer, J. Phys. B **34**, 1343 (2001).
23. H. Siegbahn, L. Asplund, P. Kelfve, Chem. Phys. Lett. **35**, 330 (1975); I. N. Levine, *Quantum Chemistry* (Prentice-Hall Inc., 1991).
24. K. J. LaGattuta, Phys. Rev. A **41**, 5110 (1990).
25. P. H. Bucksbaum, A. Zavriyev, H. G. Muller, D. W. Schumacher, Phys. Rev. Lett. **64**, 1883 (1990).
26. K. Codling, L. J. Fransiski, P. A. Hatherly, J. Phys. B **22**, L321 (1989); K. Codling, L. J. Fransiski, P. A. Hatherly, Science **246**, 1029 (1989); K. Codling, P. A. Hatherly, L. J. Fransiski, A. J. Langley, W. Shaikh, J. Phys. B **23**, L291 (1990).
27. M. J. DeWitt, R. J. Levis, J. Chem. Phys. **110**, 11368 (1999).
28. C. Guo, M. Li, J. P. Nibarger, G. N. Gibson, Phys. Rev. A **58**, R4271 (1998).
29. C. Guo, G. N. Gibson, Phys. Rev. A **63**, 040701 (R) (2001).
30. J. P. Nibarger, S. V. Menon, G. N. Gibson, Phys. Rev. A **63**, 053406 (2001).
31. M. J. DeWitt, B. S. Prall, R. J. Levis, J. Chem. Phys. **113**, 1553 (2000).
32. I. N. Levine, *Molecular Spectroscopy* (John-Wiley & Sons, 1975), p. 316.

33. W. Gordon, *Z. Phys.* **40**, 117 (1926).
34. D. M. Volkov, *Z. Phys.* **94**, 250 (1935).
35. S. Basile, F. Trombetta, G. Ferrante, *Phys. Rev. Lett.* **61**, 2435 (1988).
36. G. Duchateau, E. Cormier, H. Bachau, R. Gayet, *Phys. Rev. A* **63**, 053411 (2001).
37. M. Jain, N. Tzoar, *Phys. Rev. A* **18**, 538 (1978).
38. G. Duchateau, E. Cormier, R. Gayet, *Eur. Phys. J. D* **11**, 191 (2000).
39. A. M. Perelomov, V. S. Popov, M. V. Terent'ev, *Zh. Eksp. Teor. Fiz.* **50**, 1393 (1966) [*Sov. Phys. JETP* **23**, 924 (1966)].
40. A. I. Nikishov, V. I. Ritus, *Zh. Eksp. Teor. Fiz.* **52**, 223 (1967) [*Sov. Phys. JETP* **25**, 145 (1967)].
41. R. Cavaliere, G. Ferrante, C. Leone, *J. Phys. B* **13**, 4495 (1980).
42. P. Kalman, *Phys. Rev. A* **38**, 5458 (1988).
43. J. Z. Kaminski, A. Jaron, F. Ehlötzky, *Phys. Rev. A* **53**, 1756 (1996).
44. J. Bauer, *Phys. Rev. A* **55**, 3261 (1997).
45. W. C. Henneberger, *Phys. Rev. Lett.* **21**, 838 (1968); M. V. Fedorov, *Atomic and Free Electrons in a Strong Light Field* (World Scientific, Singapore, 1997), p. 12.
46. M. Pont, N. R. Walet, M. Gavrilu, C. W. McCurdy, *Phys. Rev. Lett.* **61**, 939 (1988).
47. M. Pont, M. Gavrilu, *Phys. Rev. Lett.* **65**, 2362 (1990).
48. V. P. Krainov, B. Shokri, *Sov. Phys. JETP* **80**, 657 (1995).
49. S. Augst, D. D. Meyerhofer, D. Strickland, S. L. Chin, *J. Opt. Soc. Am. B* **8**, 858 (1991).
50. D. Bauer, P. Mulser, *Phys. Rev. A* **59**, 569 (1999).
51. M. V. Fedorov, J. Peatross, *Phys. Rev. A* **52**, 504 (1995).
52. X. M. Tong, Z. X. Zhao, C. D. Lin, *Phys. Rev. A* **66**, 033402 (2002).
53. A. Saenz, *Phys. Rev. A* **66**, 063408 (2002).
54. A. Saenz, *Phys. Rev. A* **61**, 051402 (R) (2000).
55. I. V. Litvinyuk, K. F. Lee, P. W. Dooley, D. M. Rayner, D. M. Villeneuve, P. B. Corkum, *Phys. Rev. Lett.* **90**, 233003 (2003).
56. G. N. Gibson, M. Li, C. Guo, J. P. Nibarger, *Phys. Rev. A* **58**, 4723 (1998).
57. J. H. Posthumus, A. J. Giles, M. R. Thompson, K. Codling, *J. Phys. B* **29**, 5811 (1996).
58. L. J. Frasinski, K. Codling, P. Hatherly, *Phys. Rev. Lett.* **58**, 2424 (1989).
59. K. Codling, L. J. Frasinski, *J. Phys. B* **26**, 783 (1993).
60. E. Constant, H. Stapelfelt, P. B. Corkum, *Phys. Rev. Lett.* **76**, 4140 (1996).
61. C. Cornaggia, J. Lavancier, D. Normand, J. Morellec, H. X. Liu, *Phys. Rev. A* **42**, 5464 (1990).
62. M. Schmidt, D. Normand, C. Cornaggia, *Phys. Rev. A* **50**, 5037 (1994).
63. A. Talebpour, S. Laroche, S. L. Chin, *J. Phys. B* **31**, 2796 (1998).
64. A. Talebpour, S. Laroche, S. L. Chin, *J. Phys. B* **31**, L49 (1998).
65. R. Barnett, G. N. Gibson, *Phys. Rev. A* **59**, 4843 (1999).
66. S. Chelkowski, C. Fois, A. D. Bandrauk, *Phys. Rev. A* **57**, 1176 (1998).
67. S. Chelkowski, A. D. Bandrauk, *J. Phys. B* **28**, L723 (1995).
68. S. Chelkowski, T. Zuo, O. Atabek, A. D. Bandrauk, *Phys. Rev. A* **52**, 2977 (1995).
69. H. Yu, A. D. Bandrauk, *Phys. Rev. A* **56**, 685 (1997).
70. I. Kawata, H. Kono, A. D. Bandrauk, *Phys. Rev. A* **64**, 043411 (2001).
71. K. Harumiya, I. Kawata, H. Kono, Y. Fujimura, *J. Chem. Phys.* **113**, 8953 (2000).

72. I. Kawata, H. Kono, Y. Fujimura, *J. Chem. Phys.* **110**, 11152 (1999).
73. K. Harumiya, H. Kono, Y. Fujimura, I. Kawata, A. D. Bandrauk, *Phys. Rev. A* **66**, 043403 (2002).
74. I. Kawata, H. Kono, Y. Fujimura, A. D. Bandrauk, *Phys. Rev. A* **62**, 031401 (R) (2000).
75. I. Kawata, A. D. Bandrauk, H. Kono, Y. Fujimura, *Laser Phys.* **11**, 181 (2001).
76. S. Suhai, *J. Chem. Phys.* **73**, 3843 (1980); H. O. Villar, M. Dupuis, E. Clementi, *Phys. Rev. B* **37**, 2520 (1988); M. Springborg, C. Arcangeli, *J. Mol. Struct. (Theochem)*, **531**, 211 (2000); M. Springborg, *ibid.* **593**, 155 (2002); M. E. Vaschetto, M. Springborg, *ibid.* **460**, 141 (1999); M. Kofranek, H. Lischka, A. Karpfen, *J. Chem. Phys.* **96**, 982 (1992); B. Champagne, E. Deumens, Y. Öhrn, *ibid.* **107**, 5433 (1997); B. Champagne, E. A. Perpete, S. J. A. van Gisbergen, E.-J. Baerends, J. G. Snijders, C. Soubra-Ghaoui, K. A. Robins, B. Kirtman, *ibid.* **109**, 10489 (1998); F. L. Gu, D. M. Bishop, B. Kirtman, *ibid.* **115**, 10548 (2001); D. Jacquemin, J.-M. Andre, B. Champagne, *ibid.* **118**, 3956 (2003); J. L. Bredas, R. R. Chance, R. Silbey, G. Nicolas, Ph. Durand, *ibid.* **75**, 255 (1981).
77. F. A. Houle, J. L. Beauchamp, *J. Am. Chem. Soc.* **100**, 3290 (1978).
78. F. P. Lossing, *Can. J. Chem.* **49**, 357 (1971).
79. C.-W. Liang, C.-C. Chen, C.-Y. Wei, Y.-T. Chen, *J. Chem. Phys.* **116**, 4162 (2002); J.-C. Wu, R. Li, J.-L. Chang, Y.-T. Chen, *ibid.* **113**, 7286 (2000); T. Schultz, J. S. Clarke, T. Gilbert, H.-J. Deyerl, I. Fishcer, *Faraday Discuss.* **115**, 17 (2000).
80. T.-K. Ha, H. Baumann, J. F. M. Oth, *J. Chem. Phys.* **85**, 1438 (1986).
81. P. G. Szalay, A. G. Csaszar, G. Fogarasi, A. Karpfen, H. Lischka, *J. Chem. Phys.* **93**, 1246 (1990); F. Sim, D. R. Salahub, S. Chin, M. Dupuis, *ibid.* **95**, 4317 (1991); J. M. Oliva, J. Gerratt, D. L. Cooper, P. B. Karadakov, M. Raimondi, *ibid.* **106**, 3663 (1997).
82. M. J. DeWitt, R. J. Levis, *J. Chem. Phys.* **108**, 7739 (1998).
83. M. J. DeWitt, R. J. Levis, *J. Chem. Phys.* **108**, 7045 (1998).
84. R. Loudon, *The Quantum Theory of Light* (Oxford University Press, Oxford, 1983).
85. F. H. M. Faisal, A. Becker, *Laser Phys.* **7**, 684 (1997).
86. J. Muth-Böhm, A. Becker, F. H. M. Faisal, *Phys. Rev. Lett.* **85**, 2280 (2000).
87. F. H. M. Faisal, A. Becker, J. Muth-Böhm, *Laser Phys.* **9**, 115 (1999).
88. A. Becker, F. H. M. Faisal, *Opt. Express* **8**, 383 (2001).
89. A. M. Mebel, K. Morokuma, M. C. Lin, *J. Chem. Phys.* **103**, 7414 (1995).
90. L. A. Curtiss, K. Raghavachari, G. W. Trucks, J. A. Pople, *J. Chem. Phys.* **94**, 7221 (1991); J. A. Pople, M. Head-Gordon, D. J. Fox, K. Raghavachari, L. A. Curtiss, *ibid.* **90**, 5622 (1989); L. A. Curtiss, C. Jones, G. W. Trucks, K. Raghavachari, J. A. Pople, *ibid.* **93**, 2537 (1990).
91. J. V. Ortiz, *J. Chem. Phys.* **89**, 6348 (1988); L. S. Cederbaum, *J. Phys. B.* **8**, 290 (1975); W. von Niessen, J. Schirmer, L. S. Cederbaum, *Comp. Phys. Rep.* **1**, 57 (1984); V. G. Zakrzewski, W. von Niessen, *J. Comp. Chem.* **14**, 13 (1993).
92. M. J. Frisch, G. W. Trucks, H. B. Schlegel, G. E. Scuseria, M. A. Robb, J. R. Cheeseman, V. G. Zakrzewski, J. A. Jr. Montgomery, R. E. Stratmann, J. C. Burant, S. Dapprich, J. M. Millam, A. D. Daniels, K. N. Kudin,

- M. C. Strain, O. Farkas, J. Tomasi, V. Barone, M. Cossi, R. Cammi, B. Mennucci, C. Pomelli, C. Adamo, S. Clifford, J. Ochterski, G. A. Petersson, P. Y. Ayala, Q. Cui, K. Morokuma, D. K. Malick, A. D. Rabuck, K. Raghavachari, J. B. Foresman, J. Cioslowski, J. V. Ortiz, B. B. Stefanov, G. Liu, A. Liashenko, P. Piskorz, I. Komaromi, R. Gomperts, R. L. Martin, D. J. Fox, T. Keith, M. A. Al-Laham, C. Y. Peng, A. Nanayakkara, C. Gonzalez, M. Challacombe, P. M. W. Gill, B. G. Johnson, W. Chen, M. W. Wong, J. L. Andres, M. Head-Gordon, E. S. Replogle, J. A. Pople Gaussian 98, revision A.11.2; *Gaussian*, Inc.: Pittsburgh, PA, 1998.
93. E. Moore, B. Gherman, D. Yaron, *J. Chem. Phys.* **106**, 4216 (1997).
 94. F. A. Ilkov, J. E. Decker, S. L. Chin, *J. Phys. B* **25**, 4005 (1992).
 95. E. Wells, M. J. DeWitt, R. R. Jones, *Phys. Rev. A* **66**, 013409 (2002).
 96. S. Chelkowski, T. Zuo, A. D. Bandrauk, *Phys. Rev. A* **46**, R5342 (1992).
 97. M. J. DeWitt, R. J. Levis, *Phys. Rev. Lett.* **81**, 5101 (1998).
 98. S. Pignataro, A. Cassuto, F. P. Lossing, *J. Am. Chem. Soc.* **89**, 3693 (1967).
 99. F. V. Bunkin, I. I. Tugov, *Phys. Rev. A* **8**, 601 (1973).
 100. W. H. Press, B. P. Flannery, S. A. Teukolsky, W. T. Vetterling, *Numerical Recipes in C* (Cambridge University Press, 1988).
 101. M. S. Child, *Semiclassical Mechanics with Molecular Applications* (Clarendon Press, Oxford, 1991).
 102. A. Saenz, *J. Phys. B* **33**, 4365 (2000).
 103. X. Urbain, B. Fabre, E. M. Staicu-Casagrande, N. de Ruette, V. M. Andrianarijaona, J. Jureta, J. H. Posthumus, A. Saenz, E. Baldit, C. Cornaggia, *Phys. Rev. Lett.* **92**, 163004 (2004).
 104. S. L. Chin, Y. Liang, J. E. Decker, F. A. Ilkov, M. V. Ammosov, *J. Phys. B* **25**, L249 (1992).
 105. T. D. G. Walsh, J. E. Decker, S. L. Chin, *J. Phys. B* **26**, L85 (1993).
 106. T. D. G. Walsh, F. A. Ilkov, J. E. Decker, S. L. Chin, *J. Phys. B* **27**, 3767 (1994).
 107. M. J. DeWitt, E. Wells, R. R. Jones, *Phys. Rev. Lett.* **87**, 153001 (2001).
 108. T. Otobe, K. Yabana, J.-I. Iwata, *Phys. Rev. A* **69**, 053404 (2004).
 109. A. Talebpour, C.-Y. Chien, S. L. Chin, *J. Phys. B* **29**, L677 (1996).
 110. P. B. Corkum, *Phys. Rev. Lett.* **71**, 1994 (1993).
 111. C. Guo, *Phys. Rev. Lett.* **85**, 2276 (2000).
 112. F. Grabson, G. G. Paulus, S. L. Chin, H. Walther, J. Muth-Böhm, A. Becker, F. H. M. Faisal, *Phys. Rev. A* **63**, 041402 (R) (2001).
 113. *International Tables of Selected Constants 17. Spectroscopic Data Relative to Diatomic Molecules*, edited by B. Rosen (Pergamon, London, 1970).
 114. *Molecular Spectra and Molecular Structure, I. Spectra of Diatomic Molecules*, edited by G. Herzberg (D. Van Nostrand Company, Inc., New York, 1950).
 115. W. J. Hehre, R. F. Stewart, J. A. Pople, *J. Chem. Phys.* **51**, 2657 (1969).
 116. J. B. Collins, P. v. R. Schleyer, J. S. Binkley, J. A. Pople, *J. Chem. Phys.* **64**, 5142 (1976).
 117. A. Szabo, N. S. Ostlund, *Modern Quantum Chemistry* (Macmillan Publishing Co., Inc., New York, 1982).
 118. *Molecules and Clusters in Intense Laser Fields*, edited by J. Posthumus (Cambridge University Press, 2001).
 119. K. Mishima, M. Hayashi, S. H. Lin, *Int. J. Mass Spectrom.* **238**, 1 (2004).

120. H.-F. Lu, F.-Y. Li, K. Nagaya, M. Hayaashi, K. Mishima, S. H. Lin (unpublished).
121. H. Eyring, S. H. Lin, S. M. Lin, *Basic Chemical Kinetics* (Wiley, New York, 1980).
122. P. J. Robinson, K. A. Holbrook, *Unimolecular Reactions* (Wiley, New York, 1972).
123. J. I. Steinfeld, J. S. Francisco, W. L. Hase, *Chemical Kinetics and Dynamics* (Prentice Hall, Engelwood Cliffs, NJ, 1999).
124. V. V. Kislov, T. L. Nguyen, A. M. Mebel, S. H. Lin, S. C. Smith, *J. Chem. Phys.* **120**, 7008 (2004).
125. T. S. Zyubin, G.-S. Kim, A. M. Mebel, S. H. Lin, A. D. Bandrauk, *J. Theor. Comput. Chem.* **2**, 205 (2003).
126. K. Mishima, M. Hayashi, J. Yi, S. H. Lin, H. L. Selzle, E. W. Schlag, *Phys. Rev. A* **66**, 033401 (2002).
127. K. Mishima, M. Hayashi, J. Yi, S. H. Lin, H. L. Selzle, E. W. Schlag, *Phys. Rev.* **66**, 053408 (2002).
128. K. Mishima, M. Hayashi, S. H. Lin, *Phys. Rev. A* **71**, 053411 (2005).
129. K. Mishima, K. Nagaya, M. Hayashi, S. H. Lin, *Phys. Rev. A* **70**, 063414 (2004).
130. K. Mishima, K. Nagaya, M. Hayashi, S. H. Lin, *J. Chem. Phys.* **122**, 104312 (2005).
131. K. Mishima, K. Nagaya, M. Hayashi, S. H. Lin, *J. Chem. Phys.* **122**, 024104 (2005).
132. K. Mishima, M. Hayashi, J. Yi, S. H. Lin, H. L. Selzle, E. W. Schlag, *J. Chin. Chem. Soc.* **49**, 639 (2002).

This page intentionally left blank

3

IONIZATION AND FRAGMENTATION OF SOME ORGANIC MOLECULES WITH INTENSE FEMTOSECOND LASER PULSES

NOBUAKI NAKASHIMA*, TOMOYUKI YATSUHASHI,
MASANAO MURAKAMI, RYUJI MIZOGUCHI† and
YOSHINORI SHIMADA†

**Department of Chemistry, Graduate School of Science,
Osaka City University, Sugimoto, Sumiyoshi, Osaka 558-8585, Japan
E-mail: nakashim@sci.osaka-cu.ac.jp*

†*Institute for Laser Technology, Utsubo-honmachi, Nishi-ku,
Osaka 550-0004, Japan*

The ionization and fragmentation of some organic molecules by intense femtosecond pulses are described. One of the distinctive features of femtosecond ionization is intact molecular ion formation; but is not always the case. Therefore, this article is particularly concerned with how to produce intact molecular ions. Such phenomena are considered useful for analytical purpose. Following a description of the historical background, the recent results are briefly reviewed in the introduction. In the experimental section, the laser intensity evaluation methods of femtosecond pulse are described in detail. The laser power estimation for multi-photon ionization and barrier suppressed ionization is introduced based on the atomic model.

The key factors related with fragmentation are as follows: cation absorption (resonance *versus* non-resonance), excitation pulse width, and electron rescattering. These factors are discussed based on representative experimental results. The molecules discussed here are dienes, benzene and its halogenated compounds, polyaromatic hydrocarbons, dioxins, and C₆₀. The electron rescattering in high-intensity laser field is known to induce fragmentation; therefore, the representative mass spectra obtained by femtosecond pulse excitation are compared with the electron impact mass spectra. The applicability of this femtosecond ionization approach to the detection of dioxin has been discussed.

*Corresponding author.

3.1. Introduction

The ionization and fragmentation of organic compounds subjected to intense femtosecond laser and a possible application of the present approach has been described in this article. In 1995, DeWitt and Levis found intact molecular ion formation upon irradiation with a femtosecond laser pulse of 170 fs, 0.78 μm pulses at an intensity of $3.8 \times 10^{13} \text{ W cm}^{-2}$.¹ Although this is not always the case, femtosecond excitation can bypass dissociation channels and molecules can behave like atoms. Before these phenomena were described in the literature, it was known that nanosecond and picosecond pulse excitations give numerous fragments. Benzene fragmentation has been studied by excimer lasers with nanosecond pulse duration in the early stage of laser mass spectrometry.²⁻⁴ Eventually, elaborate experiments were carried out in this regard: benzene cations were produced by resonance-enhanced multi-photon (two-photon) ionization (REMPI), and the photo-dissociation rates have been measured by the third, tunable laser pulse.⁴ In the late 1990s, picosecond experiments were carried out by Mathur group, who found heavy fragmentation of benzene and investigated the fragmentation mechanisms.⁵

Another representative large molecule is C_{60} , which has a similar story to that of benzene in terms of fragmentation by femtosecond and nanosecond pulse excitation. Multiply charged C_{60}^{z+} ($z = 1 - 5$) ions have been observed by femtosecond excitation.⁶⁻⁸ To date, Bhardwaj *et al.* have reported the highest charged C_{60} . C_{60}^{12+} was detected with a 70 fs pulse at a wavelength of 1.8 μm ,⁹ whereas nanosecond pulse excitation gave fragments. C_{60} was irradiated with Nd:YAG laser nanosecond pulses at the wavelengths of the fundamental (1.064 μm) and the harmonics from the second (0.532 μm) to the fifth (213 nm), and the ninth (118 nm). In addition to C_{60}^+ , a C_2 loss reaction has been shown to occur and under those excitation conditions, the C_{58} , and C_{56} to C_{32} ions were detected.¹⁰

A number of molecules show heavy fragmentation, even at 0.8 μm femtosecond pulse excitation. Anthracene at a wavelength of 0.8 μm is a typical example.^{1,11-14} Recently, long wavelength excitation at 1.4 μm has been shown to be effective for reducing fragmentation and to produce molecular ions.¹⁵ Some explanations have been suggested for this type of fragmentation; among them, resonance *versus* non-resonance with the electronic levels of the cation can account for the present results. If the excitation wavelength is non-resonant with the levels of the cation, the fragmentation is suppressed and the molecular ions are observed. This point has been discussed by Fuß *et al.* in a study of hexatriene ionization¹⁶ and by Itakura *et al.* for the case of benzene ionization.¹⁷ Using pairs of organic molecules

of similar sizes but with different cation absorption spectra, our group successfully demonstrated clear examples of the effect of non-resonance excitation in molecular ion formation.¹⁸ Recently, by changing the compounds and excitation wavelengths, Trushin *et al.* clearly showed that the concept of resonance *versus* non-resonance is applicable for explaining fragmentation patterns of metal carbonyl compounds.¹⁹ Molecular ion formation was observed at even short wavelengths if they were non-resonant. The femtosecond ionization of anthracene and certain halogenated compounds can be explained along these lines.^{15,20} Markevitch *et al.* ionized a number of aromatic hydrocarbons and observed heavy fragmentation in the case of anthracene when subjected to $0.8 \mu\text{m}$ excitation. Taking into account the formation of a quasi-continuum of electronic states in a strong laser field, Markevitch *et al.* indicated a new mechanism for energy deposition and the eventual fragmentation processes; in addition, they successfully and qualitatively reproduced the fragmentation *versus* molecular ion ratios of certain aromatic hydrocarbons.¹⁴ Lezius *et al.* observed molecular ion formation with relatively little fragmentation at longer wavelengths ($1.45 \mu\text{m}$) in the case of some polyenes. They indicated that the single active electron model is inadequate, and that the nonadiabatic multi-electron (NME) dynamics are essential for the analysis of π -conjugated polyatomic molecules. Almost complete fragmentation of β -carotene is thought to have been explained for by the NME model.²¹ Moreover, recent theoretical calculations have reproduced the slow ionization rates of decatetraene.²²

Electron rescattering decomposes molecules into fragments. The electron is ejected from a molecule by an intense laser field and the molecule can be rescattered. The rescattering energy can reach far above the bond dissociation energy and ionization potentials at $10^{14} \text{ W cm}^{-2}$. Electron impact fragmentation has been reported for benzene,²³ C_{60} ,²⁴ and a series of alcoholic molecules.²⁵

Excitation by a pulse of shorter duration gives fewer fragments. Experimental results obtained with large molecules by changing the duration of the excitation pulse from the pico- to femtosecond order of magnitude are available for C_{60} ,²⁶ $\text{C}_2\text{H}_5\text{OH}$,²⁷ and 2,3-dimethyl-1,3-butadiene, which will be discussed below.²⁸ These analyses have indicated that a shorter pulse duration is a good option for producing molecular ions.

In the present study, ionic species were detected by a time-of-flight (TOF) mass spectrometer. The experimental details are described below for clarify purpose, because the experimental results obtained by various research groups can differ. Laser intensity evaluation is important in this context; direct measurement of the focal point is most likely the

best approach, though a comparative method with a standard is simple. An aperture is mounted in front of the flight tube of a TOF spectrometer. The size of the aperture may significantly affect the intensity distributions of any observed species. Molecules are ionized using a focused beam, then Coulomb explosion may be observed in the highest region of intensity while at the periphery a singly charged molecular ion may be observed. Ledingham *et al.* have pointed out the inherent difficulty of organic molecule ionization.²⁹ Other parameters, which may induce different results, can be the contrast ratio of the laser pulse (pre- and post-pulse intensities), laser stability, and the effects of the nonlinear index (called as *B* integral).

The mechanism for the formation of intact molecular ions is of great interest, and this phenomenon is of great advantage for studies involving femtosecond laser mass spectrometry (FLMS). The Ledingham group has measured aromatic hydrocarbons and nitro compounds,^{13,30} and the present authors have ionized chlorinated and fluorinated compounds, as well as dioxins, in intense laser fields.^{20,31}

Some examples of the femtosecond ionization of organic molecules are described below. The discussion will focus on the most relevant feature of the femtosecond ionization of organic molecules, namely, intact molecular ion formation as it relates to FLMS. Therefore, the irradiated laser intensity range discussed here is less than $1 \times 10^{15} \text{ W cm}^{-2}$, where the Coulomb explosion occurs. The excitation wavelengths used here were 0.8–2.0 μm , and 130 fs was the typical pulse width in a range from 35 to 1000 fs. Some of the early experimental results are reviewed in Refs. 11 and 32. A wide range of atoms, molecules, and clusters subjected to high-intensity laser fields and various experimental techniques have been described in a book.³³

3.2. Experimental

An outline of the laser system, the tunable infrared femtosecond pulses, the TOF mass spectrometer, and the methods of laser intensity evaluation are described below in some detail. The essential points of the apparatus and the experimental methods used in this study have been described elsewhere.^{18,20,32,33}

3.2.1. Femtosecond laser

Figure 1 shows the experimental arrangement used for femtosecond laser mass spectrometry. The femtosecond laser system was linked to a mass spectrometer. The laser system consisted of a Ti-Sapphire femtosecond laser

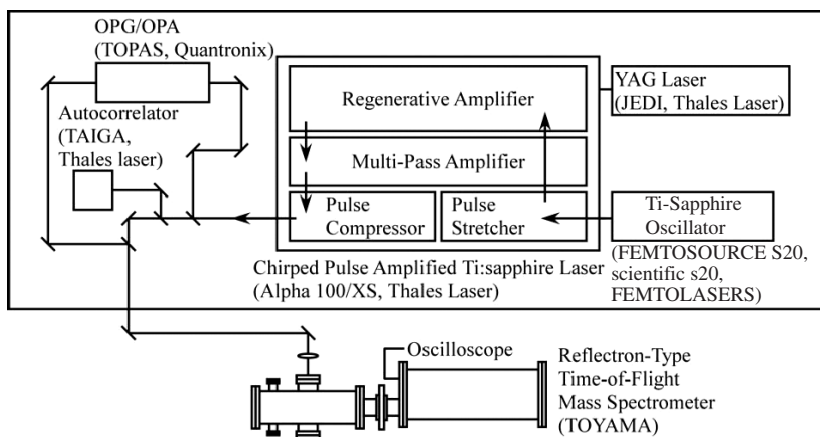


Fig. 1. The experimental arrangement for femtosecond mass spectrometry. The femtosecond laser system was a typical chirped-pulse amplified Ti-Sapphire laser linked to the reflectron-type time-of-flight mass spectrometer. The pulse width was 30 fs at a wavelength of $0.8 \mu\text{m}$. The width was variable up to a picosecond. The output energy was a few mJ/pulse (maximum: 15 mJ/pulse), and the beam intensities could rise to an order of 0.5 TW. The laser wavelengths were tunable from 1.2 to $2.4 \mu\text{m}$ by an optical parametric generation and amplifier (OPG/OPA).

(Alpha 100/XS, Thales Laser) and an optical parametric amplifier (TOPAS 100-femtosecond version, Quantronix).

The laser system delivered a short pulse width of 30 fs at the typical wavelength of $0.8 \mu\text{m}$. The seeded laser (FEMTOSOURCE S20, scientific s20, FEMTOLASERS) produced 20 fs pulses. After the pulse was stretched to 300 ps, it was amplified through a regenerative amplifier and a multi-pass amplifier, and finally the pulse was compressed to 30 fs. The output maximum was 15 mJ/pulse with a repetition rate of 100 Hz. The polarization was linear and horizontal, unless otherwise noticed. The root mean square stability was typically 1%. This high level of stability was achieved by a stable pump laser, which is a 12 W at $0.532 \mu\text{m}$ from a diode-laser-pumped YAG laser (JEDI, Thales Laser). The contrast ratios between the femtosecond pulse and amplified spontaneous emission were less than 10^{-6} for the 10 ps range pre- and post-pulses.

The laser wavelengths were tunable from 1.2 to $2.4 \mu\text{m}$ by the optical parametric amplifier (OPG/OPA) (TOPAS, Quantronix). The pulse width was almost the same as that of the input laser, but it was necessary to monitor the width, because longer or even shorter widths could occur for unknown reasons. The maximum energy was 0.4 mJ as the sum of signal and idler. The spectral width was typically 30 nm for the fundamental pulse of 30 fs, and the infrared pulses were broadened to widths of 30–90 nm for

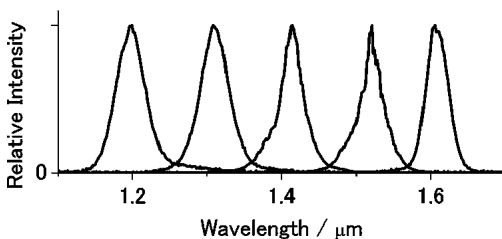


Fig. 2. Typical spectra from an optical parametric amplifier. The spectral widths of the infrared pulses have been broadened to widths of 30–90 nm for a 130 fs pulse at an excitation wavelength of $0.8 \mu\text{m}$. The output energy of the tunable infrared pulse was typically 0.4 mJ as the sum of signal and idler at an input laser energy of 1.15 mJ/pulse.

a 130 fs pulse, as shown in Fig. 2. The polarization of the signal of the OPA output (1.2 to $1.55 \mu\text{m}$) was perpendicular to the TOF axis and that of the idler wavelengths of 1.65 to $2.4 \mu\text{m}$ was parallel.

The pulse width was variable up to a few picoseconds with the use of an acousto-optic programmable dispersive filter ($0.8 \mu\text{m}$ DAZZLER, Fastlite).³⁴ A long femtosecond duration pulse with a positively or negatively chirped character was generated from the transformed limited pulse. In the case of a picosecond pulse, the grating gap at the pulse compressor had to be adjusted. The pulse widths were monitored with a single-shot autocorrelator (TAIGA, Thales Laser) and the output pulse from TOPAS was monitored by a scanning autocorrelator (PulseCheck, APE).

The beam break-up integral (B) was not measured. The pre- and post-pulses and the high value of B may have induced the fragmentation of organic molecules.^{13,35} The B value in the laser system was probably low enough, because the fragmentation was not violent. The final lens induced beam break-up by the nonlinear index n_2 , and the distorted beam could accelerate fragmentation.³⁶

3.2.2. Intensity evaluation by measuring the focusing diameter

If a parallel beam of diameter $D = 12.5 \text{ mm}$, and at $\lambda = 0.8 \mu\text{m}$ is focused with an aberration of less than $f = 200 \text{ mm}$ lens, the Airy disc diameter at the focused point is calculated using Eqs. (1) and (2) to be $ds = 31 \mu\text{m}$. The average laser intensity (P) in the disc can be calculated to be $3.5 \times 10^{16} \text{ W cm}^{-2}$ for a pulse width (τ) of 30 fs and a laser pulse energy (J) of 7.5 mJ, as seen in Eq. (3). This intensity is the atomic unit of the laser intensity of $3.5 \times 10^{16} \text{ W cm}^{-2}$, where the field intensity of $5.1 \times 10^9 \text{ V/cm}$ is the same as that felt by the electron at the Bohr radius in the hydrogen atom. Equation (4) shows the relation between a laser intensity of I and the

corresponding electric field of E .

$$\theta = \frac{2.44\lambda}{D}, \quad (1)$$

$$ds = f\theta = 3.1 \times 10^{-6} \mu\text{m}, \quad (2)$$

$$P = \frac{J}{\pi r^2 \tau} = 3.5 \times 10^{16} \text{ W cm}^{-2}, \quad (3)$$

$$E = 27.45\sqrt{I}, \quad \text{where } E: \text{V cm}^{-1} \quad \text{and } I: \text{W cm}^{-2}. \quad (4)$$

In the actual experiments, it is necessary to measure the diameter. Figure 3 shows the experimental results of the spot size at the focal point. The typical spot had an average diameter of $34 \mu\text{m}$ at an intensity of $1/e^2$. The intensity of the laser beam was reduced by the reflection of the surfaces of three wedged BK7 plates and the beam was focused with a 200 mm lens. The spot was magnified with a F/10 lens and recorded on a CCD camera. The pattern was elliptic; the ellipticity was 0.64 in the present experiments. The size was about 1.5 times the ideal value of $22 \mu\text{m}$ at the intensity of $1/e^2$ of the Airy disc. It is possible to calculate the laser intensity using these measurements and the energy of a CW power meter. The contrast ratio of the present laser between the femtosecond pulse and amplified spontaneous emission (ASE) was 10^{-3} for the 1 ps range. Therefore, most of the measured energy by the CW power meter was estimated to be confined in the 30 fs pulse. The above method represents the standard approach; however, it was not easy to monitor the size, evaluate the ratio of the main pulse and the ASE, and measure them at each wavelength on a daily basis. A more convenient method was expected, and a conventional and commonly used method is described below.

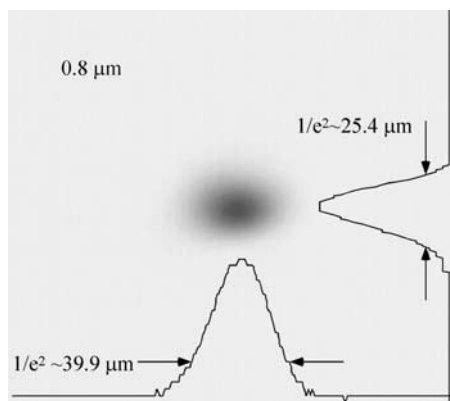


Fig. 3. Evaluation of laser intensity I based on the direct measurement of the size of the spot. The e^{-2} point size was $39.9 \mu\text{m}$ for the horizontal axis and $25.4 \mu\text{m}$ for the vertical axis, and the average was $33 \mu\text{m}$.

3.2.3. Intensity evaluation based on an intensity standard

The irradiation intensity was estimated based on the detection of Xe^{Z+} , the formation of which has been used as an intensity reference.³⁷ Hankin *et al.* have proposed a clear definition of irradiation intensity, I_{sat} , as an extrapolated value obtained from the laser intensities, whereby the ionization rate is infinite. The I_{sat} value corresponds to the extrapolated intensity from the barrier suppression ionization (BSI) model in an optical electric field. The asymptote of the plots between the Xe ion intensity *versus* the $\log I$ (laser intensity) can be drawn from the high intensity. I_{sat} is given as the crossing point with the $\log I$ axis. The I_{sat} of Xe has been reported to be $1.12 \times 10^{14} \text{ W cm}^{-2}$ for a 44 fs pulse.³⁷

At an irradiation intensity I with a Gaussian distribution in space and time, the space function is defined as given in Eq. (5).

$$I = I_0 e^{-\left(\frac{r}{R}\right)^2}, \quad (5)$$

$$S = \alpha \pi R^2 c l (\ln I_0 - \ln I_{\text{sat}}). \quad (6)$$

Finally, the ion intensity S is given by Eq. (6), where α is a proportional constant, R is the radius in Eqs. (5) and (6), c is the sample concentration, and l is the length or the depth of the irradiation area. According to Eq. (6), the point at which the value extrapolated from the high-intensity linear portion of the curve intersects with the intensity axis gives I_{sat} . Then, it is possible to determine the irradiation intensity by using the intensity of I_{sat} of Xe, which is commonly used as a standard target. The I_{sat} of Xe has been compared with the ADK theory (Ammosov–Delone–Krainov [38]) and is reasonably reproduced.³⁷

The saturated intensity for each ion can be defined as I_{sat}^s if one plots for the particular ion instead of obtaining the sum of all of the ions. In the case of anthracene at wavelengths of 0.8 and 1.4 μm , the intensities of the molecular ions were clearly observed with strong enough intensities to plot each ion, and the extrapolated value could be obtained in this manner. The intensity for each ion is indicated as I_{sat}^s in this paper; otherwise, the intensity, I_{sat} , was determined on the basis of all of the ions, as shown in Figs. 4–7. The anthracene I_{sat} in this study was determined to be $0.30 \times 10^{14} \text{ W cm}^{-2}$ at 0.8 μm using I_{sat} of Xe at $0.93 \times 10^{14} \text{ W cm}^{-2}$ for the linear polarization light with a 130 fs pulse. Apparently, the value of I_{sat} that was based on all of the ions was higher than that for the singly charged ion. The I_{sat}^s for the singly charged ion (M^+) at 0.8 μm was $0.20 \times 10^{14} \text{ W cm}^{-2}$. The same tendency

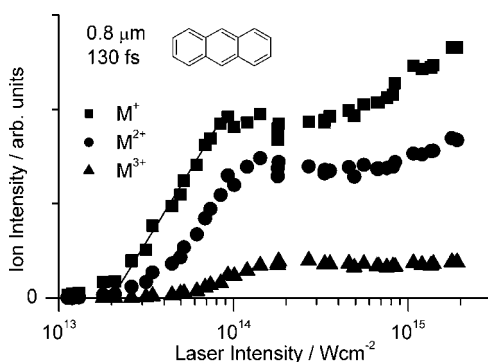


Fig. 4. Evaluation of laser intensity II. The horizontal scale is corrected by the I_{sat} of a standard sample of Xe at $0.93 \times 10^{14} \text{ W cm}^{-2}$ for a pulse width of 130 fs at a wavelength of $0.8 \mu\text{m}$. Anthracene I_{sat}^s was determined to be $0.20 \times 10^{14} \text{ W cm}^{-2}$ for the singly charged ion (M^+). M^{2+} and M^{3+} are doubly and triply charged anthracene ions, respectively.

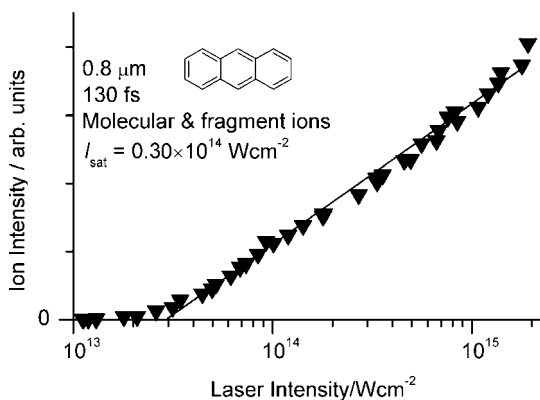


Fig. 5. Evaluation of laser intensity III. Anthracene I_{sat} was determined to be $0.30 \times 10^{14} \text{ W cm}^{-2}$ at a wavelength of $0.8 \mu\text{m}$ by obtaining the sum of all of the molecular and fragment ions.

was observed at $1.4 \mu\text{m}$, i.e. I_{sat}^s for the singly charged ion (M^+) was $0.30 \times 10^{14} \text{ W cm}^{-2}$, whereas I_{sat} was $0.40 \times 10^{14} \text{ W cm}^{-2}$ using the same data.

To carry out the above experiments laser intensities have to be varied. The laser energy was reduced with the use of a neutral density filter (Sigma Koki) and could also be controlled by the combination of a half-wave plate and polarizer at the position just before the multi-pass amplifier. The final focusing lens and chamber window may change the pulse width as well as induce ripples in the intensity spatial distribution due to the effects of the nonlinear index n_2 when the laser intensity is high. The changes in pulse width could in part be compensated by a chirp control at the position just

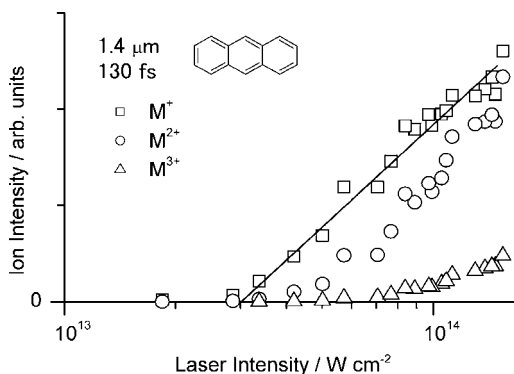


Fig. 6. Evaluation of laser intensity IV. The horizontal scale is corrected by the I_{sat} of a standard sample of Xe at $0.93 \times 10^{14} \text{ W cm}^{-2}$ for a pulse width of 130 fs at a wavelength of $1.4 \mu\text{m}$. Anthracene $I_{\text{sat}}^{\text{s}}$ was determined to be $0.30 \times 10^{14} \text{ W cm}^{-2}$ for the singly charged ion (M^+).

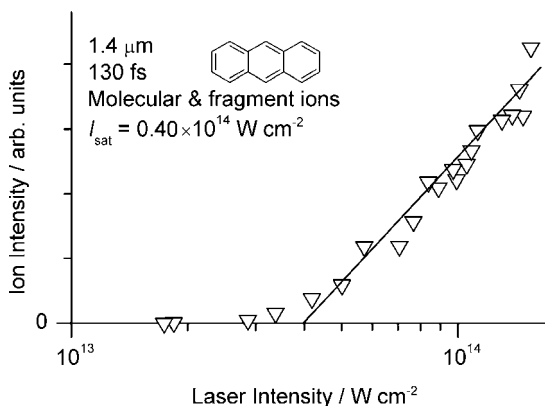


Fig. 7. Evaluation of laser intensity V. Anthracene I_{sat} was determined to be $0.40 \times 10^{14} \text{ W cm}^{-2}$ for a width of 130 fs at a wavelength of $1.4 \mu\text{m}$ by obtaining the sum of all of the molecular and fragment ions.

after the oscillator. It should be noted that the pulse distortion induced by the nonlinear index n_2 was not large, if the excitation pulse was longer than 130 fs.

The laser beam was focused with a 200 mm plano-convex lens into the TOF mass spectrometer. The pulse energy used in the experiments to measure I_{sat} was lower than 2 mJ per pulse. The laser polarization for the fundamental pulse of $0.8 \mu\text{m}$ was parallel to the direction of the ion extraction axis of the TOF tube.

3.2.4. Time-of-Flight (TOF) mass spectrometer

The present TOF mass spectrometer was a reflectron-type of spectrometer with a flight distance of 1.8 m (KNTOF-1800 TOYAMA) and a resolution of 2200 of $m/\Delta m$ at Xe^{129} . The typical voltages applied are indicated in Fig. 8.

The aperture diameters were 1 mm for anthracene and 12 mm for dioxins. An extraction aperture of 12 mm ϕ is considerably larger than that of the Rayleigh range. The intensity contours were expected to have "peanut-shaped" lobes, as in the case of an ideal beam. The intensity distribution of the focused beam of a Gaussian distribution in r (the direction of the radius) and a Lorentzian distribution in z (the beam direction) has already been presented in the literature.^{29,33,39}

The present laser beam was tightly focused to 33 μm in this study, and the e^{-2} point size was about 1.5 times the ideal value as seen in Sec. 2.2. A small aperture was indispensable for studying the Coulomb explosions, because many types of atomic ions and fragments with different momentum are produced under these conditions, and the distributions are highly dependent on the direction of the incident laser polarization. Shimizu *et al.* employed two 0.1 mm apertures⁴⁰ for studying the Coulomb explosion of benzene. Further detailed investigation of the Coulomb explosion mechanism has been carried out to examine the dependence of the volumetric intensity of ionic species from *d*-benzene, whereby the laser intensity reached $5 \times 10^{15} \text{ W cm}^{-2}$.²⁹ An aperture, even smaller than that of the size of the focal point was adopted. TOF would collect the ions from the weak intensity region in the direction of the TOF axis. When the laser intensity is approximately $1 \times 10^{14} \text{ W cm}^{-2}$ for organic molecules, the dominant

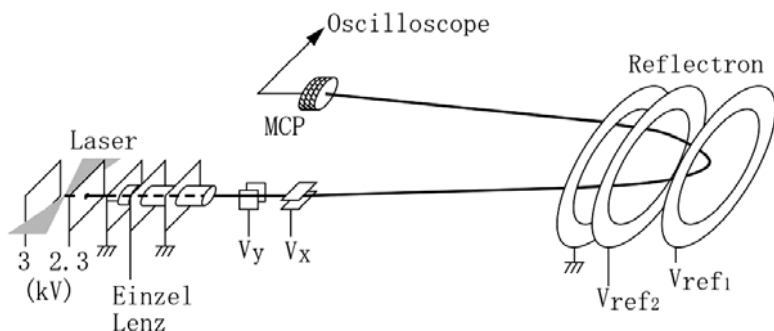


Fig. 8. Schematic diagram of a reflectron-type time-of-flight mass spectrometer. The polarization of the fundamental pulse of $0.8 \mu\text{m}$ was parallel to the flight axis. The typical applied voltages were 3, 2.3, and 0 kV (the ground), as indicated. The voltages of Einzel lens, V_x , $V_{\text{ref}1}$, $V_{\text{ref}2}$, and MCP were typically 1, 0, 0.075, 2, 3.1, and -2.1 kV, respectively. The plate which applied 2.3 kV has an aperture.

phenomena to be expected would be the ionization with some fragmentation and only a slight Coulomb explosion could occur. The differences due to aperture sizes of 1 and 12 mm were observed but were not substantial to suggest molecular ions form in low laser intensities. One of the differences was that the ratio of molecular ions to fragment ions in the case of the 12 mm aperture was twice that of the 1 mm aperture at an intensity that was twofold that of I_{sat}^s ($0.2 \times 10^{14} \text{ W cm}^{-2}$) at $0.8 \mu\text{m}$ for the case of anthracene. It should be noted that the value of I_{sat}^s was not very different; it is the same within experimental error, for both the 12 and 1 mm apertures. Even the larger aperture is advantageous for analytical purposes, because the optical alignment with a TOF tube is facilitated. Therefore, a 1 mm aperture was used for the critical mechanistic study, and a 12 mm aperture can be used for analytical purposes.

The sensitivity of an ion detector of a multi-channel plate (MCP) should not depend on the mass number to determine I_{sat} and discuss molecular ion intensity compared with small fragments. The sensitivity of a ion detector of multi-channel plate (MCP) has been studied in detail.⁴¹ According to the study the detection efficiency would be reduced approximately by three-quarter for the heaviest mass of 286 in a mass unit in this study. The ions were accelerated to 3 kV, and the voltage applied to the MCP was -2.1 kV . The efficiency of the detection of fragment ions would be somewhat higher than that for molecular ions, and, as a result, the ratio of the molecular ions to the total ions ($\Sigma(M^{z+} + \text{fragments})$) could be a maximum of 30% smaller than the actual value. In general, the detection efficiency must be taken into account for a qualitative determination of the intensities of ions with a large mass number.

The sample was introduced through a leak valve to a typical pressure level of $5 \times 10^{-5} \text{ Pa}$ under a back pressure of as low as $5 \times 10^{-7} \text{ Pa}$. The TOF data were recorded by a digital oscilloscope (Wave Runner 6100 LeCroy, 1 GHz). The mass spectra were sometimes contaminated by background gases, i.e. by signals from the H_2O^+ ion. Large molecules, the vapor pressures of which were low at room temperature, were heated and introduced as an effusive beam.

3.3. Ionization in Intense Laser Fields

3.3.1. Schematic diagram

The ionization mechanisms of organic molecules under various laser intensities can be explained with the help of a simple diagram, shown in Fig. 9. Although such schemes are originally applied for a single atom, they are

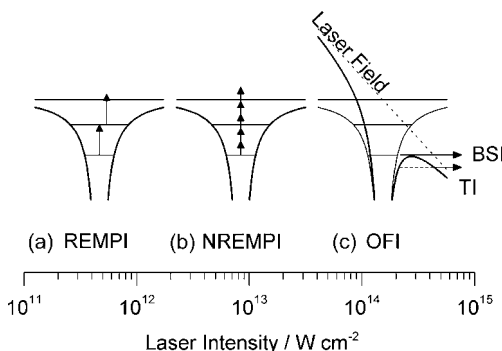


Fig. 9. Ionization mechanisms at different irradiation intensities. Schematic diagram under various laser intensities. (a) Resonance-enhanced multi-photon ionization (REMPI) is often used for the highly sensitive detection of molecules; region of laser intensity $\ll 10^{13} \text{ W cm}^{-2}$. (b) Non-resonant multi-photon ionization (NREMPI); intensity $\sim 10^{13} \text{ W cm}^{-2}$. (c) Optical field ionization (OFI), including tunnel (TI) and barrier suppression ionization (BSI); intensity $\sim 10^{14} \text{ W cm}^{-2}$. The electron energies close to the ionization potential are shifted by the ponderomotive potential, U_p , but are not indicated.

also useful to gain for understanding of the fundamental mechanisms of ionization and to estimate the order of laser intensity associated with the ionization mechanisms. In the case of molecules, multi-electron dynamics must be taken into account,^{21,22} as well as the particular shape and size of the Coulomb potential.^{11,23} Obviously, molecules often produce fragments in intense laser fields, in addition to the molecular ion formations, as discussed below.

In regions of laser intensity much lower than $10^{13} \text{ W cm}^{-2}$, occurrence of REMPI is well known.^{4,42} Laser light is tuned to a specific level, and a second photon ionizes the molecule. This approach is very effective for studying excited states and for the highly sensitive detection of molecules. Multiple perturbations or non-resonant multi-photon ionization (NREMPI) is expected to take place in the intensity region of $\sim 10^{13} \text{ W cm}^{-2}$. The absorption cross-section of two photons at $10^{13} \text{ W cm}^{-2}$ is expected to be comparable with that of the allowed transition of a dye molecule, assuming a cross-section of an allowed two-photon absorption on the order of $10^{-49} \text{ cm}^4 \text{ s}^{-1}$. Two- to four-photon absorptions have been reported for aromatic molecules, and some of the cross-sections have been determined.⁴³

Optical field ionization, including tunnel and barrier suppression ionization, starts at $10^{13} \sim 10^{14} \text{ W cm}^{-2}$. Multiple ionization eventually leads to a Coulomb explosion. Coulomb explosions for large molecules have been observed in intensity regions higher than $10^{15} \text{ W cm}^{-2}$ for C_{60} ,⁴⁴ and for benzene⁴⁰ in regions higher than $10^{16} \text{ W cm}^{-2}$. Proton dissociation from anthracene was found to occur starting at $0.5 \times 10^{14} \text{ W cm}^{-2}$.⁴⁵

3.3.2. Estimation of the order of intensity of molecular ionization

The electric field associated with a laser pulse forces electrons to oscillate. The electrons possess ponderomotive potential, or quiver energy, induced by linearly polarized laser light. The potential is the average kinetic energy of a free electron in the laser field, and is given by Eq. (7).

$$U_p = \frac{e^2 E_0^2}{4m\omega^2} = 9.33 \times 10^{-14} I_0 \lambda^2 \text{ [eV]}, \quad (7)$$

where E_0 is the electric field strength, I_0 (W cm^{-2}) is the laser intensity, and λ (μm) is the wavelength. The ponderomotive potential reaches 6 eV at $10^{14} \text{ W cm}^{-2}$ of a Ti-Sapphire laser at $0.8 \mu\text{m}$. This energy is added to the electrons which are in the highly excited Rydberg state; therefore, the ionization potential (I_p) in strong laser fields increases to $\sim I_p + U_p$. The required photon number N for multi-photon ionization should be greater than $(I_p + U_p)/h\nu$, where $h\nu$ is the photon energy. This phenomenon has been observed in the case of a Xe atom, and is referred to as above threshold ionization (ATI).⁴⁶ Concerning large molecules such as benzene and naphthalene, the ATI has been considered in the literature, and the electron kinetic energy has been measured⁴⁷; the required photon number N for the ionization of some aromatic molecules was found to support the validity of the above discussion.^{11,35}

Another important effect on molecular ionization processes is electron rescattering, which induces the fragmentation of molecules, as well as the generation of high harmonics. The maximum rescattering energy can be evaluated by the following Eq. (8).⁴⁸

$$\text{Rescattering energy}_{\text{max}} = 3.17 U_p. \quad (8)$$

Re-collision-induced fragmentation has been reported in an investigation of benzene,²³ and is claimed to be the dominant mechanism of fragmentation of C_{60} ²⁴ and CH_3OH .²⁵ The maximum re-collision energy in Eq. (8) is 19, 58, and 118 eV for 0.8, 1.4, and 2.0 μm , respectively, at $1.0 \times 10^{14} \text{ W cm}^{-2}$. These levels of energy are in excess of the average bond dissociation energy of C-H (4.38 eV)⁴⁹ as well as the ionization potentials of organic compounds, many of which are in the range of 5 to 13 eV. The efficiencies of fragmentation and/or excitation caused by re-collision have to be studied in detail.

$$h\nu_{\text{max}} = I_p + 3.17 U_p. \quad (9)$$

Equation (9) is known to depict the highest energy of harmonic generation,⁴⁸ and the VUV light in the water window region has been

generated.⁵⁰ Some organic molecules instead of rare gases have been used as nonlinear materials, and an infrared pulse was converted to VUV light.⁵¹

When U_p is similar to I_p , tunneling ionization (TI) can compete with NREMPI. The Keldysh parameter γ has been used for classifying TI or NREMPI:

$$\gamma = \frac{\omega}{\omega_t} = \sqrt{\frac{I_p}{2U_p}}, \quad (10)$$

where ω is the angular frequency of the laser light and ω_t is that of TI. TI is expected in the region of Keldysh parameter γ of less than 0.5, and NREMPI is predominant for $\gamma > 0.5$.⁵² In the case of $I_p = 9.25$ eV (benzene) and $\lambda = 0.8 \mu\text{m}$ the laser intensity at $\gamma = 0.5$ is $3.1 \times 10^{14} \text{ W cm}^{-2}$. While the Coulomb potential barrier is known to be suppressed below the ground electronic level, the electron is ionized in such cases. This type of ionization is referred to as barrier suppression ionization (BSI), and the threshold of I_{BS} is expressed by Eq. (11):

$$I_{\text{BS}} = \frac{cI_p^4}{128\pi Z^2 e^6} = 4.00 \times 10^9 \frac{I_p^4}{Z^2}, \quad (11)$$

where Z is the charge number of the produced ion. I_{BS} is calculated to be $2.9 \times 10^{13} \text{ W cm}^{-2}$ for $I_p = 9.25$ eV and $Z = 1$, and is approximately 1/10 that at the Keldysh parameter of $\gamma = 0.5$.

The I_{sat} values of rare gases can be accounted for by the ionization rate based on ADK theory,³⁸ which predicts the electron tunneling rate through a distorted potential by an external field. Although the above theory is valid for atoms, one can estimate the order of laser intensity for the I_{sat} values of large molecules. The I_{sat} values of the organic compounds, discussed here, were twice to ten times higher than the predicted values based on ADK theory. Hankin *et al.* have measured the ion signals of 23 organic molecules, including rare gases, with a 44 fs, $0.8 \mu\text{m}$ pulse of up to $1 \times 10^{15} \text{ W cm}^{-2}$.³⁷ The ionization efficiencies of benzene, cyclohexane, and other molecules were generally lower than the values predicted by ADK calculations. Similar tendencies have been observed for certain halogenated compounds.²⁰ In the case of anthracene, I_{sat} (at $1.4 \mu\text{m}$) was measured to be $3.0 \times 10^{13} \text{ W cm}^{-2}$,¹⁵ which is three times higher than the value obtained by ADK calculations. The high I_{sat} of organic compounds can be explained in terms of strong screening of the active electrons in the multi-electron system. The ionization rates observed for many organic molecules are much slower than the rates predicted by ADK calculations.

Recently, multi-electron dynamics have been considered for decatetraene²¹ etc., instead of applying a single active electron model to

examine the molecule. Regarding C_{60} , the Coulomb potential for atomic ionization was successfully revised by taking into account the size of the molecule.⁹ The suppression of ionization was observed in the case of Ni clusters,⁵³ as dynamic polarization due to the multi-electron system leads to strong screening by the active electron. Ionization rates of the transition metal atoms of V, Nb, Ta, Ni, and Pd were suppressed relative to single active electron approximation expectations.⁵⁴

Talebpour *et al.* have studied the ionization of both benzene and pyridine using a 200 fs pulse at 800 nm and an intensity range of $0.04 \sim 2 \times 10^{14} \text{ W cm}^{-2}$. Their results indicated that a multi-photon ionization model can account for the intensity dependence of the ion yields. The report by Talebpour *et al.* took into account the effective charge and molecular orbitals.⁵⁵

3.4. Ionization and Fragmentation of Large Molecules

3.4.1. Resonance versus non-resonance

We will discuss a key factor for determining the molecular and/or fragment ion formation of some organic hydrocarbons in intense femtosecond laser fields, namely, the molecular ion is predominant, provided that the excitation laser wavelength and the absorption spectrum of the target cation do not overlap, and vice versa.¹⁸ The fragmentation of hexatriene, benzene, dienes, some halogenated benzenes, and some molecules described in Sec. 3.4.4 can be reasonably accounted for in terms of the above-mentioned key factor: resonance *versus* non-resonance with the cation electronic levels.^{15–20} In fact the fragmentation is enhanced if the laser wavelength is in resonance, and is suppressed by a non-resonant wavelength.

Markevitch *et al.* quantitatively analyzed the power dependence of the fragmentation of a number of aromatic hydrocarbons in terms of sequential nonadiabatic excitation. The anthracene molecular ion was observed only in the low intensity range, and many fragment ions were observed instead of the molecular ion within the high intensity range.¹⁴ This fragmentation was explained by the transition to a dissociative state from a state, which Markevitch *et al.* referred to as a “doorway state”; the transition leads to the fragmentation of certain cyclic aromatic hydrocarbons. During this transition, the energy levels can be treated as a continuum, due to the optical Stark effect.

The irradiation of a large polyatomic molecules with a high-intensity laser pulse and measuring their ionization and fragmentation continue to be of great value. Different groups and/or different irradiation laser systems often gives different results. For example, anthracene was ionized by two different research groups using a femtosecond laser pulse at $0.8 \mu\text{m}$. Robson *et al.* observed molecular ions with many fragments from a number of aromatic hydrocarbons, including anthracene, treated at $0.8 \mu\text{m}$. They observed the molecular anthracene ion with fragmentation, even under resonant conditions with the cation absorption at $0.8 \mu\text{m}$ ^{12,13} and with rather high intensities of $1 \times 10^{15} \text{ W cm}^{-2}$. Markevitch *et al.* reported the complete fragmentation of anthracene at an intensity level of $1 \times 10^{14} \text{ W cm}^{-2}$.¹⁴ Even in our laboratory, the same molecule (2,3-dimethyl-1,3-butadiene) showed a somewhat different molecular/fragment ion pattern using different laser sources with the same intensity, pulse width, and polarization.

Infrared wavelengths with an excitation of longer than $0.8 \mu\text{m}$ of a Ti-Sapphire laser are important, because in this region, the non-resonance with the cation level can be achieved for many organic compounds. There are other issues of interest associated with long-wavelength excitation. For example, fragmentation induced by rescattering would be enhanced by a higher electron rescattering energy associated with higher ponderomotive force. The π -conjugated molecules of hexatriene, decatetraene, and β -carotene²¹ were irradiated at long wavelengths of $1.2\text{--}1.45 \mu\text{m}$, which gave substantially fewer fragment ions than when the same molecules were irradiated at $0.8 \mu\text{m}$. They explained that the ionization mechanisms are changed from nonadiabatic multi-electron ionization to a quasi-static tunneling one. C_{60} ⁹ was irradiated with long wavelengths, and the highly charged C_{60} reaching C_{60}^{12+} was detected at $1.8 \mu\text{m}$. Recently, Trushin *et al.* studied metal carbonyl compounds using various wavelengths ranging between $1.4\text{--}2.2 \mu\text{m}$.¹⁹ In fact, fragmentation was found to be enhanced when the laser wavelength was in resonance, and conversely, fragmentation was found to be suppressed by non-resonant wavelengths. Long-wavelength excitation could be effective for the investigation of organic molecular ions with few fragment ions.

3.4.2. Molecular ion formation from dienes

The molecule pair that exhibited contradistinctive TOF mass spectra consisted of 1,3-cyclohexadiene (1,3-CHD) and 1,4-cyclohexadiene (1,4-CHD).¹⁸ The results are shown in Fig. 10, along with the absorption spectra of the cations, which were taken from the literature.⁵⁶ The transition of

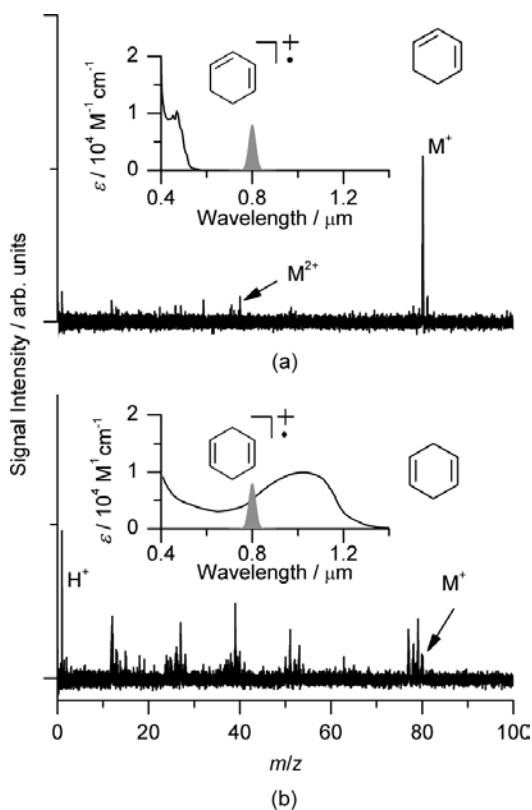


Fig. 10. (a) TOF mass spectra of 1,3-cyclohexadiene (1,3-CHD) and (b) 1,4-cyclohexadiene (1,4-CHD) at 0.8 μm with a 120 fs pulse width at an irradiation intensity of $0.6 \times 10^{14} \text{ W cm}^{-2}$. The molecular ions are indicated by M^+ , and the candidate for the doubly charged molecular ions is indicated by M^{2+} . The absorption spectra of the cations inserted here are taken from the literature.⁵⁶ The excitation laser spectrum is indicated in the figure. 1,3-CHD⁺ was not in resonance with the laser wavelength, which resulted in a high yield of molecular ions, whereas 1,4-CHD⁺ is resonant and gave many fragments.¹⁸

$1^2\text{B}_1 \leftarrow 1^2\text{A}_2$ of 1,3-CHD⁺ has a peak at 474 nm and is located in the spectral region shorter than 0.54 μm , whereas 1,4-CHD⁺ has a broad charge resonance band with a peak maximum at 1.04 μm and a molar extinction coefficient of $500 \text{ M}^{-1} \text{ cm}^{-1}$ at 0.8 μm . The highest peak in the TOF spectra of 1,3-CHD, as shown in Fig. 10(a), was due to the molecular ion, and the peak at mass number 40 was presumably the doubly charged molecular ion. 1,4-CHD⁺ [Fig. 10(b)] showed heavy fragmentation: the highest signal was that of H^+ , which observed along with a small molecular ion signal, and the fragment ions of C_nH_m^+ ($n = 1 - 6$).

The conclusion drawn based on the TOF spectra was that the degree of fragmentation is not enhanced by the size of the molecule, the number of σ bonds, or the polarizability, but it was found that resonance *versus* non-resonance with the cation electronic levels is the most important in this context. The same conclusion can be derived from another molecular pair, namely, 2,5-dimethyl-2,4-hexadiene (DH) and 2,3-dimethyl-1,3-butadiene (DB). DH showed a simple pattern, in which the major two peaks were assignable to the singly and doubly charged molecular ions, because DH^+ has a $1_2A_u \leftarrow 1_2B_g$ transition that starts from $0.65 \mu\text{m}$, peaks at $0.545 \mu\text{m}$, and the absorption intensity is negligibly small at $0.8 \mu\text{m}$. On the other hand, DB was heavily fragmented and DB^+ had an absorption transition overlapping the laser wavelength of $0.8 \mu\text{m}$, with a transition corresponding to the $1_2A_u \leftarrow 1_2B_g$ transition of butadiene⁺. DB^+ has a peak at $0.75 \mu\text{m}$, and the tail on the side of the long wavelength reached $0.85 \mu\text{m}$. The molar extinction coefficient at $0.8 \mu\text{m}$ could be read as $700 \text{ M}^{-1} \text{ cm}^{-1}$ from the spectrum in the low temperature matrix,⁵⁶ which is shown in the insert in Fig. 10. Therefore, based on these findings, it is reasonable to conclude that the fragmentation of DB^+ was caused by the resonance at the laser wavelength. The irradiation intensities were $0.6\text{--}0.7 \times 10^{14} \text{ W cm}^{-2}$, which corresponded to 0.6–0.8 times the I_{sat} values of these molecules.

3.4.3. *Wavelength dependence of 2,3-dimethyl-1,3-butadiene*

A molecular ion-dominant spectrum with small fragment ion intensities has been observed in the case of DB when excited with a $1.4 \mu\text{m}$ femtosecond pulse, as can be seen in Fig. 11(a), while many fragment ions were produced with a $0.8 \mu\text{m}$ femtosecond pulse, as shown in Fig. 11(b). The cation absorption spectrum shown in Fig. 11(c) revealed that the cation has no absorption at an excitation wavelength of $1.4 \mu\text{m}$; in this case, the non-resonant conditions hold. The fundamental laser beam was converted to a pulse of $1.4 \mu\text{m}$ with the parametric oscillator and amplifier system. The irradiation intensity was $1.6 \times 10^{14} \text{ W cm}^{-2}$, which corresponded to 1.4 times of the I_{sat} value of this molecule.

We noticed that the molecular ion intensity at $0.8 \mu\text{m}$ was higher than that obtained in previous experiments using a different laser source; the two experiments had been done under a similar irradiation intensity. The reason for this discrepancy could have been the instability of the laser. Strong signals might have been accumulated in previous experiments, because higher laser intensity is known to give higher degrees of fragmentation.

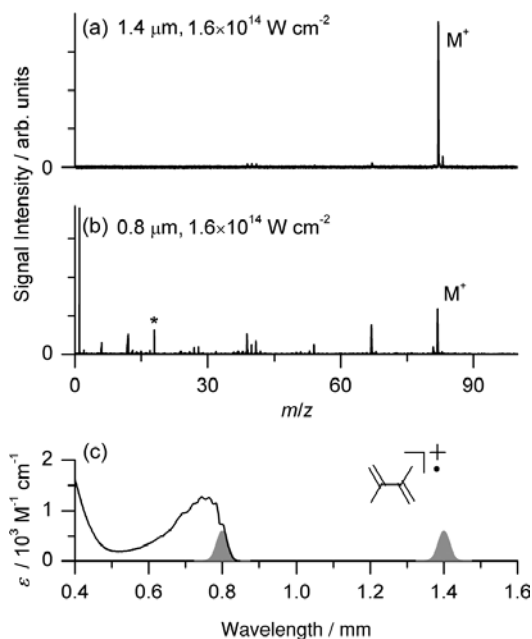


Fig. 11. TOF mass spectra of 2,3-dimethyl-1,3-butadiene, by (a) $1.4 \mu\text{m}$ excitation at an irradiation intensity of $1.6 \times 10^{14} \text{ W cm}^{-2}$ and (b) $0.8 \mu\text{m}$ excitation at an irradiation intensity of $1.6 \times 10^{14} \text{ W cm}^{-2}$. The molecular ion is indicated by M^+ . The asterisk (*) indicates H_2O^+ signal. (c) The absorption spectrum of DB at a low-temperature matrix.⁵⁶ The two shaded Gaussian shapes indicate the spectra of the excitation pulses.

In fact, the present spectrum shown in Fig. 11(b) has a high mass fragment of C_5H_7^+ , with the highest intensity among fragments observed here using a highly stable laser; the C^+ signal was found to have the highest intensity signal in a previous study.¹⁸ Carbon ion should be produced at high laser intensities.

3.4.4. Molecular ion formation of some organic molecules

Anthracene

The ionization and fragmentation of anthracene have been well studied in detail by three different groups.^{12–15} Heavy fragmentation at $0.8 \mu\text{m}$ has been observed and molecular ion remained.^{12–14} Anthracene has recently been re-examined with femtosecond pulses at two different wavelengths, i.e. $0.8 \mu\text{m}$ (resonant with the electronic levels of the cation) and $1.4 \mu\text{m}$

(non-resonant). These observations can be explained by the cation absorption spectrum, namely, the cation absorption is in resonance at $0.8 \mu\text{m}$ and heavy fragmentation occurs, but not in resonance at $1.4 \mu\text{m}$ and the molecular ion is predominant.¹⁵

Biphenyl

The TOF mass spectra of biphenyl are shown in Fig. 12(a), with $1.4 \mu\text{m}$ excitation at an irradiation intensity of $0.84 \times 10^{14} \text{ W cm}^{-2}$, and in Fig. 12(b), with $0.8 \mu\text{m}$ excitation at an irradiation intensity of $0.74 \times 10^{14} \text{ W cm}^{-2}$. The singly charged molecular ion is indicated by M^+ . The mass number of 77 reflects M^{2+} and/or the fragment ion of C_6H_5^+ . The cation absorption spectrum is shown here, and indicates almost a non-resonant at $1.4 \mu\text{m}$. The

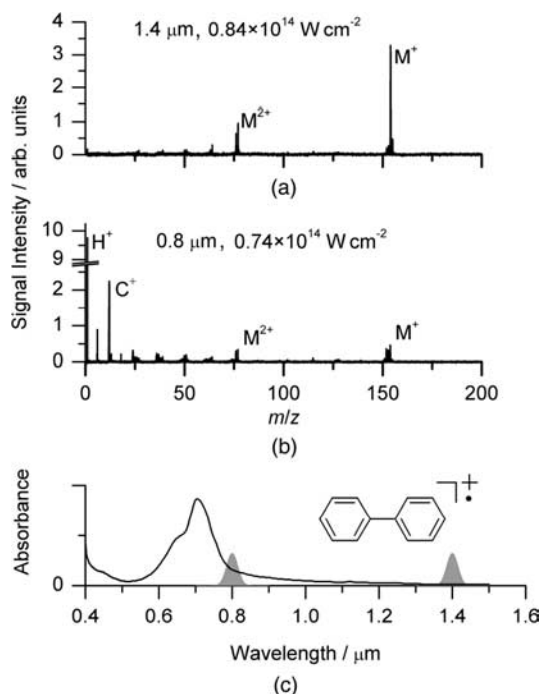


Fig. 12. TOF mass spectra of biphenyl, by (a) $1.4 \mu\text{m}$ excitation at an irradiation intensity of $0.84 \times 10^{14} \text{ W cm}^{-2}$ and (b) $0.8 \mu\text{m}$ excitation at an irradiation intensity of $0.74 \times 10^{14} \text{ W cm}^{-2}$. The singly charged molecular ion is indicated by M^+ . The mass number of 77 is M^{2+} and/or the fragment ion of C_6H_5^+ . The cation absorption spectrum is shown, and the cation has an isolated resonance at $1.4 \mu\text{m}$. The value of I_{sat} at $1.4 \mu\text{m}$ was $0.84 \times 10^{14} \text{ W cm}^{-2}$. The two shaded Gaussian shapes represent the excitation spectra.

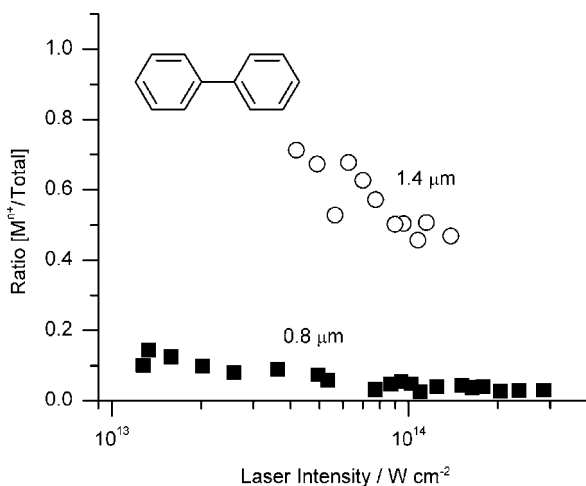


Fig. 13. The M/T ($\Sigma(M^{2+} + \text{fragments})$) ratio. Filled squares (■), 0.8 μm excitation; open circles (○), 1.4 μm excitation. The ratio was 0.5 at an I_{sat} value of $0.84 \times 10^{14} \text{ W cm}^{-2}$ at 1.4 μm , whereas heavy fragmentation at 0.8 μm excitation reflects a low ratio of 0.05.

value of I_{sat} at 1.4 μm was $0.84 \times 10^{14} \text{ W cm}^{-2}$. Figure 13 shows the ratio (M/T ratio) of the molecular ions to the total ions ($\Sigma(M^{2+} + \text{fragments})$). Filled squares (■) indicate 0.8 μm excitation, and open circles (○) indicate 1.4 μm excitation. The M/T ratio was 0.5 at the intensity of I_{sat} with 1.4 μm excitation, whereas heavy fragmentation was seen at 0.8 μm excitation. Biphenyl in femtosecond fields has been examined at 0.78 μm .⁵⁷ Although the molecular ion was observed at a weak laser intensity, fragment ions were predominant at $0.3 \times 10^{14} \text{ W cm}^{-2}$. The present results at 0.8 μm reproduced those of a previous report.⁵⁷ The long wavelength excitation was found to reduce the signals of fragmented ions.

Dibenzofuran

Figures 14 and 15 show the results of dibenzofuran. The TOF mass spectra were obtained by (a) 1.4 μm excitation at an irradiation intensity of $0.38 \times 10^{14} \text{ W cm}^{-2}$, and (b) 0.8 μm excitation at an irradiation intensity of $0.38 \times 10^{14} \text{ W cm}^{-2}$. The molecular ions are indicated in the figures by M^+ and M^{2+} . The cation absorption spectrum is shown, and indicates isolated resonance at 1.4 μm . The value of I_{sat} at 1.4 μm was $0.98 \times 10^{14} \text{ W cm}^{-2}$.

The M/T ratios are plotted in Fig. 15 for various wavelengths. Longer wavelengths gave a larger ratio. The M/T ratio reached 0.75 at 1.5 μm at an intensity of $1.0 \times 10^{14} \text{ W cm}^{-2}$, which was close to the I_{sat} value at 1.4 μm .

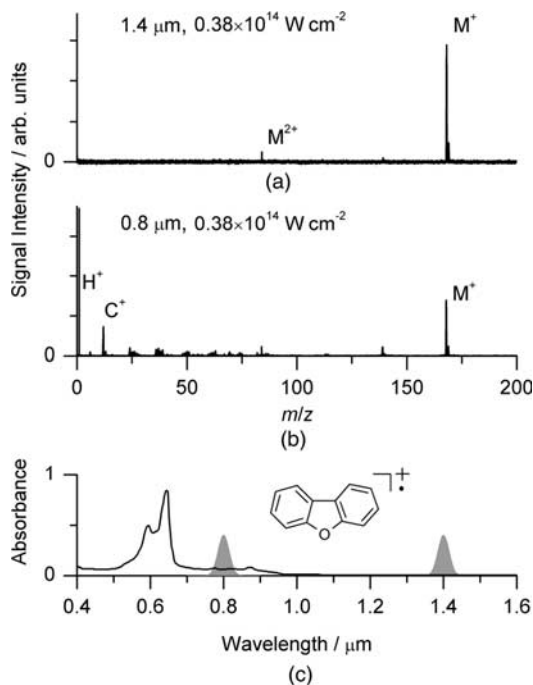


Fig. 14. TOF mass spectra of dibenzofuran by (a) 1.4 μm excitation at an irradiation intensity of $0.38 \times 10^{14} \text{ W cm}^{-2}$ and (b) 0.8 μm excitation at an irradiation intensity of $0.38 \times 10^{14} \text{ W cm}^{-2}$. The molecular ions are indicated by M^+ and M^{2+} . (c) The cation absorption and excitation pulse spectra are shown and they indicate isolated resonance at 1.4 μm. The value of I_{sat} at 1.4 μm was $0.98 \times 10^{14} \text{ W cm}^{-2}$.

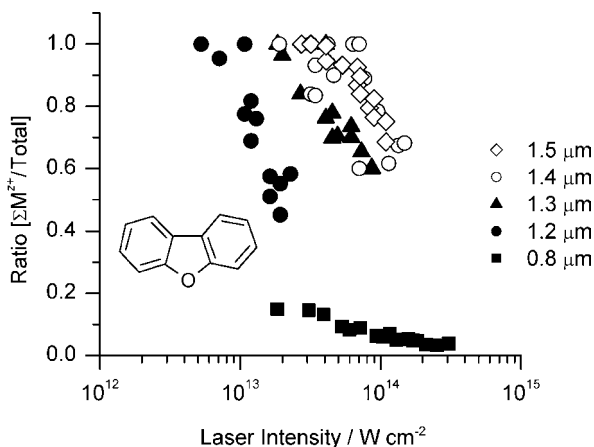


Fig. 15. The M/T ratio versus laser intensity of dibenzofuran at various wavelengths. Longer wavelength gave higher ratio. The value of the M/T ratio reached 0.75 at 1.5 μm at an intensity of $1.0 \times 10^{14} \text{ W cm}^{-2}$, which was close to the value of I_{sat} at 1.4 μm.

Dioxin

Dibenzo-*p*-dioxin (dioxin) was irradiated and heavy fragmentation was observed at $0.8 \mu\text{m}$.²⁰ Figure 16 shows the TOF spectra of dioxin at two wavelengths. Heavy fragmentation was confirmed with $0.8 \mu\text{m}$ excitation, although the molecular ion remained. Clear differences between the TOF spectra at the two wavelengths were observed. Fragment ions were suppressed at $1.4 \mu\text{m}$ excitation.³¹ The M/T ratio was 0.6 at an I_{sat} value of $0.86 \times 10^{14} \text{ W cm}^{-2}$ at $1.4 \mu\text{m}$, whereas the M/T ratio was less than 0.05 at $0.8 \mu\text{m}$ excitation, as shown in Fig. 17. Although the absorption spectrum of the ion was not available, the photoelectron spectrum could be used to judge whether the cation electronic levels were in resonance or non-resonance with the excitation wavelengths. The spectrum indicates that a laser wavelength of $0.8 \mu\text{m}$ was resonant, and a wavelength of $1.4 \mu\text{m}$ could be regarded as non-resonant.

Comments on C_{60} Ionization

Multiple charged fullerene ions C_{60}^{z+} ($z = 1 - 12$) have been observed in response to the intense femtosecond pulse irradiation. Bhardwaj *et al.*

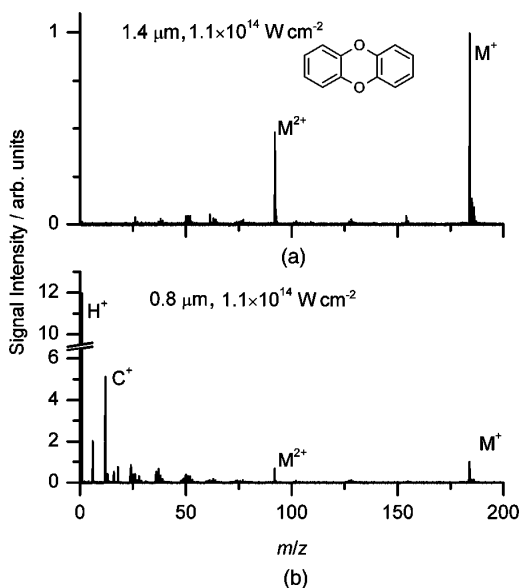


Fig. 16. TOF mass spectra of dibenzo-*p*-dioxin at an irradiation intensity of $1.1 \times 10^{14} \text{ W cm}^{-2}$ by (a) $1.4 \mu\text{m}$ excitation and (b) $0.8 \mu\text{m}$ excitation.³¹ The molecular ions are indicated by M^+ and M^{2+} , which reflect singly and doubly charged dioxin, respectively. The I_{sat} value was $0.81 \times 10^{14} \text{ W cm}^{-2}$ at $0.8 \mu\text{m}$ and $0.86 \times 10^{14} \text{ W cm}^{-2}$ at $1.4 \mu\text{m}$.

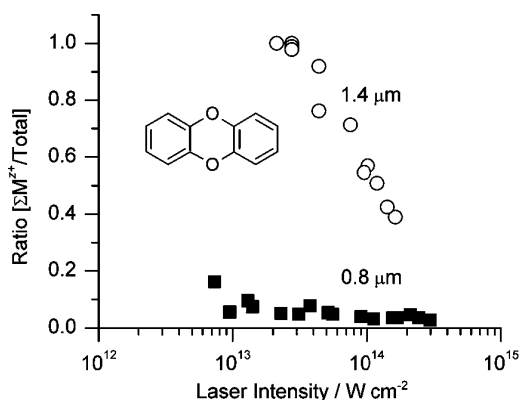


Fig. 17. M/T ratio of dibenzo-*p*-dioxin *versus* laser intensity at two wavelengths: filled squares (■), 0.8 μm excitation, and open circles (○), 1.4 μm excitation. The ratio of 0.6 was observed at an I_{sat} value of $0.86 \times 10^{14} \text{ W cm}^{-2}$ at 1.4 μm , whereas heavy fragmentation was seen with 0.8 μm excitation with a ratio of 0.05.

found up to C_{60}^{12+} at 1.8 μm with a 70 fs pulse at an irradiation intensity of $\sim 1 \times 10^{15} \text{ W cm}^{-2}$,⁹ whereas up to C_{60}^{5+} was detected by a 0.79 μm pulse with a 25 fs duration by Campbell *et al.* at an intensity of up to $6 \times 10^{14} \text{ W cm}^{-2}$.⁸ We recall that the cation absorption of C_{60} has a large molar extinction coefficient of $2700 \text{ M}^{-1} \text{ cm}^{-1}$ at an excitation wavelength of 0.8 μm , and a negligibly small coefficient at 1.8 μm ,⁵⁹ as shown in Fig. 19. The long wavelength of 1.8 μm seems suitable to produce C_{60}^{z+} molecular ions with high charges due to its non-resonance with the cation absorption, because the degree of fragmentation is expected to be reduced under non-resonant conditions.

C_{60} is fragmented to C_{60-2n} through n times of C_2 -loss reaction with nanosecond pulse excitation.¹⁰ The C_{60} cation exhibits strong absorption at

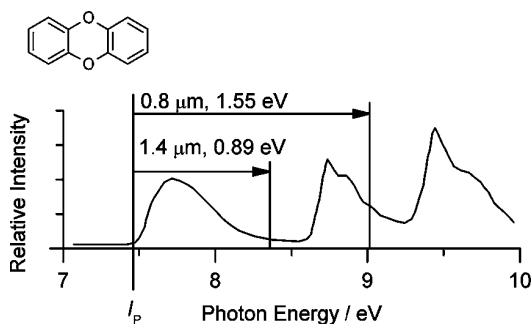


Fig. 18. The photoelectron spectrum of dibenzo-*p*-dioxin indicates that a laser wavelength of 0.8 μm is resonant, and a wavelength of 1.4 μm can be regarded as non-resonant. The spectrum is re-plotted from Ref. 58.

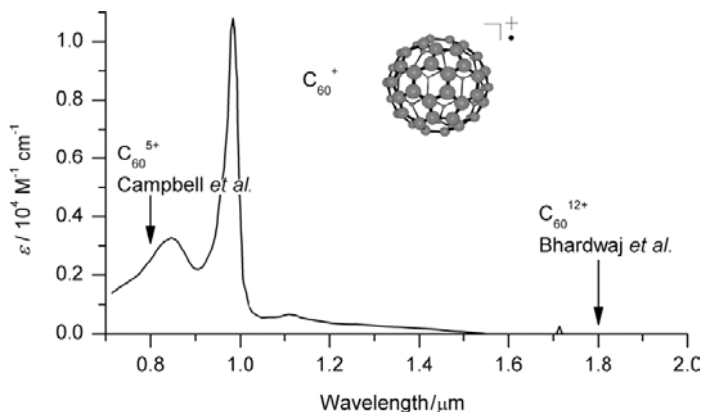


Fig. 19. The absorption spectrum of C_{60} cation.⁵⁹ Detection of multiple charged fullerene ions C_{60}^{z+} ($z = 1-12$) has been observed by Bhardwaj *et al.* C_{60}^{12+} is formed at $1.8 \mu\text{m}$ with a 70 fs pulse at an irradiation intensity of up to $1 \times 10^{15} \text{ W cm}^{-2}$,⁹ whereas up to C_{60}^{5+} was detected by a $0.79 \mu\text{m}$ pulse with a 25 fs duration by Campbell *et al.*⁸ at an intensity of up to $6 \times 10^{14} \text{ W cm}^{-2}$. Fragmentation could be reduced by non-resonant conditions in the case of $1.8 \mu\text{m}$ excitation.

the excitation wavelength of $0.532 \mu\text{m}$ with a molar extinction coefficient of $5400 \text{ M}^{-1} \text{ cm}^{-1}$,⁵⁹ and the mechanism of fragmentation can be categorized to the so-called ladder-switching model.³ Wurz and Likke have estimated the dissociation rate constant of C_{60}^+ using Eq. (12).¹⁰ The rate of the unimolecular decay of C_{60} has been calculated to be in the order of 10^6 s^{-1} using the activation energies of 4.6–5.6 eV. The internal energy is approximately 4000 kJ mol^{-1} . A compelling reason for the formation of molecular ions by femtosecond laser excitation would be that the dissociation rate is much slower than 10^6 s^{-1} . The formation of C_{60}^{z+} implies that the internal energy in the femtosecond pulses is far below 4000 kJ mol^{-1} .

According to statistical reaction rate theory, a larger ion size will reduce the rate of fragmentation. We can estimate the order of the typical bond-breaking rate by the following equation

$$k_f = \frac{W}{h\rho}, \quad (12)$$

where k_f is the fragmentation rate of the cation in an intense laser field, W is the number of channels open to dissociation, h is the Planck's constant, and ρ is the density of the state.⁶⁰

The decay rate of the benzene cation has been investigated in detail.⁴ The internal energy is sharply defined in two-laser pump-probe experiments. The actual decay reactions are composed of H, H_2 , and C_nH_m loss channels. The rate is 10^6 s^{-1} at 510 kJ mol^{-1} . In the present system, the

acceleration time in the TOF was approximately $1 \mu\text{s}$ for benzene. We know that the benzene ion is heavily fragmented under resonant conditions at 375 nm or 400 nm.^{17,61,62} At these wavelengths, the molar extinction coefficient of the benzene cation is $950\text{M}^{-1}\text{cm}^{-1}$.⁶³ The accumulated energy could be estimated to be much greater than 510 kJ mol^{-1} by 400 nm excitation. On the other hand, the energy is considered too far below 4000 kJ mol^{-1} in the case of C_{60} molecular ion formation. Polyaromatic hydrocarbons (PAHs) can represent intermediate cases between benzene and C_{60} . Larger PAHs will have a slower dissociation rate, and eventually a molecular ion of PAH could survive under resonance conditions with femtosecond pulse excitation. Figure 20 shows a summary of the above discussion.

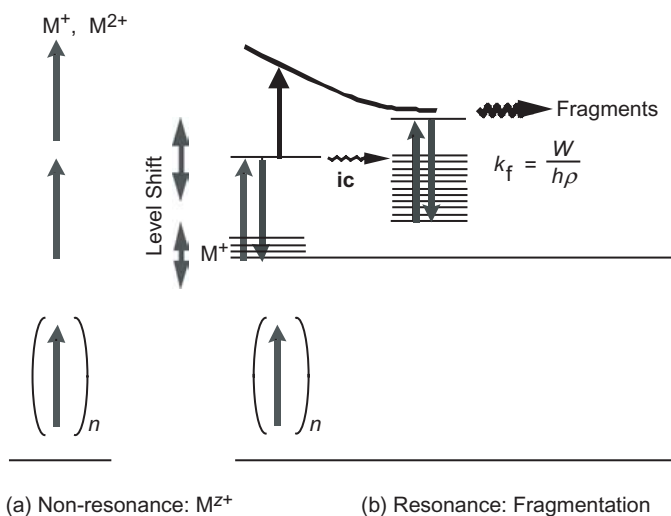


Fig. 20. Mechanisms of ionization and molecular ion formation by NREMPI. (a) Molecular-ion formation will be dominant, and a multiple charged cation will be produced, finally leading to a Coulomb explosion, provided that the excitation wavelength is non-resonant with the electronic absorption of the molecular cations. In the case of (b), fragmentation is dominant if the excitation wavelength is resonant with the electronic absorption of the molecular cations. A high-intensity pulse creates dynamic broadening of the power of the molecular electronic levels. Stark broadening (approximately several eV) of the molecular eigenstates occurs. At least the tail part of the excitation pulse could contribute to the energy deposition through the resonance, because the intensity is low. If there is a low-lying dissociation channel, the ions will dissociate immediately. Efficient non-radiative transition to the electronic ground state of the cation is also expected to occur in the laser fields. Intramolecular redistribution occurs, and a vibrationally excited ion (hot ion) forms. The laser light can be resonant with the electronic level of the hot cation. The internal energy eventually increases to far above the dissociation energy. The vibrationally excited ion undergoes dissociation at a statistically predictable rate.

It should be noted that the ions dissociate immediately, if there is a low-lying dissociation channel. Recently, Markevitch *et al.* have analyzed the transition to the dissociation channels under intense laser fields for some large organic molecules.¹⁴

3.4.5. Pulse width dependence

We have seen that irradiation with an intense and infrared femtosecond pulse can produce an intact molecular ion from certain organic compounds, whereas nanosecond pulse excitation often induces fragmentation of the molecule. It is generally accepted that a shorter pulse is better for producing a molecular ion; however, the experimental results have been limited to the pulse duration range from picoseconds to femtoseconds. A representative molecule, C₆₀, has been ionized by short pulses from 5 ps to 25 fs, and the short pulse of 25 fs has been shown to produce C₆₀^{z+} (z = 1, 2) without heavy fragmentation.²⁶

Levis *et al.* have demonstrated that tailored pulse excitation can control product distributions for some ketone molecules.⁶⁴ Optimization of the pulse shape with strong-field laser fields has been shown to govern cleavage and rearrangement pathways. By using the feedback obtained from the observed reaction products, a learning algorithm can guide a pulse shaper to best achieve the desired product.

Itakura *et al.* studied the dissociative ionization of ethanol with a chirped laser pulse.²⁷ The potential curve in the strong laser field was found to govern the two bond-breaking reactions of the C-O and C-C bonds. The negative and positive chirped pulses gave similar fragmentation patterns; therefore, the patterns indicated that the holding time of the singly ionized state is important to proceed to further ionization and fragmentation. Mathur and Rajgara studied the pulse duration and chirp direction dependencies for methane,⁶⁵ and they observed higher-intensity H₂⁺ and H⁺ ions with large chirp pulses.

Another example of pulse width dependence is shown in Figs. 21 and 22. DB was irradiated with pulses of three different durations, i.e. 35 and 300 fs, and 1 ps, at 0.8 μm.²⁸ Under the laser intensity of 0.22 × 10¹⁴ W cm⁻², the molecular ion intensity at 35 fs was the strongest relative to the fragment ions.

The molecular ion practically disappeared at the longest pulse duration of 1 ps excitation, and fragment ions with a small mass number *m/z* of less than 40 emerged, as well as a doubly charged carbon. The intermediate features are seen at a 300 fs pulse excitation. This molecule has

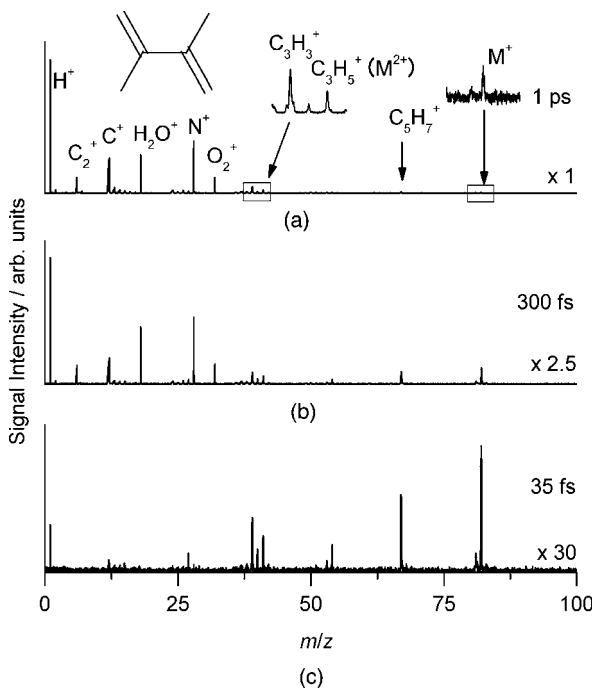


Fig. 21. (a) TOF Mass spectra of 2,3-dimethyl-1,3-butadiene at the pulse durations shown. The molecular ion signal was relatively strengthened with decreases in pulse width. Magnified signals are shown in the inset. Each irradiation intensity was maintained at ca. $0.22 \times 10^{14} \text{ W cm}^{-2}$. The signals of N_2^+ , O_2^+ , and H_2O^+ were from contaminants in the chamber, and the H^+ signal presumably reflected the ionization and dissociation of H_2O .²⁸ In (a), fragments and molecular ions are magnified by 10 and 60 times, respectively. The signal intensities in (b) and (c) were magnified by 2.5 and 30 times, respectively.

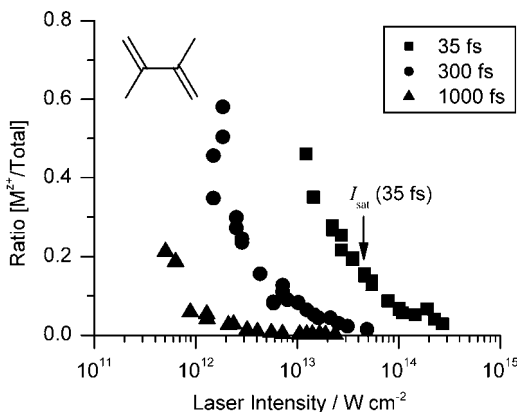


Fig. 22. The M^+/T^+ ratios of DB at three different laser pulse widths of 35 and 300 fs, and 1 ps at $0.8 \mu\text{m}$.

been examined previously and is discussed in Sec. 3.4.2 and Sec. 3.4.3. Figure 11 shows the mass spectra at 0.8 and 1.4 μm , with the absorption spectrum of the cations considered for the molecular ion formation under non-resonance at 1.4 μm . As seen in Fig. 19, the cation absorption of C_{60} , and the pulse duration dependence for C_{60} and DB were studied under resonant conditions. Short femtosecond pulses produced molecular ions, whereas picosecond pulses produced numerous fragment ions.

The total ion intensities increased with the increase of laser intensity, and the atomic ion intensities were stronger in regions of higher intensities. The M/T ratios of DB are shown in Fig. 22 at three different pulse widths, i.e. 35 and 300 fs, and 1 ps, with 0.8 μm laser pulses. Impurity ions such as N_2^+ , O_2^+ , and H_2O^+ were omitted from the evaluations. The molecular ion intensities decreased, namely, the ratios became smaller with increases in the laser intensity. It is clear from the plots of the M/T ratio in Fig. 22 that a shorter pulse gave a higher value, if the M/T ratios are compared at a certain irradiation intensity. The I_{sat} value for the 35 fs pulse was $0.45 \times 10^{14} \text{ W cm}^{-2}$.

The femtosecond pulse shape was a transform limited for the 35 fs pulse; however, other two long pulses were bell-shaped (300 fs) and triangle-shaped (1 ps). The chirp directions of the elongated pulses were negative. Even when the chirp direction was changed to either positive or negative, the changes in ion intensities and their distributions remained small within the present experimental conditions and DB. Figure 23 shows experimental results for the case of 130 fs pulse.

3.4.6. *Electron rescattering*

Re-collision-induced fragmentation has been reported for benzene,²³ and is indicated to be the important mechanism of fragmentation for C_{60} ²⁴ and methanol, as well as in other molecules.²⁵ The maximum re-collision energy in Eq. (8) is 58 eV for 1.4 μm at $1.0 \times 10^{14} \text{ W cm}^{-2}$. The energy is in excess of the average bond dissociation energy of C-H (4.38 eV) and the ionization potentials of organic compounds, many of which are in the range of 5 to 13 eV, and even well above the ionization potentials of doubly charged molecular ions (M^{2+}), which are approximately 2.7-fold that of M^+ .⁶⁶

Brief comments on electron rescattering are provided for the case of anthracene under non-resonant conditions, as shown in Fig. 24. The effects are expected to decrease due to the use of a laser pulse that deviates from

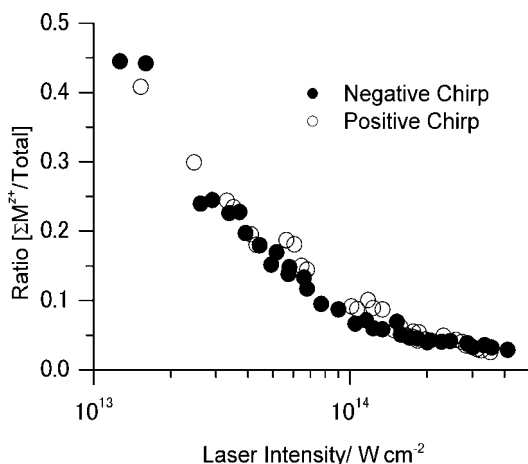


Fig. 23. The M/T ratio *versus* laser intensity of 2,3-dimethyl-1,3-butadiene at $0.8 \mu\text{m}$ excitation. Pulse width was stretched to 130 fs with the linear chirp introduced by DAZZLER. Filled circles (\bullet), negative; open circles (\circ), positive.

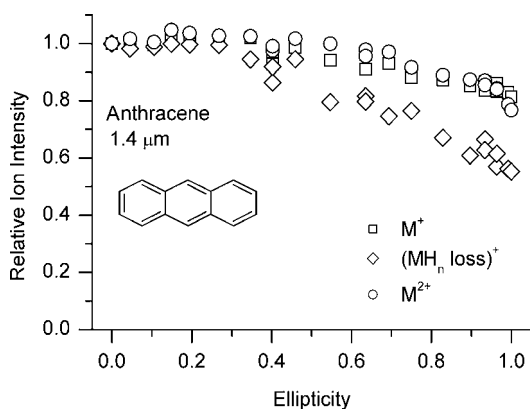


Fig. 24. Polarization dependencies of the molecular ions M^+ , M^{2+} , and fragment ions of $(MH_n \text{ loss})^+$ (nH detached fragments from M^+) at $1.4 \mu\text{m}$ at a constant intensity of $1.5 \times 10^{14} \text{ W cm}^{-2}$. The intensity was 3.75-fold of I_{sat} , and the maximum electron rescattering energy is calculated to be 87 eV. A preliminary conclusion is that the rescattering effects on the fragmentation and secondary ionization are small (see the text).

linearly polarized light, because the orbit of the launched electron does not cross the molecule on irradiation with circularly polarized light. Clear polarization dependencies have been observed for benzene, $C_{60}^{3,4+}$, and methanol; therefore, such studies provide evidence of re-collision. Some

polarization dependencies in molecular ion M^+ , M^{2+} , and fragment ions ($(MH_n \text{ loss})^+$ fragments indicate nH detached fragments from M^+) were observed in the high ellipticity range for the case of anthracene as shown in Fig. 24. Anthracene was irradiated at a wavelength of $1.4 \mu\text{m}$ and an intensity of $1.5 \times 10^{14} \text{ W cm}^{-2}$. The intensity was 3.75-fold that of I_{sat} , and the maximum electron rescattering energy reached 87 eV, which is far above the bond dissociation energy (i.e. below several electron volts) and the second ionization energy of 21.1 eV for anthracene. In the case of benzene, a drastic change was observed in the range of ellipticities from 0 to 0.4. Figure 24 shows the three species almost constant in this ellipticity range. Therefore, the efficiency of electron impact ionization and fragmentation could be small. All of the species decreased in the high ellipticity range from 0.4 to 1.0. To obtain the same ionization rate as the linearly and circularly polarized pulse, the field strength has to be adjusted (1.54 times in the intensity).⁶⁷ If a circularly polarized pulse with a 1.54 times high intensity is irradiated, all the intensities of the three species, especially the fragment intensity would increase. As a conclusion, the rescattering effects on the fragmentation and secondary ionization seemed to be small for the case of anthracene. Similar conclusions have been derived for the case of naphthalene.⁶⁸

3.4.7. Comparison with electron impact excitation spectra

Electron impact excitation and the associated spectra (EI spectra)⁶⁹ are commonly used as a standard method employed for the identification of molecules. The spectra obtained by femtosecond ionization should be compared with those obtained by EI. According to the EI method, sample molecules in the vapor phase are bombarded by fast moving electrons, conventionally those with 70 eV energy. This procedure results in ion formation. Some of the molecular ions decompose, and fragment ions are formed. The fragmentation of a given ion is due to the excess of energy required as part of the ionization. EI mass spectra contain intense fragment ion peaks. The molecular ion peak is not always the highest.

Laser excitation gives more simple spectra near the I_{sat} value, as shown in Fig. 25. In the case of DB, the EI spectrum contained intense fragment ion peaks, while the femtosecond ionization spectrum gave fragment ions of negligible intensity compared to that of the molecular ion. In the case of anthracene, the differences between the femtosecond ionization and EI

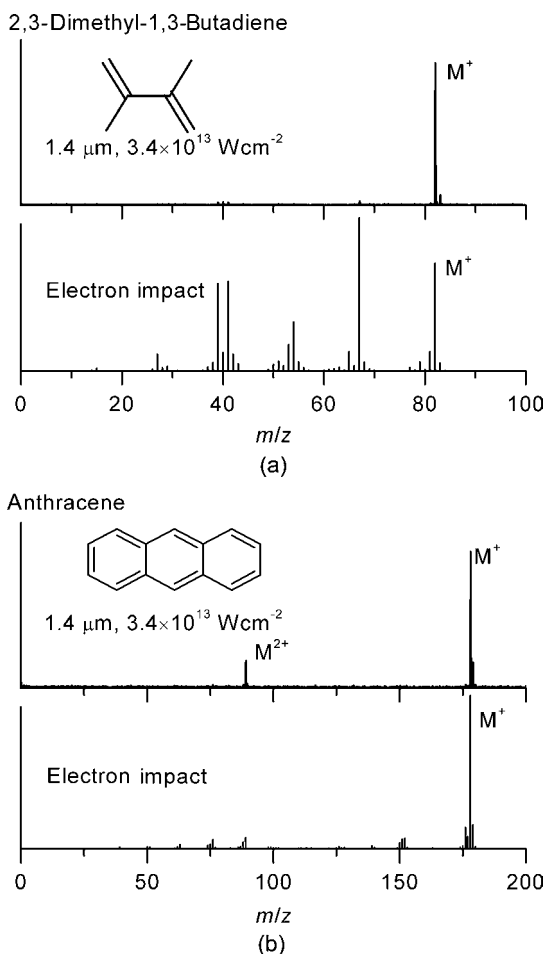


Fig. 25. Comparison of the mass spectra obtained by femtosecond laser ionization at $1.4 \mu\text{m}$ excitation of 130 fs pulses and electron impact ionization of (a) 2,3-dimethyl-1,3-butadiene and (b) anthracene. The EI spectra are taken from Ref. 69.

spectra were not significant, but the femtosecond spectrum showed both M^+ and M^{2+} , and the EI spectrum contained many fragments. It should be noted that both of these molecules were excited at $1.4 \mu\text{m}$, a level at which there is non-resonance in the zero field. Even in the case of resonance at $0.8 \mu\text{m}$ for DB, the strongest peak was still that of the molecular ion, as seen in Fig. 11. Based on these results, the femtosecond ionization method is considered to be useful for chemical analyses, and non-resonance excitation is thought to render such analysis easier.

3.5. Applicability to Femtosecond Laser Mass Spectrometry

3.5.1. FLMS and dioxins

Intact molecular ion formation with only slight fragmentation by an intense femtosecond pulse has been demonstrated above. These characteristic features are expected to be of great advantage, allowing femtosecond laser mass spectrometry (FLMS) for sensitive analytical purposes.⁶² Ledingham and coworkers have studied a number of PAHs and Nitro-PAHs for the development of FLMS.^{12,13,70–74} FLMS trials and related trials have been carried out using a variety of molecules, including metal carbonyls and biomolecules.^{75,76} Many persistent organic pollutants are chlorinated compounds. It is therefore important to examine whether or not chloro-compounds produce molecular ions. Ionization and fragmentation from more than ten chlorinated compounds have been examined by the present author's group in a high-intensity femtosecond laser field.²⁰

As regards the potential analytical applications of this approach, REMPI with a tunable laser pulse has been shown to be effective for the detection of trace quantities of organic compounds. Isomers of polychlorodioxins and polychlorobenzenes have been separately detected by REMPI. To date, the number of chlorine atoms in these molecules were thought to be limited to less than four.^{77,78} It is of great importance to be able to detect molecules containing multi-chlorine atoms, because some of these molecules are highly toxic. Pentachlorobenzene concentration levels have been shown to correlate with the concentrations of toxic equivalent dioxin in the stack gas of a hazardous waste incinerator,⁷⁷ and pentachlorobenzene was ionized without heavy fragmentation by femtosecond excitation.²⁰ It is therefore important to determine whether or not the FLMS could be of potential use in the detection of dioxins. However, FLMS trials remain in the early stages; therefore, many experimental parameters must still be investigated in detail in order to develop this method of detection. Wavelength dependency is of note in this context, and some of the relevant results are discussed below. Very recently, Kirihara and coworkers have successfully measured pentachlorodioxins by the method of REMPI.⁷⁹

Femtosecond laser mass spectrometry (FLMS) has been successfully applied for detecting three trichlorinated dioxins, 1,3,6-trichlorodibenzo-*p*-dioxin, 2,4,6-trichloro-dibenzofuran, and 2,2',5-trichlorobiphenyl.^{31,80}

The formation of molecular ions without heavy fragmentation is an important aim of FLMS; in other words, a high *M/T* ratio must be attained with FLMS. We have seen that the *M/T* ratio depends on the laser intensity as well as on the wavelength. The general tendency indicates that dioxins

are fragmented with increases in laser intensity. The chlorinated compounds studied here tend to show more fragmentation with increases in laser intensity, compared to the non-chlorinated dioxins. All of the ratios observed have been higher with increases in laser wavelength. The latter trend is most likely due to the fact that C-Cl bonds have a dissociation energy lower than C-C and C-H bonds, and the C-Cl bond is thus more easily dissociated in high-intensity laser fields; in turn, such dissociation induces further fragmentation. However, the M/T ratios attained here were 0.5 when observed under the optimum laser wavelength and intensity conditions.

Within our experimental parameters, the best laser parameters were observed as follows: 1.5 μm excitation with an intensity of $3.0 \times 10^{13} \text{ W cm}^{-2}$ for 1,3,6-trichlorodibenzo-*p*-dioxin, and 2.0 μm excitation and an intensity of $0.33 \times 10^{14} \text{ W cm}^{-2}$ for 2,2',5-trichlorobiphenyl.

3.5.2. Trichlorodioxins

2,2',5-Trichlorobiphenyl was irradiated with an intense femtosecond pulse at four different wavelengths.³¹ The TOF spectra are shown in Fig. 26. Fairly

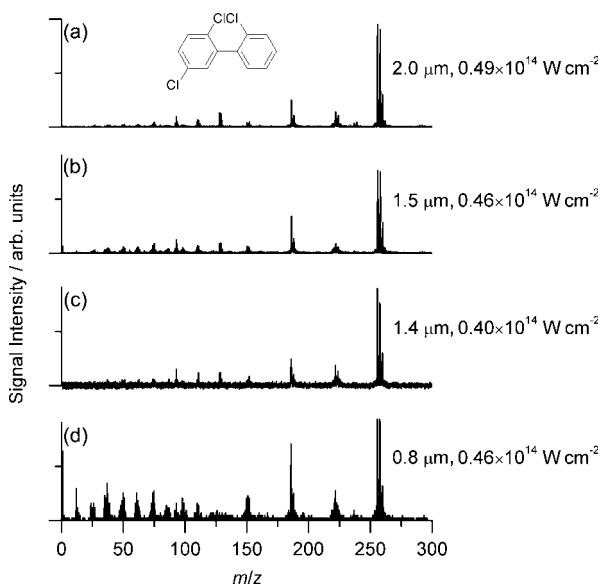


Fig. 26. TOF mass spectra obtained from 2,2',5-trichlorobiphenyl irradiated with 130 fs pulses at several different wavelengths. The singly charged molecular ion is distributed in the mass number from 256 to 262. The fragment ions are a one-chloride atom loss ($[M-\text{Cl}]^+$) radical, a two-chloride atom loss ($[M-2\text{Cl}]^+$) radical, a three-chloride atom loss ($[M-3\text{Cl}]^+$) radical, and their doubly charged ions.

large singly and doubly charged molecular ions were detected by $0.8 \mu\text{m}$ excitation, and many fragment ions were included. The chlorine atom has two isotopes of 35 (75.8%) and 37 (24.2%); therefore, the molecular ions are distributed at mass numbers from 256 to 262, and strong peaks are expected at 256 and 258. As shown in Fig. 12, biphenyl exhibited distinctly different spectra for excitation at 0.8 (with many fragments) and $1.4 \mu\text{m}$ (molecular ions are dominant). In the case of chlorinated biphenyl, the degree of fragmentation was higher than that of non-substituted biphenyl at both wavelengths. The following fragment ions were detected: a one-chloride atom loss ($[M-\text{Cl}]^+$) radical, a two-chloride atom loss ($[M-2\text{Cl}]^+$) radical, a three-chloride atom loss ($[M-3\text{Cl}]^+$) radical, and their doubly charged ions. Long wavelength excitation of $1.4\text{--}2.0 \mu\text{m}$ gave low intensities of fragments compared with those at $0.8 \mu\text{m}$. The highest intensity among the fragments was $[M-2\text{Cl}]^+$. The Cl loss reactions were consistently observed at all wavelengths examined here.

Even a short pulse of 50 fs instead of 130 fs was not found to suppress chlorine atom elimination. The C-Cl bond may have a low-lying dissociation channel in the cation, and/or the dissociation could have occurred due to the low bond dissociation energy. In the case of benzene and the chlorinated compounds, the C-Cl bond dissociation energy of 400 kJ mol^{-1} is 85% of the C-H bond.⁴⁹

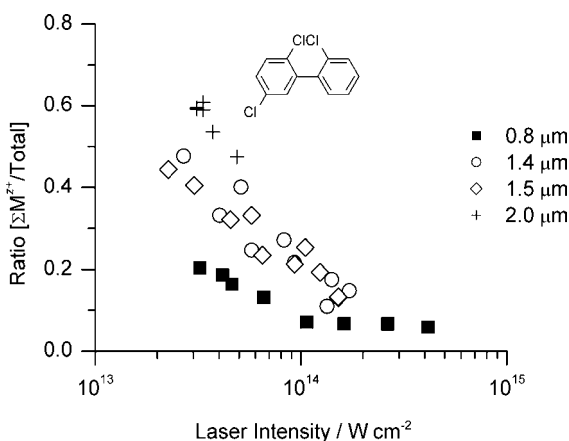


Fig. 27. 2,2',5-Trichlorobiphenyl wavelength dependence of M/T ratio. The ratio decreases with increases in laser intensity and wavelength. A similar tendency was noted in the case of biphenyl in Fig. 13. The I_{sat} values at different wavelengths were in the range of $4.4\text{--}6.5 \times 10^{13} \text{ W cm}^{-2}$.

Figure 27 shows the M/T ratios of 2,2',5-trichlorobiphenyl at four wavelengths as a function of irradiation intensity. The M/T ratio increased at the longer wavelength and lower laser intensity. A similar tendency has been observed in the case of biphenyl, as shown in Fig. 13. The I_{sat} values at different wavelengths were in the range of $4.4\text{--}6.5 \times 10^{13} \text{ W cm}^{-2}$. The M/T ratios of trichlorobiphenyl at $1.4 \mu\text{m}$ were 0.3 at an intensity near the I_{sat} , and the M/T ratio of 0.3 was smaller than 0.5 for biphenyl, as can be seen in Fig. 13. The maximum M/T ratio of 0.4 was observed at a wavelength of $2.0 \mu\text{m}$ at $5 \times 10^{13} \text{ W cm}^{-2}$ which is close to the I_{sat} values.

1,3,6-Trichlorodibenzo-*p*-dioxin was ionized $1.4 \mu\text{m}$, and the spectra are shown in Fig. 28. M^+ , M^{2+} , and numerous fragments were observed;

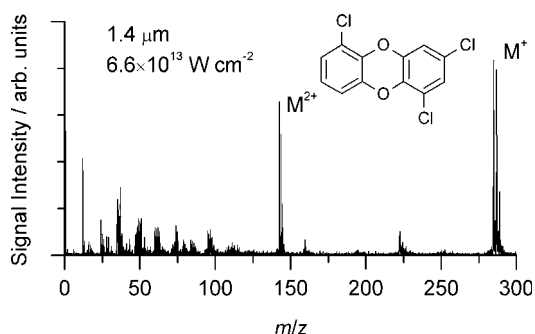


Fig. 28. TOF mass spectra of 1,3,6-trichlorodibenzo-*p*-dioxin ionized by 130 fs pulses at $1.4 \mu\text{m}$. The molecular ion intensity, M^+ , was the highest. M^{2+} is the doubly charged molecular ion.

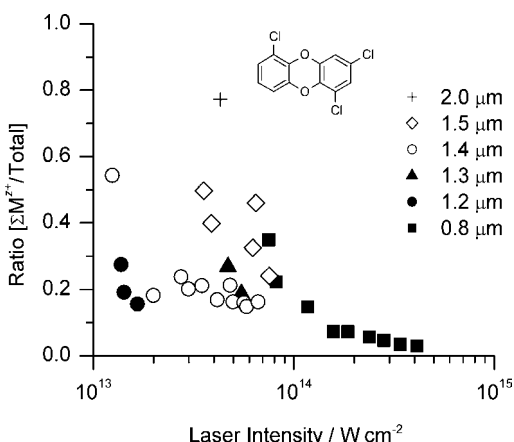


Fig. 29. The M/T ratios at several excitation wavelengths of 1,3,6-trichloro-dibenzo-*p*-dioxin. About 0.2 at the I_{sat} of $0.33 \times 10^{14} \text{ W cm}^{-2}$ ($1.4 \mu\text{m}$).

however, the molecular ion intensities were higher at 1.4 μm than at 0.8 μm . The M/T ratio was about 0.2 at an I_{sat} of $0.33 \times 10^{14} \text{ W cm}^{-2}$ (1.4 μm), as shown in Fig. 29. A longer wavelength gave a somewhat higher M/T ratio. Further study will be required to clarify the actual wavelength dependency.

In general, as regards the ionization of chlorinated compounds, longer wavelength excitation gives higher M/T ratio at the I_{sat} value.

Acknowledgments

The authors would like to thank Mr. M. Tanaka for the helpful discussions about the present topic. This work was financially supported in part by a Grant-in-Aid (No 14077214) from the Ministry of Education, Culture, Sports, Science and Technology Japan to N.N.

References

1. M. J. DeWitt, R. J. Levis, *J. Chem. Phys.* **102**, 8670 (1995).
2. J. P. Reilly, K. L. Kompa, *J. Chem. Phys.* **73**, 5468 (1980).
3. E. W. Schlag, H. J. Neusser, *Acc. Chem. Res.* **16**, 355 (1983).
4. H. J. Neusser, *J. Phys. Chem.* **93**, 3897 (1989).
5. V. R. Bhardwaj, K. Vijayalakshmi, D. Mathur, *Phys. Rev. A* **59**, 1392 (1999).
6. S. Hunsche, T. Starczewski, A. l'Huillier, A. Persson, *et al.*, *Phys. Rev. Lett.* **77**, 1966 (1996).
7. J. Kou, N. Nakashima, S. Sakabe, S. Kawato, *et al.*, *Chem. Phys. Lett.* **289**, 334 (1998).
8. E. E. B. Campbell, K. Hoffmann, H. Rottke, I. V. Hertel, *J. Chem. Phys.* **114**, 1716 (2001).
9. V. R. Bhardwaj, P. B. Corkum, D. M. Rayner, *Phys. Rev. Lett.* **91**, 203004 (2003).
10. P. Wurz, K. R. Lykke, *J. Phys. Chem.* **96**, 10129 (1992).
11. R. J. Levis, M. J. DeWitt, *J. Phys. Chem.* **103**, 6493 (1999).
12. L. Robson, K. W. D. Ledingham, A. D. Tasker, P. McKenna, *et al.*, *Chem. Phys. Lett.* **360**, 382 (2002).
13. L. Robson, A. D. Tasker, K. W. D. Ledingham, P. McKenna, *et al.*, *Int. J. Mass Spectrom.* **220**, 69 (2002).
14. A. N. Markevitch, D. A. Romanov, S. M. Smith, H. B. Schlegel, *et al.*, *Phys. Rev. A* **69**, 013401 (2004).
15. M. Murakami, R. Mizoguchi, Y. Shimada, T. Yatsushashi, N. Nakashima, *Chem. Phys. Lett.* **403**, 238 (2005).
16. W. Fuß, W. E. Schmid, S. A. Trushin, *J. Chem. Phys.* **112**, 8347 (2000).
17. R. Itakura, J. Watanabe, A. Hishikawa, K. Yamanouchi, *J. Chem. Phys.* **114**, 5598 (2001).
18. H. Harada, S. Shimizu, T. Yatsushashi, S. Sakabe, *et al.*, *Chem. Phys. Lett.* **342**, 563 (2001).
19. S. A. Trushin, W. Fuß, W. E. Schmid, *J. Phys. B: At. Mol. Opt. Phys.* **37**, 3987 (2004).

20. H. Harada, M. Tanaka, M. Murakami, S. Shimizu, *et al.*, *J. Phys. Chem. A* **107**, 6580 (2003).
21. M. Lezius, V. Blanchet, M. Yu. Ivanov, A. Stolow, *J. Chem. Phys.* **117**, 1575 (2002).
22. M. Suzuki, S. Mukamel, *J. Chem. Phys.* **120**, 669 (2004).
23. V. R. Bhardwaj, D. M. Rayner, D. M. Villeneuve, P. B. Corkum, *Phys. Rev. Lett.* **87**, 253003 (2001).
24. V. R. Bhardwaj, P. B. Corkum, D. M. Rayner, *Phys. Rev. Lett.* **93**, 043001 (2004).
25. F. A. Rajgara, M. Krishnamurthy, D. Mathur, *Phys. Rev. A* **68**, 023407 (2003); *idem*, *J. Chem. Phys.* **119**, 12224 (2003).
26. E. E. B. Campbell, K. Hansen, K. Hoffmann, G. Korn, *et al.*, *Phys. Rev. Lett.* **84**, 2128 (2000).
27. R. Itakura, K. Yamanouchi, T. Tanabe, T. Okamoto, F. Kannari, *J. Chem. Phys.* **119**, 4179 (2003).
28. R. Mizoguchi, Y. Shimada, H. Shinohara, T. Yatsushashi, N. Nakashima, *Rev. Laser Eng.* **32**, 717 (1997) (in Japanese).
29. L. Robson, K. W. D. Ledingham, P. McKenna, T. McCanny, *et al.*, *J. Am. Soc. Mass Spectrom.* **16**, 82 (2005).
30. A. D. Tasker, L. Robson, K. W. D. Ledingham, T. McCanny, *et al.*, *Int. J. Mass Spectrom.* **225**, 53 (2003).
31. Y. Shimada, R. Mizoguchi, H. Shinohara, T. Yatsushashi, N. Nakashima, *Bunseki Kagaku* **54**, 127 (2005).
32. N. Nakashima, S. Shimizu, T. Yatsushashi, S. Sakabe, Y. Izawa, *J. Photochem. Photobiol. C* **1**, 131 (2000).
33. J. Posthumus, (ed.) *Molecules, Clusters in Intense Laser Fields* (Cambridge University Press, 2001).
34. P. Tournois, *Opt. Commun.* **140**, 245 (1997).
35. A. M. Müller, C. J. G. J. Uiterwaal, B. Witzel, J. Wanner, K.-L. Kompa, *J. Chem. Phys.* **112**, 9289 (2000).
36. X.-P. Tang, A. Becker, W. Liu, M. Sharifi, O. Kosareva, V. P. Kandidov, P. Agostini, S. L. Chin, *Phys. Rev. A* **71**, 045401 (2005).
37. S. M. Hankin, D. M. Villeneuve, P. B. Corkum, D. M. Rayner, *Phys. Rev. A* **64**, 013405 (2001).
38. M. V. Ammosov, N. B. Delone, V. P. Krainov, *Sov. Phys. JETP* **64**, 1191 (1986).
39. A. A. A. El-Zein, P. McKenna, W. A. Bryan, I. M. G. Johnston, *et al.*, *J. Physica Scripta* **T92**, 119 (2001).
40. S. Shimizu, V. Zhakhovskii, F. Sato, S. Okihara, *et al.*, *J. Chem. Phys.* **117**, 3180 (2002).
41. I. S. Gilmore, M. P. Seah, *Int. J. Mass Spectrom.* **202**, 217 (2000).
42. P. M. Johnson, *J. Phys. Chem.* **64**, 4143 (1976).
43. I. Gryczynski, G. Piszczek, Z. Gryczynski, J. R. Lakowicz, *J. Phys. Chem. A* **106**, 754 (2002); K. Ogawa, A. Ohashi, Y. Kobuke, K. Kamada, K. Ohta, *J. Am. Chem. Soc.* **125**, 13356 (2003); F. E. Hermández, K. D. Belfield, I. Cohanoschi, M. Balu, K. J. Schafer, *Appl. Opt.* **43**, 5394 (2004).
44. J. Kou, V. Zhakhovskii, S. Sakabe, K. Nishihara, *et al.*, *J. Chem. Phys.* **112**, 5012 (2000).
45. A. N. Markevitch, D. A. Romanov, S. M. Smith, R. J. Levis, *Phys. Rev. Lett.* **92**, 063001 (2004).
46. P. Kruit, J. Kimman, H. G. Muller, M. J. van der Wiel, *Phys. Rev. A* **28**, 248 (1983).

47. M. J. DeWitt, R. J. Levis, *Phys. Rev. Lett.* **81**, 5101 (1998).
48. P. B. Corkum, *Phys. Rev. Lett.* **71**, 1994 (1993).
49. Y.-R. Luo, *Handbook of Bond Dissociation Energies in Organic Compounds* (CRC Press LLC, 2003).
50. C. Spielmann, N. H. Burnett, S. Sartania, R. Koppitsch, *et al.*, *Science* **278**, 661 (1997).
51. N. Hay, M. Castillejo, R. de Nalda, E. Springate, K. J. Mendham, J. P. Marangos, *Phys. Rev. A* **61**, 053810 (2000).
52. F. A. Ilkov, J. E. Decker, S. L. Chin, *J. Phys. B: At. Mol. Opt. Phys.* **25**, 4005 (1992).
53. M. Smits, C. A. de Lange, A. Stolow, D. M. Rayner, *Phys. Rev. Lett.* **93**, 203402 (2004).
54. M. Smits, C. A. de Lange, A. Stolow, D. M. Rayner, *Phys. Rev. Lett.* **93**, 213003 (2004).
55. A. Talebpour, S. Larochele, S. L. Chin, *J. Phys. B: At. Mol. Opt. Phys.* **31**, 2769 (1998).
56. T. Shida, *Electronic Absorption Spectra of Radical Ions* (Elsevier, New York, 1988).
57. R. Billotto, R. J. Levis, *J. Phys. Chem. A* **103**, 8160 (1999).
58. F. P. Colonna, G. Distefano, V. Galasso, K. J. Irgolic, *et al.*, *J. Organometallic Chem.* **146**, 235 (1978).
59. R. D. Webster, G. A. Heath, *Phys. Chem. Chem. Phys.* **3**, 2588 (2001).
60. K. A. Holbrook, M. J. Pilling, S. H. Robertson, *Unimolecular Reactions*, 2nd ed., (John Wiley & Sons Ltd., 1996).
61. M. Castillejo, S. Couris, E. Koudoumas, M. Martín, *Chem. Phys. Lett.* **289**, 303 (1998).
62. D. J. Smith, K. W. D. Ledingham, R. P. Singhal, H. S. Kilic, *et al.*, *Rapid Commun. Mass Spectrom* **12**, 813 (1998).
63. A. Matsuura, T. Nishinaga, K. Komatsu, *J. Am. Chem. Soc.* **122**, 10007 (2000).
64. R. J. Levis, G. M. Menkir, H. Rabitz, *Science* **292**, 709 (2001).
65. D. Mathur, F. A. Rajgara, *J. Chem. Phys.* **120**, 5616 (2004).
66. B. P. Tsai, J. H. D. Eland, *Int. J. Mass. Spectrom. Ion Phys.* **36**, 143 (1980).
67. M. Suresh, J. McKenna, B. Srigengan, I. D. Williams, *et al.*, *Rutherford Appleton Lab. Central Laser Facility Ann. Rep.* 67(2003/2004).
68. T. Yatsushashi, N. Nakashima, *J. Phys. Chem. A* **109**, 9414 (2005).
69. NIST Chemistry WebBook, NIST Standard Reference Database Number **69**, eds. P. J. Linstrom, W. G. Mallard, National Institute of Standards and Technology, Gaithersburg MD, 2E99 (<http://webbook.nist.gov>) 2003.
70. X. Fang, K. W. D. Ledingham, P. Graham, D. J. Smith, *et al.*, *Rapid Commun. Mass Spectrom.* **13**, 1390 (1999).
71. A. D. Tasker, L. Robson, S. M. Hankin, K. W. D. Ledingham, *et al.*, *Laser, Particle Beams* **19**, 205 (2001).
72. S. M. Hankin, A. D. Tasker, L. Robson, K. W. D. Ledingham, *et al.*, *Rapid Commun. Mass Spectrom.* **16**, 111 (2002).
73. A. D. Tasker, L. Robson, K. W. D. Ledingham, T. McCanny, *et al.*, *J. Phys. Chem. A* **106**, 4005 (2002).
74. C. Weickhardt, K. Tönnies, *Rapid Commun. Mass Spectrom.* **16**, 442 (2002).
75. C. Grun, C. Weickhardt, J. Grottemeyer, *Eur. Mass Spectrom.* **2**, 197 (1996).
76. N. P. Lockyer, J. C. Vickerman, *Int. J. Mass Spectrom.* **176**, 77 (1988).

77. R. Zimmermann, U. Bosel, C. Weickhardt, D. Lenoir, *et al.*, *Chemosphere* **29**, 1877 (1994).
78. J. Matsumoto, C.-H. Lin, T. Imasaka, *Anal. Chem.* **69**, 4524 (1997).
79. N. Kirihara, H. Yoshida, M. Tanaka, K. Takahashi, *et al.*, *Organohalogen Compounds* **66**, 731 (2004).
80. Japan Patent 2003-121416.